A synthetic approach to the construction of stimuli-responsive proteinosome membranes

Mary Jenkinson-Finch

A dissertation submitted to the University of Bristol in accordance with the requirements for award of the degree of DOCTOR OF PHILOSOPHY in the School of Chemistry, Faculty of Science

March 2022

Word count: 45,320

Abstract

A major challenge facing bottom-up synthetic biology research is the construction of protocell populations able to respond to external signals, creating functional protocellular ecosystems with emergent behaviours. The aim of this thesis is to construct stimuli-responsive protocell models (proteinosomes) via chemical programming of the crosslinked membrane as a step towards this.

The polyethylene glycol (PEG) based crosslinker traditionally used in proteinosome synthesis has the potential to be easily functionalised with the addition of responsive moieties. Chapter 2 presents the synthesis and characterisation of two novel stimuli-responsive crosslinkers with embedded responsive moieties and terminating N-hydroxy succinimide (NHS) groups for protein crosslinking. One cleaves in response to UV light, and the other in response to a decrease in pH. The synthetic routes and full characterisation are presented and crosslinker cleavage under a variety of conditions is described.

The choice was made to focus research into light-responsive proteinosomes due to ease of synthesis and higher potential with regards to disassembly control. Chapter 3 outlines the synthesis and characterisation of chemically programmed light-responsive proteinosomes. A UV laser in a confocal microscope system is employed causing complete disassembly of the proteinosome membranes. Tuneable parameters, laser power and laser scan speed, are investigated as methods to control disassembly. Confocal software-controlled positioning systems allow targeting of individual proteinosomes, and bespoke 2D patterning within proteinosome populations in a simpler method not possible for other phenotypes of proteinosome.

Chapter 4 presents an in-depth analysis of the light-responsive proteinosome membrane. A novel mathematical model to describe the inherent membrane pores is produced, agreeing with experiments determining membrane molecular weight cut-off. An investigation light-induced selective release based on molecular weight of substrates is shown with the permeability constants of substrates estimated. These experiments are a step towards the design and synthesis of bespoke proteinosome membranes and developing complex functional microsystems.

Acknowledgments

I would like to thank my supervisor, Professor Stephen Mann, for the opportunity to undertake research in his lab and for all the knowledge and insight over the years. I would also like to thank Dr Pierangelo Gobbo and Professor Wuge Briscoe who supported me, and without whom I would never be where I am today.

To my lab mates, friends, and supporters who I have worked with over the years, Liangfei Tian, Matt Mulvee, Ning Gao, Patrick Peschke, Florian Hastert, Iuliia Myrgorodska, Angela Suriyakumaran, Rafael Moreno, Hannah Taylor, Patrick Grimes, Izzy Scott Douglas, and Aina Rebasa, thank you for making my PhD fun and for being a constant source of inspiration.

To those who were not physically with me in the lab but were my supporters in evenings and weekends, Laura Sharp, Cate Jackson, Hannah Sweetnam, Kathy Cox, Ali Anthony, Ed Mahoney, Becca Daltry, Ben Willbourn, Grace Bowen, Daniel Field, Siúbhan O'Donnell, thank you for your words and support that kept me going.

To my neighbours, Hazel, Jozef, Abi, Laura, Lucy, Tom, and Cloé, those dark days of doing a PhD during a pandemic would have been considerably worse without you.

To those who lived with me over the last four years, Grace Robertson, and Mel Pereira, thank you for feeding me and keeping me sane. I truly believe I would be dead without you both.

To those who I am indebted to for their help and support, Ella Carter, Joanna Sparks, Sam Briggs, Noha Abu El Magd, and Alex Croot, without you all I would not have been able to do it and I am eternally grateful.

And finally, my family, in particular Mum, Dad, Lisa, Catriona, Amy, and Dylon, for your unwavering support and for believing in me when I had no belief in myself, thank you.

Covid-19 Statement

From the 24th March 2020 until 22nd June 2020, I was unable to undertake any laboratory work when the School of Chemistry closed due to the pandemic. My PhD project relied heavily on synthesis and microscopy, both of which I could not do during the lockdown. Upon reopening, the facilities and services were highly restricted. Social distancing requirements meant there were limitations on how many people were able to work in a laboratory at one time, and so a week-on week-off rota was put in place from June 2020 until I left the lab in February 2021. Further to this, communal centres, such as the microscope centre, have had strict limits on usage. This meant my final year was highly disrupted and has required me to change significant amounts of my thesis.

The fourth chapter was planned to be light-triggered communication between protocells which required the use of enzymes and a technique utilising confocal fluorescence microscopy. Attempts were made to synthesise protocells encapsulating enzymes however, due to the week-on week-off rota, the experiments were consistently unsuccessful as the enzymes would not survive the week out of the lab. Further, the limitation to the communal microscopy unit meant it was very difficult to book. Instead, the fourth chapter is mostly a theoretical mathematical description of the proteinosome membrane, with some experiments to compare with the theoretical results.

I declare that the work in this dissertation was carried out in accordance with the requirements of the University's *Regulations and Code of Practice for Research Degree Programmes* and that it has not been submitted for any other academic award. Except where indicated by specific reference in the text, the work is the candidate's own work. Work done in collaboration with, or with the assistance of, others, is indicated as such. Any views expressed in the dissertation are those of the author.

SIGNED: Mary Jenkinson-Finch DATE: 15th March 2022

Table of Contents

Chapter 1: Introduction

Chapter Outline

In the current field of bottom-up synthetic biology, the creation of minimal cells called protocells aims to help solve the question of how chemistry became biology. A major challenge within this field is the creation of protocell populations capable of communication and novel behaviours. The integration of “smart” material functionality into protobiology helps to tackle this challenge. This thesis aims to incorporate smart functionality into protocells (proteinosomes) and so this introduction chapter presents background information to provide context for the work in the following chapters.

1.1 What is life?

Life evolved about 600 million years after the earth formed. Today, we know lots about what makes something “alive”, but for centuries the question of “what is life?” has fascinated humans. Automata are self-operating machines which mimic life and lifelike behaviours and have been built by many different civilisations. The ancient Egyptians would build statues of divinities which kings would go to for advice, and the statues would answer by movements of the head.[1] Examples of automata can be found through medieval history as well, with lifelike lions guarding the Byzantium court by moving and roaring in the 9th century BC.[2] In the 1700’s, the French inventor Jacques de Vaucanson produced many automata, including waiters that would serve and clear dinner, and famously his “digesting duck” which seemingly ate and digested food.[3] Of course, these inventions were merely clever pieces of clockwork machinery, but they challenged thinking into what makes something “alive”.

In the early- to mid-19th century, there were limited theories about what life was, but one was spontaneous generation; the idea that life was constantly restarting. Louis Pasteur demonstrated that this could not happen with the conditions on earth today with his experiments showing microbes only grew in a boiled meat broth when particles from the air were permitted to enter.[4] These experiments were important in developing the idea of germ theory of disease, and led to his name used to name pasteurisation, as a method of preservation. In the early 20th century, Oparin’s origin

of life theory[5] was that life manifested from the evolution of chemical matter and in ca. 1952, experiments by Miller and Urey supported this. They recreated the 'atmosphere' of the early earth with mixtures of gases (methane, ammonia, hydrogen, and water vapour) and passed through electric sparks to represent lighting as a source of energy. After cooling, the condensed mixture contained many organic compounds including amino acids.[6] Oparin went on to outline coacervation into droplets as a way basic chemicals could have formed localised systems leading to more complex living things evolving through natural selection.[7]

1.1.1 The cell

It is now known that living organisms are made of cells. Cell theory began in 1665 when Robert Hooke observed cork through a microscope and described what he saw as "tiny pores", which he later named cells (**Figure 1.1**[8,9]). Shortly after, Dutch scientist Antonie van Leeuwenhoek used microscopy to discover motile bacteria and protozoa, although at the time he named them "animalcules".[10] These early discoveries have developed into cell theory known today, in which cells are the smallest unit making up an organism, much like the atom to an element or compound. It has been found that there are two types of cells: prokaryotes (without a nucleus) and eukaryotes (with a nucleus). Eukaryotic cells are the more complex of the two, and contain membrane bound compartments called organelles inside which chemical reactions take place, specific to each organelle.[11]

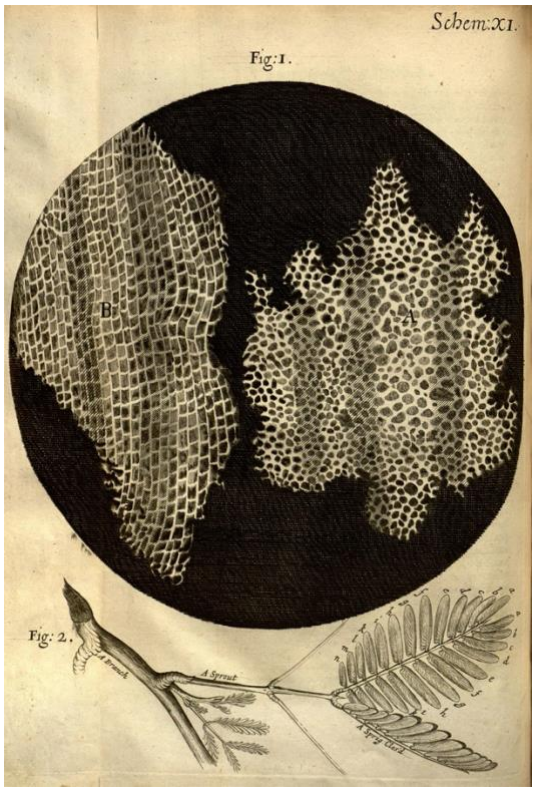

Figure 1.1 A drawing of the cells of cork seen by Hooke using an early microscope.

Living cells have certain characteristics which differentiate them from non-living matter[11,12]:

- Self-reproduction where cells divide, duplicating their genetic material into the daughter cells
- Organisation of cells into different tissues which work together to perform a function, in multi-cellular organisms
- Compartmentalisation, both the external membrane and internal organelles to ensure the system is out of equilibrium and that substrates are concentrated for chemical reactions
- The ability to respond to the environment, for example phototaxis where the organism will move toward or away from light

Further, eukaryotic cells are capable of information processing from their environment. Information can be physical stimuli such as light reaching the eyes, or chemical such as food interacting with taste buds. It can come from inside the organism like the brain communicating with heart cells to tell them to beat, or outside the organism such as

pheromones, which is the method insects use to communicate with each other. Cells have specific receptors to process specific stimuli, and the information is used to perform cellular processes. Cells inside an organism are physically far away from the external environment so they will be responding to chemical signals from the surrounding cells by local diffusion or circulation in the blood. These signals are usually very small in concentration, as low as 10^{-10} M.[11]

The cell membrane is the barrier between the internal environment of the cell and external environment. It has several functions: transporting essential chemicals into the cell and exporting waste out; providing structural support; and interacting with other cells, and the environment. The cell membrane consists of lipids, proteins, and carbohydrates. Lipids form the basis of the membrane within which proteins "float". The fluid mosaic model is used to describe the design of a biological membrane: mosaic because it is made of lots of discrete units, and fluid because the parts can move freely. Specially functioning proteins within the membrane are non-covalently embedded in the lipids by their hydrophobic regions. Carbohydrates are attached to the lipids or the proteins, and they are used to recognise specific molecules on other cell surfaces for example.[11–13]

1.2 Synthetic Biology

One of the aims of synthetic biology is to recreate the properties of living systems within chemical systems.[14] This gives insight into what it is that makes something alive, and whether this can be recreated in a laboratory setting.[12,15] Within synthetic biology, there are two approaches to the creation of artificial cells (**Figure 1.2**). The top-down approach involves the simplification of living cells to reduce complexity whilst keeping enough parts of the system for the cell to be "alive". The bottom-up approach is the use of materials, both biological and chemical, to construct a cell which displays living behaviours.[16] Both these approaches converge on the production of a minimal cell which displays life-like properties.

As discussed, there are certain properties belonging to cells which are essential for their basic function (compartmentalisation, self-organisation, self- reproduction, and the ability to communicate with the environment and other cells).[17]

Compartmentalisation is particularly important, highlighted by the fact that nearly all living processes take place within compartments or sub-compartments such as organelles. Some bottom-up approach research has therefore focused on self-assembling compartmentalisation in the synthesis of artificial cells.[15] Other bottom-up approaches have focussed on the encapsulation of biologically relevant material, such as DNA or proteins/enzymes, to perform simple biochemical reactions and therefore mimicking cell behaviours.[18] Although these are less relevant in terms of the origins of life (since the chemicals were unlikely present on early earth), they are interesting soft-matter materials capable of being engineered to perform smart functions, and so are useful in fields such as microbioreactors and drug-delivery.[19]

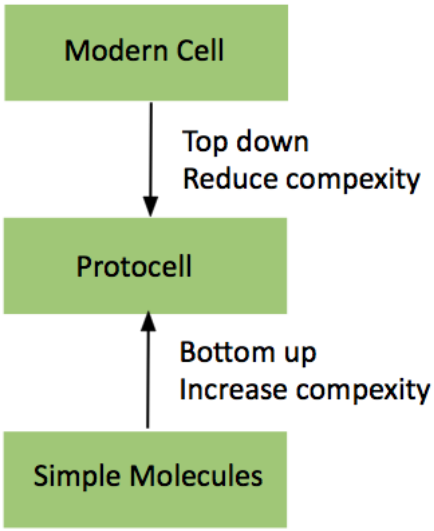

Figure 1.2 A schematic showing the two approaches to the formation of the minimal cell, or protocell. One is to reduce complexity of organisms (top down) and the other is to use molecular building blocks to construct a minimal cell (bottom up).

1.2.1 Protocell models

Protocell science has begun to address this challenge with the creation of cell-like entities that are biomimetic, often self-organising, and built using synthetic materials.[16] Many examples have been synthesized that are membrane bound; amphiphilic molecules are commonly used which spontaneously form droplets in oil and water mixtures. Phospholipids are well known amphiphiles capable of

spontaneously forming droplets called liposomes at their critical aggregation concentration. These compartments are permeable to small neutral molecules and are argued to be a plausible model for the first early cell as organic amphiphiles were likely available on the early earth.[20] Fatty acids are another amphiphilic molecule consisting of an aliphatic chain terminating in a carboxylic acid group. They assemble into vesicles at a pH range of 7-9,[21] are robust up to 90 °C[22], and are permeable to small cations.[23] They have also been shown to express simple growth cycles.[24] However, with low encapsulation efficiency, sensitivity to pH changes and a lack of internal structure, fatty acid vesicles are not likely to have formed as the first cells.[19]

Coacervates are a membrane-less protocell model formed by a liquid-liquid phase separation. They were theorised by Oparin to be a prime candidate for the first cell, as they form localised concentrations of substrates to perform chemical reactions. The high affinity the two liquids have for each other overcomes the entropy gain from mixing with the rest of the components in the system.[19,25] Usually, two oppositely charged polyelectrolytes are used but neutral polyelectrolytes are able to form coacervates via other interactions, for example pi-cation interactions.[26] Coacervation has also been shown to be pH-induced[27], and the coacervate phase can be crosslinked to form microspheres.[28] Yin *et al*[28] showed that thermally induced coacervation of aqueous solutions of poly(N,N-dimethacrylamide-co-glycidyl methacrylate) (DMA-GMA) could be chemically crosslinked with polyamides to produce hydrogel microspheres. Further, spontaneous fatty acid membrane assembly on the surface of preformed coacervate microdroplets has also been investigated, with the interior of the hybrid-protocell able to be disassembled *via* addition of salt (*i.e.* increased ionic strength) leaving the membrane intact.[29]

More recently, protocell models have been fabricated using more complex materials, sometimes non-biological. These protocell models have less origin of life relevance due to the complexity of the materials, but the materials can often be synthesised with specific functions in mind. Polymersomes are one such protocell model that are formed from self-organisation of hydrophilic-hydrophobic block co-polymers. They are similar to liposomes with their aqueous interior but are more versatile, as the thickness of the membrane, permeability, and stability can be controlled due to the large variety of polymers available to use[30,31] There are many examples of polymersomes used for

drug delivery[32] and in nanomedicine, since they show capability of encapsulating many substrates and their tough membranes are more likely to withstand circulation within the bloodstream.[33] Hybrid polymer stabilised coacervates were recently synthesised that have a spontaneous interfacial assembly of a biodegradable triblock copolymer, giving the novel protocell model higher integrity due to the membrane and allowing chemical communication between protocell populations.[34]

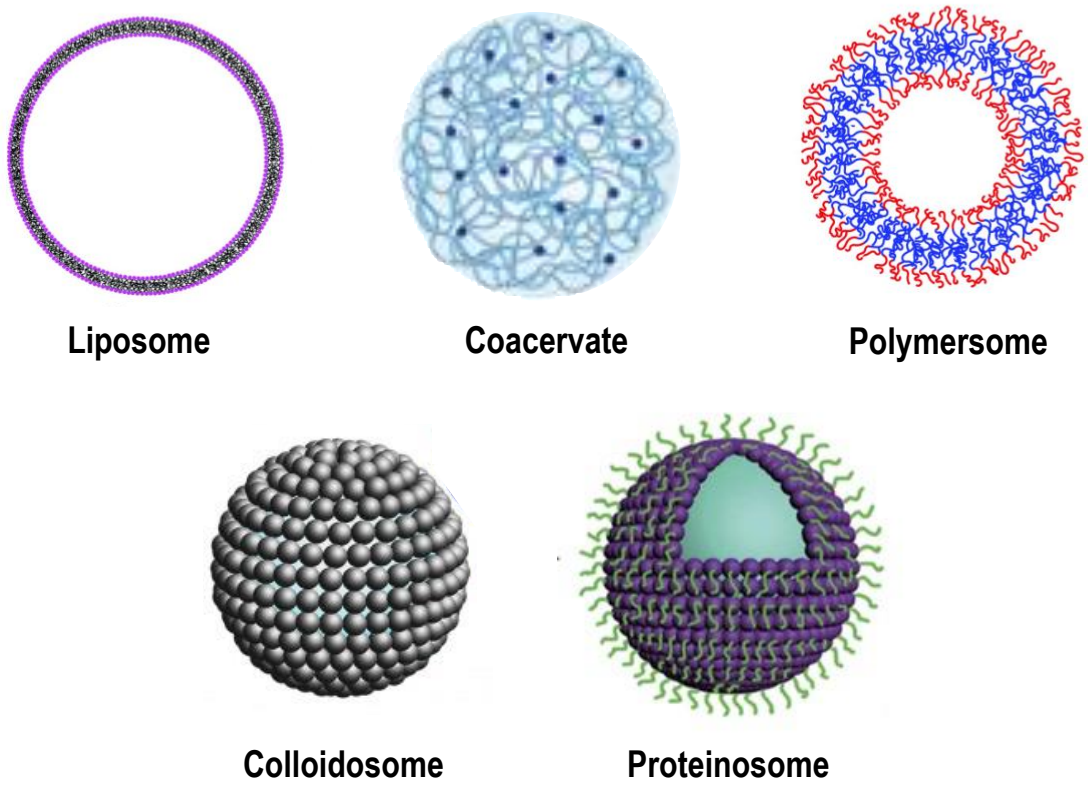

Figure 1.3 A schematic showing various protocell models used in the field of synthetic biology: liposomes which have a self-assembled lipid membrane; coacervates formed *via* liquid-liquid phase separation; polymersomes formed *via* self-organisation of hydrophilic-hydrophobic block co-polymers; colloidosomes formed *via* the stabilisation of an oil-water interface by colloidal particles (Pickering emulsion); and proteinosomes formed *via* a Pickering emulsion method using surface-active hybrid protein-polymer nanoconjugates.

1.2.2 Colloidosomes

Emulsion-based assemblies (colloidosomes) based on the stabilization of oil-water interfaces using silica nanoparticles were first developed in the early twenty first century.[35] The stabilisation of the droplet is similar to that of amphiphilic surfactants, except it is solid colloidal particles that adsorb to the interface between the two immiscible liquids.[36] This type of emulsion is called a Pickering emulsion. The particles do not need to be amphiphilic like surfactants in a classic emulsion but must be able to allow partial wetting by both the oil and water phases. Instead of reducing the surface tension of the droplet, the particles reduce the size of the oil-water interface. When the contact angle with water (θ_w) > 90º, oil in water droplets form. When θ_w < 90º, water in oil droplets form. When θ_w = 90º, the energy to remove the particles from the interface is at a maximum, and this energy rapidly falls as the contact angle deviates from 90º. As the contact angle tends to be near 90 in these systems, the ratio of oil to water is often used to decide the type of emulsion formed. The energy is proportional to the square of the size of the particle, meaning that smaller particles are easier to remove from the interface and *vice versa*.[36] Pickering emulsions have advantages over classic emulsions as the high energy to remove the particles means the membrane is very stable and prevents droplet coalescence.

Silica particles are hydrophilic in their natural form and so are modified to give them more hydrophobic character before being used in a Pickering emulsion. This is done by converting some of the silonol surface groups to dimethylsilane ($O_2Si(CH_3)_2$). The silica particles at the interface can subsequently be crosslinked using alkoxysilanes such as tetramethyl orthosilicate (TMOS) and transferred to water. These crosslinked capsules have been shown to encapsulate biomolecules and perform biochemical reactions (gene expression)[37], have selective permeability[38], and mimic cell behaviours.[39,40] To mimic cell reproduction, spontaneous growth and division has been induced in populations of colloidosomes via organosilane-mediated methanol production, resulting in the expansion and separation of a second generation colloidosome.[40] To mimic the inter- and extra-cellular cytoskeletal of cells, enzyme-mediated hydrogel motifs have been constructed within colloidosomes[39] and further shown to form an outer matrix capable of heat-induced disassembly.[41]

1.2.3 Proteinosomes

Recently, the synthesis of 'giant' amphiphilic protein-polymer nanoconjugates capable of stabilising an oil-water interface (Pickering emulsion) have been reported.[42] The construction of a crosslinked colloidal membrane forming a protein membrane capsule has been widely used as a protocell model, named proteinosomes (**Figure 1.3**).[43,44] Firstly, a hybrid material made of protein and polymer was synthesised by reacting mercaptothiozoline-activated poly(N-iosopropylacrylamide) (PNIPAAm) with surface primary amine groups on cationised proteins, via a coupling reaction. The protein-polymer nanoconjugates were crosslinked with N-hydroxysuccinimide (NHS) functionalised PEG at the interface allowing successful transfer into water. Nanoconjugates were successfully synthesised using several different proteins: bovine serum albumin (BSA), myoglobin and haemoglobin.[42]

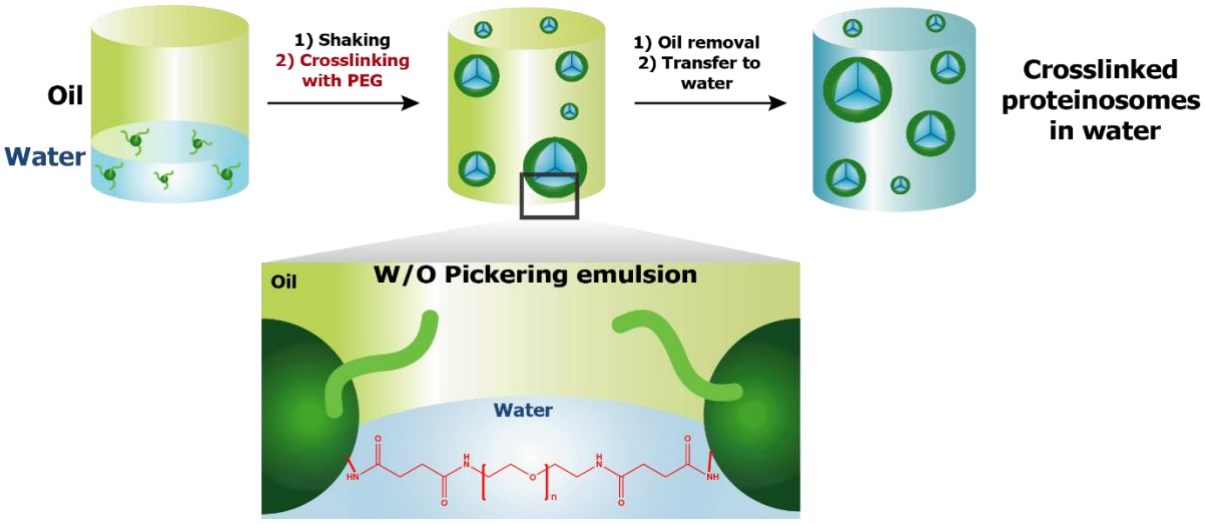

Scheme 1.1. The synthesis of proteinosomes begins with the dissolution of synthesised nanoconjugates in carbonate buffer. Oil (2-ethyl-1-hexanol) is added at a volume fraction of 0.06 and the vial is shaken which forms a Pickering emulsion. The droplets can be stabilised with PEG-bis(N- succinimidyl succinate) which reacts with the free amine groups on the protein surface before the transfer into water.

To form the Pickering emulsion, an aqueous solution of nanoconjugates was mixed with 2-ethyl-1-hexanol at an aqueous/oil volume fraction of 0.06. The crosslinker PEG-diNHS was added to the continuous oil phase before the two phases were mixed *via* shaking by hand. The resulting nanoconjugate stabilised droplets were left to sediment for 3 hours and then dialysed to remove the oil and excess crosslinker. It was shown that the size can be controlled by changing the concentration of protein-polymer nano-conjugates and keeping the volume fraction the same.[45] Fluorescent dye-labelled proteinosomes were synthesised by incorporating fluorescein O-methacrylate as a comonomer during PNIPAAm polymerization, but can also be facilely coupled to the BSA nanoconjugate surface. **Figure 1.4** shows rhodamine-b isothiocyanate (RITC) tagged proteinosome micro-capsules after transfer to water. The micro-capsules were shown to be capable of guest molecule encapsulation[42] and protein synthesis via gene expression.[42].

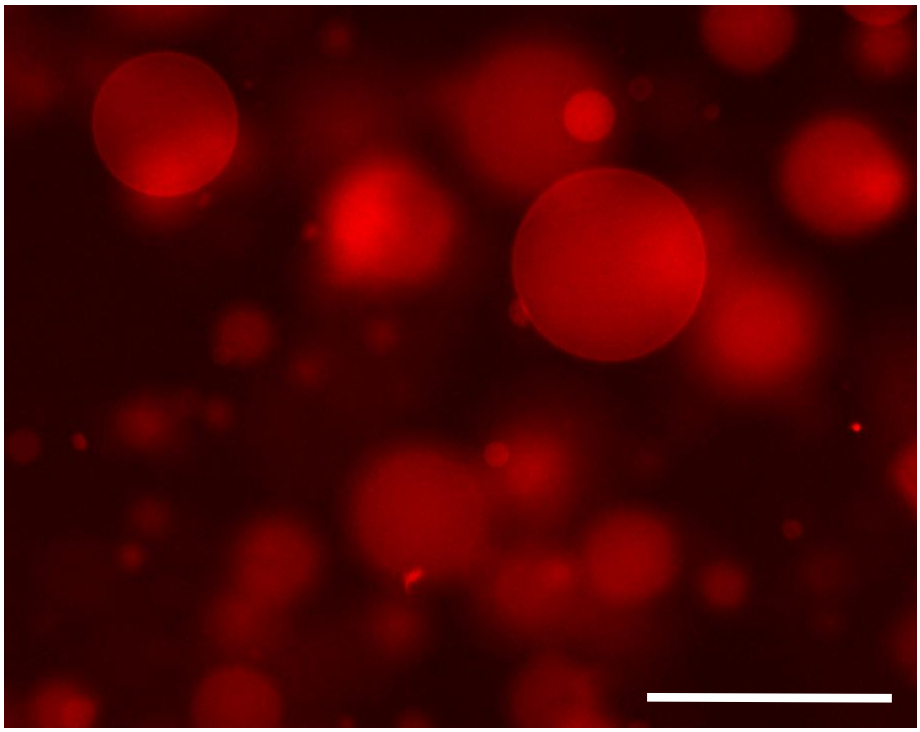

Figure 1.4. Fluorescent microscopy image of crosslinked proteinosomes tagged with rhodamine-b isothiocyanate (RITC) after transfer to water. Scale bar 50 μm.

1.2.3.1 Proteinosomes mimicking cell behaviour

Proteinosomes have been used as protocell models to mimic simple cell behaviours, such as the ability to perform biochemical reactions. They are capable of encapsulating enzymes (myoglobin) which retain their activity and do not diffuse through the membrane.[42] This enzymatic activity has been shown to be toggled-off after temperature increase due to changes in the PNIPAAm structure within the membrane. Further, through the incorporation of enzymes into the membrane, membrane-mediated enzyme cascade reactions could be performed upon substrate addition to the solution. Glucose amylase (GA), glucose oxidase (GO) and horseradish peroxidase were incorporated into the membrane by coupling PNIPAAm onto the primary amine groups on the enzyme surface. When starch was added to the solution of proteinosomes in buffered 2,2′-azino-di-(3-ethylbenzthiazoline sulfonic acid) (ABTS), a cascade reaction occurred. When GA was encapsulated within the protocell rather than integrated in the membrane, a 90% reduction in initial rate was shown. This was attributed to the impermeable membrane to macromolecules over 40 kDa preventing starch from diffusing through the membrane.[43] A cytoskeleton-like matrix has been formed within proteinosomes via amino-acid dephosphorisation of N-fluorenyl-methyloxycarbonyl-tyrosine-(O)-phosphate (Fmoc-TyrP) by encapsulation of alkaline phosphatase (ALP) enzymes, forming a hydrogel motif.[44] Proto-organelles have been constructed within the membrane of proteinosomes, both with protein nanoconjugate membranes (**Figure 1.5**)[45] and by the spontaneous formation of coacervate microdroplets.[46] These higher order proteinosome populations allow the local concentration of substrates within the protocell; they can be formed either before formation of outer membrane (proteinosome organelles) or after the formation of the outer membrane (coacervate organelles).

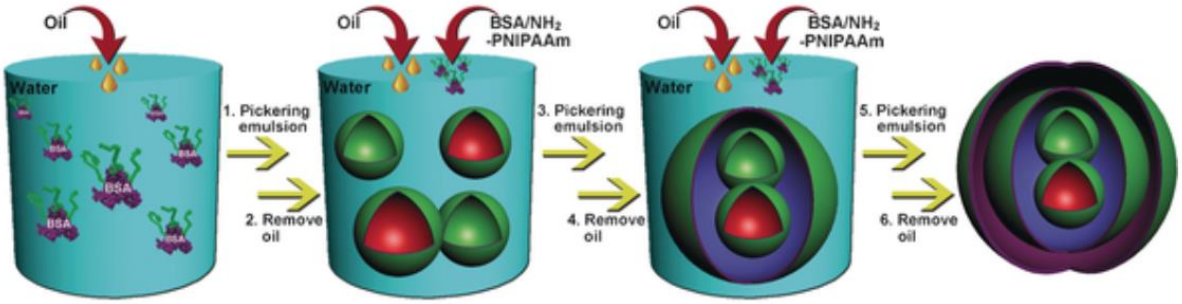

Figure 1.5. Synthesis of nested proteinosomes. Firstly, proteinosomes are made *via* a Pickering emulsion, and transferred to water. This process is repeated adding the guest proteinosomes to the aqueous phase of the Pickering emulsion, forming a larger host proteinosome membrane.[45]

1.2.4 Protocell-protocell communication

The next generation of protocells are those which should be able to interact with each other, interact with living cells, and show collective behaviours. In protocell science, communication between protocell populations is often shown using rudimentary enzyme cascade reactions. One example is that of a chemical communication pathway between a population of GOx-containing silica colloidosomes and ALP-containing Fe(III)-rich montmorillonite (FeM) clay colloidosomes. By triggering enzyme activity in the silica based population of protocells, a hydrogen peroxide signal is sent inducing polymer formation, which in turn induces membrane gating in the FeM clay protocells.[47] Another example of synthetic cell communication was demonstrated between lipid vesicles and proteinosomes. Upon addition of a transcription inducer (N-(3-oxohexanoyl)-L-homoserine lactone), lipid vesicles containing a cell-free expression system form α-hemolysin membrane pores, allowing the release of glucose molecules. Subsequently, proteinosomes containing GOx and HRP use the glucose in a cascade reaction to convert the substrate Amplex Red to a fluorescent product, resorufin. This example demonstrates the ability to for gene-directed chemical communication between protocells.[48] Recently, signalling in protocell populations over long distances (widely seen in organisms) has been achieved between lipid protocells via signal amplification, which tackles the problem of signal dilution in the extracellular environment.[49]

Other examples of protocell populations interacting are more direct; for example, a phagocytosis-inspired interaction between magnetic Pickering emulsion droplets (MPE) and colloidosomes caused by MPE droplet membrane destabilisation by surfactants (oleate molecules). The surfactants reduced the surface tension of the MPEs and creating an aperture which served as an entry point to take up the colloidosomes, and other payloads.[50] This system has the imminent potential to be implemented into existing technologies involving biological material transport, biological catalysis, and complex bioassays. Another system showing novel dynamic behaviours involved the rudimentary predation of one population of protocells by another. Coacervates loaded with protease were introduced to a population of proteinosomes loaded with other cargos such as sugar, DNA, or nanoparticles. These two populations were predisposed to interact with each other as they were synthesised to have opposite electrostatic charges. The protease in the coacervate droplets caused an enzyme-mediated breakdown of the membrane on the proteinosomes and subsequently the coacervates were able to take up the cargo within.[51,52] Controlled hydrogel-mediated membrane fusion of proteinosomes with subsequent delivery and redistribution of payloads has also been achieved.[53] Mixed populations of microcompartments, such as those described in these examples, have the potential to be used in synergistic sensing systems and biomimetic systems engineering.

Protocells can be physically linked together in a distinct spatial arrangement called prototissues. When protocells are joined in this manner, they show collective behaviours which are not seen in the individual protocells. One such prototissue is “A tissue-like printed material” first described by Hagan Bayley in 2013.[54] This was the first example of 3-dimensional conjoined protocells which showed collective behaviour in the form of programmable folding into structures unobtainable by other means. These were further developed to be light-responsive via the addition of light-activated DNA promotors to express pores and allow directional electrical communication.[55] Another example is a proteinosome-based prototissue spheroid synthesised with two proteinosome populations decorated with complimentary biorthogonal click groups. They are mixed and encapsulated within an outer proteinosome membrane and left to react for 48 hours. The outer shell can then be cleaved leaving behind the protein macrostructure, which is able to ‘beat’ upon a rise in temperature due to the thermal properties of the PNIPAAm chains, and encapsulate enzymes in the different

sub-compartments in the prototissue which are able to perform cascade reactions.[56] Further, the biorthogonal proteinosomes in combination with a floating PTFE mould were used to create prototissues on the centimetre scale, paving the way for spatially organised prototissue engineering.

1.2.5 Protocell-living cell communication

Protocells have been shown to communicate with living cells (population hybridisation)[57] through mechanisms of chemical signalling, similar to protocell-protocell communication described in **Section 1.2.4**. Mansy *et al* demonstrated the ability for lipid artificial cells to both sense and respond to chemical signals from various strains of bacteria using quorum pathways.[58] Proteinosomes have also been demonstrated to have the ability to communicate with living cells. The programmed interaction with E-coli was demonstrated through the construction of positively charged proteinosome membrane. The nanoconjugates were formed with specially synthesised methacryloxyethyl dimethylethane ammonium bromide (MEDAB) PNIPAAm via RAFT copolymerisation. Negative E-coli are attracted to the positively charged proteinosomes, then quaternary ammonium salt in the membrane selectively kills the bacteria on the surface. The inclusion of an antimicrobial within an acid-sensitive hydrogel inside the proteinosomes meant that a decrease in pH caused by local E-coli caused the release of the antimicrobial and subsequent death of surrounding E-coli.[59] Proteinosomes have also been constructed with the aim of causing cancer cell death showing promising application in gel therapy. These capsules had a glutathione-sensitive membrane (contained sulphide bonds) and contained a sodium alginate gel, so when they were taken up by cancer cells (via endocytosis), high concentrations of glutathione caused the membrane to disassemble. The release of the gel caused flow through the cytoplasm to slow to the point of cell death.[60] Other examples of protocell-living cell communication include hybrid cells where synthetic cells are encapsulated in living cells or *vice versa*,[61,62] and examples of networks of hybrid protocell-living cell prototissues.[63]

1.3 Stimuli-responsive materials

The advancements in polymer synthesis and characterisation, and subsequent understanding of polymeric systems have led to a vast toolbox of “smart” materials with predictable and tuneable properties.[64] These materials can be made with polymers that are responsive to a stimulus or sometimes multiple stimuli which cause a conformational and/or chemical change in the molecule, accompanied by changes in the physical properties[65]. Applications of these materials are vast, ranging from controlled release[66], drug delivery[67], responsive coatings[68], and patterning[69]. Many available stimuli that can induce a response in smart materials have been explored including temperature, mechanical stress, pH, and light.

1.3.1 Stimuli-responsive protocell models

The engineering of biological cells using synthetic materials, or biointerfacing, has been identified as a considerable challenge in biomedical research.[70] Natural polymeric systems within cellular environments respond to signals and triggers from the environment in order to sustain life.[65] The complex nature of microenvironments in tissues elicits a need for the synthetic materials interacting and integrating with biological systems to also have responsive behaviours, in order to further the understanding of cellular systems and for uses in the biomedical industry, such as cell-regeneration.[71] By combining smart polymer systems with biocompatible surfaces and nano/microcompartments, we can begin to create biointerfaces that are more equipped to respond and adapt to cellular environments, and with an increased potential for use in in the biomedical industry.

With a particular focus on light and pH response (light due to the precise control, and pH due to biological relevance), there are many examples of light and pH responsive protocell models including liposomes[72,73], colloidosomes[74,75], and coacervates[76,77]. Particular examples include the triggering of a chemical reaction, for example, small lipid vesicles endowed with a light-responsive membrane encapsulated inside giant unilamellar vesicles (GUVs) that release a substrate upon irradiation with UV light.[73] Light-responsive materials have been incorporated into colloidosomes as a way of controlling membrane permeability; silica colloidosomes doped with nitrophenyl moieties disassemble upon irradiation with UV light, triggering the release of a Nile

Red dye.[74] Further, *via* the UV irradiation of poly(sodium acrylate) (PAA) and trans-azobenzene trimethylammonium bromide (trans-azoTAB) coacervates, light-triggered shape transformation and self-division was achieved.[76] Other examples include exogenously triggered communication pathways between synthetic cell populations[50,55], and living-synthetic cell.[59]

1.3.2 Stimuli-responsive proteinosomes

Proteinosomes benefit from the ability to alter the building block materials, such as the protein-polymer nanoconjugates and the crosslinker, to endow specific functionality. As described earlier, proteinosomes have been shown to demonstrate membrane-mediated enzyme bio-catalysis[43], and further show inherent temperature response due to the PNIPAAm polymer.[42,43] In addition, the unreactive NHS-activated PEG-based crosslinker can be modified to display stimuli-responsive behaviours. Proteinosomes crosslinked with PEG-bis(N-succinimidyl succinate) disulfide ester (NHS-PEG-DS) were shown to disassemble upon exposure to a reducing agent (TCEP, tris(2-carboxyethyl)phosphine). Further experiments showed crosslinking with a combination of PEG-diNHS and NHS-PEG-DS could achieve selective cleavage of the disulphide bridges leading to the formation of a more permeable membrane able to release encapsulated DNA.[45] As described earlier, a host-guest synthesis process was used to create proteinosome organelles within a larger host proteinosome, and when crosslinked with NHS-PEG-DS they could be selectively cleaved using TCEP.[45]

There are very few examples of proteinosome membranes designed for light and pH response functionality. A complex proteinosome phenotype receptive to temperature, reducing agents and pH was constructed which displayed programmable release of substrates of differing molecular weights. The nanoconjugates were synthesised with a disulfide bond between the BSA and conjugated PNIPAAm which could be removed using reducing agents. Four stages of membrane permeability were distinguished. Firstly, heating the system up to 40º caused PNIPAAm to increase in hydrophobicity with a subsequent decrease in membrane permeability. As the system cooled to 25º, the permeability increased as the PNIPAAm increased in hydrophilicity and moved away from the membrane. Addition of TCEP caused the cleavage of the PNIPAAm from the BSA causing a further increase in membrane permeability. Finally, a

decrease in pH to 3.5 caused the BSA to deform into non-spherical structures which caused a decrease in membrane permeability.[78] Further to this, a complex proteinosome phenotype was created using copolymerised spiropyran units in conjunction with NIPAAm. This light and heat responsive polymer was conjugated to BSA with a disulphide linkage to form the protein-polymer nanoconjugates. The resulting proteinosomes displayed similar temperature dependent membrane permeability, and further increased permeability under ultraviolet light irradiation and exposure to reducing agent. The spiropyran moieties also gave the proteinosome membrane selective release over hydrophilic and hydrophobic cargo.[79]

1.4 Project Aim

Understanding how chemistry became biology is a challenge underpinning the field of synthetic biology. With that has come the bottom-up approach, aiming to create protocells using non-living materials as building blocks able to mimic cellular functions. A major challenge in this field is the creation of protocell populations capable of communication and novel behaviours. The integration of “smart” materials into protocell models is helping to tackle this challenge by endowing protocells with the ability to respond to stimuli, much like how living cells respond to the environment around them. Proteinosomes are a protocell model with a crosslinked protein-polymer membrane. The building block used to construct proteinosomes can be modified to give the protocells smart functionality, however very little research has gone into the creation of light- and pH- responsive proteinosomes as protocell models thus far. The work in this thesis aims to synthesise new proteinosome phenotypes able to respond to these stimuli as a step toward stimuli-triggered protocell communication.

References

[1] G. Maspero, in *Books on Demand*, **2009**, p. 108.

[2] L. Safran, Pittsburgh: Penn State Press., **1998**, p. 30.

[3] J. Riskin, *Crit. Inq.* **2015**, *29*, 599–633.

[4] M. Sebald, D. Hauser, *Anaerobe* **1995**, *1*, 11–16.

[5] A. I. Oparin, *The Origin of Life on the Earth*, **1957**.

[6] S. L. Miller, *Science (80-.).* **1953**, *117*, 528–529.

[7] T. N. Evreinova, T. W. Mamontova, V. N. Karnauhov, S. B. Stephanov, U. R. Hrust, *Cosmochem. Evol. Orig. Life* **1974**, 201–205.

[8] R. Hooke, *Micrographia*, **1665**.

[9] “Micrographia | work by Hooke | Britannica,” can be found under https://www.britannica.com/topic/Micrographia, **2022**

[10] P. Nurse, *What Is Life?*, David Fickling Books, **2020**.

[11] D. Sadava, *LIFE: The Science of Biology*, Sinauer Associates, **2014**.

[12] N. Amy Yewdall, A. F. Mason, J. C. M. Van Hest, *Interface Focus* **2018**, *8*, 5.

[13] P. L. Yèagle, *FASEB J.* **1989**, *3*, 1833–1842.

[14] S. A. Benner, A. M. Sismour, *Nat. Rev. Genet. 2005 67* **2005**, *6*, 533–543.

[15] S. Mann, *Acc. Chem. Res.* **2012**, *45*, 2131–2141.

[16] W. K. Spoelstra, S. Deshpande, C. Dekker, *Curr. Opin. Biotechnol.* **2018**, *51*, 47–56.

[17] P. Schwille, J. Spatz, K. Landfester, E. Bodenschatz, S. Herminghaus, V. Sourjik, T. Erb, P. Bastiaens, R. Lipowsky, A. Hyman, P. Dabrock, J.-C. Baret, T. Vidakovic-Koch, P. Bieling, R. Dimova, H. Mutschler, T. Robinson, D. Tang, S. Wegner, K. Sundmacher, *Angew. Chemie Int. Ed.* **2018**, *57*, 13382-13392.

[18] A. J. Dzieciol, S. Mann, *Chem. Soc. Rev.* **2012**, *41*, 79–85.

[19] M. Li, X. Huang, D. Tang, S. Mann, P. L. Luisi, P. Stano, C. Chiarabelli, *Curr. Opin. Chem. Biol.* **2014**, *22*, 1–11.

[20] P.-A. Monnard, D. W. Deamer, *Anat. Rec.* **2002**, *268*, 196–207.

[21] W. R. Hargreaves, D. W. Deamer, *Biochemistry* **1978**, *17*, 3759–3768.

[22] S. S. Mansy, J. W. Szostak, G. F. Joyce, *PNAS* **2008**, 105, 13351-13355.

[23] S. S. Mansy, *Cold Spring Harb. Perspect. Biol.* **2010**, *2*, 8.

[24] T. F. Zhu, J. W. Szostak, *J. Am. Chem. Soc.* **2009**, *131*, 5705–5713.

[25] C. P. Brangwynne, *J. Cell Biol.* **2013**, *203*, 875–81.

[26] S. Kim, J. Huang, Y. Lee, S. Dutta, H. Y. Yoo, Y. M. Jung, Y. Jho, H. Zeng, D. S. Hwang, *Proc. Natl. Acad. Sci. U. S. A.* **2016**, *113*, E847-53.

[27] K. Kaibara, T. Okazaki, H. B. Bohidar, P. L. Dubin, *Biomacromolecules* **2000**, *1*, 100–107.

[28] X. Yin, H. D. H. Stöver, *Macromolecules* **2003**, *36*, 9817–9822.

[29] T.-Y. Dora Tang, C. Rohaida Che Hak, A. J. Thompson, M. K. Kuimova, D. S. Williams, A. W. Perriman, S. Mann, *Nat. Chem.* **2014**, *6*, 527–533.

[30] F. Meng, Z. Zhong, *J. Phys. Chem. Lett.* **2011**, *2*, 1533–1539.

[31] R. Rodríguez-García, M. Mell, I. López-Montero, J. Netzel, T. Hellweg, F. Monroy, *Soft Matter* **2011**, *7*, 1532.

[32] J. S. Lee, J. Feijen, *J. Control. Release* **2012**, *161*, 473–483.

[33] X. Zhang, P.-Y. Zhang, *Curr. Nanosci.* **2016**, *13*, 124–129.

[34] A. F. Mason, B. C. Buddingh ', D. S. Williams, J. C. M. Van Hest, *J. Am. Chem. Soc.* **2017**, 139, 17309-17312.

[35] A. D. Dinsmore, M. F. Hsu, M. G. Nikolaides, M. Marquez, A. R. Bausch, D. A. Weitz, *Science* **2002**, *298*, 1006–9.

[36] B. P. Binks, *Curr. Opin. Colloid Interface Sci.* **2002**, *7*, 21–41.

[37] M. Li, D. C. Green, J. L. R. Anderson, B. P. Binks, S. Mann, *Chem. Sci.* **2011**, *2*, 1739.

[38] A. D. Dinsmore, M. F. Hsu, M. G. Nikolaides, M. Marquez, A. R. Bausch, D. A. Weitz, *Science* **2002**, *298*, 1006–9.

[39] R. K. Kumar, M. Li, S. N. Olof, A. J. Patil, S. Mann, *Small* **2013**, *9*, 357–362.

[40] M. Li, X. Huang, S. Mann, *Small* **2014**, *10*, 3291–3298.

[41] K. Akkarachaneeyakorn, M. Li, S. A. Davis, S. Mann, *Langmuir* **2016**, *32*, 2912–2919.

[42] X. Huang, M. Li, D. C. Green, D. S. Williams, A. J. Patil, S. Mann, *Nat. Commun.* **2013**, *4*, 1–9.

[43] X. Huang, M. Li, S. Mann, *Chem. Commun.* **2014**, *50*, 6278–6280.

[44] X. Huang, A. J. Patil, M. Li, S. Mann, *J. Am. Chem. Soc.* **2014**, *136*, 9225–

9234.

[45] X. Liu, P. Zhou, Y. Huang, M. Li, X. Huang, S. Mann, *Angew. Chemie - Int. Ed.* **2016**, *55*, 7095–7100.

[46] R. Booth, Y. Qiao, M. Li, S. Mann, *Angew. Chemie Int. Ed.* **2019**, *58*, 9120–9124.

[47] S. Sun, M. Li, F. Dong, S. Wang, L. Tian, S. Mann, *Small* **2016**, *12*, 1920–1927.

[48] T. Y. D. Tang, D. Cecchi, G. Fracasso, D. Accardi, A. Coutable-Pennarun, S. S. Mansy, A. W. Perriman, J. L. R. Anderson, S. Mann, *ACS Synth. Biol.* **2018**, *7*, 339–346.

[49] B. C. Buddingh', J. Elzinga, J. C. M. vanHest, *Nat. Commun.* **2020**, *11*, 1652.

[50] L. Rodríguez-Arco, M. Li, S. Mann, *Nat. Mater.* **2017**, *16*, 857–863.

[51] Y. Qiao, M. Li, R. Booth, S. Mann, *Nat. Chem.* **2017**, *9*, 110–119.

[52] S. S. Mansy, *Nat. Chem.* **2017**, *9*, 107–108.

[53] P. Wen, X. Liu, L. Wang, M. Li, Y. Huang, X. Huang, S. Mann, *Small* **2017**, *13*, 1–8.

[54] G. Villar, A. D. Graham, H. Bayley, *Science (80-.).* **2013**, *340*, 48–52.

[55] M. J. Booth, V. R. Schild, A. D. Graham, S. N. Olof, H. Bayley, *Sci. Adv.* **2016**, *2*.

[56] P. Gobbo, A. J. Patil, M. Li, R. Harniman, W. H. Briscoe, S. Mann, *Nat. Mater.* **2018**, *17*, 1145–1153.

[57] Y. Elani, *Angew. Chemie* **2021**, *133*, 5662–5671.

[58] R. Lentini, N. Y. Martín, M. Forlin, L. Belmonte, J. Fontana, M. Cornella, L. Martini, S. Tamburini, W. E. Bentley, O. Jousson, S. S. Mansy, *ACS Cent. Sci.* **2017**, *3*, 117–123.

[59] C. Zhao, M. Zhu, Y. Fang, X. Liu, L. Wang, D. Chen, X. Huang, *Mater. Horizons* **2020**, *7*, 157–163.

[60] Y. Zhou, J. Song, L. Wang, X. Xue, X. Liu, H. Xie, X. Huang, *Biomacromolecules* **2017**, *18*, 2446–2453.

[61] Y. Elani, T. Trantidou, D. Wylie, L. Dekker, K. Polizzi, R. V. Law, O. Ces, *Sci. Reports 2018 81* **2018**, *8*, 1–8.

[62] L. M. P. E. Van Oppen, L. K. E. A. Abdelmohsen, S. E. Van Emst-De Vries, P. L. W. Welzen, D. A. Wilson, J. A. M. Smeitink, W. J. H. Koopman, R. Brock, P. H. G. M. Willems, D. S. Williams, J. C. M. Van Hest, *ACS Cent. Sci.* **2018**, *4*,

917–928.

[63] X. Wang, L. Tian, H. Du, M. Li, W. Mu, B. W. Drinkwater, X. Han, S. Mann, *Chem. Sci.* **2019**, *10*, 9446–9453.

[64] P. Theato, B. S. Sumerlin, R. K. O'reilly, T. H. Epps, *Chem. Soc. Rev* **2013**, *42*, 7055.

[65] M. A. Cohen Stuart, W. T. S Huck, J. Genzer, M. Müller, C. Ober, M. Stamm, G. B. Sukhorukov, I. Szleifer, V. V Tsukruk, M. Urban, F. Winnik, S. Zauscher, I. Luzinov, S. Minko, *Nat. Mater.* **2010**, 9, 101-113.

[66] J. Jiang, X. Tong, D. Morris, Y. Zhao, *Macromol.* **2006**, 39, 4633-4640.

[67] X. Yang, X. Liu, Z. Liu, F. Pu, J. Ren, X. Qu, *Adv. Mater.* **2012**, *24*, 2890–2895.

[68] J. E. Stumpel, D. J. Broer, A. P. H. J. Schenning, *Chem. Commun.* **2014**, *50*, 15839–15848.

[69] K. A. Mosiewicz, L. Kolb, A. J. Van Der Vlies, M. M. Martino, P. S. Lienemann, J. A. Hubbell, M. Ehrbar, M. P. Lutolf, *Nat. Mater.* **2013**, *12*, 1072–1078.

[70] C. A. Custódio, R. L. Reis, J. F. Mano, *Adv. Healthc. Mater.* **2014**, *3*, 797–810.

[71] H. S. Dhowre, S. Rajput, N. A. Russell, M. Zelzer, *Nanomedicine* **2015**, *10*, 849–871.

[72] D. Konetski, D. Zhang, D. K. Schwartz, C. N. Bowman, *Chem. Mater.* **2018**, *30*, 8757–8763.

[73] J. W. Hindley, Y. Elani, C. M. McGilvery, S. Ali, C. L. Bevan, R. V. Law, O. Ces, *Nat. Commun.* **2018**, *9*, 1–6.

[74] S. Li, B. A. Moosa, J. G. Croissant, N. M. Khashab, S. Li, B. A. Moosa, J. G. Croissant, N. M. Khashab, *Angew. Chemie* **2015**, *127*, 6908–6912.

[75] M. Li, R. L. Harbron, J. V. M. Weaver, B. P. Binks, S. Mann, *Nat. Chem.* **2013**, *5*, 529–536.

[76] N. Martin, K. P. Sharma, R. L. Harniman, R. M. Richardson, R. J. Hutchings, D. Alibhai, M. Li, S. Mann, *Sci. Rep.* **2017**, *7*, 1–12.

[77] R. Krishna Kumar, R. L. Harniman, A. J. Patil, S. Mann, *Chem. Sci.* **2016**, *7*, 5879–5887.

[78] P. Zhou, X. Liu, G. Wu, P. Wen, L. Wang, Y. Huang, X. Huang, *ACS Macro Lett.* **2016**, *5*, 961–966.

[79] P. Zhou, S. Wu, X. Liu, M. Hegazy, G. Wu, X. Huang, **2018**, DOI 10.1021/acsami.8b11216.

Chapter 2: The synthesis and characterisation of PEG-based NHS-functionalised and stimuli-responsive crosslinkers

Publications

Publications pertaining to the work in this chapter:

Iuliia Myrgorodska, **Mary Jenkinson-Finch**, Rafael O. Moreno-Tortolero, Stephen Mann, Pierangelo Gobbo, A Novel Acid-Degradable PEG Crosslinker for the Fabrication of pH-Responsive Soft Materials, *Macromol. Rapid Commun.,* **2021**, *42*, 2100102

Mary Jenkinson-Finch synthesised and characterised the acid-degradable PEG crosslinker and performed the hydrolysis kinetics investigated.

Preliminary experiments on the synthesis of a light-responsive crosslinker were undertaken as part of a MSci project.

Chapter Outline

The crosslinker traditionally used in proteinosome synthesis is a relatively simple polymer (polyethylene glycol (PEG)) with terminating N-hydroxy succinimide (NHS) groups commonly used for protein crosslinking. Advances in the design and facile synthesis of stimuli-responsive molecules mean that there is the potential to create functionalised crosslinkers *via* the addition of responsive moieties. In this chapter, the synthesis and characterisation of two novel stimuli-responsive PEG-based crosslinkers containing common responsive functional groups is presented. The first is designed to cleave in response to a decrease in pH by incorporating a ketal moiety in between two PEG polymer chains. A 5-step chemical synthesis and associated characterisation is outlined, and the pH-driven lysis of the crosslinker is investigated. The second is designed to cleave in response to UV light in the range of 340 to 410 nm by the addition of two *o*-nitrobenzyl moieties on the termini of a PEG chain. A 3-step synthetic route and full characterisation is presented, and light-induced cleavage is investigated.

2.1 Introduction

Stimuli responsive polymers – “smart materials” – have piqued the interest of scientists in the last few decades due to their versatility (light response, pH response, etc.) which leads to an array of potential applications in which they can be used.[1] [2] These polymers are designed to respond to an external signal in a controlled way, causing a physical change in the polymer. PNIPAAm is one such polymer, famous for going through a lower critical solution temperature (LCST) phase transition at ca. 32 ºC. Transforming from a hydrated to dehydrated state, it becomes more hydrophobic and insoluble in water above this temperature.[3] Recently, applications of smart polymers with advanced functionality have been reported, for example, with the development of complex stimuli responsive soft microrobots synthesised from functionalised smart polymer/liquid crystal hybrid materials.[4] Developments in the synthesis of smart polymers have allowed for a deeper understanding of their properties and towards development into materials which are tuneable and predictable.[5]

2.1.1 pH responsive moiety

One particularly attractive external stimulus is pH, due to simplicity and its biological relevance; many tissues in the human body for example, exist at a lower pH such as cancer tissue which is around 6.4 - 7.[6] This provides the opportunity for targeted release of caged molecules. pH-responsive materials have been designed to respond to the environment by changing physiochemical properties. An example of this is the pH-responsive moiety 2-(diethylamino)ethyl methacrylate (DEA) which was incorporated into copolymers that were used to construct polymersomes. Under low pH conditions, the protonation of the tertiary ethyl groups on the nitrogen causes a swelling and subsequent release of the payload into cells.[7] Another response mechanism is the cleavage of covalent bonds in the molecule. This method has found applications in bio-related areas such as drug-delivery systems,[8] diagnostic and sensing devices,[9] and lithography.[10]

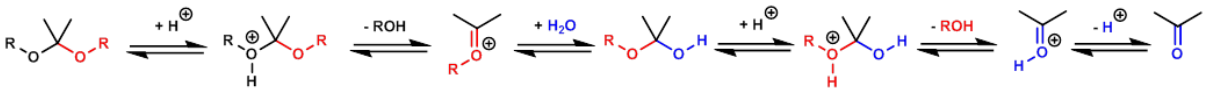

Scheme 2.1 The general acid-catalysed hydrolysis of a ketal moiety, showing the release of two primary alcohol groups and the formation of acetone. The rate determining step is considered to be the resonance-stabilised carboxonium ion intermediate.[11]

Ketal groups have become popular acid-cleavable moieties due to their ability to readily hydrolyse under mildly acidic conditions into the corresponding ketone and alcohols (**Scheme 2.1**).[11] They have good stability in mildly alkaline and neutral conditions, have relatively simple synthetic routes, and hydrolysis times have been shown to be tuneable.[12] For these reasons they have been used to synthesise polymers for a range of acid-degradable soft materials including hydrogels[13], and micro- and nano- carriers.[14] Although there has been a wide range of these types of polymers, the general method to synthesise these is through polymerisation directly into a copolymer backbone and are subsequently used for molecule release through acid-mediated cleavage.[15] The use of the ketal moiety within a crosslinker capable of reacting through bioconjugation has little to no research available.

2.1.2 Light-responsive moiety

One of the most controllable and versatile stimuli is light because of its abundance and accessibility. The extreme tuneability means it can be manipulated into a single wavelength, and advances in laser precision have led to great inventions such as the fluorescence microscope for which Stefan Hell received the Nobel prize in 2014. Biophotonics is a relatively new scientific discipline which is developing applications for light and lasers in the life sciences, particularly in pharmaceutical research, clinical diagnostics and therapy. With such advances in using light as a tool in the biomedical industry, the development of light responsive biointerfacing materials is of great interest.

The *o*-nitrobenzyl moiety is one of the most commonly used photo-active groups.[16] *o*-Nitrobenzyl compounds were originally developed for organic synthesis but began to be used for biological application and the extensive research has led to a variety of applications for caged biomolecules, for example caged-DNAzyme[17] or the release of Ca^{2+} ions from the ethylene glycol tetraacetic acid (EGTA) chelator complexes.[18]

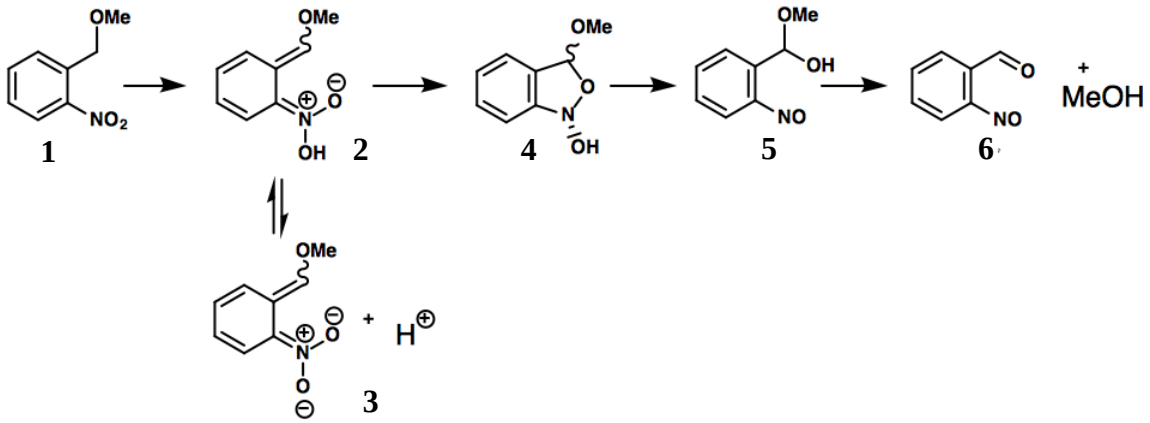

Scheme 2.2 The general mechanism of the photolysis of the o-nitrobenzyl moiety.[19]

o-Nitrobenzyl compounds are commonly referred to as following a Norrish type II reaction. This type of mechanism was described by Norrish in 1935, where an incident photon in the range of 300-450 nm breaks the nitro group N=O π-bond causing it to move to a diradical excited state (**Scheme 2.2**).[19] The nitronic acid (aci-nitro) compound **2** is formed when the nitrogen radical abstracts a proton from the benzylic carbon (an intramolecular 1,5-H shift). This is followed by cyclisation to benzisoxazolidines **4**, a ring opening step to form **5** and a dehydration to the final aldehyde **6** and, in this case, release of methanol. Small changes in the substituents can cause a large bathochromic or hypsochromic shift in absorption wavelength (λ_{max}) which has influenced the production of a diverse variety of analogues, leading to the extensive use in smart polymer materials.[20] Another important observation was that quantum yield could be heavily increased with the addition of a methyl group at the benzylic position when compared with the derivate without and the water solubility can be increased with the addition of CO_2H at the same position.[19] Interestingly, upconversion particles have been used in conjunction with o-NB moieties, absorbing

near-infrared (NIR) light and emitting ultraviolet (UV) light.[21] NIR light is a much better wavelength for use in biomedical applications due the increased penetration depth into tissue than UV wavelengths, and the decrease in damage to the cellular environment.[22]

One application of light responsive materials has been their use in drug delivery. For example, block copolymers have been shown to form micellar structures, which show irreversible and reversible responses to light when different moieties are used, such as o-nitrobenzyl and azobenzene. These nanocontainers can encapsulate or release molecules upon irradiation by destabilising the micelles.[23] Release of Nile Red dye from micellar solutions of PEO-*b*-PPy due to the photocleavage of pyrenylmethyl (Py) ester side groups demonstrated the concept of light-triggered drug delivery.[11] Further to this, PEO-*b*-PPy micellar solution with o-NB ester modification was irradiated and also showed the release of the molecules but with a higher degree of control due to the fact that the light intensity could be varied, which in turn varied how much of the dye was released.[24,25]

Herein is described the synthesis and characterisation of two novel NHS-functionalised crosslinkers for use in soft materials chemistry. They have been designed with the aim of introducing functionality in the form of stimuli-responsive groups; a ketal group for acid hydrolysis, and an ortho-nitrobenzyl group for UV-response. The NHS terminus are for the crosslinking of nucleophilic groups such as primary amine containing lysine amino acids in protein, or carboxymethyl-chitosan hydrogels. The hydrolysis and photolysis of each crosslinker are investigated to understand the rate behaviours.

2.2 Materials and methods

The following reagents and solvents were purchased and used as received. Poly(ethylene glycol)bis(3-aminopropyl) (Mn 1500), 4-[4-(1-hydroxyethyl)-2-methoxy-5-nitrophenoxy]butyric acid, N,N'-dicyclohexylcarbodiimide (DCC) (99%), 4-dimethylaminopyridine (DMAP) (>99%), N,N-diisopropylethylamine (DIPEA) (>99%), p-toluenesulfonyl chloride (TsCl), 3,5-dihydroxy-2-naphthoic acid, triethylamine (TEA) (>99%), sodium iodide (NaI), 2,2-dimethoxypropane, p-toluenesulfonic acid monohydrate (TsOH), DMF (anhydrous, 99.8%), deuterated methanol (CD_3OD) (99.8 atom %), and deuterated chloroform ($CDCl_3$) (99.8 atom %) were purchased from Sigma-Aldrich. Succinic anhydride and poly(ethylene glycol) (Mn 1000) were purchased from Merck. N-hydroxysuccinimide (NHS) (98+%), N-(2-hydroxyethyl)phthalimide, and 1-ethyl-3-(3-dimethylaminopropyl)carbodiimide (EDAC) (98+%) were purchased from Alfa Aesar. Sodium hydroxide (NaOH) was purchased from Fischer Scientific. Sulphuric acid (H_2SO_4) (95%) was purchased from VWR Chemicals. Dialysis bags with MWCO 1,000 were purchased from Millipore.

5 Å molecular sieves were purchased from Sigma-Aldrich and were activated (to remove water) by heating in the microwave at 800 W for 1 minute and then stirred for a few seconds. This was repeated for 5 minutes. They were then heated for 30 second intervals with stirring in between for 5 minutes. They were then immediately put under vacuum and were only used once cooled.

2.2.1 Ultraviolet-visible spectroscopy (UV Vis)

Ultraviolet-visible spectroscopy (UV Vis) is a technique used to investigate quantitatively how much light is absorbed by a sample. This is performed by measuring the intensity of light which has passed through the sample in comparison to the intensity of a reference sample. Molecules containing pi (π) electrons are able to absorb light in the ultraviolet and visible light range which excites them into a higher anti-bonding molecular orbital. The smaller the energy gap between the highest occupied molecular orbital (HOMO) and the lowest unoccupied molecular orbital (LUMO), the longer the wavelength of light absorbed, as this corresponds to a lower

energy. According to the Beer-Lambert law, the absorbance of a chemical species relates directly to the concentration in solution and the path length as follows:

$$A = \varepsilon c l \quad (1)$$

Where A is the absorbance in AU, ε is the extinction coefficient in L mol^{-1}, c is the concentration in mol L^{-1}, and l is the path length in cm.

The molar attenuation coefficient is a measurement of how strongly a chemical absorbs light at a certain wavelength, and indicates how quickly a chemical species absorbs light with change in concentration. According to the beer-lambert law,

$$\varepsilon = \frac{A}{cl} \quad (2)$$

Where ε is the extinction coefficient in L mol^{-1} cm^{-1}, A is the absorbance in AU, c is the concentration in mol L^{-1}, and l is the path length in cm. This can be determined from a calibration curve.

UV vis spectra were recorded using a PerkinElmer Lambda 35 spectrometer and 1 cm quartz cuvettes. For polymers, solutions of 0.1 mM were prepared using phosphate buffer solution (PBS) (0.1 M, pH 7.4).

2.2.2 Nuclear magnetic resonance (NMR) spectroscopy

Nuclear magnetic resonance (NMR) spectroscopy is a technique used to characterise and elucidate chemical molecular structure.[26] When spin half nuclei are placed into a strong magnetic field and perturbed by an oscillating magnetic field, they produce an electromagnetic signal (resonant frequency). This is because spin half nuclei have two possible spin states where one opposes the magnetic field and the other aligns with it. At certain frequencies, the perturbing field causes the nuclei to move to the excited state, and as they relax, they emit the same frequency. The signal is detected, and a plot is produced showing peaks at their corresponding resonance frequency. ^{1}H and ^{13}C NMR are the most commonly used nuclei in NMR spectroscopy, with ^{13}C having

a longer relaxation time and therefore taking longer to obtain a spectrum. This electromagnetic signal, or frequency, differs depending on the environment surrounding the nuclei (different molecular functional groups). Local magnetic fields produced within the molecule cause shielding and de-shielding effects, where neighbouring nuclei require varying energy to be excited. For example, when the considered nucleus is next to an electron withdrawing group, the electron density is lowered, shielding is low and resonance frequency will be lower.

In ^{1}H NMR, J-coupling between NMR active nuclei gives information about the local chemical bonds in a molecule. The adjacent nuclei will have different magnetic fields depending on whether they are aligned or not with the external magnetic field, causing the considered nuclei signal to split. Splitting patterns depend on the number of neighbouring nuclei; for example, one neighbouring proton has two possible energy states and therefore causes the considered nuclei signal to split into two.

Correlation spectroscopy (COSY) is a type of 2D NMR spectroscopy used to provide more information about the structure of a molecule. The spectrum will give information on whether there is correlated through-bond coupling with another nucleus. The spectrum shows frequencies for ^{1}H spectra along both axes. Peaks along the diagonal correspond to peaks in the ^{1}H NMR spectra, and cross peaks are where there is coupling between two nuclei. The coordinated of the cross peak will indicate which two nuclei are coupled. A better picture of the structure of the molecule is gained through this information and so this technique was used to elucidate and confirm the assignment of proton peaks for the synthesised polymers.[26]

^{1}H and ^{13}C NMR spectra were obtained using Varian 400 MHz or 500 MHz spectrometers, indicated below each NMR spectra. ^{1}H NMR spectra are reported as δ in units of parts per million (ppm) relative to chloroform (δ 7.26, s) or methanol (δ 4.87, s). Multiplicities are reported as follows: s (singlet), d (doublet), t (triplet), q (quartet), p (quintuplet) and m (multiplet). Coupling constants are reported as *J* values in units of Hertz (Hz). The number of protons (n) is reported as nH, and based on spectral integration values. ^{13}C NMR are reported as d in units of parts per million (ppm) relative to $CDCl_3$ (δ 77.16, t) or CD_3OD (δ 49.00, septet). All of the spectra were processed using Mestrenova.

2.2.3 Fourier transform infrared (FT-IR) spectroscopy

FT-IR spectroscopy is a technique which measure the absorption (or emission) of IR light of a sample. Light of many different frequencies is used to irradiate the sample and the amount of light absorbed by the sample is measured. This is repeated until all wavelengths have been used, and a Fourier transform technique is used to turn this information into the desired result, showing light absorption at each wavelength. Molecules will absorb IR light at particular frequencies corresponding to the resonant vibrational frequencies of their bonds, which in turn relate to the strength of the covalent bond (single or double) and the mass of the atoms at either end. IR active vibrational modes require the bond to have a change in dipole moment. Many molecular functional groups have characteristic absorptions which can be identified through look-up tables and references.

Infrared spectra were recorded on a PerkinElmer Spectrum One FT-IR spectrometer. The backgrounds were automatically subtracted from each spectrum.

2.2.4 Matrix assisted laser desorption-ionisation mass spectrometry (MALDI-MS)

Matrix assisted laser desorption-ionisation mass spectrometry (MALDI-MS) is a technique in mass spectrometry used to find the mass of large molecules. The use of a laser energy absorbing matrix causes ions to be produced with minimal fragmentation. The matrix is a compound used to absorb the laser light and convert it to heat, causing vaporisation of the matrix together with the sample. Typical matrices have strong absorption properties in the UV range, and therefore often contain highly conjugated double bonds. A sample is typically mixed with a solution of matrix and spotted onto a metal plate, often with a highly acidic compound like trifluoracetic acid to provide protons. Irradiation of the matrix/sample is performed using a pulsed laser causing ablation and desorption before acceleration of the ionised sample into the instrument, such as a time-of-flight (TOF) spectrometer. TOF uses the velocity of a molecule and the flight time to work out the mass to charge ratio (m/z); ions with a

larger mass will travel slower, but ions with higher charge will also travel faster. The length of time to travel a known distance is measured which depends on the velocity. It is advantageous for polymer and protein analysis due to its large mass range.[27]

MALDI spectra were recorded on a Bruker UltrafleXtreme (TOF-TOF). Alpha-cyano-4-hydroxycinnamic acid (7 mg mL^{-1} in CH_3CN/0.1% v/v TFA) was used as the matrix solution. The matrix solution was mixed with the polymer sample (1-2 mg mL^{-1} in CH_3CN/0.1% v/v TFA) in 1:1 v/v ratio.

2.2.5 Synthesis of 2,a2-bis(phthalimidoethoxy)propane 1

Compound 1 was synthesized following the previously reported procedure.[28] N-(2-hydroxyethyl)phthalimide) (5 g, 26 mmol, 2 eq.) was dissolved in 200 mL of dry toluene; residual water was removed by azeotropic distillation in a Dean-Stark distillation setup. The solution was cooled to room temperature and 2,2-dimethoxypropane (1.58 mL, 13 mmol, 1 eq.) was added to the solution along with p-toluenesulfonic acid (55 mg). The reaction mixture was heated to 110 ºC for 3 h. Finally, the reaction mixture was cooled to room temperature and triethylamine (TEA) (6 mL) was added to quench the reaction. To facilitate further purification, acetic anhydride (2 mL) was added to convert any unreacted alcohol groups into the corresponding acetate and the reaction mixture was allowed to stir overnight. The product was then precipitated by dropwise addition into a large excess of hexanes. The precipitated powder was collected and recrystallized from ethyl acetate and the excess solvent was removed in vacuo to yield **1** (3.7 g, 8.76 mmol, 67%). ^{1}H NMR (400 MHz, CDCl3) δH 7.82 (m, 4H, Ar-H), 7.67 (m, 4H, Ar-H), 3.81 (t, 4H), 3.59 (t, 4H), 1.25 (s, 6H). ^{13}C NMR (400 MHz, $CDCl_3$) δC 168.2,134.1, 133.9, 132.1, 123.3, 100.6, 57.9, 38.1, 24.7. HRMS (ESI): calc. for $C_{23}H_{22}N_2NaO_6$+ [M+Na] 445.1370, found 445.1375.

2.2.6 Synthesis of 2,2-bis(aminoethoxy)propane 2

2,2-Bis(phthalimidoethoxy)propane **1** (2 g, 4.9 mmol) was re-dispersed in 6 M NaOH (60 mL) and refluxed overnight. When the solution reached the reflux temperature it became yellow and clear. The product was extracted with *i*PrOH / 30% dichloromethane (200 ml). The organic fractions were combined and dried over anhydrous Na_2SO_4, and the solvents removed *in vacuo*. To remove residual NaOH,

the crude was dissolved in dichloromethane and filtered through a cotton plug. Solvents were removed in vacuo to yield **2** as a thick yellow oil (376 mg, 2.31 mmol, 76% yield). ^{1}H NMR (400 MHz, $CDCl_3$) δ_H 3.46 (t, 4H), 2.84 (t, 4H), 1.37 (s, 6H). ^{13}C NMR (400 MHz, $CDCl_3$) δ_C 99.8, 62.9, 42.0, 25.0. HRMS (ESI): calc. for $C_7H_{19}N_2O_2$+ [M+H] 163.1441, found 163.1446.

2.2.7 Synthesis of $(PEG)_{23}$-dicarboxy 3

Under an inert atmosphere, DMAP (0.1 g, 0.8 mmol) added directly followed by poly(ethylene glycol) $(PEG)_{23}$ (MW 1000 Da, 2 g, 2 mmol). The solids were dissolved in dry DMF (4 ml). Succinic anhydride (1.2 g, 0.79 mmol) was directly added. The reaction was heated to 50 °C and stirred overnight. The yellow solution turned bright purple. Air was bubbled through and the solution turned light brown. The solvent was removed *in vacuo*. The solid product was dissolved in water and centrifuged - the supernatant containing dissolved polymer was decanted. It was dialysed against water using a 1KDa membrane overnight and lyophilised to yield **3** (1.2 g, 1 mmol, 50 %). ^{1}H NMR (400 MHz, $CDCl_3$) δ_H 4.24 (t, 4H), 3.68-3.63 (m, 95H), 2.63 (tt, 8H). ^{13}C NMR (400 MHz, $CDCl_3$) δ_C 174.5, 172.0, 70.5, 68.9, 63.7, 29.3, 28.9. *Mn* (MALDI-TOF MS) = 1250 Da.

2.2.8 Synthesis of $(PEG)_{23}$-dicarboxy-N-hydroxysuccinimide (Di-NHS-PEG) 4

Dicarboxy-PEG **3** (1 g, 0.83 mmol), DMAP (50.1 mg, 0.41 mmol) and NHS (383 mg, 3.32 mmol) were dissolved in dry dichloromethane (5 mL) and the solution was cooled to 0 ºC. To this solution, a solution of DCC (687 mg, 3.33 mmol) (dissolved in 5 mL dry dichloromethane and cooled to 0 ºC) was directly added. The reaction mixture was stirred overnight at room temperature and under inert atmosphere. After ~5 min solution started to become cloudy. The urea was filtered through a Pasteur pipette. The polymer was recrystallised from diethyl ether (1 L) at -20 ºC. The polymer was then centrifuged and dried to yield **4** (1.07 g, 0.7 mmol, 90%). ^{1}H NMR (400 MHz, $CDCl_3$) δ_H 4.27 (t, 4H), 3.71-3.63 (m, 92H), 2.95 (t, 4H), 2.84 (s, 8H), 2.78 (t, 4H). ^{13}C NMR (400 MHz, $CDCl_3$) δ_C 170.9, 168.8, 167.7, 70.6, 68.9, 64.2, 28.7, 26.3. 25.6. *Mn* (MALDI-TOF MS) = 1450 Da.

2.2.9 Synthesis of O,O'-(15,15-dimethyl-7,10,20,23-tetraoxo-3,6,14,16,24,27-hexaoxa-11,19-diazanonacosane-1,29-diyl) bis(2,5-dioxopyrrolidin-1-yl) disuccinate 5 (PEG-ketal-NHS)

Di-NHS-PEG **4** (200 mg, 0.14 mmol) was dissolved in chloroform (10 mL). Separately, di-amino ketal (18 mg, 0.11 mmol) was dissolved in chloroform (10 mL) and was added dropwise to the stirring PEG solution. This was stirred at room temperature and under a normal atmosphere for 48 hours. The solvent was then removed in vacuo to yield the final crosslinker **5**. ^{1}H NMR (500 MHz, $CDCl_3$) δ_H 4.27 (t, 4H), 4.22 (t, 4H), 3.71-3.63 (m, 182H), 3.46 (t, 4H), 3.40 (t, 5.57), 2.95 (t, 4H), 2.84 (s, 8H), 2.78 (t, 4H), 2.71 (s, 8H), 2.50 (m, 4H), 1.33 (s, 6H). *Mn* (MALDI-TOF MS) = 2800 Da.

2.2.10 Kinetics studies of PEG-ketal-NHS using ^{1}H NMR spectroscopy

PEG-ketal-NHS (20 mg) was dissolved in deuterated phosphate buffer (PBS, 100 mM, 500 μL) of appropriate pH. After dissolution the pH was measured and adjusted accordingly using NaOH solution (5 M). An array of ^{1}H NMR spectra were recorded by using a pre-acquisition delay parameter on a Varian 500 MHz spectrometer with time delays between 1 minute and 5 minutes for acidic and basic pH respectively. The resulting spectra were analysed by integrating the ketal peak (d1.33, s, 6H) and the acetone peak (d2.22, s, 6H). The percentage hydrolysis at a given time was calculated according to the following equation:

$$\%hydrolysis = \frac{I_{acetone}}{(I_{ketal}+I_{acetone})} \times 100\% \quad (3)$$

Where $I_{Aacetone}$ is the integral of the acetone peak, and I_{Ketal} is the integral of the ketal peak.

The hydrolysis kinetics of PEG-ketal-NHS follows a pseudo first-order kinetics.

$$[Ketal]_t = [Ketal]_0 e^{-k_{obs}t} \quad (4)$$

Where $[Ketal]_t$, is the concentration of PEG-ketal-NHS at time *t*, which is proportional to I_{Ketal} derived from the time-dependent ^{1}H NMR spectroscopy measurement, and $[Ketal]_0$ is the initial concentration of acid-degradable crosslinker (**5**) (0.014 M). Equation *(2)* can be re-written by taking the natural log of both sides to yield a linear plot where the slope is equal to k_{obs}.

$$ln\left(\frac{[Ketal]_t}{[Ketal]_o}\right) = -k_{obs}t \quad (5)$$

Or, using the integrals obtained from the ^{1}H NMR spectra:

$$ln\left(\frac{I_{ketal}}{I_{acetone}+I_{ketal}}\right) = -k_{obs}t \quad (6)$$

The k_{obs} values were determined as a negative value of the slope obtained through the linear fitting of the plot $ln\left(\frac{I_{ketal}}{I_{acetone}+I_{ketal}}\right)$ against incubation time *t* for the different kinetics carried out at different pH values. The half-life of hydrolysis of the acid-degradable crosslinker (**5**) was determined as follows:

$$t_{1/2} = \frac{ln\,(2)}{k_{obs}} \quad (7)$$

2.2.11 Synthesis of $(PEG)_{31}$-bis(o-nitro benzyl) 6

Under argon and in a round bottom flask was added poly(ethylene glycol)bis(3-aminopropyl) (PEG - amine terminated) (601 mg, 0.400 mol), 4-[4-(1-Hydroxyethyl)-2-methoxy-5-nitrophenoxy]butyric acid (360 mg, 1.20 mmol) and DMAP (19.8 mg, 0.162 mmol) which were dissolved in dry DMF (4 ml). DIPEA (210 μl, 1.20 mmol) and DCC (252 mg, 1.20 mmol) were added directly. The reaction mixture was stirred overnight at room temperature, under argon and in the dark. A white precipitate formed. The product was precipitated directly into diethyl ether (50 ml) and washed twice more with diethyl ether (2 x 50 ml). The solvent was removed *in vacuo*. The product was finally dialysed for 48 h against a 1:1 ratio of ethanol:water and dried to yield the product **6** (400 mg, 0.200 mmol, 89 %) as a yellow solid. ^{1}H NMR (400 MHz, Methanol-d_4) δ_H 7.60 (d, *J* = 3.0 Hz, 2H, ArH), 7.40 (d, *J* = 8.3 Hz, 2H, ArH),

5.46 (q, *J* = 6.4 Hz, 2H), 4.09 (t, *J* = 6.2 Hz, 4H), 3.97 (s, 6H), 3.65 (m), 3.52 (t, *J* = 6.1 Hz, 4H) 3.29 (t, *J* = 6.8 Hz, 4H), 2.39 (t, *J* = 7.4 Hz, 4H), 2.11 (p, *J* = 7.1 Hz, 4H), 1.77 (m, 4H), 1.48 (d, *J* = 6.2 Hz, 6H). ^{13}C NMR (500 MHz, Methanol-*d*$_4$) δ_C 175.2, 163.9, 144.4, 148.3, 140.7, 139.0, 110.0, 73.7, 69.9, 66.1, 56.8, 37.9, 33.5, 30.3, 26.5, 25.3. IR ν_{max} cm^{-1}) 2882.6 (Alkane C-H stretch), 1516.7 (Aromatic N-O stretch), 1101.6 (C-O stretch). MALDI-TOF (m/z) found: M_n 2023, estimated PDI 1.01.

2.2.12 Synthesis of (PEG)$_{31}$-bis([o-nitro benzyl] N-succinic acid) 7

Under argon in a flask, a catalytic amount of DMAP (9.5 mg, 0.078 mmol) was added directly followed by the photosensitive polymer **6** (400 mg, 0.200 mmol) dissolved in DMF (2 ml). Succinic anhydride (116 mg, 1.16 mmol) was added directly and the flask heated to 50 °C and stirred overnight under argon and in the dark. The yellow solution turned amber. The polymer product was precipitated directly into diethyl ether (50 ml) and washed twice more with diethyl ether (2 x 50 ml). The solvent was removed *in vacuo.* The product was finally dialysed for 48 h against a 1:1 ratio of ethanol:water and dried to give the product **7** (395 mg, 0.180 mmol, 94 %) as dark yellow solid. ^{1}H NMR (400 MHz, Methanol-*d*$_4$) δ_H 7.62 (s, 2H, ArH), 7.17 (s, 2H, ArH), 6.37 (q, *J* = 6.5 Hz, 2H), 4.11 (t, *J* = 6.1 Hz, 4H), 4.01 (s, 6H), 3.64 (m, 344H), 3.53 (m, 4H), 3.27 (m, 4H), 2.65 (m, 4H), 2.47 (t, *J* = 7.0 Hz, 4H), 2.41 (t, *J* = 7.4 Hz, 4H), 2.12 (p, *J* = 6.9 Hz, 4H), 1.77 (m), 1.62 (d, *J* = 6.4 Hz, 6H). ^{13}C NMR (500 MHz, Methanol-*d*$_4$) δ_C 76.0, 175.2, 174.5, 173.3, 155.6, 148.7, 141.0, 134.3, 110.0, 109.6, 71.5, 69.9, 69.8, 57.0, 37.9, 33.5, 31.8, 30.6, 30.3, 26.4, 22.2. IR ν_{max} (cm^{-1}) 2882.7 (Alkane C-H stretch), 1732.6 (Carbonyl C=O stretch), 1520.5 (Aromatic N-O stretch), 1103.1 (C-O stretch). MALDI-TOF (m/z) found: M_n = 2164, estimated PDI 1.01.

2.2.13 Synthesis of (PEG)$_{31}$-bis([o-nitro benzyl] N-succinimidyl succinate) (PEG-oNB-NHS) 8

The polymer **7** (160 mg, 0.0740 mmol) was dissolved in CH_2Cl_2 (2 ml) before N-hydroxysuccinimide (11 mg, 0.095 mmol) was added directly and dissolved. EDAC (14 mg, 0.0090 mmol) was added directly and the solution was stirred for 48 hours at room temperature, under a normal atmosphere and in the dark. The solvent was removed to give product **8** (133 mg, 0.0580 mmol, 75 %) as a dark yellow solid. ^{1}H NMR (500 MHz, Methanol-*d*$_4$) δ_H 7.61 (d, *J* = 4.6, 2H, ArH), 7.17 (d, *J* = 4.3, 2H, ArH),

6.37 (q, *J* = 6.0, 5.3 Hz, 2H), 4.2-4.11 (m, 4H), 3.99 (m, 6H), 3.65 (m, 306H), 3.26 (m, 4H), 2.88 (s, 8H), 2.59 (m, 4H), 2.47 (m, 4H), 2.42 (m, 4H), 2.13 (m, 4H), 1.77 (m, 4H), 1.64 (m, 6H). ^{13}C NMR (500 MHz, Methanol-*d*$_4$) δ_C 180.0, 176.1, 175.1, 174.5, 173.0, 155.6, 148.7, 141.1, 134.1, 110.1, 109.6, 69.9, 69.8, 57.1, 37.9, 33.5, 31.4, 30.4, 30.2, 29.5, 26.4, 22.2. MALDI-TOF (m/z) found: 2175, estimated PDI 1.01.

2.2.14 Investigation of PEG-oNB-NHS photolysis using UV Vis

PEG-oNB-NHS (**3**) was dissolved in phosphate buffer (PBS) (0.1 M, pH 7.4) at a concentration of 0.1 mM. The solution was irradiated (350 or 365 nm xenon light source, 13 mW cm^{-2}) inside a quartz cuvette at one-minute intervals and a UV-Vis spectrum taken after each for a total of 25 minutes. Between measurements the cuvette was inverted to ensure the sample remained homogenously mixed throughout the experiment.

2.2.15 Determining the molar attenuation coefficient of PEG-oNB-NHS

A calibration curve was used to determine the molar attenuation coefficient of PEG-oNB-NHS **8.** A series of dilutions of 8 (0.025, 0.021, 0.017, 0.013, 0.009, 0.006 and 0.003 mM) were made in deionised water. The absorbance at 350 nm was measured and plotted against concentration in M. The gradient of the straight line gave the molar attenuation coefficient.

2.3 Results and discussion

2.3.1 Design and synthesis of pH-responsive NHS-functionalised crosslinker

The following synthesis and characterisation data (^{1}H NMR, ^{13}C NMR, MALDI, HMBC) for the following synthesis is reported Myrgorodska *et al*.[29]

2.3.1.1 Synthesis and characterisation

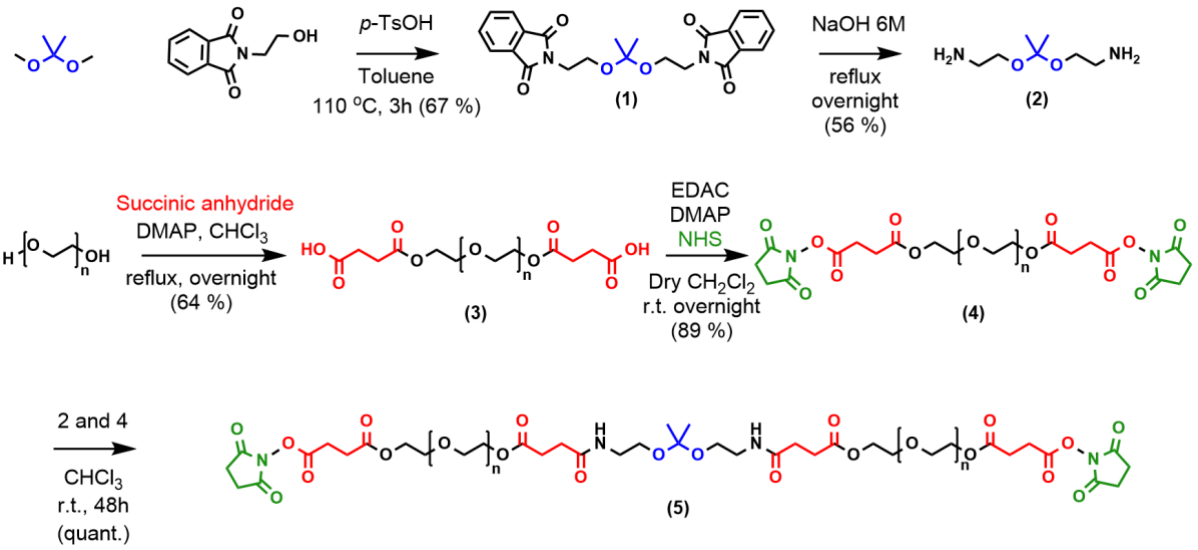

Scheme 2.3 Route to the synthesis of pH-responsive crosslinker **5**.

The synthetic route is seen in **Scheme 2.3.** Firstly, to create the pH-sensitive ketal diamine core, 2,2-dimethoxypropane was refluxed with N-(2-hydroxyethyl)phthalimide in dry toluene, with toluenesulfonic acid as a catalyst, resulting in **1**. Residual water was removed by azeotropic distillation in a Dean-Stark setup. Recrystallisation in ethyl acetate removed any unreacted starting material. A yield of 67 % was achieved and the product was characterised by ^{1}H and ^{13}C NMR. Crucially, the typical ketal peak at 1.37 ppm was observed in the product NMR indicating no hydrolysis in the final product.

The phthalimide protected intermediate **1** was deprotected by refluxing overnight in sodium hydroxide to reveal primary amine groups affording the bi-amine product **2** in high purity. A 56 % yield was achieved after extraction of the product into

dichloromethane. The product was characterised by ^{1}H and ^{13}C. The low yield can be attributed to a loss of some of the product into the aqueous phase during extraction. The typical ketal peak can be observed at 1.37 ppm indicating no hydrolysis during synthesis.

Separately, poly ethylene(glycol) (MW 1000) was functionalised, with the alcohol groups being transformed to carboxylic acids to form polymer **3**. This was done via addition of succinic anhydride in the presence of a strong base (4-dimethylaminopyridine, DMAP) in anhydrous conditions and under an inert atmosphere. The polymer was dialysed against water overnight to remove excess succinic anhydride and DMAP. Successful reaction was confirmed using ^{1}H NMR spectroscopy by the appearance of a broad peak at 4.24 ppm due to the methylene alpha to the ester group, and the appearance of the new signal due to the methylene groups of the succinic anhydride moieties at 2.63 ppm. The MALDI-TOF spectrum of **3** confirmed the addition of two succinic anhydride moieties to each end of the polymer chain as seen from an increase in Mn from 1000 Da to 1250 Da.

Subsequently, the terminal carboxylic acid moieties were activated in an N,N'-dicyclohexylcarbodiimide (DCC)-mediated coupling reaction with N-hydroxysuccinimide (NHS), to yield **4**. A biproduct of the reaction is urea which was seen as a precipitate in the solution as it is insoluble in organic solvents, such as dichloromethane used as the reaction solvent. This was removed by aqueous extraction. The organic layer was concentrated and removal of excess NHS and DMAP was achieved by precipitation into a large volume of diethyl ether and recrystallistion at -20 ºC. The solid product was then dried in a desiccator to afford **4** in 89 % yield. The polymer was characterised by ^{1}H and ^{13}C NMR spectroscopy which showed successful removal of excess starting materials and urea. The successful synthesis of PEG-diNHS (**4**) was confirmed by the appearance of a singlet at 2.84 ppm and of the two triplets at 2.78 and 2.95 ppm in the ^{1}H NMR spectrum of the product, associated with the methylene protons of the terminal NHS groups, and the methylene groups of the NHS-activated succinic acid, respectively. The MALDI-TOF spectrum also confirmed the addition of two NHS moieties as seen from an increase in mass from 1250 Da to 1450 Da, the approximate mass of two NHS molecules.

2,2-Bis(aminoethoxy)propane **2** and the PEG-diNHS **4** were then coupled by stirring in a dilute solution of chloroform in a 2:1 molar ratio for 48 hours to yield the final acid-degradable crosslinker **5** in quantitative yield. The dilute solution is essential in order to avoid over polymerisation and to achieve the desired crosslinker in the correct stoichiometry, which meant the reaction was performed for an extended period of time in order to go to completion. The ^{1}H NMR spectrum of compound **5** (PEG-ketal-NHS, **Figure 2.1**) showed the appearance of the ketal peak at 1.33 ppm, of the methylene protons peak at 3.40 and 3.46 ppm and by a 2-fold increase of the PEG peak at 3.63 to 3.71 ppm. MALDI-TOF mass spectrometry also confirmed coupling of 2 polymers (**4**) to 1 acid-degradable ketal-diamine core (**2**). PEG-ketal-NHS was found to be stable for months if stored at –20 °C and under inert atmosphere and was used directly in the subsequent experiments without any additional purification steps.

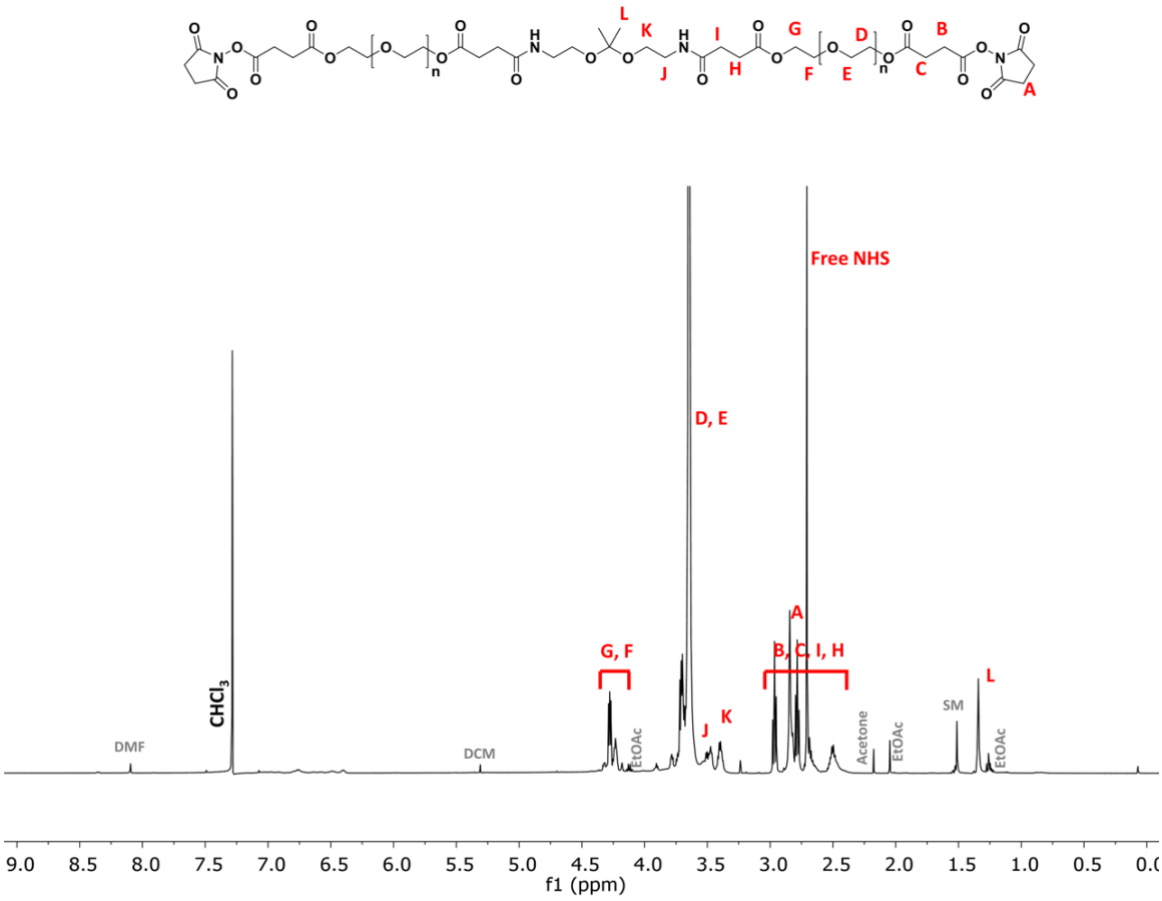

Figure 2.1 ^{1}H NMR spectrum of polymer **5** (PEG-ketal-NHS) acquired in $CDCl_3$. The spectrum was obtained using a Varian 400 MHz spectrometer. Residual solvent peaks have been labelled.

2.3.1.2 Investigation of the hydrolysis of pH-responsive crosslinker (PEG-ketal-NHS)

The kinetics of hydrolysis of crosslinker **5** were studied using a series of ^{1}H NMR spectral arrays in which the integration of the characteristic acetone peak was used to determine the percentage hydrolysis. This information is critical for designing tuneable methodologies for creating acid degradable soft-materials. The mechanism in which a ketal group hydrolysis can be seen in **Scheme 2.1**. The crosslinker **5** (20 mg) was dissolved in deuterated PBS buffer made with D_2O (0.1 M, 500 uL) at the appropriate pH. The pH was finally measured and adjusted accordingly using NaOH solution (5 M). A range of pH from 5 to 8.5 was investigated in order to establish the rate of hydrolysis of the central moiety. As seen in **Scheme 2.1**, acetone production occurs as a result of ketal hydrolysis, therefore the percentage acetone formation could be used to assess hydrolysis. The integration of the appearing acetone peak at 2.22 ppm in each spectrum compared to the integration of acetone plus ketal peaks gave overall percentage hydrolysis.

Ketal hydrolysis follows pseudo first order kinetics and therefore k_{obs} values could be found using the method described in **Section 2.2.10**, via the negative of the gradient of the initial slope of plotting $Ln(I_{acetone}/I_{ketone}+I_{acetone})$ vs incubation time for the various kinetic experiments carried out at different pH values. As seen in **Figure 2.2**, as the pH of the solutions increased there was a decrease in the k_{obs} values associated with a reduction in speed of the hydrolysis reaction. This can be attributed to the reduction in H^+ ion concentration at higher pH. A plot of k_{obs} versus pH (**Figure 2.3**) shows a sharp increase in k_{obs} values when pH is decreased to 6 and below, with the highest stability of the crosslinker in solution at pH values above 7.5.

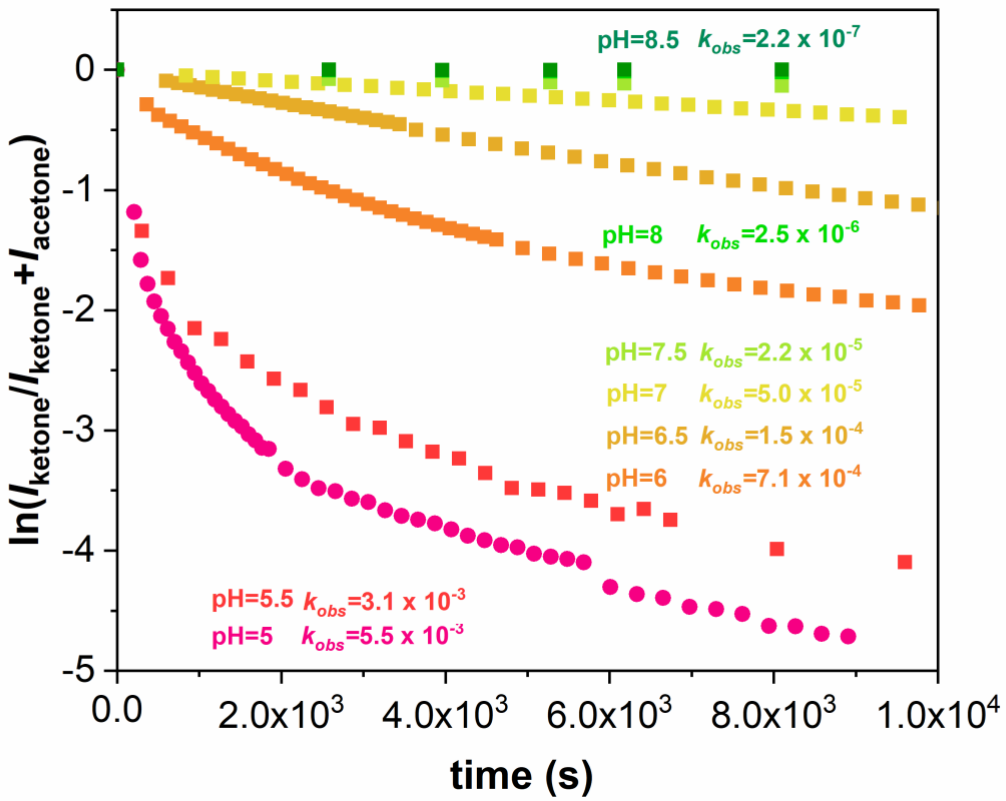

Figure 2.2 Plot of Ln($I_{acetone}$/I_{ketone}+$I_{acetone}$) versus incubation time of solutions of crosslinker 5 in deuterated PBS with varying pH from 5 to 8.5. k_{obs} values were determined by taking the negative of the initial slope of each of the curves. Colour coding has been used; each k_{obs} value colour matches the colour of the curve they were determined from.

Values of $t_{1/2}$ were calculated using **Equation 7** from **Section 2.2.10**. Significantly it was found that the crosslinker was stable in solution at pH values above 7.5, with a corresponding $t_{1/2}$ of 9 hours and above, even after a week of monitoring. When the pH was decreased to between 6 and 7.5, the corresponding $t_{1/2}$ values decreased to between 9 hours and 16 minutes, showing a dramatic reduction in stability at pH 6. When pH was decreased to 5 and 5.5, the $t_{1/2}$ values reduced to 3.7 and 2.1 minutes respectively.

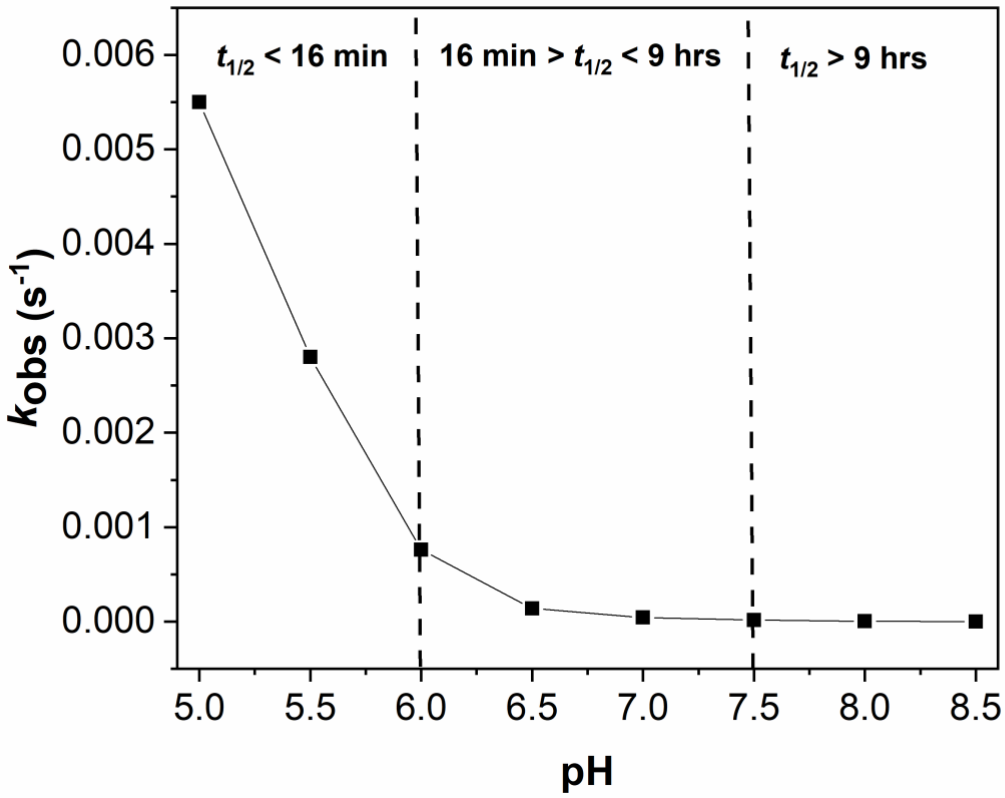

Figure 2.3 Plot of the pseudo-first order rate constants, k_{obs}, determined for the hydrolysis of crosslinker (5) over a range of pH values. The dashed vertical lines highlight three different pH regions where the acid-degradable crosslinker (5) hydrolyses in less than 16 minutes (left, pH < 6.0), hydrolyses in 16 min to 9 h (middle, 6.0 > pH < 7.5), and shows good stability for more than 9 h (right, pH > 7.5).

The $t_{1/2}$ values found crosslinker 5 mean that there will be a rapid hydrolysis at pH of 5 and 5.5, which make it ideal for the creation of soft materials able to respond rapidly to the stimulus. However, there may be the need to increase or decrease the speed of hydrolysis at low pH to increase the versatility of the crosslinker when needed to be used at lower pH. Recent investigations into the substituent effect on pH sensitivity of ketal containing molecules by Liu *et al* show that by changing the length of carbon chain between the ketal and electron-withdrawing amido group at the core of the molecule, they were able to modify the $t_{1/2}$ value of the molecule at pH 5.[28] The addition of four carbon atoms, increasing the chain length from two to six was shown

to decrease the $t_{1/2}$ by 80 times, from to 32 hours to 24 minutes respectively on acyclic ketal molecules. The closer proximity of the electron-withdrawing amido-group stabilises the carboxonium ion intermediate during hydrolysis. They also showed they could increase the $t_{1/2}$ by ca.7 times, from 32 to 221 hours by using cyclic ketal moieties over acyclic. These results show the potential of controlling the $t_{1/2}$ values, and therefore the speed of hydrolysis, in the pH-cleavable crosslinker 5 via lengthening the carbon chain or using cyclic ketal moieties. Such a marked difference between the results found by Liu et al and crosslinker **5** could be attributed to the increase in electron donating character from the amine groups in the final product, therefore destabilising the carboxonium ion intermediate.

2.3.2 Design and synthesis of light-responsive NHS-functionalised crosslinker

2.3.2.1 Synthesis and characterisation

The photoactive moiety needed to be carefully considered due to the complex nature of the system being synthesised. The proteins which are form the membrane of proteinosomes have an absorption maximum between 275 and 300 nm, whilst the most common fluorescent tags (Fluorescein and Rhodamine) have maximum absorptions at 495 and 555 nm respectively. The widely researched *o*-nitrobenzyl moiety (*o*-NB) is therefore a good candidate for the photoactive moiety as it has a broad absorbance from 320-420 nm, with a maximum absorbance at 347 nm (**Figure 2.4**), meaning that all the energy from the incident light will be used to activate the moiety. Further, derivatives of the *o*-NB moiety can be seen to absorb as high as 410 nm allowing for the potential of using safer wavelengths above 400 nm light to trigger photolysis. The addition of two methoxy groups shows an increase in the absorbance at longer wavelengths (λ > 350 nm). Rayonet lamps were shown to provide photolysis at reasonable rates as high as 420 nm.[19,20]

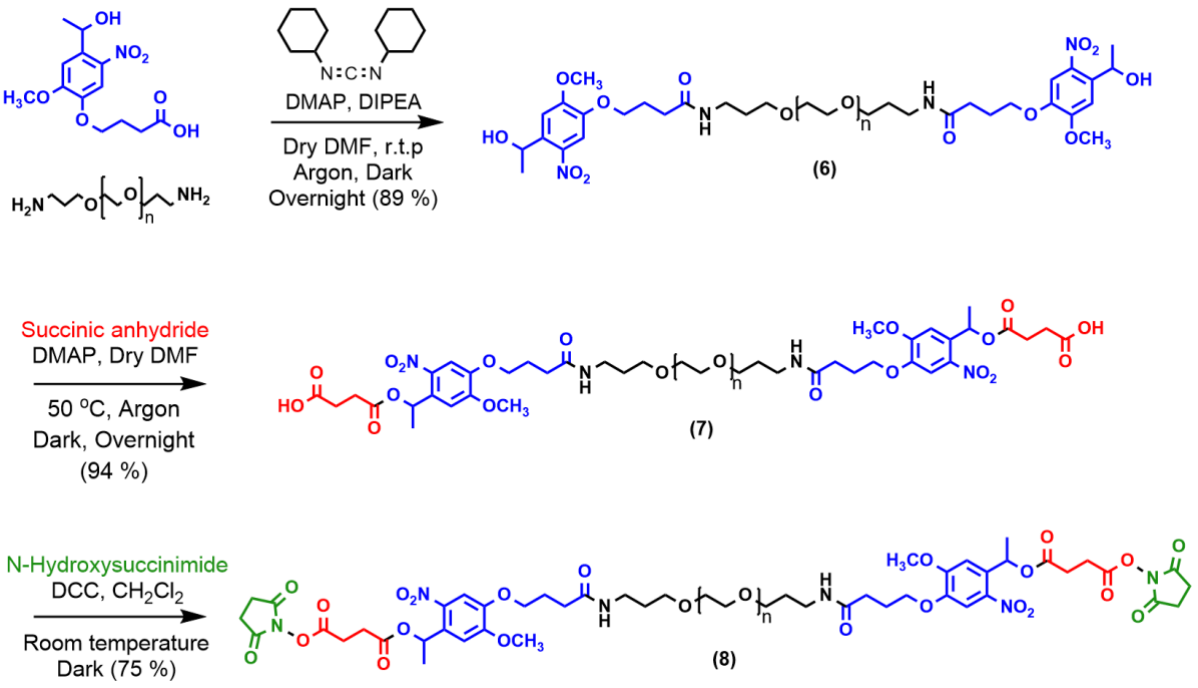

Scheme 2.4 Route to the synthesis of light-responsive crosslinker **8,** PEG-oNB-NHS.

For these reasons, a novel crosslinker for the synthesis and functionalisation of proteinosome membranes was designed, incorporating a commercially available chemical containing the o-NB moiety. Two of these molecules were coupled to each end of a poly(ethylene glycol) (PEG, MW 1500 g mol^{-1}) chain. This doubles the likelihood of photon absorption in the final product compared with only coupling one molecule. A high molecular weight PEG chain increased the water solubility of the final product meaning that the procedure to form the emulsion was modified slightly to account for this. From a technical perspective, it was important to ensure that all the reactions were performed under argon as the coupling agents used were air and moisture sensitive. The reactions were also performed in the dark in order to minimise any decomposition of the photosensitive compounds. The synthesis route to the *o*-NB functionalised crosslinker **3** can be seen in **Scheme 2.4**.

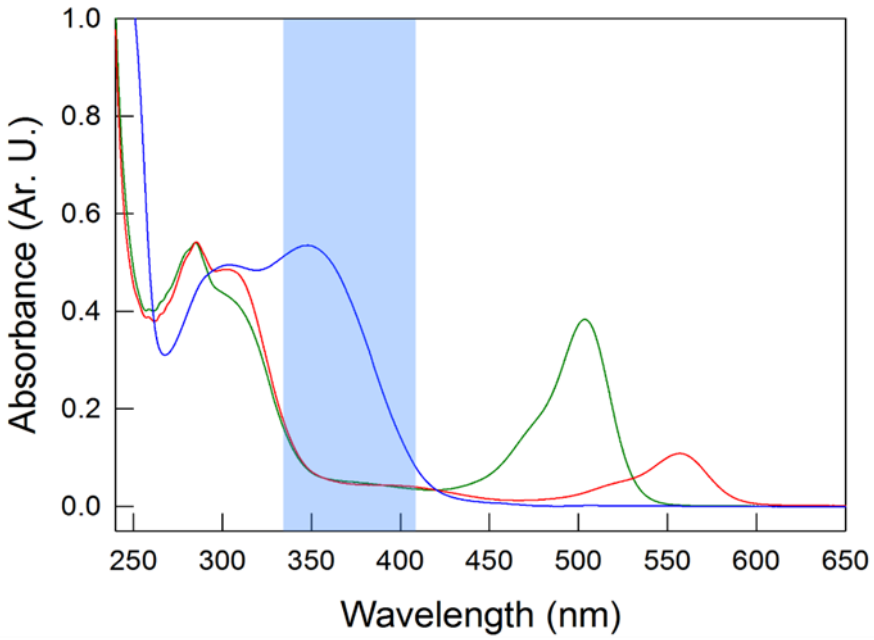

Figure 2.4 UV-Vis spectrum of FITC-tagged nanoconjugate (green line), RITC-tagged nanoconjugate (red line), and of o-NB functionalised crosslinker (blue line). Highlighted with a blue band is the ideal wavelength window of irradiation, in which there is minimal absorbance from the FITC- or RITC-labelled BSA/PNIPAm nanoconjugate constructing the proteinosome membrane and maximum absorbance from the o-NB moiety.

Synthesis of PEG-oNB-NHS began by coupling a molar excess of the *o*-nitrobenzylic acid to an amine terminated poly (ethylene glycol) (PEG) chain (MW 1500 g mol^{-1}) to give **2** in 94 % yield. The base *N,N*-diisopropylethylamine (DIPEA) was used to increase nucleophilicity of the amine. The ^{1}H NMR (**Figure S1**), 2D ^{1}H COSY NMR (**Figure S2**), and ^{13}C NMR spectra (**Figure S3**) gave structural evidence of addition of the two *o*-NB groups to the PEG chain. Importantly, the final C-H protons on the PEG chain which neighbour the amine group (a triplet at 2.82 ppm in the starting material) shift downfield to 3.29 ppm due to the increased electronegativity as the amide bond it formed as seen in **Figure S1**. The characterisation of end groups of polymers by 1D NMR techniques is limited by the low concentration of these groups in comparison to the polymer chain, and the difficulty in distinguishing between proton environments close in chemical shift. 2D ^{1}H COSY NMR was employed to identify and label proton

environments which were ambiguous. For example, the ^{1}H-^{1}H COSY map (**Figure S2**) shows cross peaks connecting through $^{3}J_{HH}$ couplings to their respective neighbouring protons for K, L, and J, and for G, H, and F, which were difficult to distinguish in the 1D ^{1}H NMR spectra. FTIR (**Figure S4**) showed the typical alkane C-H stretch and C-O stretch of the PEG chain at 2883 cm^{-1} and 1102 cm^{-1} respectively, the N-O stretch of the o-NB moiety at 1517 cm^{-1}. The MALDI spectrum (**Figure S5**) shows that the polymer chain stayed intact as the mass found (m/z = 2023) was consistent with the predicted mass of 2098 g mol^{-1} due to the 1,500 g mol^{-1} PEG polymer plus two of the *o*-nitrobenzyl groups of mass 299 g mol^{-1} each. MALDI also showed the repeating mass unit of 44.1 m/z typical of PEG. The UV-Vis spectrum (**Figure S6**) confirmed the incorporation of the *o*-nitrobenzyl group, at λ_{max} = 348 nm and λ_{max} = 306 nm, in the product.

The final crosslinker must be terminated with NHS esters in order to react with amine groups in the protein therefore it was necessary to perform a functional group change from the alcohol **1** to the carboxylic acid **2.** This was achieved with the base-mediated nucleophilic addition of succinic anhydride. There is the appearance of two new triplets in the ^{1}H NMR spectrum (**Figure S7**), which integrate to 8 protons with signals at 2.47 and 2.41 ppm, from the addition of the succinic anhydride on each end of the polymer. There are shifts of signals close to the reaction centre, specifically of proton B with integration of 1 from 5.46 to 6.37 ppm, protons C and E at 7.40 and 7.60 ppm to 7.17 and 7.62 ppm respectively, and doublet A which shifts from 1.48 to 1.62 ppm, all due to de-shielding effects as the alcohol is transformed to an ester. 2D ^{1}H COSY NMR (**Figure S8**) was employed to identify and label proton environments which were ambiguous. MALDI (**Figure S10**) was consistent with the theoretical mass of precursor **1** with the addition of 2 succinic acid groups (200 g mol^{-1}). The product was also characterised by UV-Vis spectroscopy (**Figure S11**) which showed the characteristic absorbance of the o-NB group at 348 nm.

The final step was the addition of the NHS groups via a 1-ethyl-3-(3-dimethylaminopropyl)carbodiimide (EDAC)-mediated coupling reaction to form the NHS ester. ^{1}H NMR and ^{13}C NMR spectra (**Figure 2.5** and **S12**) show the addition of the NHS group which has a signal at 2.88 ppm with an integration of 12

protons. Ideally the signal would integrate to 8 protons but the lack of purification due to sensitivity of the final product meant that the spectrum contains many extra peaks relating to excess reagents and by-products. Free NHS in deuterated methanol shows a signal at 2.65 ppm, and a shift from 2.65 to 2.88 ppm indicates that reaction has occurred, although there is limited information on whether it went to completion due to impurities making it difficult to integrate accurately. MALDI (**Figure S13**) was very noisy and shows a molecular weight of around 2175 Da which is not comparative to the theoretical weight of 2529 Da.

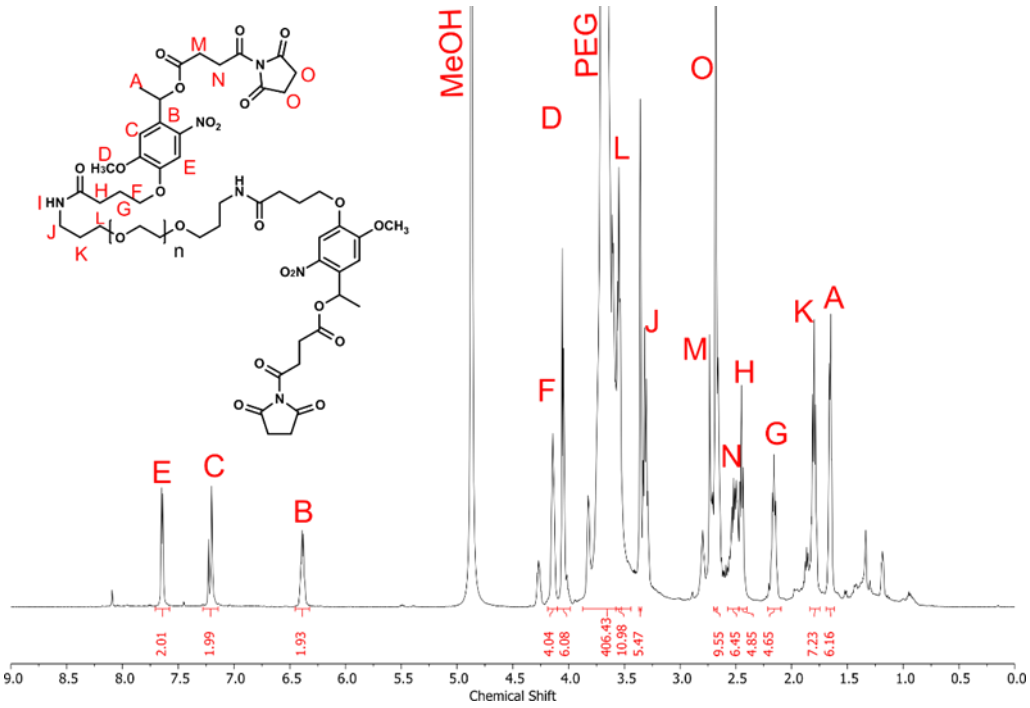

Figure 2.5 ^{1}H NMR spectrum of polymer **3** (PEG-oNB-NHS) recorded on 500 MHz NMR spectrometer in CD_3OD and calibrated against residual methanol.

Gel permeation chromatography was also used to investigate the molecular weights of each product in the synthesis (**Figure S14**). Plots of normalised intensity versus retention volume show a general decrease in retention volume for **1** and **2**, which corresponds to an increase in molecular weight as the polymers pass more easily through the column and interact less with the solid phase. Similar to MALDI, the retention volume increases for **3** corresponding to an apparent decrease in molecular weight. The use of polystyrene standards meant that the molecular weights were

grossly overestimated at around 6000 Da, however more reliable PDI values of between 1.14 and 1.4 were given, compared with MALDI estimations of 1.01.

2.3.2.2 Investigation of the photolysis of PEG-oNB-NHS using UV-Vis

As described in the chapter 2 introduction, o-nitrobenzyl moieties are responsive to UV-light; the N=O π-bond electron will absorb a photon and move into the excited state before the nitrogen extracts the benzylic proton. Subsequently, a cyclisation occurs before the alcohol is released. The photolysis mechanism of the PEG-oNB-NHS crosslinker is shown in **Figure 2.6**. The addition of an electron-donating methoxy group para to the nitro group was found to increase the absorption wavelengths to >350 nm, and even shows good absorption above 400 nm.[20] Wavelengths above 400 nm are much more penetrable through things like skin and tissue, meaning that the material could be used in drug delivery and tissue engineering.

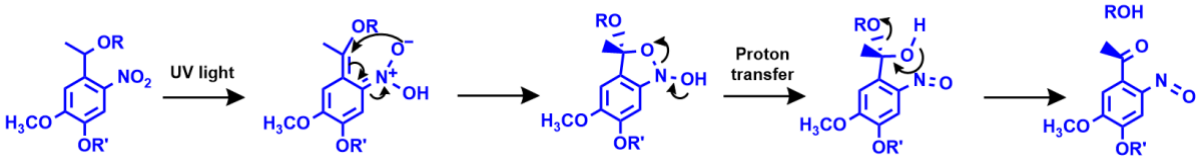

Figure 2.6 The general mechanism of the o-nitrobenzyl moiety, embedded within the light-responsive crosslinker. R is the NHS-succinic anhydride group, and R' is the amide-PEG chain.

The absorption characteristics of the crosslinker analysed through UV-Vis spectra **Figure S8** and **S12** showed that it absorbs light readily across the UV range from 330 nm tailing off at around 400-410 nm, due to the reasons above. The light source available to use for experiments had a variety of irradiation wavelengths to select including 350 and 365 nm. Given that the maximum absorbance of the moiety was 347 nm, it was hypothesised that irradiation at 350 nm would cause the higher rate of photolysis. An investigation to observe whether there was successful photolysis of the

crosslinker, then if there was any difference between the two wavelengths of light in terms of rate of photolysis, was performed.

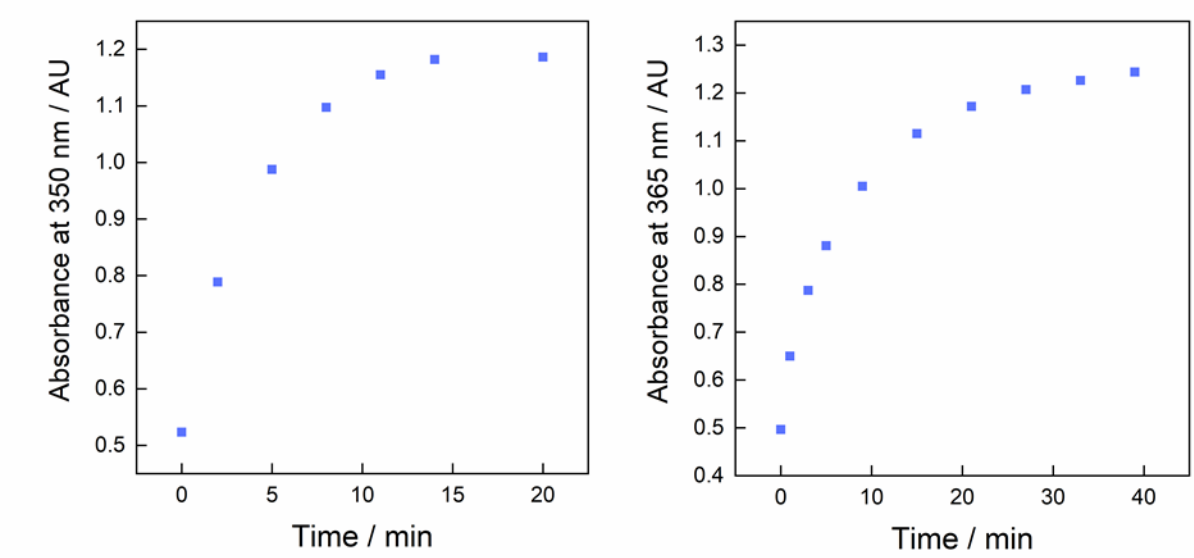

Figure 2.7 Absorbance versus time curves of a sample of PEG-oNB-NHS (0.01 mM, PBS pH 7.4) irradiated at either 365 nm or 350 nm with a xenon light source (11 mW)

The experiment was performed according to the method in **Section 2.2.14**. PEG-oNB-NHS crosslinker was dissolved in PBS (pH 7.4) to make a solution at 0.01 mM and irradiated using either 350 or 365 nm light. The absorbance at 347 nm was plotted against irradiation time to give plots (**Figure 2.7**) which were used to compare the rate of photolysis using the two wavelengths. The initial rate was estimated via the gradient of a linear plot of the first 5 minutes of irradiation. The initial rates were found to be 0.09 and 0.07 AU s^{-1} for irradiation with 350 and 365 nm light respectively. As expected, the use of 350 nm light showed 1.3 times faster initial rate which can be explained by the higher absorbance of photons by the crosslinker.

2.3.2.3 Molar attenuation coefficient determination of PEG-oNB-NHS

The molar attenuation coefficient (ε, **Equation 2**) is a measurement of how strong a chemical species absorbs light at a particular wavelength. It was important to

determine this value in order to understand whether the incorporation of *o*-nitrobenzyl into the polymer was affecting the photolysis behaviour. Using **Equation 2**, ε was determined by plotting a calibration curve of absorbance versus concentration of the chemical species, for the PEG-oNB-NHS crosslinker. As described in **Section 2.2.15**, a solution of the crosslinker in deionised water was made at a series of concentrations ranging from 0.025 to 0.003 mM. The absorbance of each solution was measured at 350 nm and plotted against concentration in mol L^{-1} (molar). The gradient of the linear plot gave the molar attenuation coefficient of 36561 L mol^{-1} cm^{-1}. The molar attenuation coefficients of other o-nitrobenzyl moiety derivatives have been found in the range of 10^3 to 10^4.[30] An ortho-nitrobenzyl moiety with no ring substituents tends to have values on the lower end of that scale, whereas the addition of methoxy groups and other ring substituents have been shown to increase the molar attenuation coefficient. The crosslinker does however have a molar attenuation coefficient one order of magnitude higher compared with an o-nitrobenzyl derivative with methoxy groups meta and para to the nitro group.[31] It is possible that the addition of the PEG chain could be increasing the molar attenuation coefficient.

2.4 Conclusion

The synthesis and characterisation of a novel pH responsive crosslinker **5** was described, which was designed to have an acid-degradable ketal core with a water-soluble PEG chain on either side terminating in N-hydroxysuccinimide (NHS) moieties for reaction with nucleophilic molecules, such as lysine amino acids and carboxymethyl-dextran. Each stage of the synthesis was characterised using: ^{1}H and ^{13}C NMR spectroscopy, to analyse the chemical structure of the molecules and confirm the corresponding functional group changes; and mass spectrometry (ESI for 1 and 2, MALDI-TOF for 3, 4 and 5) to analyse the molecular mass changes at each synthesis stage and confirm the mass of the final molecule as compared to theoretical mass. HMBC ^{13}C NMR spectroscopy was used to correctly assign the proton and carbon peaks in the final acid-cleavable crosslinker **5** (PEG-ketal-NHS).

The hydrolysis behaviour of PEG-ketal-NHS was investigated using 1H NMR spectroscopy. Using spectral arrays, the integration of the characteristic acetone peak was used to determine the percentage hydrolysis of the crosslinker. A plot of k_{obs} versus pH showed a sharp increase in k_{obs} values when pH is decreased to 6 and below, with the highest stability of the crosslinker in solution at pH values above 7.5. By calculating $t_{1/2}$ values, it was found that the crosslinker was stable in solution at pH values above 7.5, with a corresponding $t_{1/2}$ of 9 hours and above. When the pH was decreased to between 6 and 7.5, the corresponding $t_{1/2}$ values decreased to between 16 minutes and 9 hours, showing a dramatic reduction in stability at pH 6. When pH was decreased to 5 and 5.5, the $t_{1/2}$ values reduced to 3.7 and 2.1 minutes respectively. The $t_{1/2}$ values found for crosslinker 5 mean that there will be a rapid hydrolysis at pH of 5 and 5.5, which make it ideal for the creation of soft materials able to respond rapidly to the stimulus. There is also the opportunity to explore the synthesis of NHS functional acid-degradable crosslinkers with tuned the hydrolysis time by changing the length of the carbon chain or using cyclic ketal moieties over acyclic.

The synthesis and characterisation of a novel UV-light responsive crosslinker **8** (PEG-oNB-NHS) was described, which was designed to have a water-soluble PEG chain terminated by two light-responsive o-nitrobenzyl moieties with NHS functionality

for reaction with nucleophilic groups. Each stage of the synthesis was characterised using: ^{1}H and ^{13}C NMR spectroscopy, to analyse the chemical structure of the molecules and confirm the corresponding functional group changes; MALDI-TOF mass spectrometry to analyse the molecular mass changes at each synthesis stage; COSY ^{1}H NMR spectroscopy was used to correctly assign the proton peaks in polymers **6** and **7**; IR spectroscopy and UV Vis spectroscopy to identify characteristic functional groups of the PEG polymer and o-nitrobenzyl moiety in the synthesis products. Gel permeation chromatography was used to estimate the polydispersity index of each of the synthesis products, estimating them to be between 1.14 and 1.4.

The photolysis behaviour of the novel crosslinker PEG-oNB-NHS was investigated using UV Vis spectroscopy to compare initial rates of photolysis when using two different wavelengths of UV-light, 350 and 365 nm. The crosslinker showed a maximum absorption at 347 nm and so, as expected, the initial rate of photolysis was 1.3 times faster at 0.09 compared to 0.07 AU s^{-1} for irradiation with 350 and 365 nm light respectively. The molar attenuation coefficient was determined using a calibration curve of absorbance versus concentration. A value of 36561 L mol^{-1} was found using the gradient of the linear plot. This was the upper end of literature values which are seen in the range of $x10^{3}$ to $x10^{4}$ which could be to do with the addition of the PEG polymer.

An investigation to determine the k_{obs} of photolysis of PEG-oNB-NHS would be useful to perform in the future to compare to literature values and help improve understanding of the photolysis behaviour. In turn, this will help design crosslinkers with different properties to make tuneable functional soft-materials.

2.5 Appendix

Supplementary data (^{1}H NMR, ^{13}C NMR, MALDI, HMBC) for the characterisation of PEG-ketal-NHS **5** can be found in the cited publication by Myrgorodska *et al*.[29]

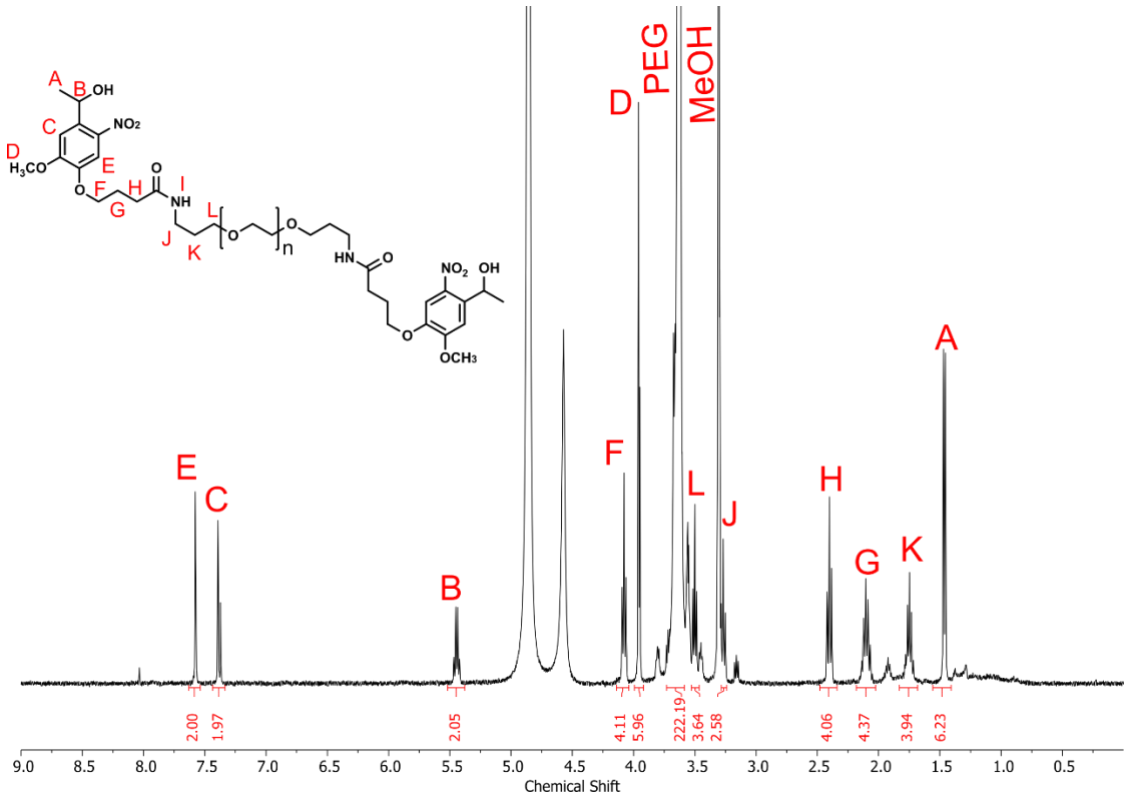

Supplementary Figure S*1* ^{1}H NMR spectrum of polymer **1** recorded on 400 MHz NMR spectrometer in deuterated CD_3OD and calibrated against residual methanol.

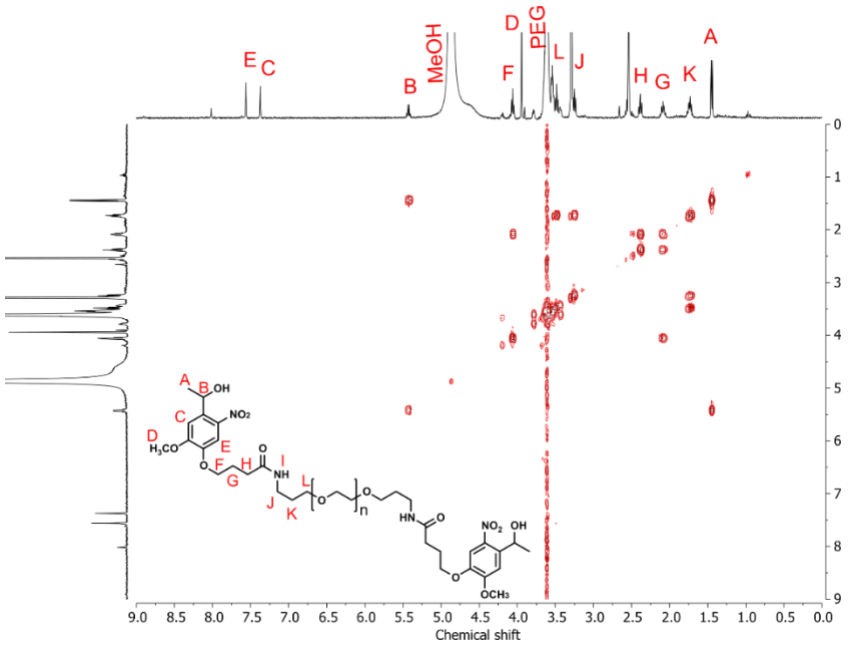

Supplementary Figure S2 2D ^{1}H COSY NMR spectrum of polymer **1** recorded on a 400 MHz NMR spectrometer in deuterated CD_3OD and calibrated against residual methanol.

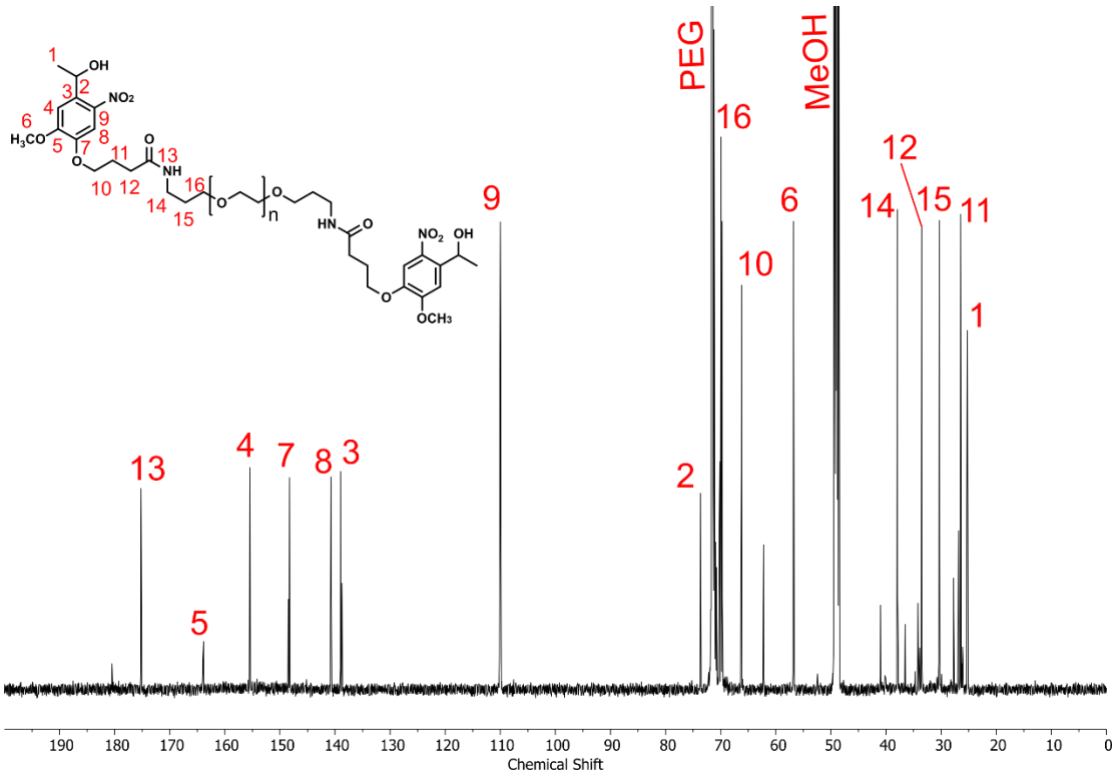

Supplementary Figure S3 ^{1}H decoupled ^{13}C NMR spectrum of polymer **1** recorded on 500 MHz NMR spectrometer in deuterated CD_3OD and calibrated against CD_3OD.

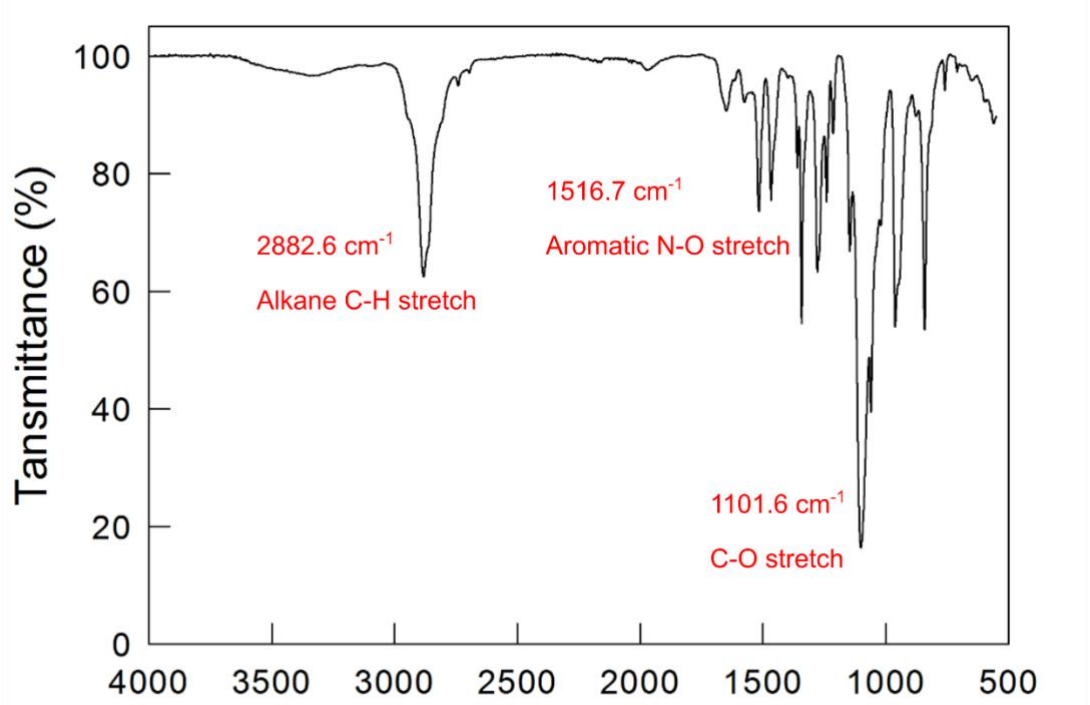

Supplementary Figure S4 FT-IR spectrum of polymer **1** recorded on a PerkinElmer Spectrum One FT-IR spectrometer.

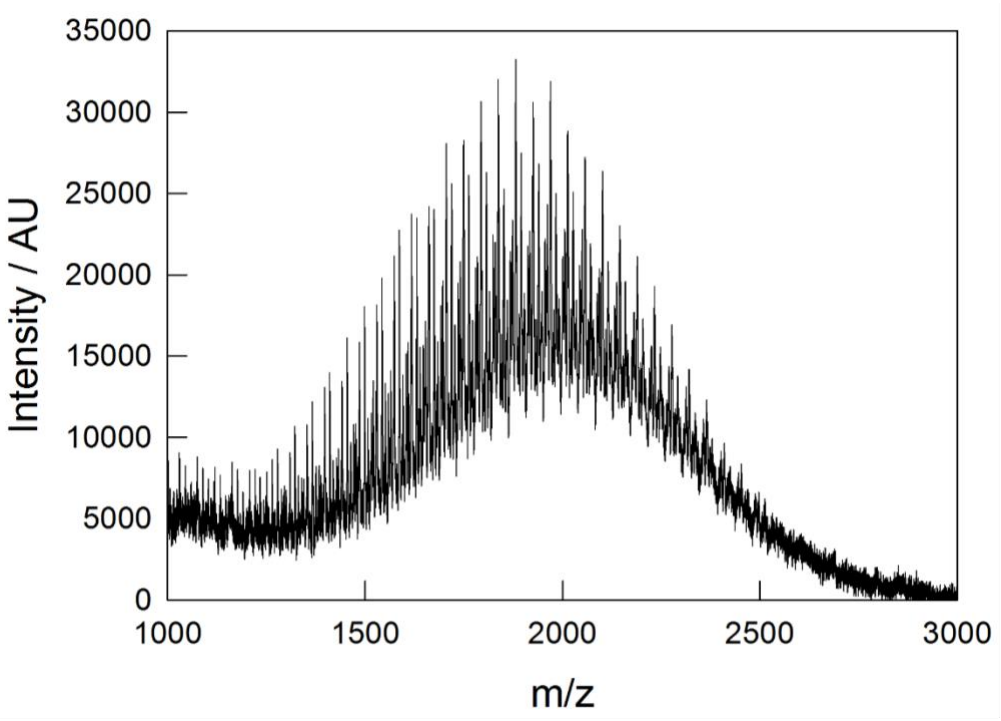

Supplementary Figure S5 MALDI-TOF spectrum of polymer **1** recorded using alpha-cyano-4-hydroxycinnamic acid (7 mg/mL in ACN/0.1%TFA) as the matrix solution, on a Bruker UltrafleXtreme (TOF).

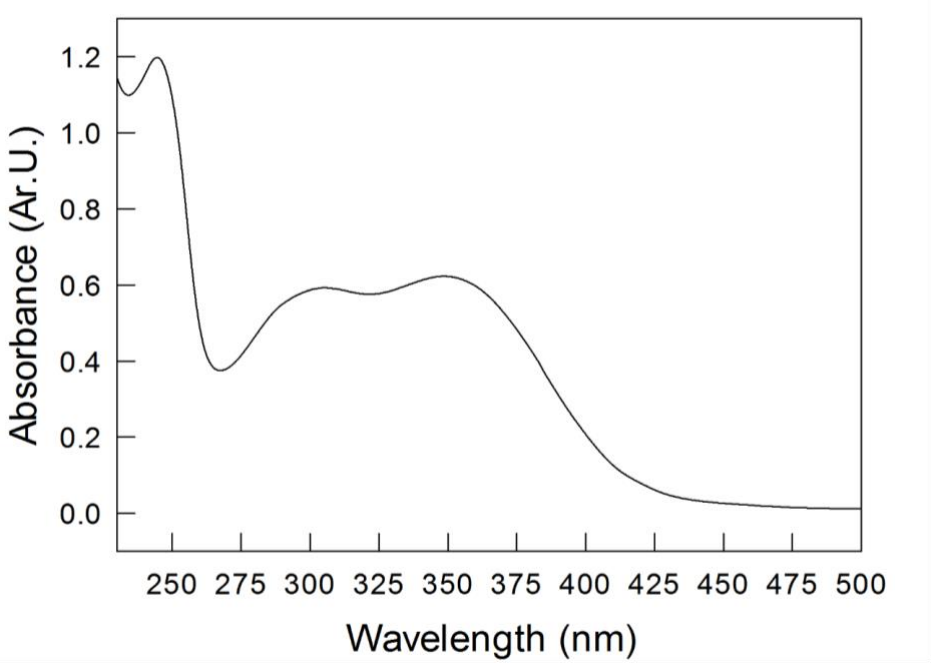

Supplementary Figure S6 UV-Vis spectrum of a 0.1 mM solution of polymer **1** in PBS buffer (0.1 M, pH 7.4). Spectrum recorded on a PerkinElmer Lambda 35 spectrometer.

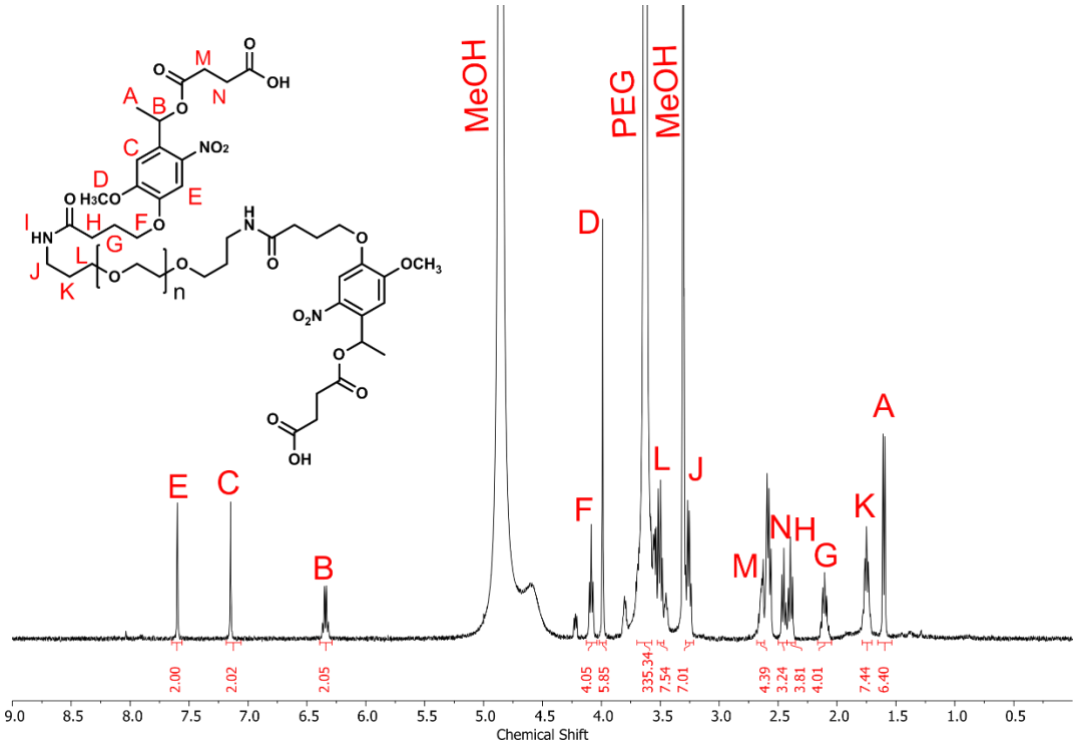

Supplementary Figure S7 ^{1}H NMR spectrum of polymer **2** recorded on 400 MHz NMR spectrometer in deuterated CD_3OD and calibrated against residual methanol.

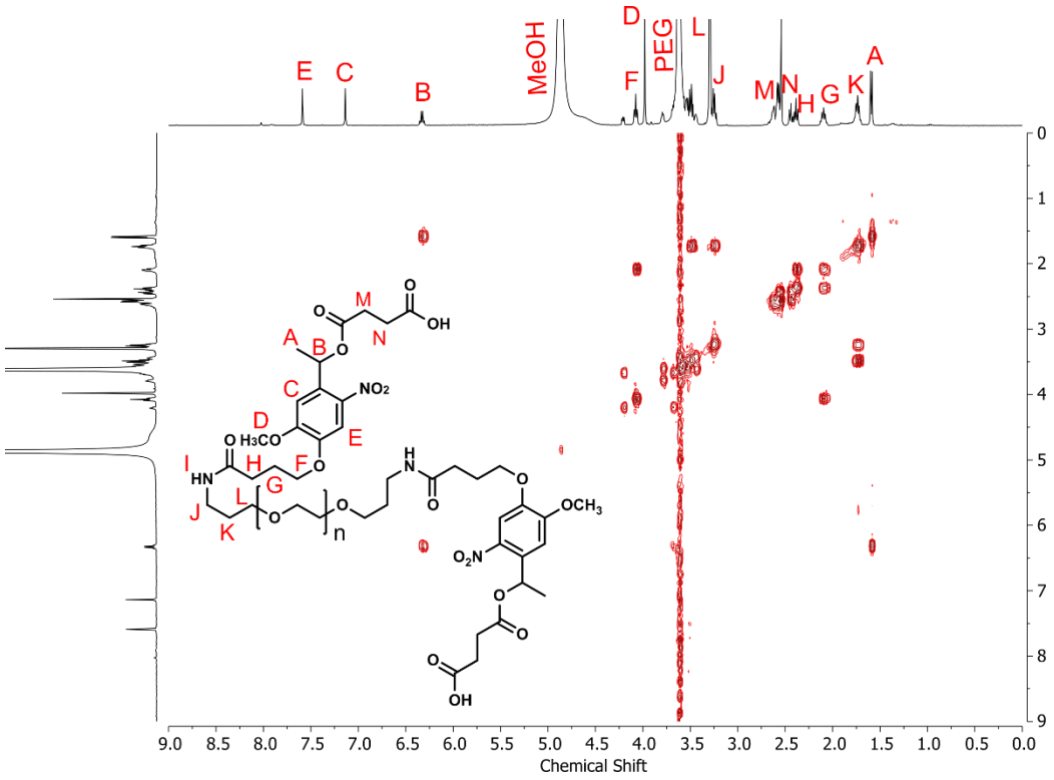

Supplementary Figure S8 2D ^{1}H COSY NMR spectrum of polymer 1 recorded on a 400 MHz NMR spectrometer in deuaterated CD_3OD and calibrated against residual methanol.

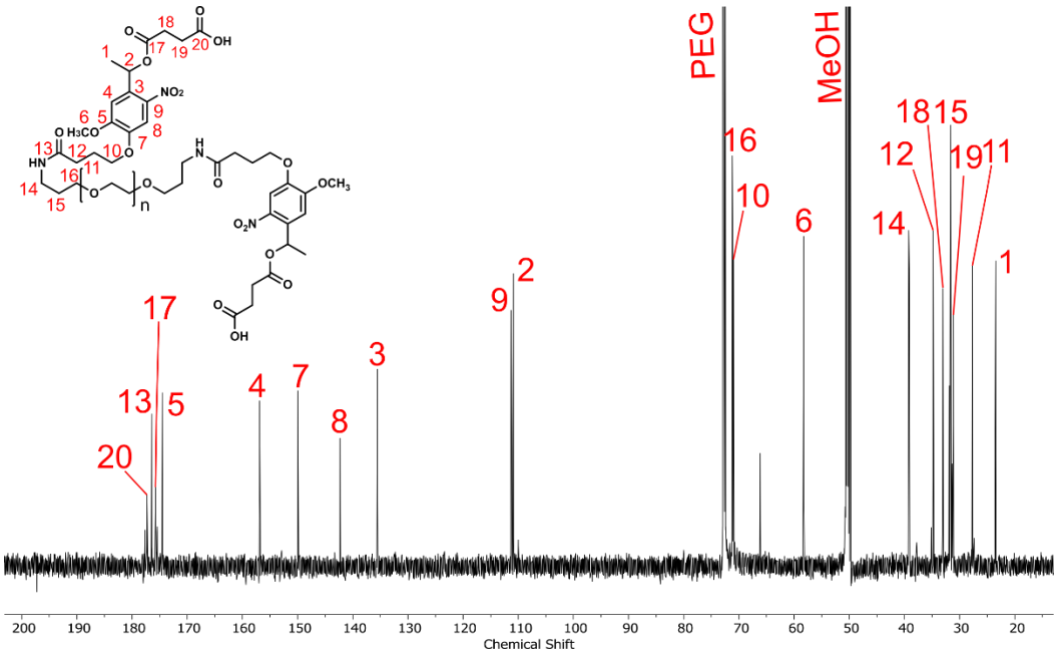

Supplementary Figure S9 *^{1}H decoupled* ^{13}C NMR spectrum of polymer **2** recorded on 500 MHz NMR spectrometer in deuterated CD_3OD and calibrated against CD_3OD.

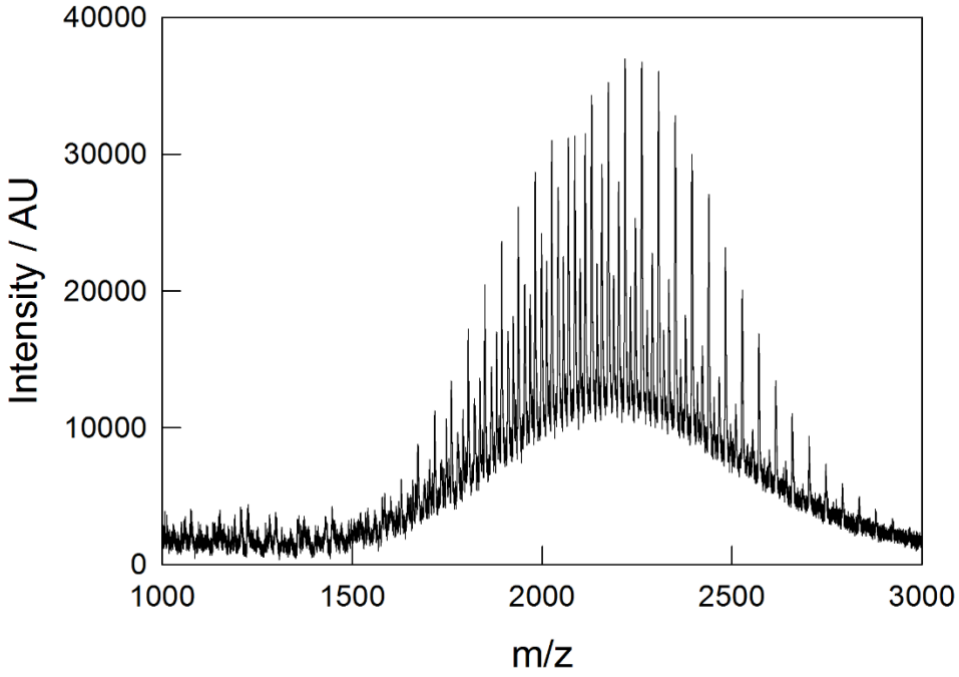

Supplementary Figure S10 MALDI-TOF spectrum of polymer **2** recorded using alpha-cyano-4-hydroxycinnamic acid (7 mg/mL in ACN/0.1%TFA) as the matrix solution, on Bruker UltrafleXtreme (TOF).

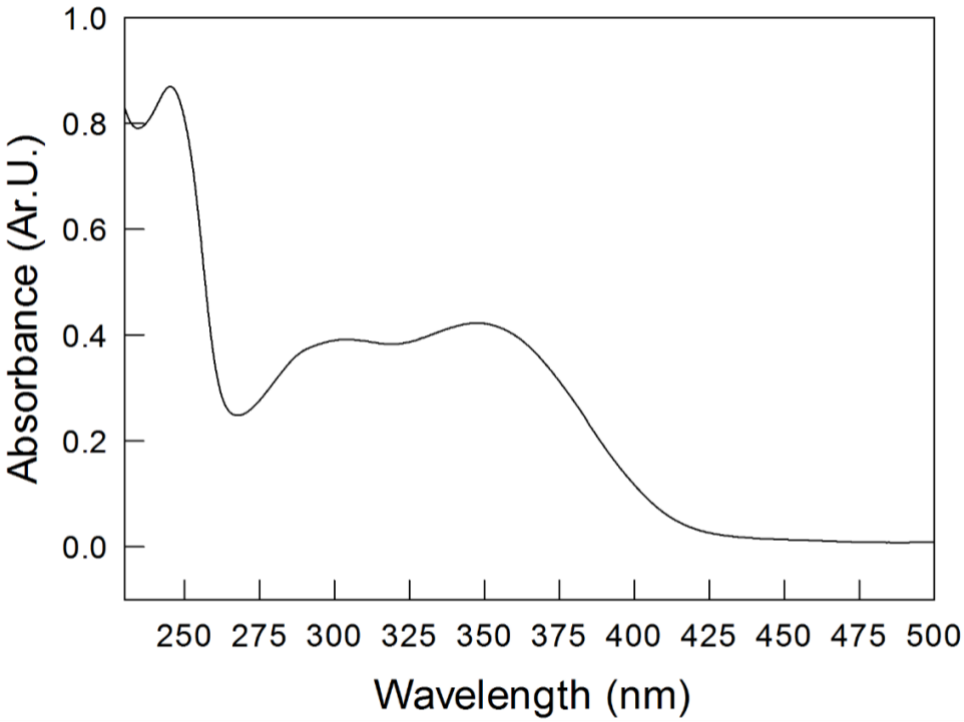

Supplementary Figure S11 UV-Vis spectrum of a 0.1 mM solution of polymer **2** in PBS buffer (0.1 M, pH 7.4). Spectrum recorded on a PerkinElmer Lambda 35 spectrometer.

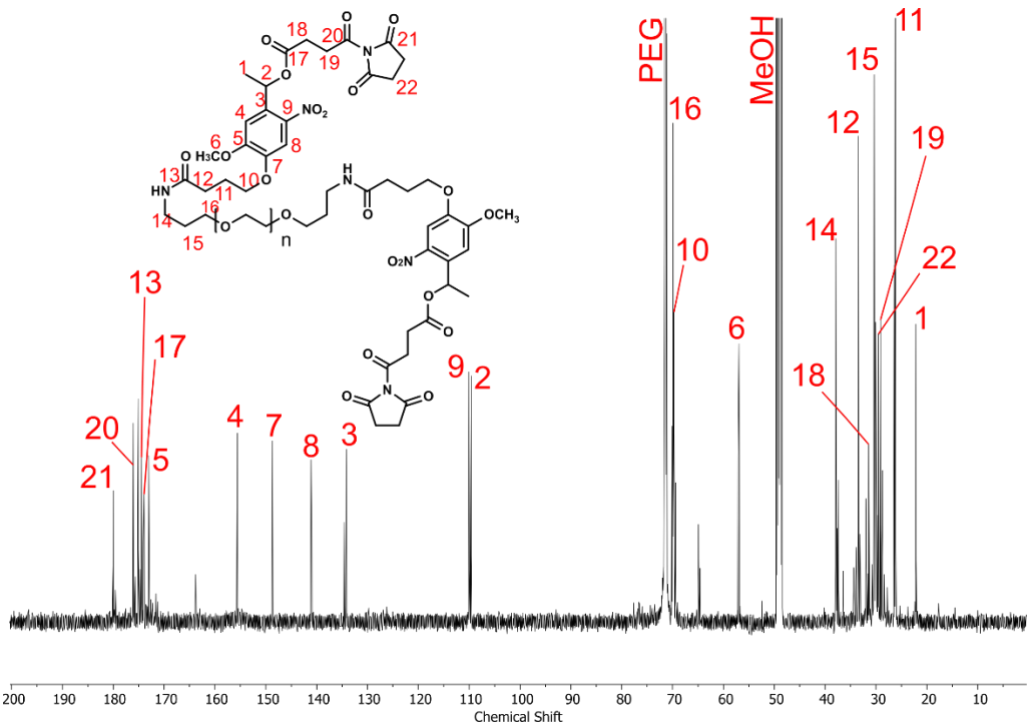

Supplementary Figure 12 ^{1}H decoupled ^{13}C NMR spectrum of polymer **3** recorded on 500 MHz NMR spectrometer in CD_3OD and calibrated against CD_3OD.

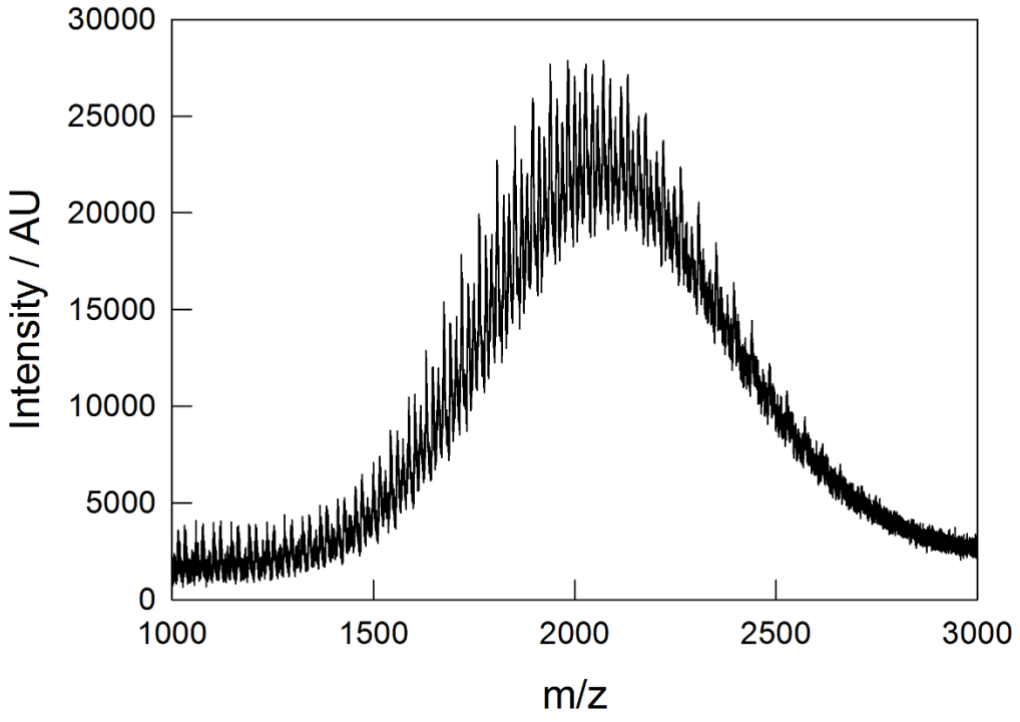

Supplementary Figure S13 MALDI-TOF spectrum of polymer **3** recorded using alpha-cyano-4-hydroxycinnamic acid (7 mg mL^{-1} in ACN/0.1%TFA) as the matrix solution, on Bruker UltrafleXtreme (TOF).

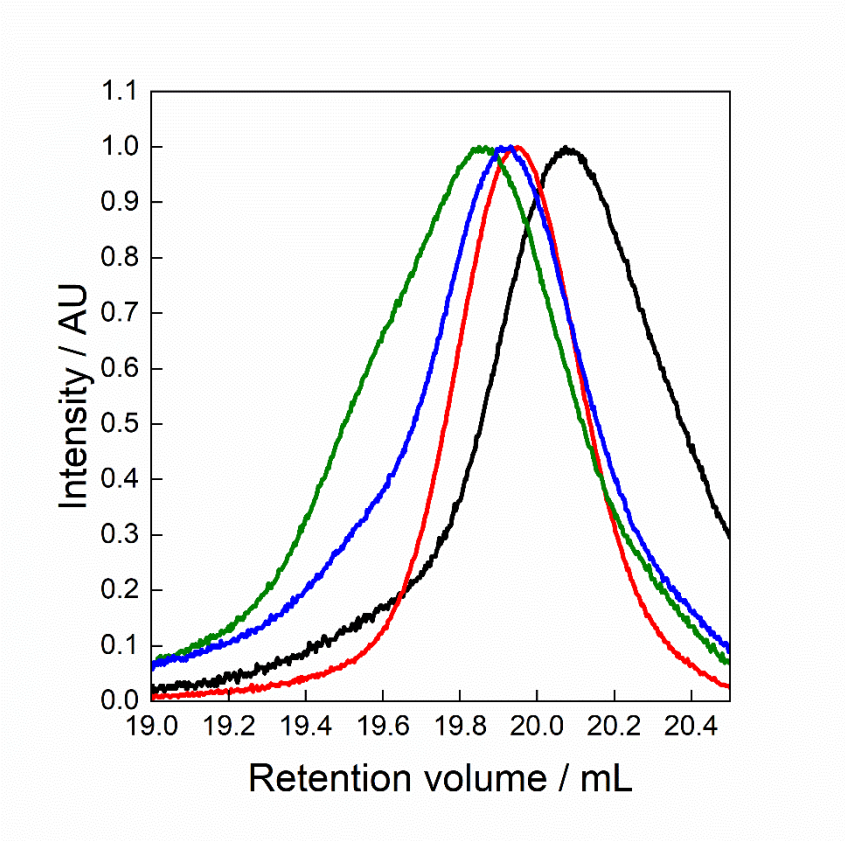

Supplementary Figure S14 Gel permeation chromatograph of the PEG-diNH_2 starting material (Black curve), polymer **1** (red curve), polymer **2** (Green curve), and polymer **3** (Blue curve).

References

[1] M. A. Cohen Stuart, W. T. S Huck, J. Genzer, M. Müller, C. Ober, M. Stamm, G. B. Sukhorukov, I. Szleifer, V. V Tsukruk, M. Urban, F. Winnik, S. Zauscher, I. Luzinov, S. Minko, *Nat. Mater.* **2010**, 9, 101-113.

[2] F. D. Jochum, P. Theato, *Chem. Soc. Rev.* **2013**, *42*, 7468–7483.

[3] A. Halperin, M. Kröger, F. M. Winnik, *Angew. Chemie Int. Ed.* **2015**, *54*, 15342–15367.

[4] H. Zeng, P. Wasylczyk, D. S. Wiersma, A. Priimagi, *Adv. Mater.* **2018**, *30*, 1703554.

[5] P. Theato, B. S. Sumerlin, R. K. O'reilly, T. H. Epps, *Chem. Soc. Rev* **2013**, *42*, 7055.

[6] G. Hao, Z. P. Xu, L. Li, *RSC Adv.* **2018**, *8*, 22182–22192.

[7] F. Wang, J. Gao, J. Xiao, J. Du, *Nano Lett.* **2018**, *18*, 5562–5568.

[8] L. Sun, H. Wei, X. Zhang, C. Meng, G. Kang, W. Ma, L. Ma, B. Wang, C. Yu, *Polym. Chem.* **2020**, *11*, 4469–4476.

[9] X. Su, B. Ma, J. Hu, T. Yu, W. Zhuang, L. Yang, G. Li, Y. Wang, *Bioconjug. Chem.* **2018**, *29*, 4050–4061.

[10] M. S. Ober, D. R. Romer, J. Etienne, P. J. Thomas, V. Jain, J. F. Cameron, J. W. Thackeray, *Macromolecules* **2019**, *52*, 886–895.

[11] E. H. Cordes, H. G. Bull, *Chem. Rev.* **1974**, *74*, 581–603.

[12] B. Liu, S. Thayumanavan, *J. Am. Chem. Soc.* **2017**, *139*, 2306–2317.

[13] H. Pohlit, D. Leibig, H. Frey, *Macromol. Biosci.* **2017**, *17*, 1600532.

[14] H. U. Kim, D. G. Choi, H. Lee, M. S. Shim, K. W. Bong, *Lab Chip* **2018**, *18*, 754–764.

[15] Y. Y. Peng, D. Diaz-Dussan, P. Kumar, R. Narain, *Biomacromolecules* **2018**, *19*, 4052–4058.

[16] A. Patchornik, B. Amit, R. Woodward, *J. Am. Chem. Soc* **1970**, *92*, 6333.

[17] S. G. Chaulk, A. M. MacMillan, *Nat. Protoc. 2007 25* **2007**, *2*, 1052–1058.

[18] G. C. R Ellis-Davies, J. H. Kaplan, S. Francisco, J. M. Annu Rev Biophys Bioeng, *J. Org. Chem.* **1988**, *53*, 843.

[19] C. G. Bochet, *J. Chem. Soc. Perkin Trans. 1* **2002**, *0*, 125–142.

[20] P. Klán, T. Šolomek, C. G. Bochet, A. Blanc, R. Givens, M. Rubina, V. Popik, A. Kostikov, J. Wirz, *Chem. Rev.* **2013**, *113*, 119–191.

[21] X. Wang, Y. Yang, C. Liu, H. Guo, Z. Chen, J. Xia, Y. Liao, C. Y. Tang, W. C. Law, *Polymer (Guildf).* **2021**, *229*, 123961.

[22] M. C. Sharp, *Biophotonics Med. Appl.* **2015**, 79–98.

[23] J.-M. Schumers, C.-A. Fustin, J.-F. Gohy, *Macromol. Rapid Commun.* **2010**, *31*, 1588–1607.

[24] J. Jiang, X. Tong, Y. Zhao, *J. Am. Chem. Soc* **2005**, 127, 8290-8291.

[25] J. Jiang, X. Tong, D. Morris, Y. Zhao, *Macromolecules* **2006**, 39, 4633-4640.

[26] J. Clayden, *Organic Chemistry*, Oxford Press, **2012**.

[27] R. Zenobi, R. Knochenmuss, *Mass Spectrometry Reviews* **1998**, 17, 337-366.

[28] B. Liu, S. Thayumanavan, *J. Am. Chem. Soc.* **2017**, *139*, 2306–2317.

[29] I. Myrgorodska, M. Jenkinson-Finch, R. O. Moreno-Tortolero, S. Mann, P. Gobbo, *Macromolecular Rapid Communications* **2021**, 42,

[30] R. Weinstain, T. T. Slanina, D. Kand, P. K. Klán, *Chem. Rev.* **2020**, 120, 13135-13272.

[31] K. Takaoka, Y. Tatsu, N. Yumoto, T. Nakajima, K. Shimamoto, *Bioorg. Med. Chem. Lett.* **2003**, *13*, 965–970.

Chapter 3: The construction of stimuli-responsive proteinosomes

Publications

Publications pertaining to the work described in this chapter:

Iuliia Myrgorodska, **Mary Jenkinson-Finch**, Rafael O. Moreno-Tortolero, Stephen Mann, Pierangelo Gobbo, A Novel Acid-Degradable PEG Crosslinker for the Fabrication of pH-Responsive Soft Materials, *Macromol. Rapid Commun.,* **2021**, *42*, 2100102

Mary Jenkinson-Finch and Iuliia Myrgorodska performed the acid-degradable hydrogel synthesis and degradation experiments, and the proteinosome synthesis and degradation experiments. Iuliia Myrgorodska performed the enzyme-catalysed hydrolysis experiments with hydrogels and proteinosomes.

Chapter Outline

In this chapter, light-responsive proteinosomes are constructed from protein-polymer nanoconjugates and crosslinked using PEG-oNB-NHS synthesised in chapter 2. The proteinosome disassembly upon irradiation with a confocal microscope UV laser is characterised, demonstrating the high precision and versatility of the technique, which has potential to be used for patterning, or the construction of bespoke 3D prototissues. The synthesis and characterisation of acid-degradable hydrogels and proteinosomes is discussed briefly in the appendix.

3.1 Introduction

Protocells, as discussed in **Chapter 1**, are synthetic cell-like entities that have been proposed as a candidate precursor to the first biological cell, helping to decipher how chemistry became biology.[1] The proteinosome is a protocell model which has a semi-permeable membrane comprised of hybrid protein-polymer nanoconjugate building blocks. They are synthesised via a Pickering emulsion method, much like colloidosomes, and the nanoconjugates can be crosslinked together *via* amine groups on the protein before being transferred to water.[2,3] They have been shown to exhibit a range of protocell properties such as: encapsulation of a variety of guest molecules and reactions, including enzymes and enzyme cascade reactions; the incorporation of enzymes into the membrane structure for the demonstration of membrane-mediated enzyme cascade reactions[4]; the generation of an enzyme-mediated cytoskeleton-like matrix within the interior, creating a molecularly crowded environment[3]; and the encapsulation of gene directed protein synthesis[2].

Organisms have evolved to be able to respond to their environment through the tailoring of molecular assemblies providing them with specific chemical function. This means that more recently, there has been an interest in synthesising stimuli-responsive and programmable proteinosomes. The crosslinked protein-membrane has the potential to be easily manipulated due to the modular nature of the building blocks. Prototissues have been constructed using proteinosomes with modified nanoconjugate building blocks for pre-programmed inter-proteinosome crosslinking.

As demonstrated by Gobbo *et al*, The PNIPAAm chains on the bovine serum albumin (BSA) nanoconjugates were adapted to incorporate complementary click-chemistry groups in two separate proteinosome populations so that upon mixing, the different proteinosomes were bound together chemically to form a tissue-like structure.[5,6] Further, Huang *et al* showed that multi-functional proteinosomes have been constructed similarly via the functionalisation of polymer nanoconjugates with spiropyrans. They showed that membrane spiropyrans responded to UV-light and redox conditions, whilst the PNIPAAm responded to temperature, meaning a variety of stimuli could be utilised to increase and decrease the membrane permeability.[7] Responsive proteinosome populations have also been constructed via manipulation of the crosslinker, specifically by using a crosslinker containing a disulphide bond (NHS-PEG16-DS), which can be cleaved upon the addition of a reducing agent such as tris(2-carboxyethyl)phosphine (TCEP). Huang *et al* were able to show that programmed release of guest molecules could be achieved in nested proteinosome populations by crosslinking the host and guest proteinosomes with either non-responsive PEG-diNHS crosslinker or with TCEP responsive NHS-PEG16-DS.[8]

Inspiration from nature has driven the design of complex polymeric systems, which have been shown to mimic certain functions such as cell differentiation[9], self-reproduction[10], and even phagocytosis-inspired behaviours[11]. The engineering of biological cells using synthetic materials, or biointerfacing, has been identified as a considerable challenge in biomedical research.[12] Natural polymeric systems within cellular environments respond to signals and triggers from the environment in order to sustain life.[13] The complex nature of microenvironments in tissues elicits a need for the synthetic materials interacting and integrating with biological systems to also have responsive behaviours, in order to further the understanding of cellular systems and for uses in the biomedical industry, such as cell-regeneration.[14] The interaction between the cellular environment and materials depends on the surface properties of the material, and therefore materials should reflect the same level of complexity. This requires an increased dynamic functionality in the materials being developed for the use at the biointerface to reflect the dynamic behaviour observed in, and required by natural systems.[15] By combining smart polymer systems with biocompatible surfaces and nano/microcompartments, we can begin to create biointerfaces that are more equipped to respond and adapt to cellular environments, and with an increased

potential for use in in the biomedical industry. Further, being able to pattern cells in a controlled manner provides the opportunity to have cells in predetermined locations and positions relative to one another aiding the facile investigation of certain cell behaviours, including cell-cell communication.

Due to the more complex synthesis, greater difficulty in handling, and minimal potential for precise controlled stimuli-response, compared with light-responsive proteinosomes, the construction of pH responsive soft materials and proteinosomes using a pH responsive crosslinker is detailed briefly in **Chapter 3 appendix**. Herein, the construction of UV-light responsive proteinosome membranes by utilising the PEG-oNB-NHS crosslinker, synthesised in **Chapter 2**, is described. These proteinosome populations have the advantage of being responsive to light, which is well known to be versatile, with technology existing to emit very specific wavelengths in very specific locations. In addition, power can be easily adjusted to further control the membrane response.

3.2 Materials and methods

Bovine serum albumin (BSA), fluorescein isothiocyanate (FITC), Rhodamine-B isothiocyanate (RITC), fluorescein isothiocyanate-dextran (FITC-dextran) (MW 40, 70, 150 and 2000 kDa), 1,6-diaminohexane, and PEG-(bis(N-succinimidyl succinate) (PEG-diNHS) were purchased from Sigma-Aldrich. 1-Ethyl-3-(3-dimethylaminopropyl)carbodiimide (EDAC) (98+%) was purchased from Alfa Aesar. Dialysis bags with MWCO 12,000–14,000 Da were purchased from Millipore. All solvents were purchased from commercially available sources and used without further purification. Water was filtered using a MilliQ integral 3 system before use. PNIPAAm (M_n = 8745.5 Da, PDI = 1.1) was synthesised according to literature procedures.[2]

3.2.1 Optical/light microscopy

Light microscopy (**Figure 3.1**) is an optical imaging technique first invented in the 1600s allowing the study of objects below the limits of human perception.

The human eye contains cone and rod cells, which are used to sense colour (the visible part of the spectrum) and levels of brightness and intensity (from black to white and all the shades of grey in between). The cells are located on the retina at the back of the eye and the front of the eye houses the iris, cornea and lens which control the admittance of light into the eye from the environment, focusing it on the retina. A clear, in-focus image is seen when the incident light is spread at a sufficient visual angle on non-adjacent rows of retinal cells. If this condition is not met, the image will not be resolved, and details will not be seen. For these reasons, if an object is too close to the eye (less than 25 cm), it will not be in focus. The early microscopes were simple magnifiers which contained a convex lens between the eye and the object to increase the visual angle on the retina, spreading out the image.

Over the proceeding centuries, compound microscopes were invented which have two lenses in series achieving further magnification of the image and can be adjusted in height to maintain focus of the sample. Depending on the objectives used, the magnification of the sample can be varied; standard magnifications include 4, 10, 20, 40, 63 and 100 times. The variables which are adjusted to achieve different

magnifications are: the angle in which the light hits the lens (incidence angle); the curvature of the lens; and the density of the glass (refractive index). To form the image, parallel light from the object which enters the lens is brought into focus at a point behind the lens and magnified into a real image below the eyepiece. From the mid 1900's to now, there have been many advancements in optical microscopes including the use of cameras to capture the light coming from the sample, negating the use of an eyepiece and allowing the images to be directly saved on a computer.[16]

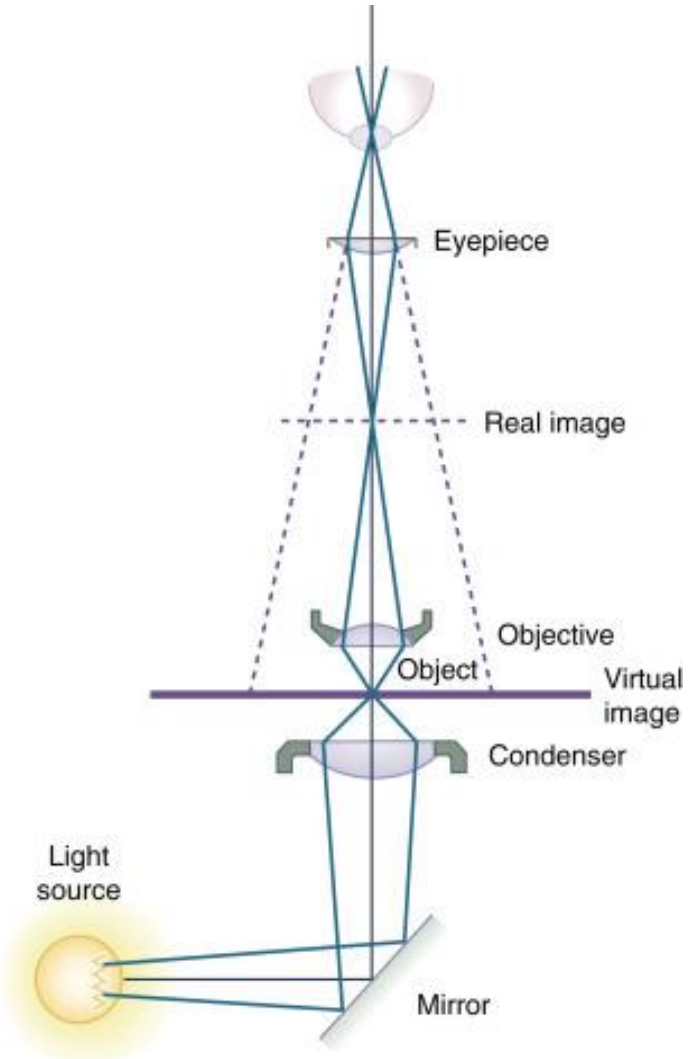

Figure 3.1 Schematic showing the basic principle of light microscopy. The incidence ray from the light source is reflected off a mirror before being focused by the condenser onto the object. Light from the object goes through an objective of certain magnification before travelling along a tube and through the eyepiece giving the user a magnified real image.[16]

There are several limitations to traditional optical microscopy including diffraction-limited resolution because of the incidence wavelength of visible light; resolution is therefore limited to 0.2 um. Another limitation is that bright field microscopy only works for strongly refracting objects. One of the biggest downsides to traditional optical microscopy is the fact that the lens has a depth of field where the image forms and subsequently multiple images are formed at multiple focal planes. Superimposition of the images at the eyepiece/detector results in a blurred image. Several microscopy techniques have been invented that circumvent these limitations such as fluorescence and confocal microscopy.

3.2.1.2 Fluorescence and confocal microscopy

Fluorescence microscopy uses fluorescence of an object to generate an image. A specific wavelength of light is used depending on the fluorescent properties of the object, specifically the excitation wavelength of a fluorophore. A wavelength of light is used that is absorbed by fluorophores in the object causing emission of a longer wavelength of light. This is called a Stokes' Shift. An excitation filter is used to select the chosen wavelength from the light source before it is passed through the objective onto the object. The light emitted from the object goes through the same objective to be focussed onto the detector. The light from the sample passes through a dichroic mirror so that any excitation light is reflected to the light source, before passing through a spectral emission filter used to filter only the emission light.

Fluorescence microscopy (**Figure 3.2**) is a sensitive technique owing to how little fluorophore is needed to create a strong emission and therefore a good image. Multiple parts of an object may be tagged with different fluorophores and a multi-colour image can be formed by combining all the channels. This is of particular use in the life sciences as specific parts of biological samples can be tagged with high specificity amid non-fluorescing material, meaning characteristics such as protein distribution can be analysed using this technique.[17][18] It is also extremely useful when objects are not strongly refracting and so are difficult to image using traditional optical microscopy. Superimposition is still a problem in fluorescence microscopy as there is a large cone of illumination directed onto the sample resulting in significant emission signal out of the focal plane being directed back up to the detector.

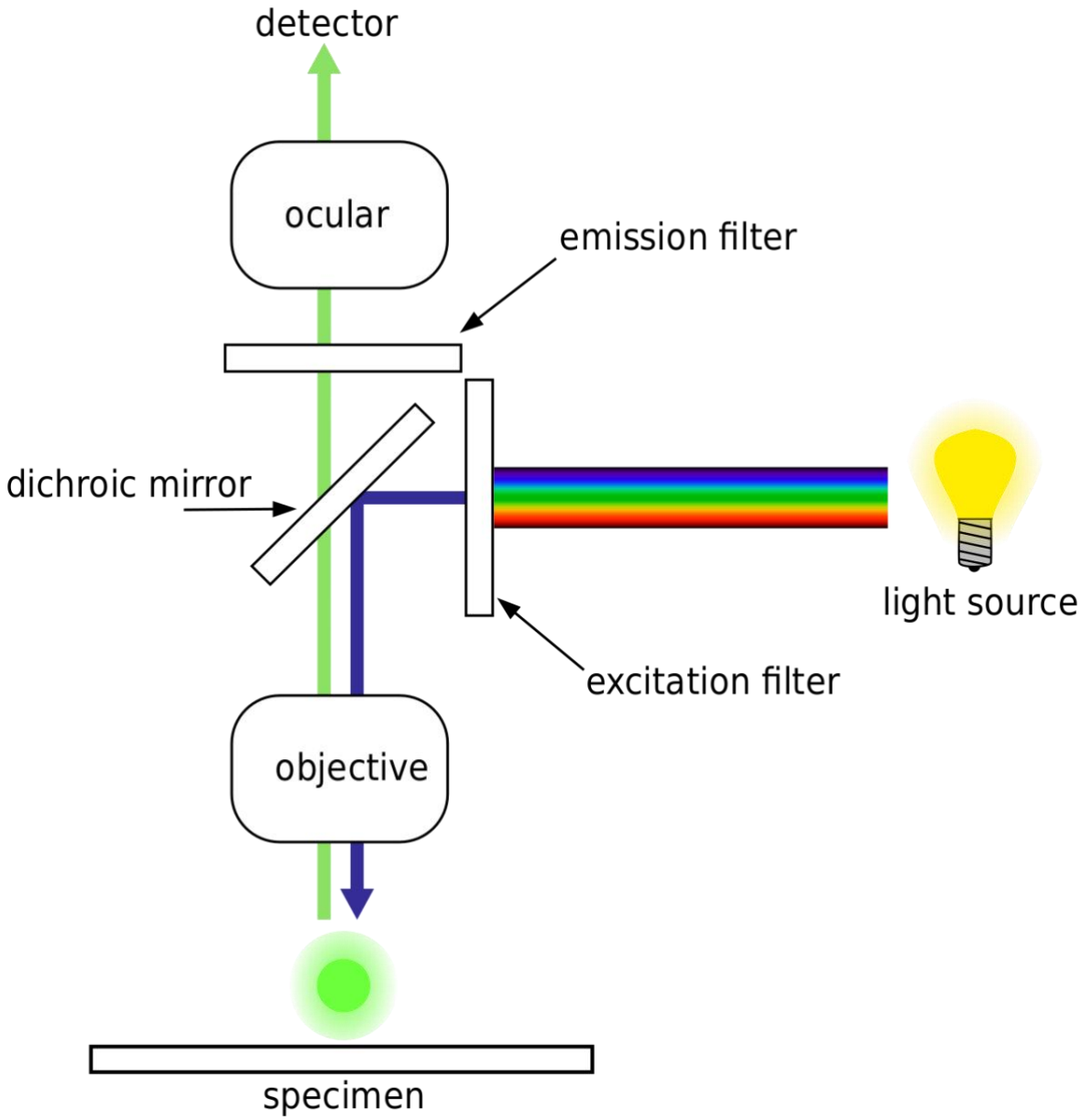

Figure 3.2 Schematic showing the light path through a fluorescence microscope. The excitation light of a specific wavelength is selected using a filter before illuminating the specimen. Upon irradiation, the fluorophores in the specimen move into an excited state. Energy loss during relaxation means a longer wavelength emission travels back through the objective, dichroic mirror and then into the detector, producing a fluorescent image of the specimen. Schematic by Henry Mühlpfordt used under the CC BY-SA 3.0 license.

Confocal microscopy (**Figure 3.3**) was invented to overcome the limitations of resolution and superimposition in traditional light and fluorescence microscopy. This technique utilises a pinhole and point illumination in an optically conjugate plane in front of the detector which removes out-of-focus signal and forms an image of only one focal plane. The optical resolution is also improved because only emission light close to the focal plane is picked up through the pinhole. This means there is a reduction the signal intensity, causing this technique to require longer exposures. Confocal laser scanning microscopy (CLSM) uses a focused laser beam to scan the object point-by-point along with the use of a pinhole to eliminate all fluorescence not within the focal plane. The beam scans in a raster pattern (parallel scanning lines) across the sample by using two motorised oscillating mirrors, with one mirror moving the beam laterally in the x direction and the other in the y direction. Slower scanning rates lead to better contrast in the image by reducing signal-to-noise ratios. Signal-to-noise ratios can also be improved by using more sensitive photodetectors or increasing the intensity of the laser light source.

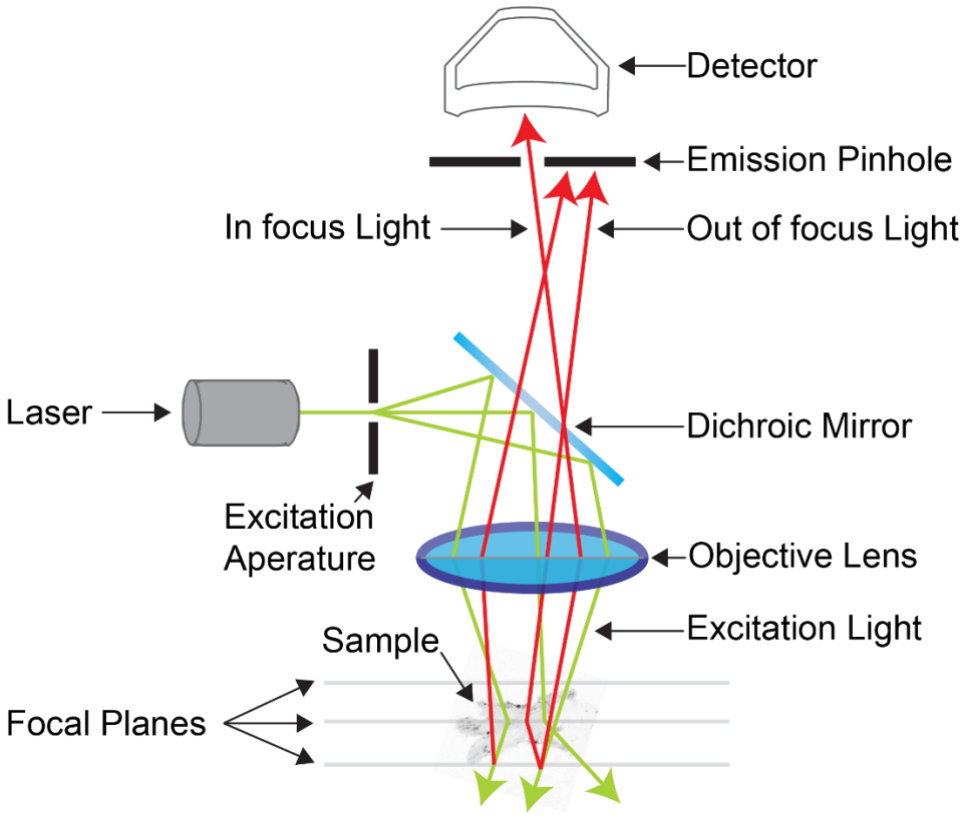

Figure 3.3 Schematic showing the light path through a fluorescence confocal microscope. A laser generating a beam of monochromatic excitation light is focussed

onto the sample via the objective. The out of focus emission light is eliminated by the utilisation of a pinhole only allowing the in-focus light to get to the detector.[19]

Confocal scanning microscopy can have multiple detectors available, and therefore multiple fluorophores can be used simultaneously. Further, there are many adjustable parameters associated with the confocal microscope allowing a high level of precision and complexity when taking images. Magnification of a sample can be adjusted electronically as the area scanned by the laser can be reduced (which in turn reduces the laser scan rate) without the need to change objectives.[20] Optical sections can be combined (stacked) to create more complex three-dimensional images (z-stack) of the object in the range of tens or sometimes hundreds of micrometres. Confocal imaging software also allows a time series of images to be captured to create a video, with the time between each image less than a second – much faster than if taken manually. These parameters can all be adjusted independently of one another meaning confocal microscopy lasers can be extremely precise and bespoke for the user.

As improvements have been made to CLSM instruments, the technique has been more frequently used for live cell and protein-based material imaging. This was difficult in early instruments because the level of excitation light needed to generate a good emission was very high as detectors were inefficient, especially when the pinhole was in a closed position.[21] This led to live cell death and a high occurrence of fluorophore bleaching. Photomultiplier tubes with higher quantum efficiency, lenses with improved light transmission, and more efficient mirrors have all improved photon efficiency in CLSM.[20] Today they are used for a multitude of live-cell and synthetic cell imaging applications, including for the characterisation and monitoring of synthetic cell populations and behaviour.

3.2.1.2 Photobleaching

When a fluorescently tagged sample is irradiated with an excess of fluorescent light, photobleaching of the tag can occur. Photobleaching is the permanent loss of fluorescence from excited state molecules due to irreversible decomposition after interaction with molecular oxygen before emission.[22] Protein-based samples are normally lightly tagged with fluorescent molecules to prevent the altering of protein

structure, therefore care must be taken when imaging using fluorescence and confocal microscopy.

3.2.2 Flow cytometry and Fluorescence-Activated Cell Sorting (FACS)

Flow cytometry (**Figure 3.4**) is a method for detecting and measuring characteristics of cells and particles, both physical and chemical. It can be used for cell counting, cell sorting, biomarker detection, and determining cell characteristics. After injection of the sample, tens of thousands of cells are guided through a narrow stream into the sheath fluid where they go through hydrodynamic focusing to pass individually through a series of lasers. The light scattered from the cells (forward and side scatter) is detected and converted into an electrical signal with specific voltage.[23][24] Fluorescent-activated cell sorting (FACS) is particular type of cell sorting which is used for sorting heterogeneous mixtures of cells based on cell characteristics and fluorescence of the cell. Initially, high-speed vibration of the nozzle splits the stream of sample into droplets containing individual cells. An electrical signal is applied to the individual droplets based on the gating selected at the beginning of the experiment. The droplets subsequently pass-through deflection plates which will separate them based on the previous charge applied. The subsequent cell separation is at very high levels of axenicity and cell recovery.[24]

Forward (FSC) and side scatter (SSC) are the result of photons being scattered by the cell in different directions. There are many things that influence FSC and SSC signals, but relative size and inner complexity are the main factors. Other factors include cell orientation, morphology and their refractive index.[24][25]

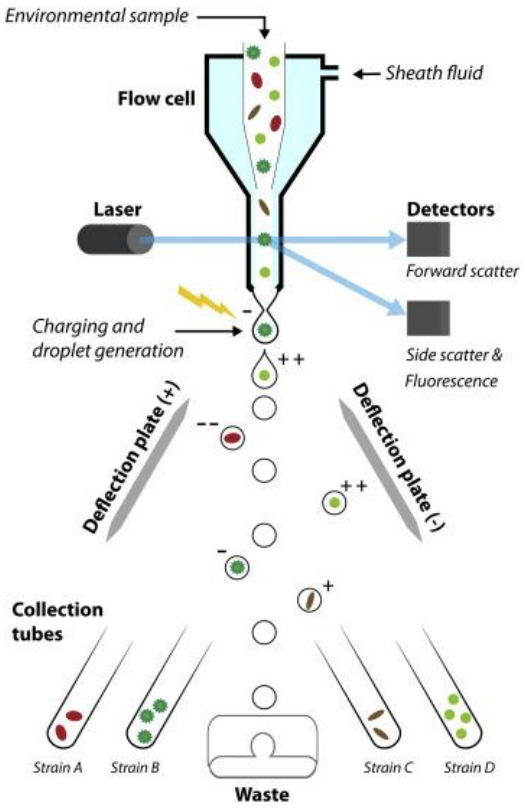

Figure 3.4 Schematic from Pereira *et al* 2018[24] showing the principles of fluorescence-activated cell sorting. The sample enters the cytometer where the cells undergo hydrodynamic focusing. They pass through the laser(s) individually before droplets form containing individual cells which are given a specific charge. They are then separated based on type and intensity of charge into collection tubes.

3.2.3 Synthesis and characterisation of nanoconjugate starting materials

3.2.3.1 Conjugation of FITC/RITC

BSA (20 mg) was dissolved in 7.4 mL carbonate buffer (pH 8.5, 100 mM) to obtain a 2.7 mg mL^{-1} solution. An aliquot (193.5 μL) of a solution of FITC/RITC in DMSO (1 mg mL^{-1}) was added to the BSA solution and the mixture stirred overnight at 4 ºC. The next day the BSA/fluorophore conjugate was dialysed against water for 8 hours, changing the water at least 3 times, and then centrifuged to remove aggregates. The supernatant was taken and lyophilised overnight to give the fluorescently tagged-BSA. Zeta potential: -15.2 mV. MALDI-TOF (m/z) found: 66200. Degree of labelling: 20%.

3.2.3.2 BSA cationisation

In a vial, BSA (18 mg) was dissolved in 1.8 mL of water to make a 10 mg mL^{-1} solution. Separately, a solution of 1,6-diaminohexane (180 mg) was dissolved in 1.8 mL water to make a 100 mg mL^{-1} solution. The pH of the solution was adjusted to 6 to 6.5 using NaOH/HCl (5 M). The solution of 1,6-diaminohexane was slowly added to the solution of BSA. The pH was readjusted to 6 to 6.5 before a solution of EDAC (9 mg) in water (0.5 mL) and added to the solution of protein. The pH was adjusted to 6 to 6.5. After 1 hour, in an Eppendorf was weighed a further aliquot of EDAC (9 mg) which was dissolved in water (0.5 mL) and added to the vial. The solution was left to stir overnight. The next day the reaction mixtures were dialysed and centrifuged (5000 rpm, 5 min) to remove precipitate (crosslinked protein). The supernatant was taken and lyophilised overnight to give the cationised BSA. Zeta potential: +41.5 mV. MALDI-TOF (m/z) found: 69692. Cationisation: 28.8 %.

3.2.3.3 Conjugation of PNIPAAm

In a vial, FITC- or RITC-labelled cationised BSA (20 mg) was dissolved in 10 mL of water to make a 2 mg mL^{-1} solution. In a separate vial, PNIPAAm (20 mg) was dissolved in 10 mL water (2 mg/mL solution) and subsequently added dropwise to the solution of FITC- or RITC-labelled cationised BSA and left to stir at room temperature overnight. The reaction mixture was centrifuged in 50 kDa centrifugal filters and washed 4 times with water to remove unreacted polymer. Finally, the samples were lyophilised to give the FITC- or RITC-labelled BSA/PNIPAAm nanoconjugates. Zeta potential: -7.2×10^{-2} mV.

3.2.4 Synthesis of proteinosomes

In a small Eppendorf tube, 2 mg PEG-oNB-NHS crosslinker were dissolved in 30 μL of Na_2CO_3 buffer (pH 8.5, 100 mM) to obtain a 66.6 mg/mL solution. In a vial, 30 μL of the FITC- or RITC-labelled BSA/PNIPAAm nanoconjugate solution (8 mg mL^{-1} in water) was mixed with 30 μL of the crosslinker solution and swirled gently to obtain a homogenous solution. To this mixture were readily added 1000 μL of oil (2-ethyl-1-hexanol) (0.06 v/v %). The vial was vigorously shaken manually for 30 seconds. The solution became turbid. After 2.5 days, the photo-sensitive proteinosomes sedimented and the upper oil layer was removed from the vial.

Subsequently, 1 mL of ethanol/water solution (70 % EtOH/H_2O) was used to dissolve the photo-sensitive proteinosomes before they were dialysed against (70 % EtOH/H_2O) for 4 hours. The dialysis solution was then switched to 35 % EtOH/H_2O and the photo-sensitive proteinosomes dialysed for a further 3 hours. Finally, photo-sensitive proteinosomes were dialysed against water overnight. In order to wash the sample from broken proteinosomes, it was left to sediment overnight and the top water was removed and replaced. This washing procedure was repeated twice more to yield a photo-sensitive proteinosome sample in a final volume of 1 mL.

For the control experiments the same procedure described above was adopted, where instead of using the PEG-oNB-NHS crosslinker, 30 μL of a solution of PEG-diNHS (50 mg mL^{-1}) was used.

3.2.5 Flow cytometry preparation and investigation of population dynamics

Typically, 100 μL of a washed FITC-tagged proteinosome sample was transferred into a 1.5 mL Eppendorf tube and irradiated for 1-30 minutes using a Xenon light source (11.5 mW) fitted with the UV on 100 % laser power, fitted with a solution probe clamped 0.5 cm above the solution, and using a 365 nm filter. The solution was diluted by 10 using MilliQ water and was analysed using a Novacyte 3000 equipped with a 488 nm laser. Thresholds used were as follows: FSC-H > 500; SSC-H and FITC-H ungated. Flow rate: medium, 35 μL min^{-1}. Stop condition: 50 μL.

3.2.6 Measurement of rate of proteinosome disassembly by modulating laser power or laser scan speed

Typically, 20 μL of a washed sample of proteinosomes was sealed in a channel slide. On a confocal microscope using the 40x HCX PL APO oil lens and the fluorescence recovery after photobleaching (FRAP) wizard, the 488 (FITC-tagged) or 561 nm (RITC-tagged) laser was set to 15 %. A region of interest of 388x388 μm^2 was drawn on the sample using the region of interest tool (**Figure 3.5**). This region of interest was fixed for every laser power. The 405 nm laser (50 mW) intensity was set between 5 and 100 % (17-2266 μW), pre-bleach was left at 1 iteration, bleach was set to 2000 iterations, and post-bleach was set to 1 iteration. The bleach setting on the FRAP

wizard was used purely to precisely control the period of 405 nm irradiation. The experiment was conducted at 0.648 sec/frame.

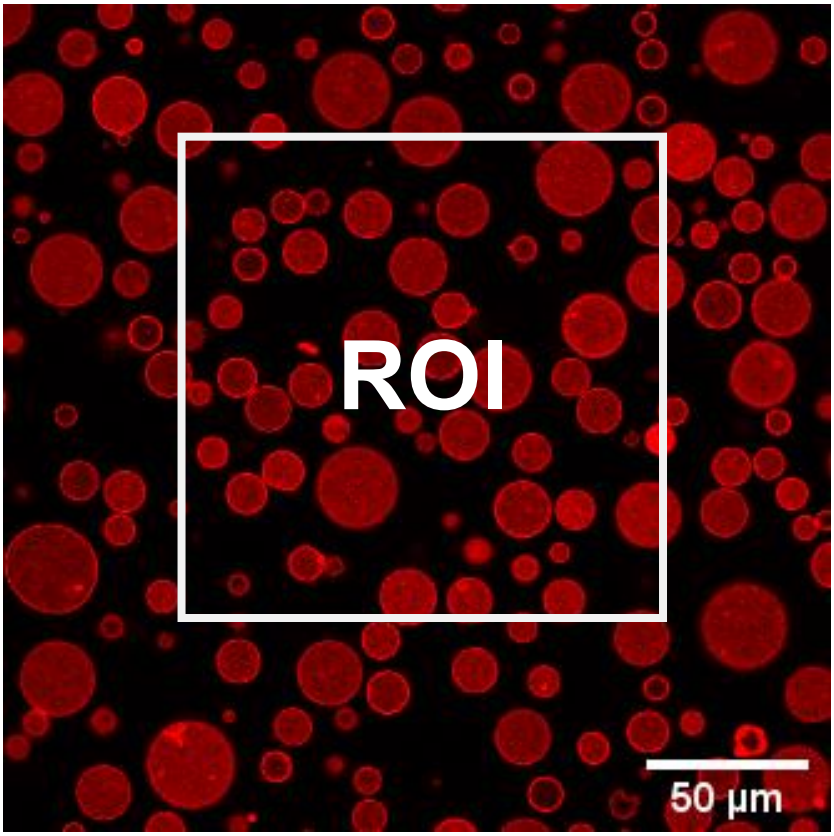

Figure 3.5 A confocal microscopy image of PEG-oNB-NHS crosslinked proteinosomes with a region of interest (ROI) of 200x200 μm^2. The 450 nm confocal laser irradiated the sample inside this ROI.

To analyse the changes in fluorescence intensity, fluorescence intensity of one tenth of the population was measured over time using ImageJ software. A circular ROI was drawn inside each proteinosome, and fluorescence intensity was measured at each time point in the experiment, which were subsequently plotted against time to obtain fluorescence decay curves over time. The proteinosome degradation time was defined as the intercept point between the linear regressions of the initial decay (first 10 seconds) and the plateau region. This was repeated for each of the laser powers. Initial rates were determined by approximating a linear fit to the first 10 seconds of decay and taking the gradient.

For laser scan speed dependent rate of proteinosome disassembly, 20 μL of a washed sample of proteinosomes was sealed in a channel slide. On a confocal microscope using the 40x HCX PL APO oil lens, the 488 (FITC-tagged) or 561 nm (RITC-tagged) lasers was set to 15 % intensity. A region of interest between 388x388 and 100x100 μm^2 (laser scan speed 0.16 - 0.63 $\mu m\ s^{-1}$) was drawn using the region of interest tool. The 405 nm laser (50 mW) intensity was set to 100 %, pre-bleach was left at 1 iteration, bleach was set to 500 iterations, and post-bleach was set to 1 iteration. The bleach setting on the FRAP wizard was used purely to precisely control the period of 405 nm irradiation. Images were acquired at 0.648 sec/frame. Analysis of changes in fluorescence intensity of the membrane was performed using the same method as for the laser power dependent analysis.

3.2.7 Calculating laser scan speed from ROI size

The relationship between laser scan speed and ROI size is defined as follows. This example calculation is for an ROI of 100x100 μm^2. Due to there being a fixed pixel number within the ROI, pixel size is related to the ROI size via the following equation:

$$pixel\ size = \frac{length}{pixel\ number} \quad (1)$$

Where *length* is the varied length in μm of one side of the ROI (100 μm). For the experiments in this thesis, the pixel number was fixed to 512 regardless of the length of the ROI. Using **Equation 1**, the pixel size is calculated to be 0.20 μm. The pixel scan speed, or laser scan speed, can be calculated as follows:

$$laser\ scan\ speed = \frac{pixel\ size}{dwell\ time} \quad (2)$$

Where dwell time is the length of time in μs the laser spends on each pixel. For the confocal microscope used for all experiments in this thesis, the dwell time is fixed at 1.2 μs. Using **Equation 2**, the laser scan speed for an ROI with length 100 μm is 0.16 $\mu m\ \mu s^{-1}$.

3.2.8 Patterning of a protocell population

Typically, 20 μL of a washed sample of proteinosomes was sealed in a channel slide. The slide was placed into the microscope, it was left for 5 minutes so the proteinosomes settled on the glass in a monolayer. Using the 40x HCX PL APO oil lens and the fluorescence recovery after photobleaching (FRAP) wizard, for negative shapes the desired pattern was drawn using the ROI tool. This area was irradiated with a 50 mW diode laser (405 nm, 0.648 seconds/frame) causing the disassembly of the proteinosomes in the selected area. For positive images, the areas around the desired pattern were selectively disassembled.

3.2.9 Selective photo induced disassembly of a single proteinosome or partial proteinosome

Two populations of proteinosomes were synthesised according to the method in **section 3.2.4**. One population was tagged with RITC and synthesised using the non-responsive PEG-diNHS crosslinker, and the other was tagged with FITC and crosslinked using light-responsive PEG-oNB-NHS. Once transferred to water and washed 3 times, they were left to settle at the bottom of the vial. 10 μL of each proteinosome sample was taken from the bottom of the vial and pipetted into an Eppendorf and mixed. 10 μL of the mixed population was taken and pipetted into a channel slide before it was sealed with vacuum grease. The proteinosomes were left to settle on the bottom of the channel slide for 5 minutes before imaging.

Using the 40x HCX PL APO oil lens and the fluorescence recovery after photobleaching (FRAP) wizard, a 100x100 μm^2 area was selected containing both an RITC and FITC tagged proteinosome. This area was irradiated with a 405 nm diode laser (2266 μW, 0.648 seconds/frame) for 80 seconds causing the disassembly of the UV-responsive FITC proteinosome in the selected area.

For the probing of a partial proteinosome, the same oil lens and software was used as above. The area selected using the software was carefully chosen to cover a

proportion of the proteinosome, for example the top half. This area was irradiated with a 405 nm diode laser (2266 μW, 0.648 seconds/frame) for 40 seconds causing the disassembly of the membrane within the selected area.

3.2.10 Investigating the effect of concentration of encapsulated substrate on disassembly time

In order to encapsulate FITC-dextran, 10 μL of a solution of FITC-dextran (6 mg mL^{-1}, H_2O) was mixed with 30 μL of FITC- or RITC-labelled BSA/PNIPAAm nanoconjugate solution (8 mg mL^{-1} in water). The PEG-*o*-NB-NHS crosslinker (2 mg) was dissolved in 20 μL of Na_2CO_3 buffer (pH 8.5, 100 mM) and added to the nanoconjugate/dextran mixture to give a final FITC-dextran concentration of 1 mg mL^{-1}. An oil layer of 1-ethyl-2-hexanol (1 mL) was carefully added on top and the vial was shaken vigorously for 30 seconds. The resulting emulsion was left to sediment and crosslink for 48 hours before being transferred to water. After transfer, the proteinosome sample was washed 3 times to make sure broken proteinosomes and FITC-dextran in the bulk solution were completely removed.

Final concentrations of 0.5, 1, 1.5 and 3 mg mL^{-1} were achieved by using initial FITC-dextran concentrations of 3, 6, 9 and 18 mg mL^{-1}, respectively. Each batch containing the different dextran concentrations was synthesised three times mixed, creating a larger batch at each concentration. After they were washed 3 times and allowed to settle, an aliquot (20 μL) was placed into a channel slide before being sealed. On a confocal microscope using the 40x HCX PL APO oil lens, the 488 and 561 nm lasers were set to 15 % intensity and optimised to eliminate crossover of the lasers. A 200x200 μm^2 area was drawn in the middle of a 388x388 μm^2 total frame size using the region of interest tool. The 405 nm laser intensity was set to 25 % and 'Fly Mode' was selected. Pre-bleach was left at 1 iteration, bleach was set to 400 iterations, and post-bleach was set to 1 iteration.

Fluorescence intensity of one tenth of the population in the red channel was measured over time using ImageJ software to obtain average fluorescence decay curves over time. The proteinosome degradation time was defined as the intercept point between the linear regressions of the initial decay and the plateau region (**Figure 3.15**).

3.3 Results and discussion

3.3.1 Synthesis of PEG-oNB-NHS crosslinked proteinosomes

3.3.1.1 Synthesis of fluorescent tagged BSA nanoconjugates

Scheme 3.1 shows the synthetic route to light-responsive proteinosomes which is based on previous work developed by Huang *et al*.[2] To synthesise membrane engineered proteinosomes with light-responsive properties, the basic building block forming the membrane needed to be synthesised. The membrane is made of protein/polymer hybrid nanoconjugates with amphiphilic properties that are crosslinked together at the interface of a water-in-oil droplet. Firstly, the protein/polymer nanoconjugate needed to be synthesised before self-assembly at the water/oil interface.

To be able to easily visualise the final proteinosomes via microscopy, the nanoconjugates are tagged with a fluorescent dye. The choice of dye will depend on the design of the experiment to be performed and the other dyes in the system. The important thing to note about protein nanoconjugates is that the amine functionality makes them extremely versatile in terms of tagging. Any fluorescent tag which can react with amines can be used on BSA. In this case, rhodamine-b-isothiocyanate (RITC) was used as the fluorescent tag. The reaction was performed under basic conditions (pH 8.5) so that the amines on the protein were deprotonated. A solution of RITC was mixed with the protein at 4ºC overnight before the solution was dialysed to remove the excess dye. The tagging efficiency can be estimated by UV VIS and efficiencies of between 20 and 100 % was considered ideal for visualisation on both fluorescent and confocal microscopy, and not influencing the addition of PNIPAAm chains to the protein surface. In this case, the tagging efficiency was found to be 20 % meaning that on average 1 in every 5 BSA proteins were tagged.

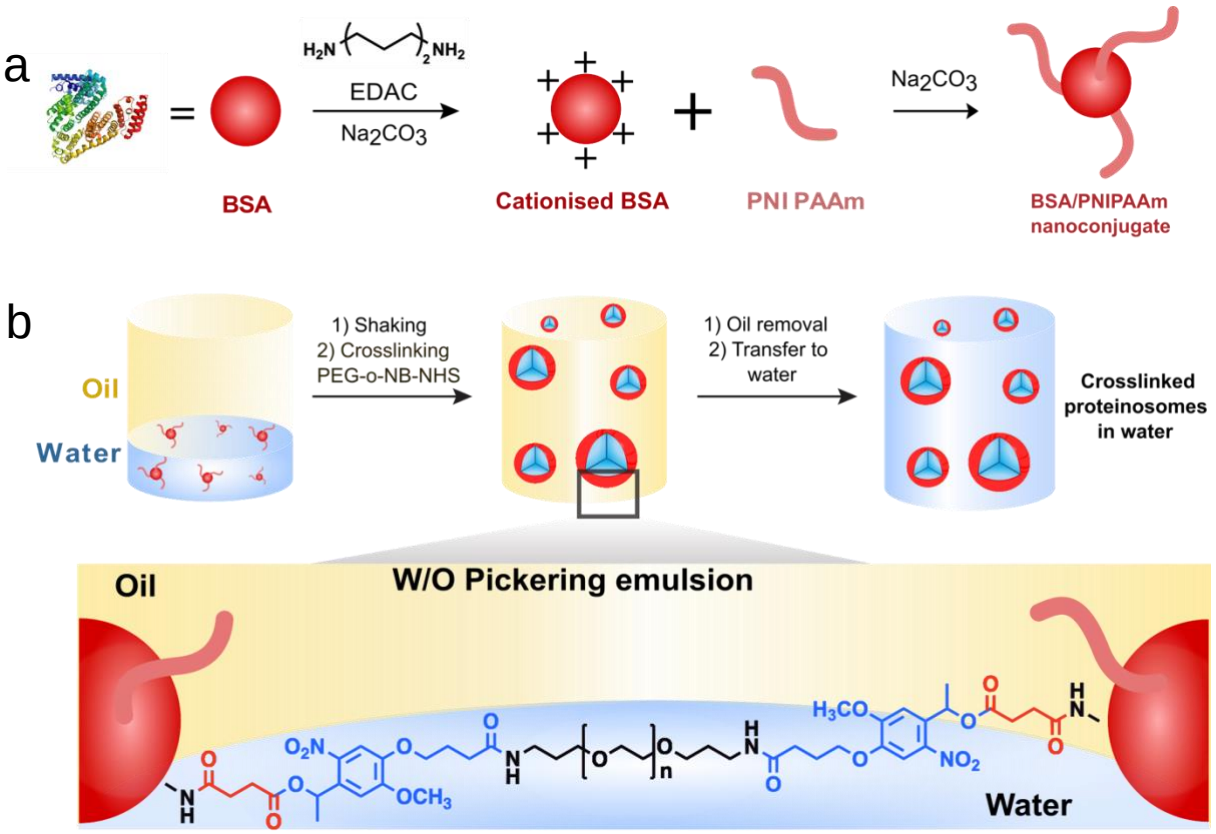

Scheme 3.1. General synthesis of membrane engineered proteinosomes with light-responsive properties **a.** The synthesis of proteinosomes begins with the formation of protein-polymer nanoconjugates with amphiphilic properties. BSA protein is cationised by the EDAC-mediated addition of 1,6-diaminohexane molecules onto the carboxylic acid residues of the protein. The next step is the addition of PNIPAAm chains onto the surface amine groups to form the final nanoconjugates. **b**. Proteinosomes are formed via a Pickering emulsion technique where the protein-polymer nanoconjugates stabilise the surface of the water-in-oil droplets. PEG-*o*-NB-NHS crosslinker is added to the water phase during the synthesis and reacts with free primary amine groups on the surface holding the nanoconjugates in place. The oil is removed before the protein capsules are transferred to water via dialysis.

The number of surface amine groups on the protein was increased, to increase the probability of reaction of BSA with PNIPAAm, the next step in the synthesis. This was done by addition of 1,6-diaminohexane molecules onto the carboxylic acid functionalised (aspartate and glutamate) residues on the protein. This reaction was done using water soluble EDC as the coupling agent under acidic conditions (pH 6-

6.5). As the number of amine groups on the protein increases, the pH of the solution becomes basic, and this was used as an indication as to whether the reaction has been successful. MALDI-TOF (**Figure 3.6**) was used to measure the mass to charge ratio (m/z) and therefore the number of 1,6-diaminohexane molecules successfully added. The molecular weight increase from tagged BSA at 66200 Da to the cationised BSA at 69692 Da which indicated an addition of ca. 29 1,6-diaminohexane molecules. When added to the ca. 60 native amine[26] containing residues, there is a total of 89 surface amines available for reaction with PNIPAAm and the crosslinker. An increase in zeta potential from -15.2 to +41.5 mV was a further indication of the addition of positive amine groups on the surface of the protein.

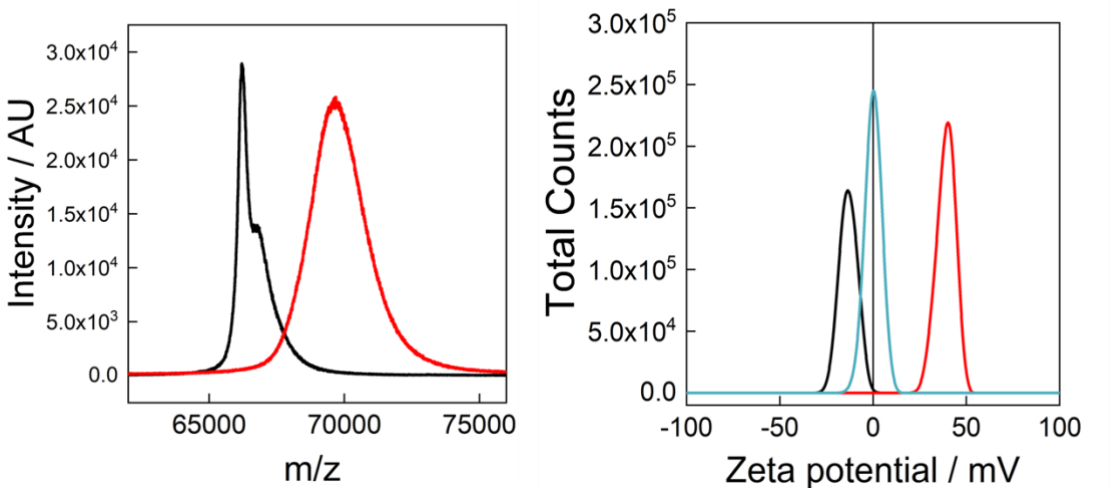

Figure 3.6. MALDI and zeta potential plots of native BSA (black curve), cationised BSA (red curve) and BSA/PNIPAAm nanoconjugates (blue curve). After cationisation the mass increased by 3492 Da indicating the addition of ca. 29 molecules of 1,6-diaminohexane onto the surface. The increase in zeta potential from -15.2 to +41.5 mV further indicates that amine groups have been added to the surface to give an overall positive charge. After addition of PNIPAAm, the zeta potential decreases from +41.5 mV to 0 mV

Once the number of protein surface amine groups had been increased and a fluorescent tag added, the final step in the synthesis of the BSA nanoconjugates was the addition of mercaptathiozoline-activated PNIPAAm chains onto the protein surface. PNIPAAm was synthesised via a RAFT (reversible addition-fragmentation

chain transfer) polymerisation of the momomer NIPAAm (N-isopropylacrylamide) with a RAFT agent containing a mercaptathiozoline leaving group terminus to react with primary amine groups on the protein. RAFT polymerisation is an effective method of producing polymers with precise molecular weight and polydispersity.[27]

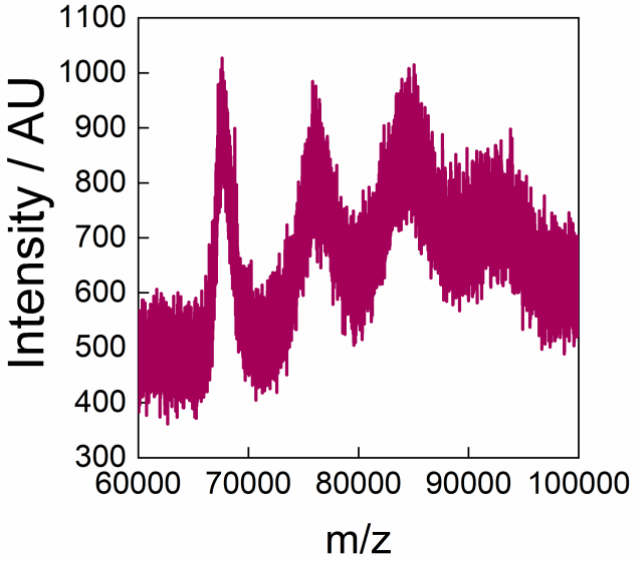

Figure 3.7 MALDI-TOF spectrum of RITC-labelled BSA/PNIPAAm nanoconjugate showing the addition of 0, 1, 2 and 3 PNIPAAm chains onto the RITC-tagged and cationised protein.

PNIPAAm with a molecular weight of ca. 9000 g mol^{-1} was used as per previous methods.[2] The synthesised PNIPAAm chains were covalently bonded to the surface amines of the cationised BSA with the primary amine functional groups reacting with the terminating mercaptathiozoline moieties on PNIPAAm. The number of polymer chains can be assessed using MALDI spectroscopy. Typically, between 0 and 4 polymer chains are conjugated to the surface to form the final nanoconjugates. The zeta potential of the protein-polymer nanoconjugates was analysed via DLS to reveal a decrease from +41.5 mV to 0 mV. This indicated a decrease in the number of amine groups on the surface further demonstrating a successful reaction had occurred.

3.3.1.2 Construction of proteinosomes

After the successful synthesis and characterisation of the protein-polymer nanoconjugates, proteinosomes were synthesised via a Pickering emulsion technique described in **section 3.2.4** (**Scheme 3.1b**). Firstly, a solution of 2-ethyl-1-hexanol was added on top of a solution of protein-polymer nanoconjugates in 0.1 M carbonate buffer (8 mg mL^{-1}, pH 8.5) at a water/oil volume fraction (φ_w) of 0.06, and vigorously shaken for 30 seconds to mix. This produced water-in-oil droplets which were stabilised by the protein-polymer nanoconjugates at the water/oil interface. A higher concentration of 8 mg mL^{-1} was used (rather than the common 4 mg mL^{-1}).

To crosslink the proteinosome membrane, a crosslinker can be added to the water phase before the addition of oil. The PEG-oNB-NHS crosslinker was added to the water phase before the addition of oil and vigorous shaking. Once the microcapsules had formed, they were left to sediment and crosslink for 48 hours and in the dark to avoid premature photolysis of the crosslinker. After this, they were dialysed against 70 % ethanol to dissolve the oil. The ethanol was diluted to 35 % and eventually replaced with water in which the proteinosomes were left overnight to remove any remaining impurities. After transfer, the proteinosomes were kept at 5 °C and in the dark where they remained stable for several weeks demonstrating the stability of the o-NB crosslinker under these conditions. The microcapsules are denser than water meaning they sedimented at the bottom of the vial after a few hours. The water layer was removed carefully to avoid disturbing the proteinosomes and replaced with clean MilliQ water (1 mL) after which they were left to settle again. This was repeated at least three times to ensure a significant amount of free crosslinker and other impurities were removed.

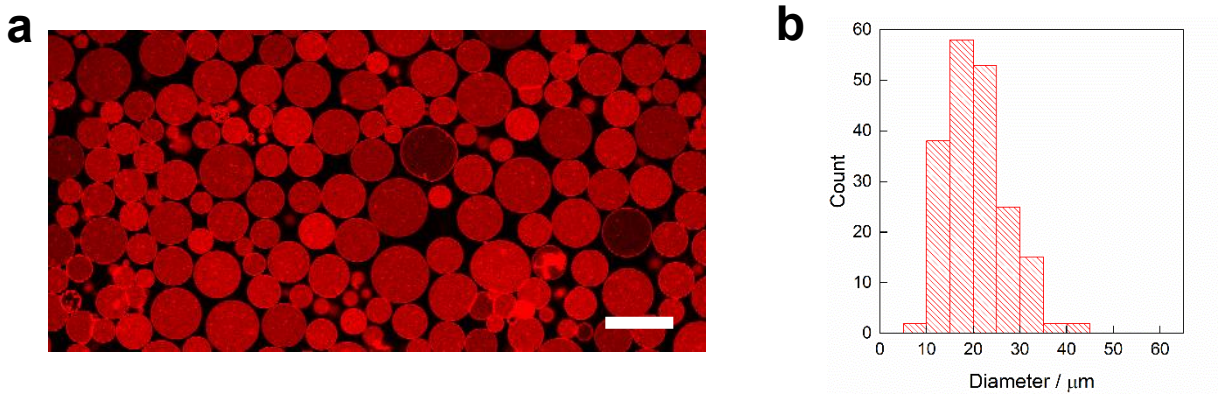

Figure 3.8 a. Confocal laser scanning microscopy image of a population of RITC-tagged o-NB proteinosomes in water. **b**. Size distribution of o-NB proteinosomes showing an average diameter of 22.5 ± 6.1 μm. Scale bar 25 μm.

The proteinosomes were characterised via fluorescence and confocal microscopy (**Figure 3.8a**), which showed the presence of a fluorescently tagged membrane and an excess of protein-polymer nanoconjugate within the interior of the capsule, showing as a highly fluorescent centre. The presence of the intact fluorescent membrane after being transferred into water confirms the crosslinker had remained intact through the procedure. Some broken proteinosomes can always be seen due to the numerous transfers and their delicate nature. The resulting microcapsules were consistent with literature, being spherical in shape with an average size of 22.5 ± 6.1 μm (**Figure 3.8 b**) compared to an average size of 20 ± 5 μm for the proteinosomes crosslinked using PEG-diNHS.[2] Aggregation can be seen due to the dense packing of the proteinosome population during crosslinking, combined with the slight solubility of the crosslinker in the oil phase resulting in crosslinking between proteinosomes.

3.3.2 Investigating the photolysis of the proteinosome membrane

3.3.2.1 Disassembly of proteinosome membranes via UV-laser microirradiation within confocal microscopy

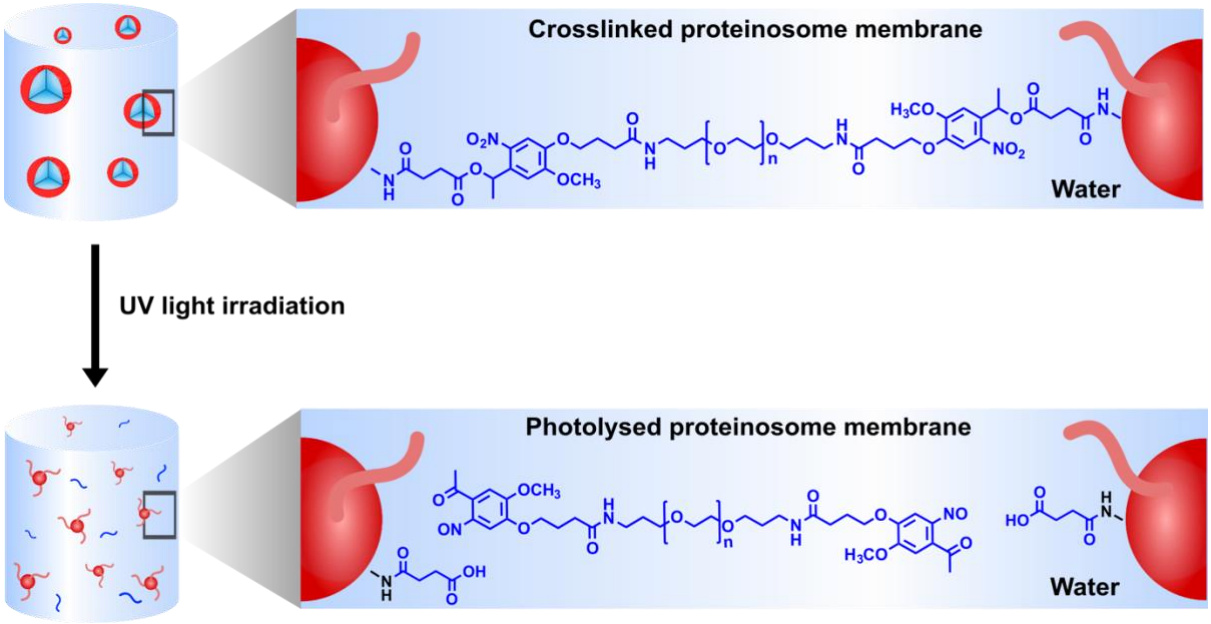

Scheme 3.2. The hypothesised method of photolysis of the engineered proteinosome membrane. Upon irradiation with a UV-light source, PEG-o-NB-NHS is photolyzed via the cleavage of the ester linkages at each end of the crosslinker. As the crosslinker is broken, the membrane of the proteinosome is no longer stable and begins to break up. As more crosslinkers are photolysed, the nanoconjugates go back into solution and the proteinosome membrane completely disassembles.

Proteinosomes synthesised using the unique PEG-oNB-NHS crosslinker were predicted to have the ability to react to UV-light, owing to the photosensitivity of PEG-oNB-NHS. As seen in **Scheme 3.2**, the proteinosome membranes are stable until irradiation with UV-light occurs. The UV-light is absorbed by the crosslinker and causes a rearrangement within the molecular structure, as discussed in **Chapter 2 Section 2.1.2**. This rearrangement causes a breaking of the ester linkages within the crosslinker, and therefore between the nanoconjugates, resulting in destabilisation of the membrane and eventual disassembly of the membrane structure. It was

hypothesised that small populations and individual proteinosomes could be photolyzed using lasers integrated in confocal microscopes. The lowest wavelength available in the system was 405 nm which is within the tail-end of the main absorption band of the crosslinker (chapter 2, **section 2.3.2.1, Figure 2.4**). Since the power of the laser is high (50 mW), it was predicted there would still be enough photons to cause photolysis of the crosslinker.

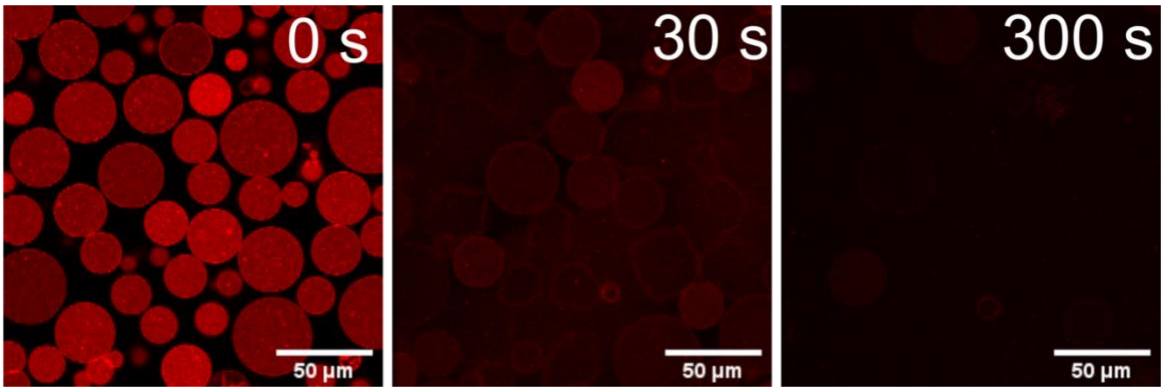

Figure 3.9 Time-dependent confocal laser scanning microscopy images of a population of o-NB proteinosomes disassembling over a period of 300 seconds, as indicated in the top left corner. The population is exposed to 405 nm light from a 50 mW laser, at a power of 2266 µW, for the whole experiment. Size of scale bars indicated on each image.

Microirradiation of an area of proteinosomes in 388x388 μm^2 with a 50 mW (at a power of 2266 µW) 405 nm laser was used to investigate the photolysis the PEG-oNB-NHS crosslinker bonding the nanoconjugates in the membrane together. Time-dependent CLSM images show irradiation from 0-300 seconds (**Figure 3.9**). At 30 seconds of irradiation, the visual fluorescence of the proteinosomes had decreased significantly and there was an expansion of the proteinosome membrane in the first few seconds of irradiation before a steady loss of fluorescence. By 300 seconds of irradiation there is almost a complete loss of proteinosome fluorescence.

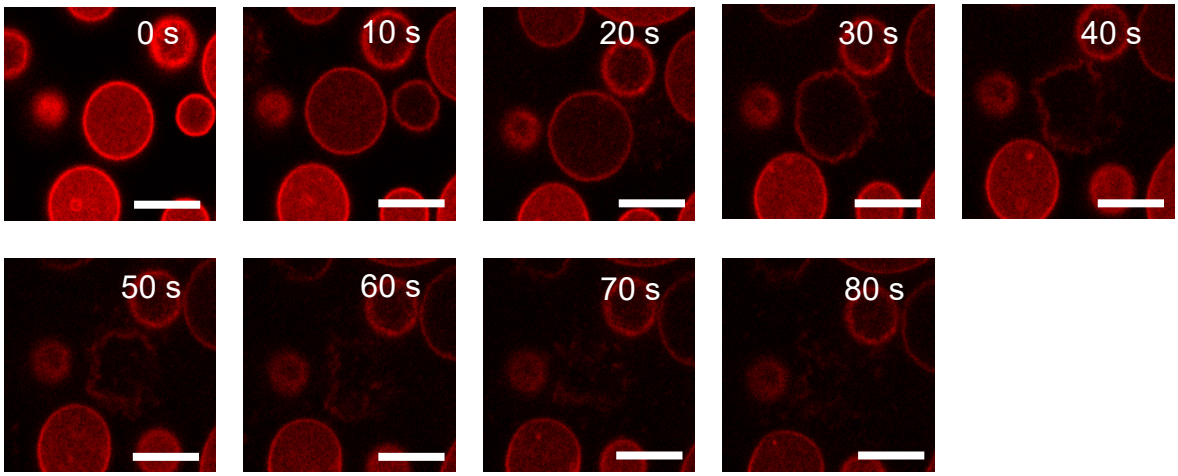

Figure 3.10 An individual proteinosome at a higher magnification to highlight the UV-induced disassembly of the membrane. The brightness has been manually increased by 20 % for these images to aide in visualisation of the proteinosome membrane behaviour during microirradiation. All scale bars 15 μm.

Figure 3.10 shows a series of confocal microscopy images with increased magnification to highlight the membrane disassembly of one proteinosome within a population. The increase in volume of the proteinosome after 10 seconds of irradiation can be more clearly seen in these images. Following the expansion, the brightness decreases whilst the membrane becomes less defined, the proteinosome becomes less circular, and it appears to spread out into the surrounding media **Figures 3.9** and **3.10** are evidencing the breakdown of the membrane during irradiation. The general decrease in fluorescence was associated with the loss of RITC-tagged BSA nanoconjugates from the membrane due to the UV-induced photolysis of the crosslinker binding them together. The membrane expansion is hypothesised to be due to osmosis effects: as crosslinkers are cleaved, the membrane is weakened and water flows into the lumen.

3.3.2.2 Control PEG-diNHS crosslinked proteinosomes irradiation experiment

As discussed in the methods **Section 3.2.1.2**, photobleaching is a common occurrence when samples are exposed to irradiation light for long periods of time. To ensure the decrease in fluorescence intensity was due to membrane disassembly rather than photobleaching, the same irradiation experiment was performed using proteinosomes crosslinked using an unreactive PEG-diNHS crosslinker. **Figure 3.11** shows time-dependent confocal microscopy images of PEG-diNHS crosslinked proteinosomes after 0, 100, 200 and 300 seconds of irradiation with the 405 nm laser. A small decrease in fluorescence of the membrane was seen after 300 seconds of irradiation, but there were no other changes in membrane behaviour observed.

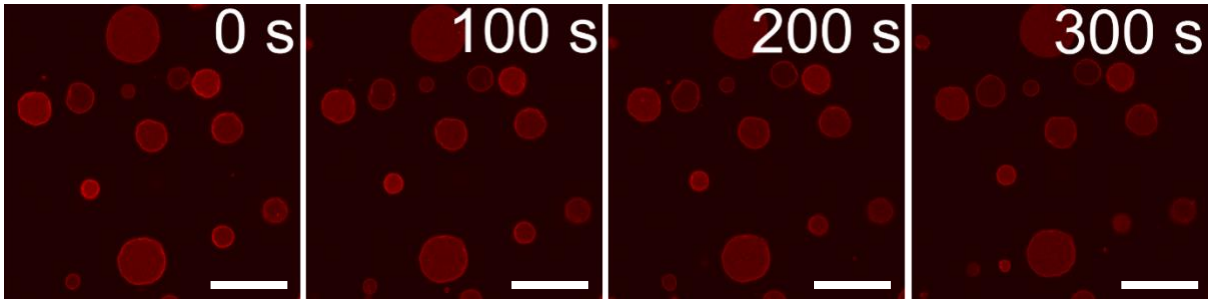

Figure 3.11 Control experiment showing confocal microscopy images of proteinosomes crosslinked with PEG-diNHS during 300 seconds of irradiation with a 50 mW 405 laser at a power of 2266 μW. All scale bars 50 μm.

3.3.2.3 Quantitative analysis of membrane fluorescence

To quantify the membrane degradation and compare the behaviour of the PEG-oNB-NHS to the control PEG-diNHS proteinosomes, the average fluorescence intensity of the population was plotted against time (**Figure 3.12**). There is a significant difference in the membrane fluorescence behaviour between the two experiments. The PEG-oNB-NHS proteinosomes lose fluorescence at an exponential rate, decreasing to a normalised value of ca. 10 ± 5 AU after 200 seconds. This remaining fluorescence is due to background fluorescence of the solution as the BSA nanoconjugate concentration increases. Conversely, the PEG-diNHS proteinosomes

lose fluorescence more steadily to ca. 75 ± 1 AU in the same time period. Although there is some fluorescence loss in the control, this is due to bleaching effects on the fluorophore. The visual data from the confocal images of the population and individual proteinosome plus the significant levels of fluorescence intensity decrease above the control are good evidence that PEG-oNB-NHS proteinosomes are disassembling due to UV-light exposure.

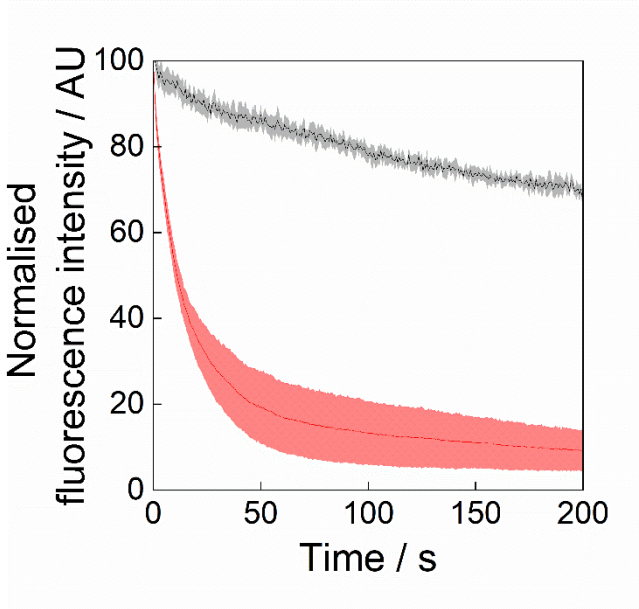

Figure 3.12 Plot of fluorescence intensity versus time of a population of o-NB proteinosomes (red) and PEG-diNHS proteinosomes (black) during 200 seconds of irradiation with a 405 nm laser. The fluorescence of the o-NB population decreases rapidly before beginning to plateau as the proteinosome membranes disassemble. The PEG-diNHS population loses fluorescence intensity at a significantly lower rate. This loss in fluorescence was attributed to bleaching effects. This experiment was performed at least three times on a mixture of proteinosomes from three separate batches.

3.3.3 Investigating the spatiotemporal control of proteinosome disassembly

Section 3.3.2.1 explored disassembly of proteinosome membranes using confocal microscopy lasers. The confocal microscopy system has many different parameters

that can be adjusted, such as laser power, laser scan speed (associated with ROI area size), and a software-controlled positioning system. It was hypothesised that the disassembly could be very well controlled using these parameters and so investigations into disassembly with respect to all three were investigated in the following sections.

3.3.3.1 Controlling the rate of photolysis using laser power and laser scan speed

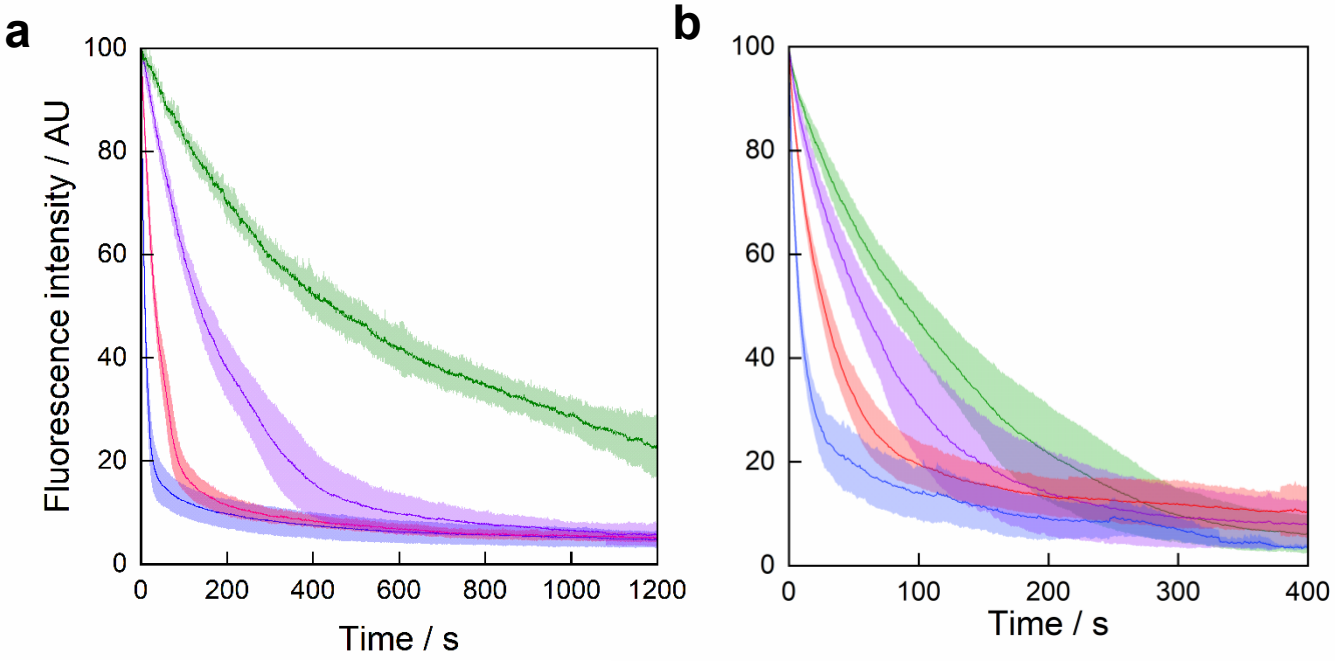

Figure 3.13 a. Fluorescence intensity against irradiation time plots (irradiation wavelength: 405 nm) of photo-sensitive proteinosomes irradiated at different laser powers (100 % = blue line, 25 % = red line, 10 % = purple line, 5 % = green line). Bands = standard deviation. The initial rate of disassembly increases from 0.25 to 6.33 AU s^{-1} for 10 and 100 % laser power, respectively. **b.** Fluorescence intensity against irradiation time plots (irradiation wavelength: 405 nm) of photo-sensitive proteinosomes irradiated at different laser scan speed (0.63 μm $μs^{-1}$ = blue line, 0.49 μm $μs^{-1}$ = red line, 0.33 μm $μs^{-1}$ = purple line, 0.16 μm $μs^{-1}$ = green line) at a constant power of 330 μW. Bands = standard deviation. The initial rate of disassembly increased from 1.1 to 5.6 AU s^{-1} for 0.63 and 0.16 μm $μs^{-1}$. These experiments were performed at least three times on a mixture of proteinosomes from three separate batches.

Initially the disassembly was investigated with respect to changing laser power. It was shown that the rate of disassembly could be controlled by modulating the laser power (**Figure 3.13 a**). ROI size (or laser scan speed) was kept constant at 388x388 μm^2 (0.16 $\mu m\ \mu s^{-1}$). Over four experiments, the percentage laser power was decreased from 100 to 25, 10 and 5 % (blue, red, purple, and green curves, respectively). These corresponded to laser powers of 2266, 330, 70 and 17 μW respectively, measured and provided by the technicians in the Wolfson bioimaging centre at the University of Bristol. Using the method in **section 3.2.6** fluorescence intensity versus time curves were plotted for the laser power experiments to reveal decay curves of varying rate, very similar to the proteinosome disassembly plot (red curve) in **Figure 3.12**. An increase in the laser power from 17 to 2266 μW showed a 25 times increase in the initial rate of disassembly, going from 0.25 to 6.33 AU s^{-1} (for 10 and 100 % laser power respectively).

The same method was used to investigate the effect on disassembly time by changing laser scan speed. Laser power was kept constant at 330 μW. The laser scan speed is changed on the microscope by changing the size of the ROI and calculated as shown in the method **section 3.2.7**. **Figure 3.13b** shows fluorescence intensity versus time plots for ROI area from 388x388 μm^2 (green curve) and 100x100 μm^2 (blue curve) corresponding to laser scan speeds of 0.16 and 0.63 $\mu m\ \mu s^{-1}$ respectively. The initial rate of disassembly showed an increase of 5 times, going from 1.1 to 5.6 AU s^{-1} for laser scan speeds of 0.63 and 0.16 $\mu m\ \mu s^{-1}$.

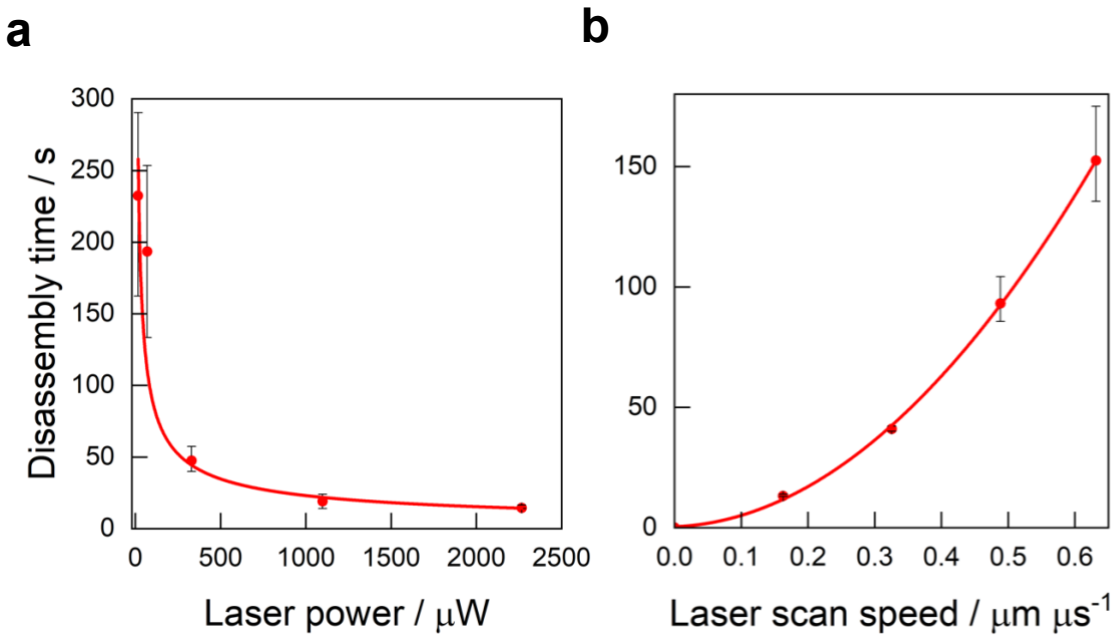

Figure 3.14 a. Plot of disassembly time as a function of laser power. The laser power was increased from 17 to 2266 μW and the disassembly time decreased exponentially from 232 to 14 s. **b.** Plot of disassembly time as a function of laser scan speed. The laser scan speed was increased from 0.16 to 0.63 μm ms^{-1} and the disassembly time increased from 13 to 152 s.

The fluorescence intensity versus time curves were subsequently used to elucidate disassembly times for the different laser powers and laser scan speeds. The disassembly time was defined as the time at which the linear regressions of the initial decay and the plateau region intercept (**Figure 3.15**). Disassembly time was found to have a negative exponential relationship with respect to the laser power (**Figure 3.14a**), decreasing from 232 to 14 seconds as power was increased from 17 to 2266 W. An increase in laser scan speed from 0.16 to 0.63 μm μs^{-1} showed a monotonic increase in the disassembly time, from 13 to 152 seconds (**Figure 3.14b**).

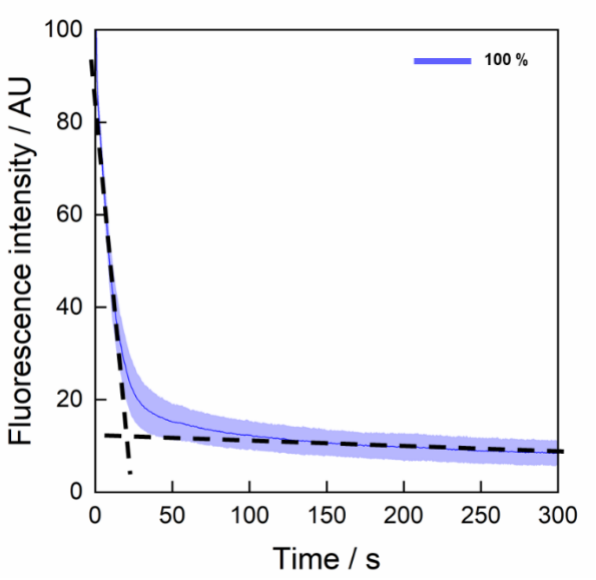

Figure 3.15 Schematic showing the method of estimating a disassembly time. A linear fit is taken for both the initial decrease and final plateau in fluorescence intensity. The time at which the two plots intercept is taken as the disassembly time.

The trend in disassembly time with respect to laser power can be explained with regard to the number of total photons reaching the sample. As the laser power increases more photons are reaching the sample in a given time, photolysing more crosslinkers. At a certain power (~750 μW) the threshold is reached where the addition of more power (more photons) does not decrease the disassembly time further, and we hypothesise that this is because the maximum number of crosslinkers are breaking. The trend in disassembly time with respect to laser scan speed can be explained by looking at the relationship between ROI size and laser scan speed. As the ROI length increases, the pixel size increases due to there being a fixed number of pixels. The fixed dwell time per pixel means the laser scan speed also follows this trend and increases with ROI length. The dwell time being constant means that the larger pixels receive the same number of photons as the small pixels. The photons are spread over a wider area in the larger pixels so there will be a lower photon flux density and therefore the disassembly time is longer.

3.3.3.2 Spatial control of disassembly within proteinosome populations

Exploiting the software-controlled positioning system of the confocal microscope, the possibility of creating photo-generated patterns using laser light was explored (**Figure 3.16**). The method used is described in **Section 3.2.8**. A sample of proteinosomes were sealed inside a channel slide with vacuum grease and left for 5 minutes to settle creating a monolayer of proteinosomes on the glass. The confocal software allows spatially defined ROIs to be drawn onto the proteinosomes in view. Within the user-defined ROIs, the UV-illumination caused the photo-degradation of the proteinosomes leaving empty regions and forming negative shapes. This could also be exploited to leave positive shapes by irradiating and disassembling the regions of proteinosomes around the desired pattern, and a combination of the two allowed more complex patterns to be created. Using this technique, the photo-generation of bespoke patterns of any shape in the 100 μm scale could be achieved.

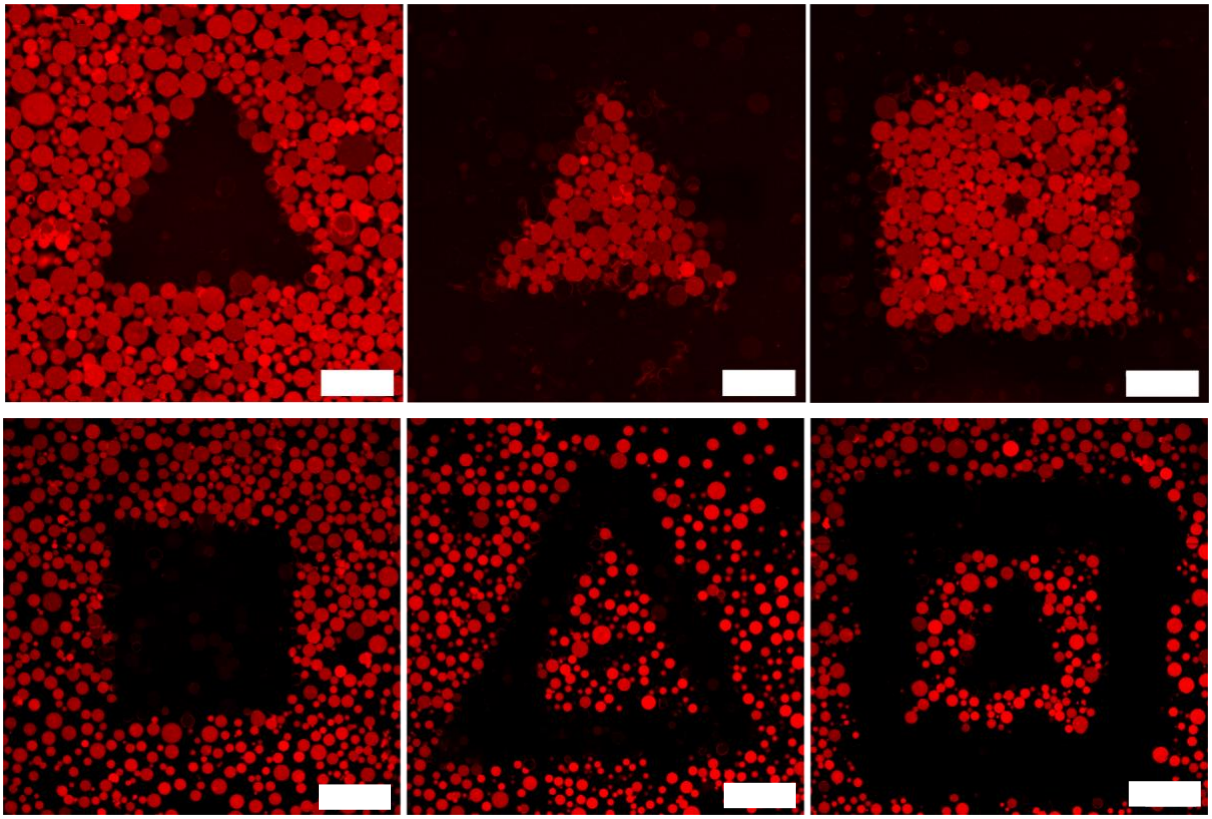

Figure 3.16 Photo-generated proteinosome patterns obtained by irradiating a sample of RITC-labelled photo-sensitive proteinosomes for 5-10 mins at 405 nm using a confocal fluorescence microscope equipped with a software-controlled positioning system. There are two examples of negative shapes, two examples of positive shapes, and two examples of more complex combinations of the shapes formed within populations of proteinosomes. These experiments showcase the ease in which photo-generated patterns can be created. All scale bars: 100 μm.

3.3.3.3 Single proteinosome disassembly

To demonstrate the selectivity and accuracy of using the software-controlled positioning laser system, single proteinosomes were targeted within a mixed population of responsive and non-responsive proteinosomes. The two populations were synthesised using different crosslinkers and tagged with different fluorescent dyes to identify them. A non-responsive population was synthesised using the PEG-diNHS crosslinker and the membrane was tagged with RITC (**Figure 3.17a**, red proteinosome). The UV-responsive proteinosomes were synthesised using the PEG-oNB-NHS crosslinker and the BSA nanoconjugate membrane was tagged with

FITC (**Figure 17b**). The populations were mixed in an Eppendorf before being pipetted into a channel slide, sealed, and left to settle at the bottom of the glass.

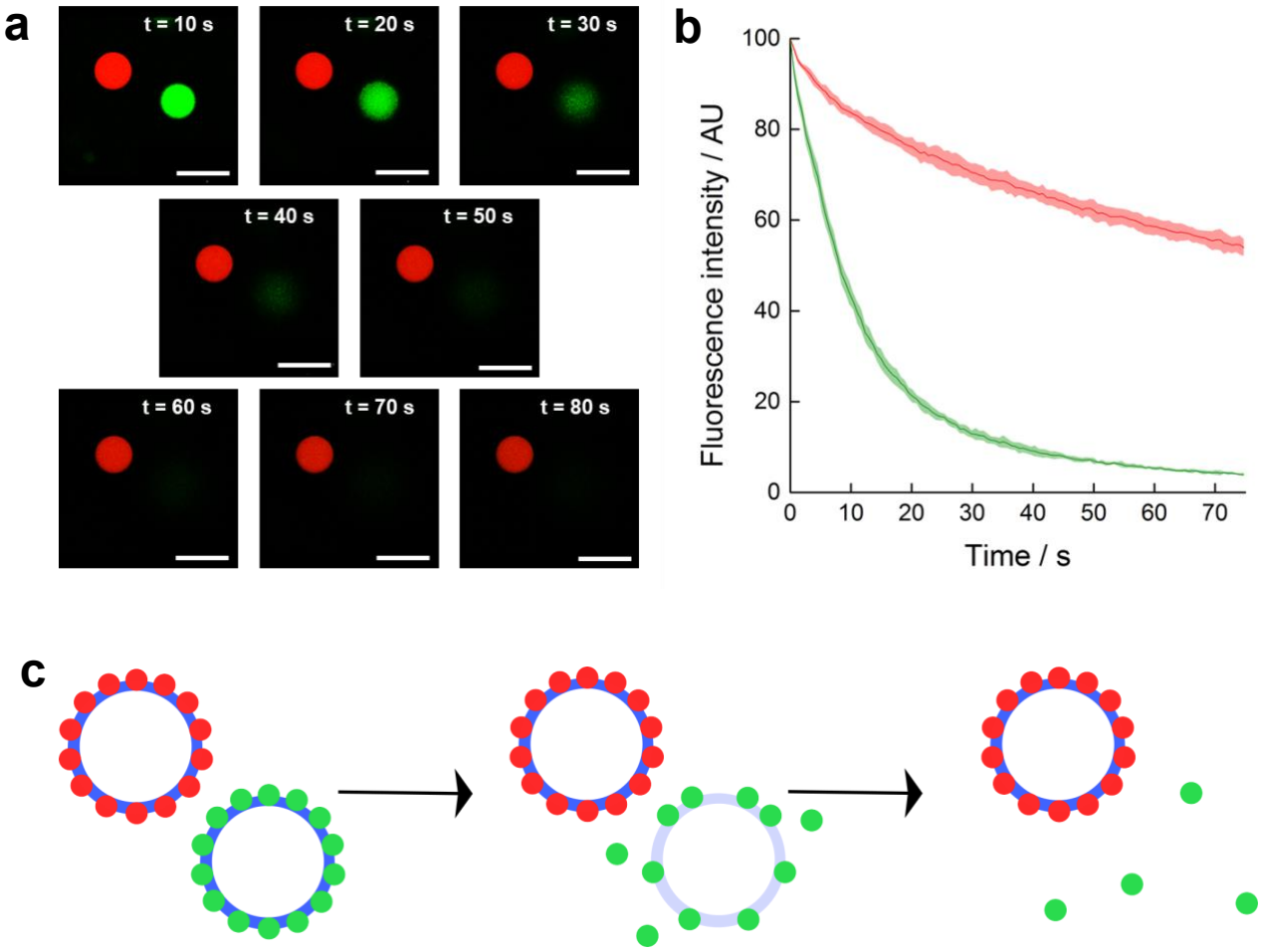

Figure 3.17 a. Confocal microscopy images during irradiation of a PEG-oNB-NHS crosslinked FITC-tagged proteinosome (green) next to a PEG-diNHS RITC-tagged proteinosome (red). Irradiation with a 405 nm diode laser induces photolysis of the PEG-oNB-NHS crosslinker, resulting in rupture of the membrane in the FITC-tagged proteinosome only. Time points show the photo-induced disassembly of the FITC-labelled proteinosome with time indicated in the top right-hand corner of each image. All scale bars are 25 μm. **b.** Graph showing the fluorescence intensity of the proteinosome membranes versus time, during irradiation. The green curve corresponds to the FITC-tagged proteinosome, and the red curve corresponds to an RITC-tagged proteinosome. The fluorescence intensity declines rapidly during the 80s

irradiation. There is a decrease in florescence intensity of the RITC-tagged proteinosome to ca. 60 AU. The shaded areas above and below the curves represent the standard deviation. These experimental results are for one single experiment; however the experiment was repeated in lab to ensure reproducibility. **c.** Schematic of the experiment showing a red proteinosome stable in the presence of UV light, next to a green proteinosome which has been crosslinked with PEG-oNB-NHS and disassembles upon irradiation with light.

Figure 3.17a shows a series of confocal microscopy images taken during 405 nm laser (2266 μW) irradiation of both the proteinosomes. The fluorescence intensity of both the FITC-tagged and RITC-tagged proteinosome membranes can be seen to decrease over the course of the irradiation, with the FITC-tagged proteinosome membrane decreasing most rapidly. The normalised fluorescence intensity was plotted against time to give the plots in **Figure 3.17b**. Over the course of 80 seconds of irradiation, the FITC proteinosome membrane decreased from 100 to ca. 2 AU. The RITC membrane decreased to ca. 55 ± 2 AU. This is indicative of the FITC-tagged UV-responsive proteinosome disassembling, and the RITC-tagged non-responsive proteinosome experiencing some fluorescence bleaching. There is a significant difference between this experiment and the control experiment in **Figure 3.12** (black curve) where we see only 20 AU of fluorescence intensity loss. This is hypothesised to be due to difference in size of the irradiation area and therefore the difference in laser scan speed. In the initial control experiment, the irradiation area was 388x388 μm^2 corresponding to a laser scan speed of 0.63 $\mu m\ s^{-1}$, compared to 100x100 μm^2 corresponding to 0.16 $\mu m\ s^{-1}$. The slower scan speed in the experiment in **Figure 3.17** is indicative of the sample being exposed to a higher number of photons which in turn causes the higher amount of bleaching in the sample.

As demonstrated in **Section 3.3.3**, the versatility of the confocal microscope laser allows the disassembly on the scale of hundreds of microns down to tens of microns when irradiating an individual proteinosome. Beyond this, the use of lasers as a method of irradiation raises the opportunity for even more specific targeting. To showcase this, a proteinosome was partially irradiated inducing disassembly of a selected area of the membrane only. As seen in a series of confocal images in

Figure 3.18, the area of irradiation was carefully selected to encompass the top half of the proteinosome, which behaved similarly to others presented in this chapter. At 10 seconds, there is an increase in diameter where there is irradiation of the membrane combined with a loss of internal fluorescence throughout the experiment. The membrane at the top then begins to get less defined at 20 seconds, before a complete loss of definition and fluorescence from 30 to 40 seconds of irradiation. Where there is no irradiation at the bottom of the proteinosome, we don't see any expansion of the membrane. The fluorescence intensity of the interior decreases over the course of 20 seconds irradiation, however the intensity of the membrane stays high during this period. From 20 to 40 seconds irradiation, there is a dramatic change in the shape of the bottom half of the membrane. The membrane begins to contract at 30 seconds, the same time as the top half of the membrane has lost all structure. The edges appear to curve over onto the outside and the shape changes from circular to more linear.

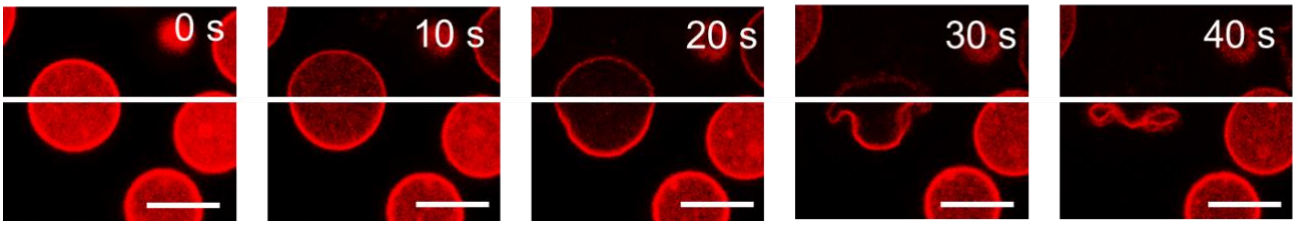

Figure 3.18 A series of confocal microscopy images of a proteinosome which is being exposed to 405 nm light only on one half. Irradiation is occurring above the white line in the images, delivering photons to the top half of the proteinosome. At 10 seconds of irradiation, the typical expansion of the membrane is apparent. From 20 to 30 seconds, the top half of the membrane has clearly become less fluorescent and undefined before completely disappearing at 40 seconds. The bottom half of the membrane never loses its definition or fluorescence however at 30 to 40 seconds, there is a large change in the shape and behaviour. The interior fluorescence decreases throughout the experiment. All scale bars 20 μm.

The behaviour of the top part of the proteinosome that is exposed to the 405 nm light is typical of the behaviour in **Section 3.3.2.1**. The expansion is evidence that the crosslinkers in the membrane are breaking, as was seen in earlier experiments. The loss of fluorescence from the interior of the entire proteinosome is hypothesised to be due to a loss of the excess RITC-tagged BSA as the top of the proteinosome disassembles. The precision of this technique is shown through the clean disassembly point at the perimeter of the laser light. Interestingly, the elasticity of the membrane can be seen through the curving behaviour at 30 to 40 seconds when the top of the membrane is fully cleaved, resulting in an almost full inversion.

Overall, **Section 3.3.3** shows that proteinosomes can be precisely targeted within a population due to the spatio-temporal control of the confocal microscope. The experiments showed that the ability to control confocal laser parameters independently of each other facilitates control of the disassembly time for a population. This could be used to create bespoke disassembly times for proteinosome populations dependent on the final application and conditions. The software-controlled positioning system in the microscope was utilised to demonstrate spatial control of disassembly within a population. It was shown that anything from a single proteinosome to the whole population within a 388x388 μm^2 area can be targeted and disassembled. This technique could be used to explore the creation of customized 3D protocellular materials and cargo-release gradients within a pattern of protocells by using the laser power or laser scan speed to control the disassembly times.

3.3.4 Bulk proteinosome disassembly analysis via FACS

Given the successful synthesis of proteinosomes crosslinked using PEG-oNB-NHS, the light-response of the population was tested. To demonstrate the large-scale photolysis of UV-responsive proteinosomes, 100 μL of a dispersed sample of proteinosomes was pipetted into a 1.5 mL Eppendorf and irradiated with a 365 nm UV xenon lamp (11 mW) (**Figure 3.19b**). Fluorescence-Activated Cell Sorting (FACS) was subsequently used to assess the level of photolysis.

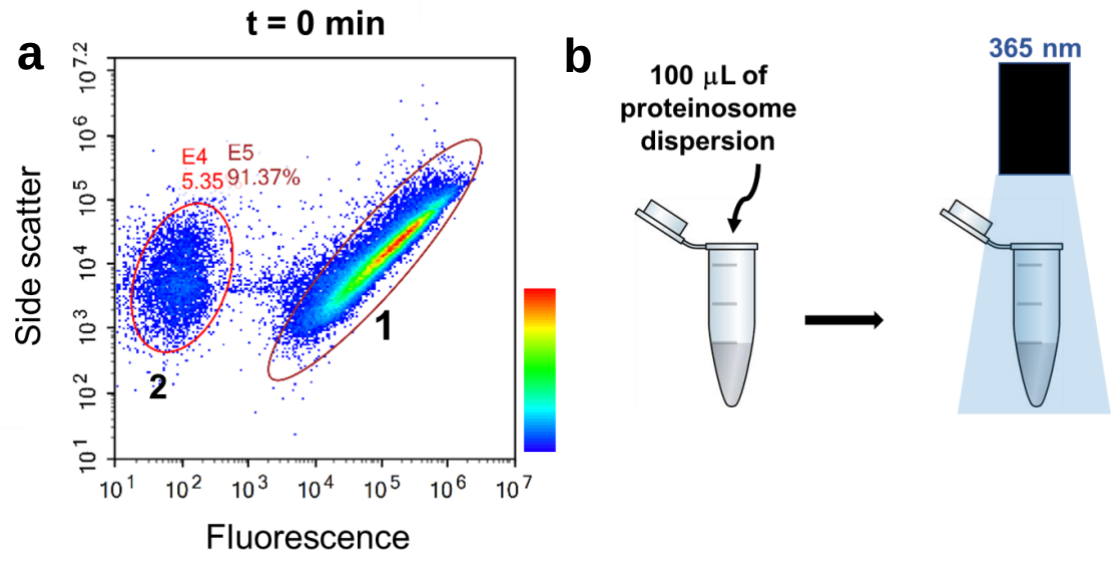

Figure 3.19 a. 2D plots of fluorescence versus side scatter light for proteinosomes crosslinked with the PEG-oNB-NHS crosslinker analysed by FACS. Population **1** with higher fluorescence are single proteinosomes with corresponding fluorescence and side scatter. Population **2** was hypothesised to be contaminants in the water in which they are dispersed. Density plots are displayed in pseudocolour. In this view, areas of the plot with a higher density of events are shown in warmer colours (colours toward the top of the colour bar next to the dot plot) and areas of the plot with a lower density of events are shown in cooler colours (colours toward the bottom of the colour bar next to the dot plot).

Firstly, populations of FITC-tagged proteinosomes crosslinked with PEG-oNB-NHS were synthesised and analysed using FACS with no irradiation to characterise the sample at time = 0 (**Figure 3.19a**). Two-dimensional plots of fluorescence intensity (FITC-H) versus side scattered area (SSC-A) showed a distinguishable population **1** with a high fluorescence reading which was assigned to be the population of proteinosomes. Whenever the experiment was performed there was always a population with a low fluorescence reading (population **2** in **Figure 3.19a**) and a similar side-scatter. The deionised water used during proteinosome synthesis was passed through the cell sorter and showed the same low fluorescence scatter plot and so this population was hypothesised to be dust particles and other contaminants. Furthermore, comparison of these scatter plots to work by Yan *et al*[28] showed

proteinosome populations with dot plots of strikingly similar size and shape in the same region of the graph. This confirmed that the higher FITC population **1** was the proteinosomes.

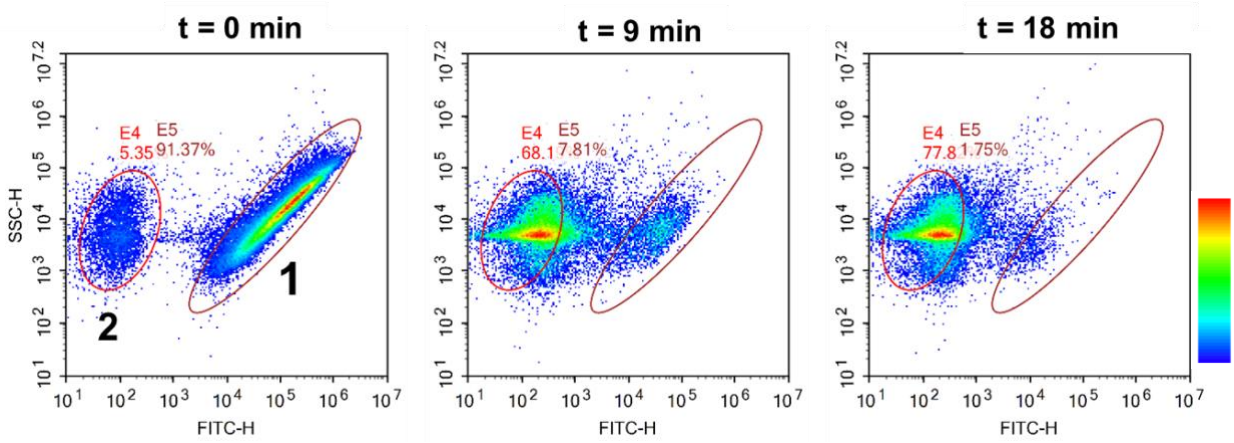

Figure 3.20 From left to right: irradiation time increases from 0 - 18 minutes. As irradiation occurs, population 1 decreases in size from 91.37 to 1.75 %, and population 2 increases in size from 5.35 to 77.80 %. These changes in the populations were hypothesised to be indicative of the breakdown of the bulk population 1 and subsequent increase in smaller fragments within the solution, increasing the size of population 2. Density plots are displayed in pseudocolour. In this view, areas of the plot with a higher density of events are shown in warmer colours (colours toward the top of the colour bar next to the dot plot) and areas of the plot with a lower density of events are shown in cooler colours (colours toward the bottom of the colour bar next to the dot plot).

At 9-minute intervals during irradiation with a 350 nm Xenon lamp (11 mW), the sample was analysed using FACS. **Figure 3.20** shows plots of fluorescence versus side-scatter. A significant reduction was seen in the population **1** after 9 minutes, from 91.37 to 7.81 % with the population reducing to 1.75 % after 18 minutes of irradiation. The concurrent increase in size of population **2** from 5.35 to 77.80 % indicated that there was an increase in smaller fragments in the solution, which were hypothesised to be the broken proteinosome membrane.

3.3.5 Disassembly of proteinosomes with encapsulated substrates

Given that PEG-oNB-NHS crosslinked proteinosomes where able to encapsulate FITC-dextran of 70 kDa and above, an investigation into the disassembly times of these proteinosome populations was performed to find out whether there was any correlation between the concentration of encapsulated FITC-dextran and the disassembly time. There should be a decrease in disassembly time with increasing concentration of substrate because as substrate concentration increases, the osmotic pressure increases inside the proteinosome. When proteinosomes are irradiated, the covalent crosslinks are photolysed, and the increased pressure should cause the membrane to rupture faster than with a lower interior concentration (and therefore pressure) of FITC-dextran. A molecular weight of 150 kDa FITC-dextran was chosen as at this molecular weight the proteinosomes were easily visible during confocal microscopy without heavy bleaching of the fluorophore.

Firstly, populations of proteinosomes were synthesised containing concentrations of 150 kDa FITC-dextran from 0.5 to 3 mg mL^{-1} (**Figure 3.21a**). The samples were washed 3 times to minimise the broken proteinosome membrane or excess FITC-dextran in the solution. The fluorescence intensity in the green channel inside the proteinosomes increases as concentration of the tagged substrate increases. To disassemble the membrane, each population was irradiated via confocal microscopy using a 405 nm laser (25 %, 330 μW) for 300 seconds, taking an image every 1.48 seconds. Average fluorescence intensity against time curves were obtained by measuring the average fluorescence intensity of one tenth of the population.

The average disassembly times for each concentration of FITC-dextran were found to be 63.5, 56.0, 64.5 and 58.4 seconds for 0.5, 1, 1.5 and 3 mg mL^{-1}, respectively (**Figure 3.21b**). The results show no correlation between the concentration of encapsulated FITC-dextran and the disassembly time. One hypothesis is that the concentrations used are simply not high enough for the interior osmotic pressure to increase significantly to show any decrease in disassembly time. Further experiments could be completed in the future encapsulating a higher concentration of FITC-dextran to investigate whether this is a factor.

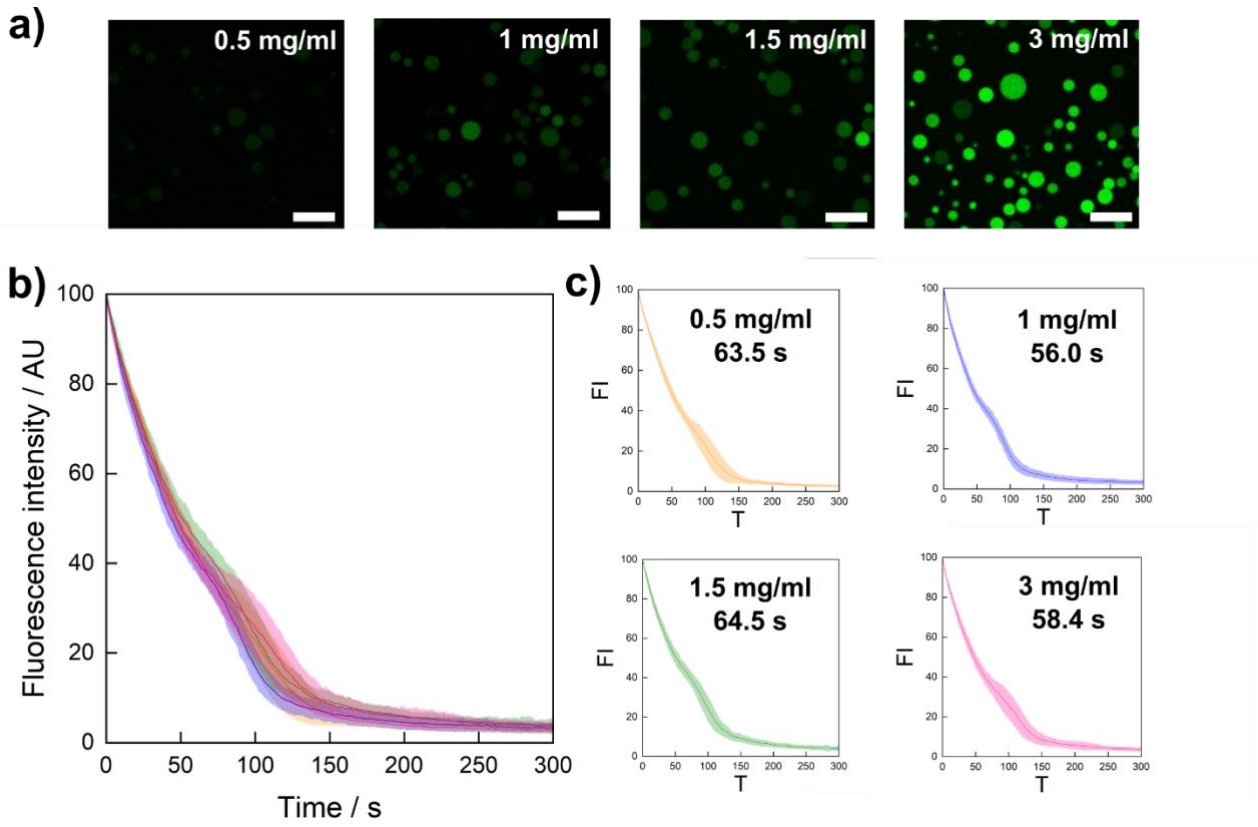

Figure 3.21. Investigation into the relationship between concentration of encapsulated 150 kDa FITC-dextran and disassembly time. **a.** Confocal microscopy images of concentrations ranging from 0.5 to 3 mg mL^{-1} of 150 kDa FITC-dextran. Scale bars are 50 μm. **b.** Fluorescence intensity versus time graph showing the decrease in average membrane intensity of 150 kDa FITC-dextran encapsulated proteinosome populations during irradiation at 25 % laser intensity (330 μW) showing no significant difference between concentrations. **c.** Individual average membrane fluorescence intensity curves with FITC-dextran concentrations and disassembly times indicated. Disassembly time was determined by finding the intercept of the initial decrease and final plateau.

3.4 Conclusions

A novel stimuli-responsive proteinosome membrane was synthesised using the PEG-oNB-NHS crosslinker described in chapter 2. The nanoconjugate building blocks were synthesised and characterised using: UV Vis spectroscopy, to estimate the degree of fluorescent labelling on the protein surface; zeta potential measurements, to determine the surface charge of the protein and hence estimate the number of positively charged surface reactive groups; and MALDI spectrometry, to measure the mass to charge (m/z) ratio of the protein and therefore the number of 1,6-diaminohexane molecules chemically added to the surface, and the number of PNIPAAm polymer chains grafted to the protein surface. The presence of stable PEG-oNB-NHS crosslinked proteinosomes in solution, constructed via a Pickering emulsion method, was characterised using fluorescence confocal microscopy showing protein capsules with an average size of 22.5 ± 6.1 μm.

The proteinosome membranes were found to be responsive to 405 nm laser light (50 mW) within a confocal microscope system. Confocal microscopy images showed the membrane disassembly behaviour during irradiation, with typical observations of an initial membrane expansion (hypothesised to be due to osmotic factors) and subsequent dissolution of the membrane fragments. Control experiments performed on proteinosomes crosslinked using unreactive PEG-diNHS showed no, or very little, observed reduction in fluorescence. A quantitative analysis of the membrane disassembly was performed by plotting the average normalised fluorescence intensity of the membrane against time during irradiation experiments. A comparison of the two experiments showed a very significant difference in change of fluorescence intensity during irradiation (a difference of 60 AU after 200 seconds irradiation), which combined with visual observations, confirmed the membrane disassembly.

The ability to change and adjust the laser parameters (laser power and laser scan speed) independently of each other offered the opportunity to be able to tune the rate of disassembly of the proteinosome population. An increase in laser power from 17 to 2266 μW showed a 25 times increase in initial rate from 0.25 to 6.33 AU s^{-1}, respectively. An increase in the laser scan speed (by increasing the size of the irradiation region of interest) also showed a decrease in initial rate from 5.6 to

1.1 AU s^{-1} for laser scan speeds of 0.63 and 0.16 μm $μs^{-1}$, due to the reduction in dwell time per pixel, and therefore a reduced number of photons reaching the sample. Disassembly time was used as a comparative value, which was defined to be the time associated with the intercept between the linear regressions of the initial decay and the plateau region and plotted against both laser power and laser scan speed. These plots could be used in future experiments to predict the disassembly time of proteinosome populations when using specific laser powers and scan speeds. A software-controlled positioning system was used to demonstrate photo-patterning of proteinosome populations with positive, negative, and more complex designs. The software also allowed very precise targeting demonstrated through the selective disassembly of an individual capsule out of a large mixed population of responsive and non-responsive proteinosomes. The laser can be used so precisely that even parts of the membrane can be targeted and disassembled, demonstrated by the selective disassembly of the top half of a proteinosome. Using this targeting method, investigations into the light-activated communication between protocell populations could be explored to create smart and functional protocell communities. Further, the photopatterning technique could be used as a method to create bespoke shaped 3D prototissues or prototissue patterning.[29]

The bulk disassembly of PEG-oNB-NHS FITC-tagged proteinosomes was demonstrated by irradiating 100 μL of a dispersed proteinosome sample with a 350 nm xenon light source. Fluorescence-activated cell sorting was used as a method to analyse the behaviour by plotting 2D dot plots of the proteinosome population before and after irradiation. After 18 minutes of irradiation, there was a significant decrease in the population of proteinosomes from 91.37 to 1.75 %. This shows the possibility of proteinosome population disassembly on a large variety of length scales, from millimetres down to tens of microns. Further experiments could be performed patterning populations at the millimetre length scale to compliment earlier photo-patterning demonstrations.

3.5 Appendix

3.5.1 Supplementary methods

The following methods are published in the paper “A Novel Acid-Degradable PEG Crosslinker for the Fabrication of pH-Responsive Soft Materials”.[30]

3.5.1.1 Preparation of acid-degradable chemically crosslinked CM-chitosan hydrogels

Hydrogel samples were prepared with a final concentration of PEG-ketal-NHS (5) ranging from 5, 12.5, 25, 50, and 100 mg mL^{-1} or 1, 2.5, 5, 10, and 20 mg by the total mass. In general, 190 μL of an aqueous solution of CM-chitosan (40 mg mL^{-1}, pH = 9.56) was pipetted into a 1.75 mL vial, 5 μL of acid-degradable crosslinker (5) in Na_2CO_3 buffer solution (pH = 8.5, 0.1 M), and 5 μL of a commercial solution of universal indicator were mixed vigorously for 20 sec. Gelation was confirmed by turning the vial upside-down.

3.5.1.2 Acid-mediated degradation of CM-chitosan hydrogels

Degradation of the hydrogels prepared in **appendix section 3.5.1.1** was triggered by the addition of hydrochloric acid (5 μL, 1 M). The vial was vortexed for 10s following the addition of HCl. The decrease in pH was confirmed by the universal indicator colour change, and gel degradation was monitored over 48 h. Corresponding images were taken with 1 h intervals for the first 10 h, and then at 24 h and 48 h (data shown in **Figure 21**).

3.5.1.3 Preparation of acid-degradable hydrogel-filled proteinosomes

Different proteinosomes samples were prepared with a final concentration of crosslinker (5) ranging from 16.7, 83.3, and 167 mg mL^{-1} or 1, 5, and 10 mg by mass. In general, acid-degradable proteinosomes were prepared by combining 15 µL of an aqueous solution of PEG-ketal-diNHS (5) in Na_2CO_3 buffer solution (pH 8.5, 0.1 M) with 30 µL of an aqueous solution of RITC-labelled BSA/PNIPAAm (8.0 mg mL-1), and an aqueous solution of CM-chitosan (15 µL, 40 mg mL^{-1}, pH 8.5-9) in 1.75 mL vials. The samples were mixed followed by the addition of 1 mL of 2-ethyl-1-hexanol. The vials were vigorously shaken for 60 s. After 48 hrs, the clear upper oil layer was

discarded, and 1 mL of a 70% ethanol/Na_2CO_3 buffer (pH=8.5, 10 mM) mixture was used to dissolve the emulsion. The solution was then dialyzed against 70%, 50%, and 30% ethanol/Na_2CO_3 buffer (pH 8.5, 10 mM) for 2 hrs, then against carbonate buffer for 1 day to complete the transfer into an alkaline solution. Proteinosomes were then let to sediment at the bottom of the vial overnight at 4 °C. The day after, the supernatant was removed and replaced in 1 mL of Na_2CO_3 buffer (pH 8.5, 10 mM). Proteinosomes remained stable over several days if stored in buffer and kept at 4 °C.

Control proteinosomes were prepared as in **section 3.2.4**.

Glucose oxidase- (GOx)- containing proteinosomes were prepared following the same general procedure described above with the only exception that 15 µL of a solution of GOx (50 mg mL^{-1}) in Na_2CO_3 (pH 8.5, 0.1 M) were added to the aqueous phase.

3.5.2 Synthesis of acid-degradable biomaterials using pH responsive crosslinker, PEG-ketal-NHS

The crosslinker PEG-ketal-NHS is an attractive tool in the synthesis of acid-degradable soft materials, because of the high stability in basic conditions (pH > 7.5), and rapid hydrolysis in acidic conditions (pH < 6). Further, the NHS-activated termini make it an ideal candidate in bioconjugation reactions with biomolecules containing nucleophiles, such as amine groups, leading to acid degradable chemically crosslinked biomaterials. As a proof of concept, hydrogels were synthesised using an amine containing polysaccharide, carboxymethyl-chitosan (CM-chitosan), and crosslinked using PEG-ketal-NHS. To do this, 5 µL of six different concentrations (0, 5, 12.5, 25, 50, and 100 mg mL^{-1}) of **5** was mixed with 190 µL of CM-chitosan, with 5 µL of a commercially available universal indicator. The samples were mixed for 20 seconds and gelation occurred in less than 30 minutes for concentrations above 25 mg mL^{-1}. At a concentration of 5 ml mL^{-1} the hydrogel failed to form, likely due to the concentration of crosslinks being too low. The universal indicator showed a yellow colour once gelation had taken place, indicative of an alkaline pH caused by the amine groups in the CM-chitosan.

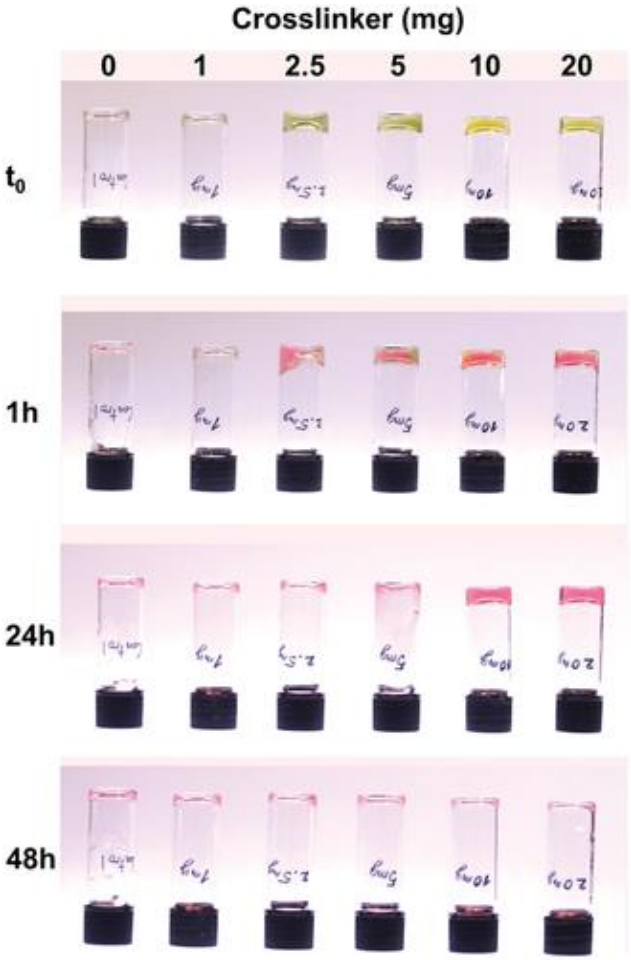

Figure 3.22 Images of inverted vials containing CM-chitosan hydrogels (4 wt%, 190 µL) crosslinked with PEG-ketal-NHS ranging from 0 to 20 mg (0 to 100 mg mL^{-1}), as specified at the top of the figure. The top image (t_0) shows the hydrogel at the beginning of the experiment. The hydrogels were then exposed to 5 µL of HCl (1 M) and photographs were acquired after 1, 24, and 48 h, as indicated on the left-hand side of the figure. The hydrogels were preloaded with a commercially available universal indicator, which showed the pH was alkaline at t_0 (top row, yellow colour) and the pH was acidic after addition of HCl (pink colour). The addition of HCl gave rise to hydrolysis of PEG-ketal-NHS and disassembly of the hydrogel at a rate that depended on the crosslinker concentration.

The addition of HCl (1M) was used to show the acid-degrading properties of the crosslinked hydrogel (**Figure 3.22**). The acid (5 µL) was simply added to the vials containing hydrogel, with concentrations of 12.5 and 25 mg mL^{-1} degrading in around 2 hours. Higher concentrations of 50 and 100 mg mL^{-1} degraded in 48 hours, indicating

a much higher proportion of chemical crosslinks within the hydrogel. Measurement of the pH showed that the pre-gelation, pH of the solution was 8 and after degradation the pH of the solution was 2. Control experiments using the pH-stable crosslinker PEG-diNHS to chemically crosslink the hydrogel saw stability for over a week following addition of acid, proving that the reason for the hydrogel degradation was the breakdown of PEG-ketal-NHS. A quantitative study of the time-dependent acid-mediated hydrogel degradation was carried out using a freeze-drying technique. The hydrogels were exposed to acid for various periods of time, promptly freeze-dried and then weighed to calculate the residual hydrogel amount. Data showed a linear increase in gel degradation which reached completion after ca. 2 hours.

Glucose oxidase (GOx) was co-crosslinked within the hydrogel matrix and used as an endogenous trigger for acid-mediated disassembly. Upon exposure to D-glucose, GOx-mediated oxidation to gluconolactone and subsequent hydrolysis to gluconic acid occurred decreasing the pH to ca. 4.5. Disassembly of the hydrogel was observed starting at ca. 4 hours and plateauing at 80% after 18 hours. After 30 hours, an 80% degradation rate was still observed which was hypothesised to be a loss of activity from GOx due to the acidic environment and depletion of the substrate.[31][32]

3.5.3 Construction of pH-responsive hydrogel-filled proteinosomes

The construction of proteinosomes using the PEG-ketal-NHS crosslinker was explored as a method to create pH-responsive capsules for substrate release. To achieve this, the crosslinker was added to the alkaline aqueous phase, along with CM-chitosan, during proteinosome synthesis (**supplementary method 3.5.1.3**). Upon transfer to Na_2CO_3 buffer (0.01 M, pH 8.5), hydrogel-filled crosslinked proteinosomes were obtained. Fluorescent labelling of the CM-chitosan and BSA nanoconjugates showed a CM-chitosan core surrounded by a well-defined proteinosome membrane. These were more fragile than PEG-oNB-NHS crosslinked proteinosomes, observing stability for several days stored in buffer, rather than months. Attempts to construct proteinosomes without CM-chitosan failed, as the transfer to buffer step was unsuccessful. Experiments were performed to investigate the stability of the proteinosomes during synthesis. Specifically, the crosslinker was analysed using ^1H NMR during exposure to carbonate buffer and sodium hydroxide (the water phase of

the Pickering emulsion) and ethanol/PBS buffer (the transfer conditions of the proteinosomes). These investigations showed that the crosslinker was not stable during exposure to ethanol/PBS buffer as there was evidence of hydrolysis. In light of these results, the proteinosomes containing the chitosan hydrogel core were taken forward as these showed a much higher level of stability and were able to be transferred to water.

Similarly to analysis of PEG-oNB-NHS proteinosome disassembly, the reduction in fluorescence intensity was used as an analysis technique. **Figure 3.23a** shows fluorescence microscopy images of PEG-ketal-NHS proteinosomes during exposure to HCl over a period of 1.5 hours. Fluorescence intensity against time plots (**Figure 3.23b**) show the reduction in membrane fluorescence compared to proteinosomes crosslinked with PEG-diNHS, showing a significant difference in behaviour. This confirmed that the PEG-ketal-NHS proteinosomes were disassembling due to the acid exposure. FACS was used to investigate the pH-responsive behaviour of the proteinosome populations. Proteinosomes were exposed to HCl (0.25 M) which initiated cleavage of the crosslinker and subsequent disassembly of the membrane after ca. 2.5 hours. **Figure 3.23c** shows overlapped histograms obtained using FACS showing a decrease in the population size to 27 % of the original value during exposure to HCl.

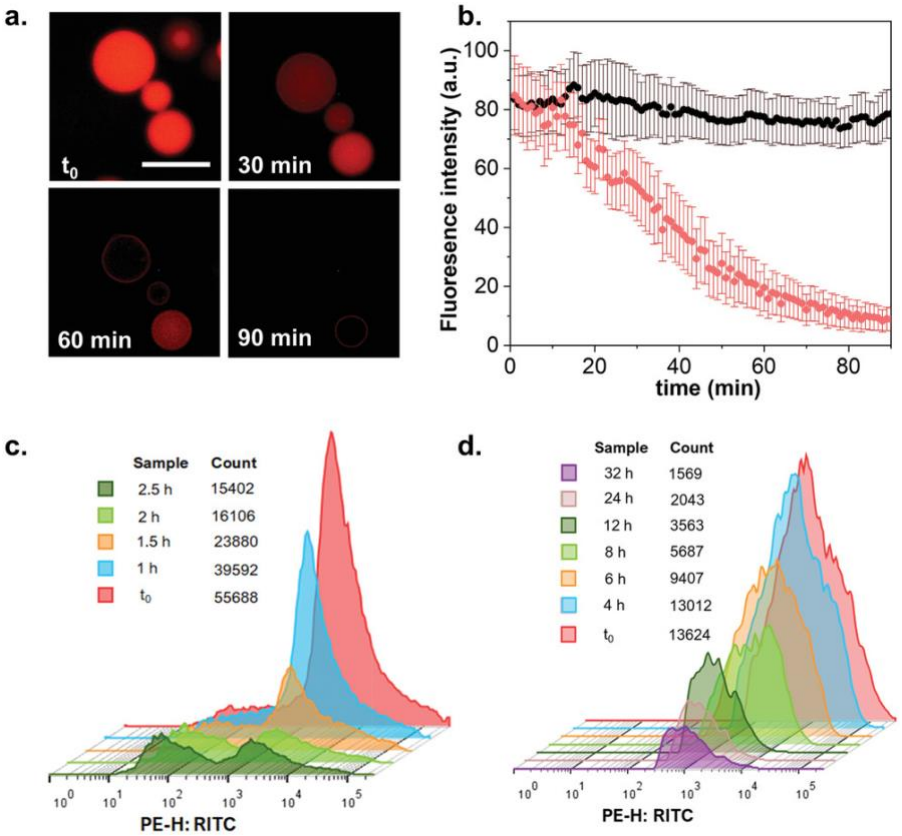

Figure 3.23 Characterisation of pH-responsive proteinosome degradation. **a.** Time-dependent fluorescence microscopy images of proteinosomes after 0, 30, 60 and 90 minutes of exposure to HCl. Scale bar 100 mm. **b.** Plots of fluorescence intensity versus time of proteinosomes crosslinked with PEG-ketal-NHS (red) and proteinosomes crosslinked with PEG-diNHS after exposure to HCl (50 μL, 1M). Error bars represent the standard deviation. **c.** Overlapped FACS-derived histograms showing the count of individual proteinosomes after exposure to HCl (50 μL, 1M) for the time intervals indicated. **d.** Overlapped FACS-derived histograms showing the count of individual GOx-encapsulated proteinosomes after exposure to D-glucose (50 μL, 0.5 M) for the time intervals indicated.

Finally, the encapsulation of GOx within the hydrogel matrix as a method of triggering disassembly was explored. As previously, the GOx was added to the aqueous phase of proteinosome synthesis in order to encapsulate the enzyme. Incubation with D-glucose solution (0.5 M) was analysed using FACS (**Figure 3.23d**) and showed a slow reduction in proteinosome population count reaching 11 % after 32 hours. This increase in time taken for disassembly to occur was hypothesised to be due to slow oxidation and subsequent hydrolysis of gluconolactone and gluconic acid.

As proteinosomes are used as protocells in synthetic biology, the experiments shown here demonstrate a step toward the pH-triggered communication pathways between communities of protocells. Further, the use of enzymes to initiate the disassembly brings about the opportunity for programmable enzyme-mediated pH decreases for the desired system.

References

[1] A. J. Dzieciol, S. Mann, *Chem. Soc. Rev.* **2012**, *41*, 79–85.

[2] X. Huang, M. Li, D. C. Green, D. S. Williams, A. J. Patil, S. Mann, *Nat. Commun.* **2013**, *4*, 1–9.

[3] X. Huang, A. J. Patil, M. Li, S. Mann, *J. Am. Chem. Soc.* **2014**, *136*, 9225–9234.

[4] X. Huang, M. Li, S. Mann, *Chem. Commun.* **2014**, *50*, 6278–6280.

[5] P. Gobbo, A. J. Patil, M. Li, R. Harniman, W. H. Briscoe, S. Mann, *Nat. Mater.* **2018**, *17*, 1145–1153.

[6] A. Galanti, R. O. Moreno-Tortolero, R. Azad, S. Cross, S. Davis, P. Gobbo, *Adv. Mater.* **2021**, *33*, 2100340.

[7] P. Zhou, S. Wu, X. Liu, M. Hegazy, G. Wu, X. Huang, *ACS Applied Materials and Interfaces* **2018**, 10, 38565-38573.

[8] X. Liu, P. Zhou, Y. Huang, M. Li, X. Huang, S. Mann, *Angew. Chemie - Int. Ed.* **2016**, *55*, 7095–7100.

[9] L. Tian, M. Li, A. J. Patil, B. W. Drinkwater, S. Mann, *Nat. Commun. 2019 101* **2019**, *10*, 1–13.

[10] M. Li, X. Huang, S. Mann, *Small* **2014**, *10*, 3291–3298.

[11] L. Rodríguez-Arco, M. Li, S. Mann, *Nat. Mater.* **2017**, *16*, 857–863.

[12] C. A. Custódio, R. L. Reis, J. F. Mano, *Adv. Healthc. Mater.* **2014**, *3*, 797–810.

[13] M. A. Cohen Stuart, W. T. S Huck, J. Genzer, M. Müller, C. Ober, M. Stamm, G. B. Sukhorukov, I. Szleifer, V. V Tsukruk, M. Urban, F. Winnik, S. Zauscher, I. Luzinov, S. Minko, *Nater. Mat.* **2010**, 9, 101-113.

[14] H. S. Dhowre, S. Rajput, N. A. Russell, M. Zelzer, *Nanomedicine* **2015**, *10*, 849–871.

[15] P. Roach, A. E. David, E. Ae, K. R. Ae, C. C. Perry, *J. Mat. Sci.* **2007**, 18, 1263-1277.

[16] J. Bancroft, in *Bancroft's Theory Pract. Histol. Tech.*, **2019**, pp. 33–52.

[17] J. Bancroft, A. Floyd, in *Bancroft's Theory Pract. Histol. Tech.*, **2013**.

[18] "Introduction to Fluorescence Microscopy | Nikon's MicroscopyU," can be found under https://www.microscopyu.com/techniques/fluorescence/introduction-to-fluorescence-microscopy, **2022.**

[19] T. U. of Q. Australia, “Confocal Microscopy,” can be found under https://imb.uq.edu.au/facilities/microscopy/hardware-software/confocal-microscopes, **2021**.

[20] S. W. Paddock, *Biotechniques* **1999**, *27*, 992–1004.

[21] D. R. Sandison, R. M. Williams, K. S. Wells, J. Strickler, W. W. Webb, *Handb. Biol. Confocal Microsc.* **1995**, 39–53.

[22] R. I. Ghauharali, G. J. Brakenhoff, *J. Microsc.* **2000**, *198*, 88–100.

[23] J. Picot, C. L. Guerin, C. Le Van Kim, C. M. Boulanger, *Cytotechnology* **2012**, *64*, 109–130.

[24] H. Pereira, P. S. C. Schulze, L. M. Schüler, T. Santos, L. Barreira, J. Varela, *Algal Res.* **2018**, *30*, 113–120.

[25] A. Brunsting, P. F. Mullaney, *Biophys. J.* **1974**, *14*, 439–453.

[26] B. Huang, H. Kim, C. Dass, *JACS* **2004**.

[27] G. Moad, S. H. Thang, *Aust. J. Chem* **2009**, *62*, 1402–1472.

[28] Y. Qiao, M. Li, R. Booth, S. Mann, *Nat. Chem.* **2017**, *9*, 110–119.

[29] K. A. Mosiewicz, L. Kolb, A. J. Van Der Vlies, M. M. Martino, P. S. Lienemann, J. A. Hubbell, M. Ehrbar, M. P. Lutolf, *Nat. Mater.* **2013**, *12*, 1072–1078.

[30] I. Myrgorodska, M. Jenkinson-Finch, R. O. Moreno-Tortolero, S. Mann, P. Gobbo, *Macromol. Rapid Commun.* **2021**, *42*.

[31] M. K. Weibel, H. J. Bright, *J. Biol. Chem.* **1971**, *246*, 2734–2744.

[32] K. Podual, F. J. Doyle, N. A. Peppas, *J. Control. Release* **2000**, *67*, 9–17.

Chapter 4: A deeper analysis of proteinosome membrane structure

Chapter Outline

The current understanding of the structure of any proteinosome membrane is limited within the scientific community. Specifically, it is unknown how the component parts affect the global properties of the mesh-like membrane and how this affects membrane function, in particular, the membrane porosity. In this chapter, the structure of light-responsive proteinosome membranes is investigated to formulate a model which allows us to characterise these global properties. Firstly, the molecular weight cut-off (MWCO) was investigated by diffusion of FITC-dextran out through the membrane from the interior. Subsequently, a novel mathematical description is formulated to describe the structure of the membrane using De Gennes scaling polymer theory. This description gives an estimation of the mesh size of the membrane allowing a deeper understanding of the size of substrates able to pass through, and with this an understanding about how to begin to control the MWCO of the membrane. Finally, experiments underpinning progression towards light-responsive specific permeability of the membrane is presented with permeability constants estimated.

4.1 Introduction

4.1.1 The cell membrane and function

Cell membranes are a common characteristic of all cells (in all domains) and are composed of a bilayer of lipids, or sometimes a monolayer in archaeal cells.[1] The cell membrane possesses many different functions which are crucial to the survival of the organism. The primary function of a membrane is to separate the internal environment from the exterior, therefore allowing a concentration of substrates required for critical chemical reactions to build up. Substrates must enter and leave the cell *via* the cell membrane, either by passive diffusion through the lipid bilayer or by active transportation *via* proteins situated within the membrane.[2] Active transport is facilitated by membrane proteins and allows the uptake or intake of specific substrates which would otherwise be excluded because of the impermeable lipid bilayer or

because it is against the concentration gradient. Some active transport can therefore be thought of as a gated tunnel.

One vital cell function facilitated by the membrane is cellular communication. For communication to occur, for example in a multi-celled organism or a population of bacteria, the cells need to be able to send signals to each other. This enables them to perform functions such as coordinated responses. Bacteria communicate via quorum sensing to share information from one cell to another[3] whilst in animal cells, there are different types of extracellular signalling which target cells based on proximity, age, or health.[4] The way these processes work with regards to the membrane is fairly similar. Quorum sensing is the release and subsequent sensing of signalling molecules giving information about the bacterial population and producing a response.[3] In animal cells endocrine signalling typically sees chemical signals travel through the circulatory system and cause a response in another part of the organism. Paracrine signals are chemical signals sent locally *via* the membrane and picked up by a nearby membrane in another cell.[4] The release of the chemical signal is *via* a process called exocytosis, where vesicles are transported to the membrane of the cell and fuse at secretory portals called porosomes.[4] The signal is then released through the membrane into the extracellular environment.

An example of paracrine signalling can be seen in neuron communication. At the neuromuscular junction, a chemical signal (neurotransmitter) is released *via* exocytosis through the porosomes of the pre-synaptic cell and diffuses across the synapse. The post-synaptic cell membrane contains receptor proteins able to recognise the signal and cause an action potential to be fired down the next neuron.[4]

4.1.1.1 Communication in artificial cells

To create artificial cells able to mimic the ability of natural cells to communicate, a system must be created where artificial cells can send, receive, and respond to chemical signals. Artificial cells which can send chemical signals must have a trigger which in turn causes the release of the substrate. As discussed in chapter 1, There are some recent examples in the literature of communication pathways between

artificial cells and living cells such as lipid vesicles translating chemical messages for bacteria in order to activate a chemical response,[5] and a system in which lipid vesicles both sense and send quorum signalling molecules to communicate with bacterial populations.[6] Further, there have been examples of protocell-protocell communication through the sending and receiving of chemical signals.[7][8]

4.1.1.2 Communication in proteinosomes

There have been multiple examples of systems where proteinosome populations shown communication and interacted with synthetic or living cells.[7,9,10] In all of these examples, the proteinosome membrane plays a key role in the interaction, whether that is to allow a substrate to enter, release a substrate, or have a physical interaction with the other population in the case of artificial phagocytosis.

In terms of the current understanding of the proteinosome membrane, the molecular weight cut-off of the proteinosome membrane has been examined in previous publications,[11–13] however, the structure of the membrane is something that has never been explored in in terms of how the protein-polymer nanoconjugates are structured within the membrane. In the first publication regarding proteinosomes in 2013 by Huang *et al*[11], cryo-transmission electron microscopy (TEM), atomic force microscopy (AFM), optical, and fluorescent microscopy were used to analyse the membrane experimentally. Optical and fluorescence microscopy are low resolution (limited to ca. 180 nm)[14] techniques therefore the membrane structure cannot be observed with these. TEM and SEM have higher resolution (sometimes < 1 nm)[15] however the method to prepare samples involves freeze-drying which can disrupt the structure. AFM also has good resolution (limited to ca. 1 nm laterally)[16] however in these articles exploring the proteinosome membrane, AFM was purely used to analyse the membrane thickness rather than surface properties. Further, there is mention of a membrane pore size in the publication however there is no discussion about what this pore size could be. A deeper understanding of the proteinosome membrane is essential if proteinosomes are to be used as an effective tool in synthetic biology and in applications such as drug delivery.

4.1.2 Polymer scaling concepts

An understanding of polymer properties and their subsequent behaviours are vital in understanding the findings presented in this chapter. Within this area, care must be taken to distinguish between local and global properties of polymers. Focussing on universal features rather than individual chains will give information about the polymer system as a whole and how it behaves collectively. Scaling concepts were made famous by De Gennes in his seminal book “Scaling Concepts in Polymer Physics”[17]. They can be used to help understand the universal features of polymer systems by predicting polymer behaviour which would otherwise need to be predicted using renormalisation group theory. Herein, concepts relating to multi-chain polymer systems are briefly summarised.

Polymers are long chains of repeated units called monomers which, with the exception of supramolecular polymers, are covalently bonded together. Contour length is the end-to-end distance of an outstretched polymer chain, $CL = Na$, where N is the total number of monomers and a is the length of the monomer, also known as the step size, consequently they can be extremely long (up to 10^5 units for synthetic polymers) with a contour length that can reach hundreds of micrometres, and this means their behaviour in dominated by a large configurational entropy. The simplest way to model a polymer is as an ideal chain. In this model the C-C bonds can take any conformation and the in-plane angles are not constrained, instead of the typical 120° C-C bond angle. The monomers have no volume and there is no solvent, meaning that no interactions are considered e.g. monomer-monomer interactions, monomer-solvent interactions. Using these assumptions, the radius of the coiled ideal chain is estimated using a random flight model which models the chain as a random walk on a lattice. This estimation gives an end-to-end distance of $R_0 = N^{1/2}a$. However, modelling polymer chains this way is very simplistic and does not take into account any of the aforementioned interactions between the monomers and solvent molecules.[17]

To make a better assumption of the size of a polymer in solution some interactions between the chain and the solvent must be considered. The chain of a real polymer will also take up some sort of coiled formation but will be dependent on some factors: intrachain monomer-monomer interactions, interchain interactions, and finally

monomer-solvent interactions. Logically, a balance of these factors will cause the chain to assume a coiled-up formation with some size, *R*. If there are strong intrachain monomer-monomer interactions then *R* will be smaller, like the conformation of a protein which have large monomer-monomer interactions due to hydrogen bonding and sulphide bridges. These will have a size $R^{1/3}$. DNA demonstrates the other end of the extreme as they are rigid linear structures and have a size R^{1}.[18] Most polymers will adopt a radius somewhere between these two extremes depending on the different interactions.

One of the most important interactions is the excluded volume effect. The ideal chain model assumes that the volume that each monomer occupies does not affect the overall conformation of the chain *e.g.* in the random flight model, the random walk can step back onto the chain at any point. The excluded volume is defined as the volume that each chain occupies and therefore is an inaccessible volume. This gives rise to a self-repelling effect along the chain with long-range repulsion from distant monomers causing the random coil to swell. Therefore, the two ends of the polymer chain will be farther apart than is estimated in the ideal chain model. Further to this, solvent-monomer interactions are a large driving force in the excluded volume effect. When the polymer is dissolved in a good solvent (where there is a good interaction between solvent molecules and monomer) the excluded volume will be positive causing swelling of the random coil. When the polymer is in a bad solvent (where there is a repulsion between solvent molecules and monomers), chain attraction interactions will dominate giving a negative excluded volume causing a shrinking of the random coil.[19]

In order to account for the excluded volume effect, the polymer chain can be modelled using a self-avoiding walk (SAW) on a lattice. This means the random walk cannot visit a site on the lattice more than once, hence it takes into account the excluded volume effect. Using this model, Flory showed the end-to-end distance of the polymer chain to be $R_f = a\,N^{v}$ where R_f is the Flory radius, and v is a critical exponent depending on the space dimensionality. He also showed that the scaling factor v can be estimated taking into account the repulsions between monomers and solvent-monomer interactions (Flory-Huggins parameter). For a real SAW chain, v can be estimated to be 3/5 or 0.6[20]. We must not forget that the Flory-Huggins parameter does have limitations: it has an entropic contribution which is not accounted for, and is

temperature dependent i.e. there is better mixing at high temperatures and phase separation occurs at low temperatures.

Another important factor affecting the random coil radius, *R*, is the polymer concentration which can be broken down into three regimes: dilute, semi-dilute, and concentrated (**Figure 4.1**)[21]. In the dilute regime, polymer chains are far away from each other so *R* can be estimated using RW and SAW models as described above. When the polymer concentration begins to increase, the chains begin to interact, and some chain overlap can be seen. This is called the semi-dilute regime where polymer chain numbers range widely (10^{-4} – 10^{3}), with the volume fraction range being 0.05 to 0.2[22], and has been reported to be wider at between 0.0001 and 0.1.[18] The concentrated regime consists of heavily overlapping polymer chains where polymers begin to behave like ideal chains.[23]

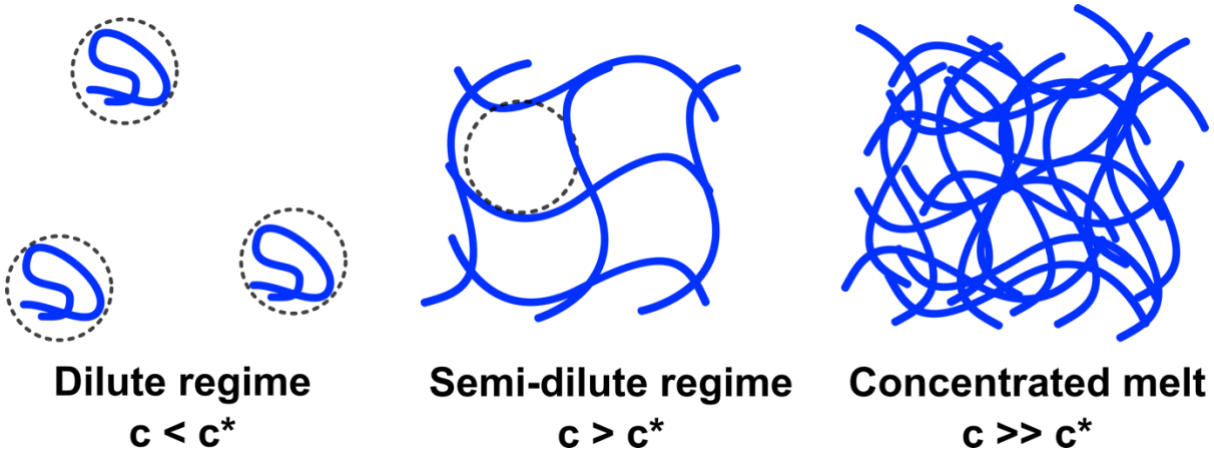

Figure 4.1 From left to right, schematics showing the three regimes associated with polymer chain concentrations in solution: dilute, semi-dilute and concentrated melt. In the dilute regime, the polymer concentration, *c*, is much lower than the overlap concentration, *c** (= N / R^3). In the semi-dilute regime, *c* is above *c** as the chains begin to overlap. In the concentrated melt, there is significant chain overlap and *c* is much larger than *c**.

Focussing on the semi-dilute regime, we observe volume fractions (Φ) of the polymer ranging from $\Phi < \Phi^*$ up to $\Phi \sim \Phi^*$, where Φ^* is the concentration at which there is

significant chain overlap. At this range of volume fractions, we can define the mesh size as the length scale above which hydrodynamic interactions are screened.[24,25] In other words, above this length scale, the excluded volume effect does not occur. This is due to the fact that there is no free energy gain caused by surrounding polymer chains screening the self-repulsion of the individual chains. The mesh size, ζ, will be around the length of the average separation between the chains and will dictate the size of objects that can diffuse through the solution of polymer. As seen in **Figure 4.1**, the polymers in the semi-dilute regime look like a network. Taking an object of diameter $D < \zeta$, that object would diffuse easily through the network. If $D > \zeta$, the object would struggle to diffuse through the network. The mesh size depends on the volume fraction of the polymer in solution. Logically, as Φ increases, there will be more chain overlap and therefore a smaller mesh size. An expression for the mesh size can be derived as $\zeta = \alpha \Phi^{-3/4}$, where α is the monomer length.[18]

4.1.3 Fick's first law of diffusion

It is well known that there is a net movement of molecules in a solution from a high concentration to a low concentration over time due to random thermal movements, called diffusion.[26] Diffusion plays a large part in many natural processes, for example, ripening in fruits is caused by the diffusion of small molecules such as ethylene, and the brining of meat is caused by the diffusion of salt and sugar molecules.[27] This phenomenon can be described mathematically using Fick's law of diffusion.

Firstly, the way molecules move in solution must be described. Generally, flux is defined as the net number of particles passing through a cross sectional area per unit time:

$$J = \frac{m}{A \times t} \tag{1}$$

where J is the flux of a mass of compound m (aka the number of molecules), moving through a cross-sectional area A, over a certain unit time t. The units of flux are given in mole cm^{-2} s^{-1}. Diffusion is a process which requires there to be a concentration gradient in the solution. The diffusion velocity will depend on the molecule size and the viscosity of the solvent. These factors manifest in the diffusion coefficient (D_i) of

the solute in a particular solvent in units of $cm^2\ s^{-1}$. D_i is normally a value that can be looked up and is specific to the chosen system. It is described by the Einstein-Stokes equation:

$$D_i = \frac{RT}{6\pi\eta N_A r_A} \tag{2}$$

Where R is the gas constant, T is the temperature, η is the viscosity of the solution, N_A is Avogadro's number, and r_A is the spherical radius of the solute. According to the equation, when the viscosity of the solution or the molecular weight of the solute increase, the diffusion coefficient will decrease. Fick's first law of diffusion describes diffusional flux of molecules in solution:

$$J = -D_i \frac{\partial C_i}{\partial z} \tag{3}$$

where D_i is the diffusion coefficient for the particles, ∂C_i is the change in concentration, and ∂z is distance in length in the z direction. This is one dimensional diffusion of substrate *i*. Change in distance ∂z is always positive whereas change in concentration, ∂C_i, will be a negative number. Therefore, there is a negative sign before the diffusion coefficient so that the overall flux turns out to be a positive value.

4.1.3.1 Flux across a membrane

Within organisms, molecules required for cellular processes and molecules that a cell does not need must enter and leave the cell *via* the membrane. This happens *via* processes such as active transport and passive diffusion. Passive diffusion in cells involves the movement of molecules through the lipid membrane requiring no energy input from the cell. Experimental studies into the movement of molecules and substrates across biological barriers are common in the field of pharmacokinetics and give an insight into the design of experiments and the interpretation of data. An example of this is transport investigations of drug candidates across tissues such as intestinal tissue.[26] Permeability constants can be estimated from these experiments which can then be compared with other permeability values in order to compare the

permeability of drugs candidates. This permeability constant of a molecule consists of specific variables[26]:

$$P = \frac{D_i}{h} \tag{4}$$

Where D_i is the diffusion coefficient, and h is the thickness of the barrier. In application, the permeability value will give an idea of the bioavailability of a drug candidate, as it indicates how easily it can diffuse across the membrane.

4.1.3.2 Permeability constants in proteinosomes

The permeability constant of proteinosome membranes was estimated by Joesaar *et al* by observing the diffusion of fluorescently labelled DNA across the membrane into the lumen.[28] The levels of internal fluorescence directly related to the concentration of DNA, therefore they were able to convert fluorescence to concentrations in ([A]) and outside ($[A]_{out}$) the proteinosome. The assumption was made that the diffusion was the rate limiting step during the initial linear phase of the reaction and so the permeability constant was calculated using the following equation:

$$P = \frac{\Delta[A]}{\Delta t}\frac{r}{3[A]_{out}} \tag{5}$$

where P is the permeability constant in μm min^{-1}, and r is the radius of the proteinosome. They go on to use P to estimate the bimolecular rate constant of DNA-strand displacement (DSD) reactions encapsulated in proteinosomes, and compare this to batch DSD reactions showing an order of magnitude difference in the rate constants. Based on their derivation of the permeability constant, permeability constants for the proteinosome system in this chapter were derived and estimated in the **appendix**.

4.2 Materials and Methods

Bovine serum albumin (BSA), fluorescein isothiocyanate (FITC), Rhodamine-B isothiocyanate (RITC), fluorescein isothiocyanate-dextran (FITC-dextran) (MW 40, 70, 150 and 2000 kDa), 1,6-diaminohexane, and PEG-(bis(N-succinimidyl succinate) (PEG-diNHS) were purchased from Sigma-Aldrich. 1-Ethyl-3-(3-dimethylaminopropyl)carbodiimide (EDAC) (98+%) was purchased from Alfa Aesar. Dialysis bags with MWCO 12,000–14,000 Da were purchased from Millipore. All solvents were purchased from commercially available sources and used without further purification. Water was filtered using a MilliQ integral 3 system before use. PNIPAAm (M_n = 8745.5 Da, PDI = 1.1) was synthesised according to literature procedures.[11]

4.2.1 Dynamic Light Scattering (DLS)

Dynamic light scattering (DLS) is a technique used to study the motion of macromolecules in solution[29]. When a beam of light enters a solution of macromolecules, it is scattered in all directions dependent on the molecular size and shape. If we put a screen in front of the particles, then a speckled pattern will be shown on the screen with bright and dark areas. This is because the light undergoes Doppler broadening and will either form destructive or constructive phases.

Constructive interference patterns from the scattered light form light patches and destructive interference will cause dark patches. The bombardment of solvent molecules with macromolecules causes them to move around in solution. This is called Brownian motion. When the particles start moving the interference patterns also start to fluctuate in intensity. The speed at which they are moving is related to their size as defined in the Stoke-Einstein equation (**equation 2**). **Equation 2** indicates that smaller molecular weight particles move more quickly, and larger molecular weight particles move more slowly since the diffusion coefficient is proportional to the inverse of the particle radius. The zetasizer measures the rate in change in intensity of the bright and dark spots and calculates the size.

The digital correlator measures the similarity between a certain part of the pattern, and the same area at time intervals. At very short time intervals the signals will be very highly correlated and at longer time scales they will be less and less correlated due to the particles moving randomly due to Brownian motion. A plot is generated of time versus correlation showing it decreasing at long time scales. Larger particles will show a slower decrease in correlation due to them moving more slowly. Similarly, smaller particles will show a fast decrease due to the fast movement. This information is used to calculate the size distribution by using algorithms to extract the decay rates for a number of size classes. The software will always plot the size distribution as an intensity distribution, which shows the relative intensity of the scattered light. Using Mie theory, this can be converted to both volume and number distributions.

DLS was used to calculate the hydrodynamic radius of FITC-dextran (MW 70-2000 kDa), RITC-BSA, and the PEG-*o*-NB-NHS crosslinker. Measurements were performed using a Malvern Zetasizer Nano-NS with a He-Ne laser (633 nm). The experiments were carried out in water. In a typical experiment, 0.8 mL of a 0.1 mg mL^{-1} solution was pipetted into a Zetasizer cell. All water used in the solutions was filtered through a 0.22 μm syringe filter before use.

4.2.2 Synthesis of proteinosomes with encapsulated substrates

In order to encapsulate FITC-dextran, 10 μL of a solution of FITC-dextran (6 mg mL^{-1}, H_2O) was mixed with 30 μL of FITC- or RITC-labelled BSA/PNIPAAm nanoconjugate solution (8 mg mL^{-1} in water). The PEG-*o*-NB-NHS crosslinker crosslinker (2 mg) was dissolved in 20 μL of Na_2CO_3 buffer (pH 8.5, 100 mM) and added to the nanoconjugate/dextran mixture to give a final FITC-dextran concentration of 1 mg mL^{-1}. An oil layer of 1-ethyl-2-hexanol (1 mL) was carefully added on top and the vial was shaken vigorously for 30 seconds. The resulting emulsion was left to sediment and crosslink for 48 hours before being transferred to water. After transfer, the proteinosome sample was washed 3 times to make sure broken proteinosomes and FITC-dextran in the bulk solution were completely removed.

4.2.3 Confocal imaging of FITC-dextran encapsulated proteinosomes

Confocal microscopy images were obtained on either a Leica SP5-II AOBS confocal laser scanning microscope with “adaptive focus control” to correct focus drift during time courses, or SP5 AOBS confocal laser scanning microscope attached to a Leica DM I6000 inverted epifluorescence microscope, at magnifications of x20 (HC PL APO CORR oil lens, working distance 0.17-0.26 mm, numerical aperture 0.7) or x40 (PL APO CS oil lens, 0.22 mm working distance, numerical aperture 1.3). Typically, 20 μL of a dispersed proteinosome sample was taken and imaged on a confocal slide, or in a sealed channel slide. For confocal images FITC and RITC labelled proteinosomes were imaged using a 65 mW argon laser (488 nm) and a 20 mW solid state yellow laser (561 nm). Fluorophores were excited by using specific filters with the following excitation (λ_{ex}) and emission wavelength cut offs (λ_{em}); FITC, λ_{ex} = 488 nm, cut off 520 nm; RITC, λ_{ex} = 561 nm, cut off 590 nm. Image analysis was performed with Image J.

4.2.4 Uptake of FITC-dextran for molecular weight cut-off measurements

For each molecular weight of FITC-dextran, three separate batches of proteinosomes were mixed, and subsequently, 10 μL of pre-settled RITC-tagged proteinosomes were taken from the bottom of a vial and put into an Eppendorf. FITC-dextran solution (10 μL, 1 mg mL^{-1}) was added to the proteinosomes and subsequently left to equilibrate for 30 minutes. Images of the proteinosomes were taken by confocal microscopy.

To determine the uptake percentage, analysis of the images was based on analysis performed by Huang *et al* in 2013[30], although no written method was given on how to use the graph to estimate the molecular weight cut-off. A line profile was drawn through proteinosomes, and the fluorescence intensity of the interior and exterior were averaged. A ratio of the inside to the outside the was taken to give the percentage uptake of the molecular weight FITC-dextran. The standard deviation of the ratios was taken and are shown on the graph as error bars above and below the average.

4.2.5 Release of 150 and 2000 kDa FITC-dextran *via* confocal microscopy

To perform the selective release experiments, three separate batches of proteinosomes at each molecular weight were mixed before 20 μL of pre-settled proteinosomes (150 or 2000 kDa FITC-dextran) were taken from the bottom of the

vial, sealed in a channel slide, and left to sediment to the bottom for 10 minutes. On a confocal microscope using the 40x HCX PL APO oil lens, the 488 and 561 nm lasers were set to 15 % and optimised to eliminate crossover of the lasers. A 200x200 μm^2 area was drawn in the middle of a 388x388 μm^2 total frame size using the region of interest tool. The 405 nm laser intensity was set to 100 % and 'Fly Mode' was selected. Pre-bleach was left at 1 iteration, bleach was set to 5 (150 kDa) or 12 (2000 kDa) iterations, and post-bleach was set to 200 iterations.

Fluorescence intensity of one tenth of the population was measured over time using ImageJ software to obtain fluorescence decay curves over time. The proteinosome degradation time was defined as the intercept point between the linear regressions of the initial decay and the plateau region. The standard deviation was used to calculate the error above and below the average.

FITC-dextran release was monitored as the fluorescence intensity increase of the solution directly next to the proteinosomes. Once average fluorescence intensity curves over time were found, they were normalised to peak at 100.

4.3 Results and Discussion

4.3.1 Analysing proteinosome membrane structure

4.3.1.1 Experimental characterisation of the proteinosome membrane molecular weight cut off (MWCO)

An investigation into the MWCO was undertaken in order to experimentally understand the proteinosome membrane structure and encapsulation properties. **Scheme 4.1** shows the general method of encapsulation of substrates, in this case fluorescently tagged dextran (FITC-dextran). Fluorescently tagged substrates were chosen so that the encapsulation efficiency could be analysed via fluorescent microscopy. Dextran was chosen as it is a widely used unreactive substrate in synthetic biology and is readily available at several different molecular weights, from the low thousands to two million Daltons.

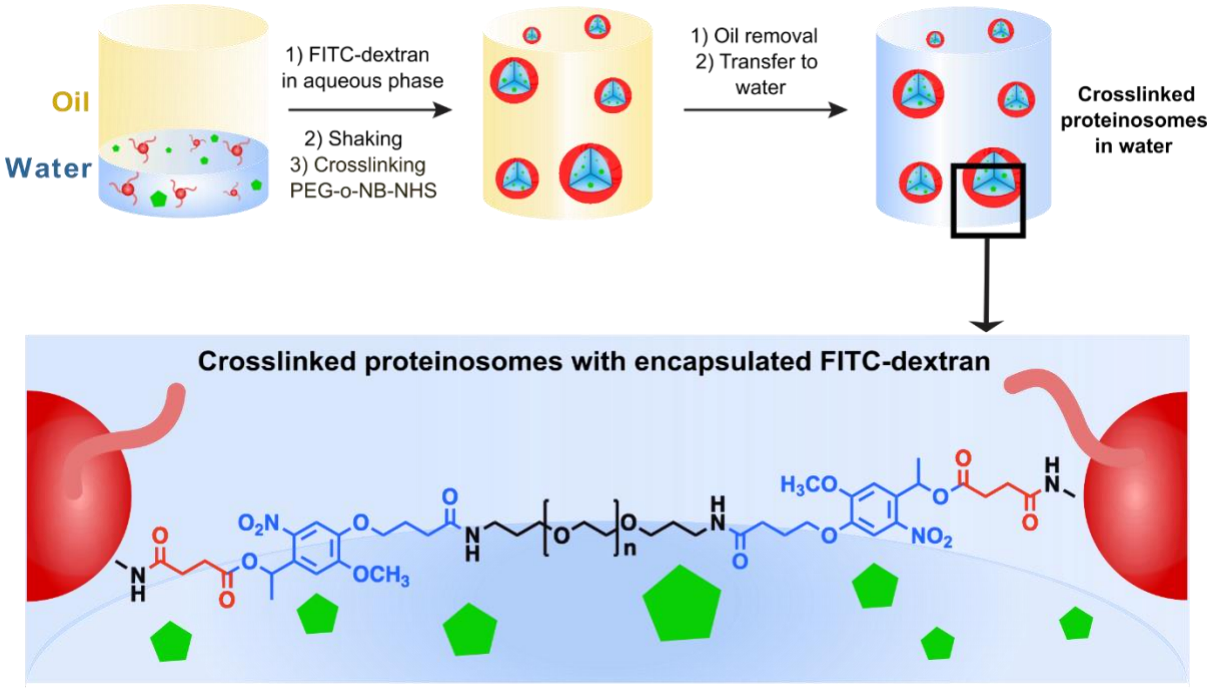

Scheme 4.1 A schematic representation of the method of encapsulation of FITC-dextran within the o-NB crosslinked proteinosome lumen. FITC-dextran polymer of over 40 kDa can be added to the aqueous phase during synthesis and will remain encapsulated inside after transfer to water.

According to previous articles by Huang *et al* and Gobbo *et al*, the approximate molecular weight cut-off (MWCO) can be estimated by analysing the percentage diffusion of FITC-dextran through the porous membrane into the proteinosomes interior.[31][30] Therefore, this method was used to try to estimate the MWCO of PEG-oNB-NHS crosslinked proteinosomes. Proteinosome populations were incubated with FITC-dextran with molecular weights of 4, 10, 40, 70, and 150 kDa at a concentration of 1 mg mL^{-1}. After 30 minutes, the proteinosomes were imaged using confocal microscopy and analysed using fluorescence line profiles to reveal the average uptake diffusion of each polymer through the membrane.

As seen in **Figure 4.2**, the average uptake diffusion initially falls from 73 to 46 % as the molecular weight of the polymer increases from 4 to 70 kDa. Contrary to the previous articles, at 150 kDa, the average uptake percentage increases again to 59 %. In addition, the standard deviation increases from 4 to 20 % when comparing 4 and 150 kDa FITC-dextran. This indicates that there is a large variation in uptake percentage 150 kDa dextran. One possible explanation for these findings is that there may be a high number of proteinosomes with compromised membranes in the samples. This means that at low molecular weights where there is a lot of diffusion through the membrane, no difference in uptake diffusion is seen between a proteinosome with intact membrane and a broken one. At high substrate molecular weights, typically there is less diffusion of the substrate and therefore there is a large disparity between the uptake diffusion in proteinosomes with intact membranes and broken membranes.

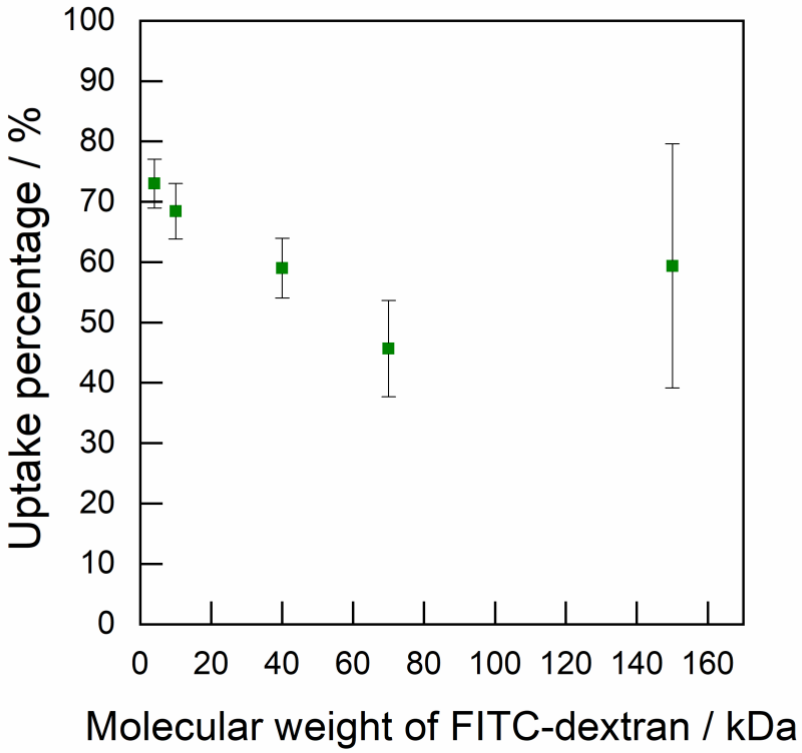

Figure 4.2 Plot of relative percentage diffusion uptake of FITC-dextran polymers of various molecular weights (4, 10, 40, 70 and 150 kDa) after 30 minutes of incubation. Data is based on fluorescence intensity line profiles of one tenth of the population at each concentration. Error bars are plus and minus the standard deviation of the average.

A new method was devised to find a more accurate way of determining the molecular weight cut off of the membrane. Instead, it was decided to encapsulate different sized dextran molecules inside the proteinosomes and then observe whether they were retained within the membrane. Dextran above 10 kDa behaves as if highly branched, and as all dextrans used were above this molecular weight threshold, it was assumed they all behaved this way. It must be noted that all dextrans were tagged in the range of 0.003:0.025 FITC:glucose, so there may be a variety in the levels of tagging within and between the different dextran polymers of different molecular weights.[32]

The method described in **section 4.2.2** was used to synthesise populations of proteinosomes with substrates encapsulated in the interior; FITC-tagged dextran (MW 40-2000 kDa). To do this, 10 uL of an aqueous solution of dextran (6 mg mL^{-1}) was added to the aqueous phase of the Pickering emulsion to give a final encapsulated substrate concentration of 1 mg mL^{-1}. The fluorescent tag attached to the BSA/PNIPAm nanoconjugates was chosen to be RITC for dextran encapsulation so the substrates could be distinguished from excess nanoconjugate within the lumen. Once synthesised, the proteinosomes were washed three times by carefully replacing the excess water once the proteinosomes had settled to the bottom of the vial. This allows any fluorescently tagged dextran or broken proteinosomes membrane to be removed from the exterior solution.

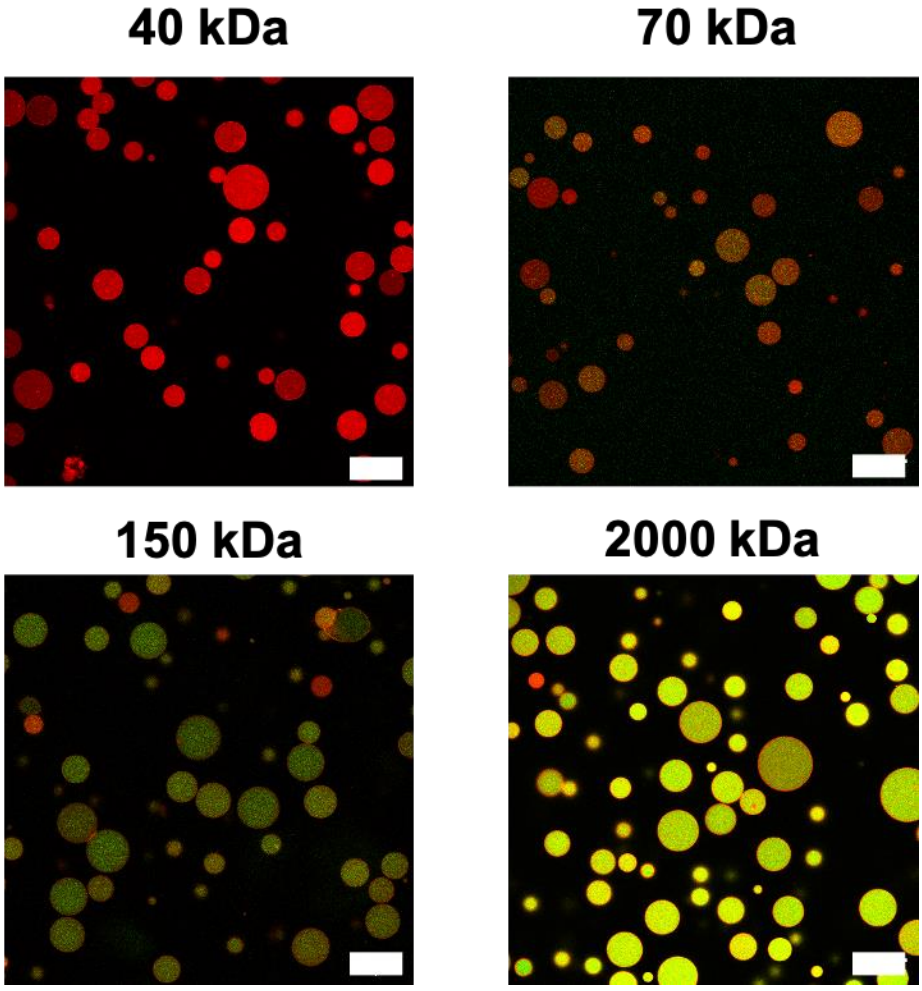

Figure 4.3 Fluorescence confocal microscopy images of RITC-tagged proteinosomes with encapsulated FITC-dextran within. Top left is a fluorescent image of 40 kDa FITC dextran encapsulated RITC-tagged proteinosomes after washing, showing no

encapsulation. Top right is a fluorescent image of 70 kDa FITC dextran encapsulated RITC-tagged proteinosomes after washing, showing some internal green fluorescence indicating dextran encapsulation. Bottom left and right are fluorescent images of 150 and 2000 kDa FITC encapsulated RITC-tagged proteinosomes, respectively, after washing showing higher degrees of internal green fluorescence and therefore a higher degree of encapsulation. All scale bars in the bottom right-hand corner are 50 μm.

Confocal microscopy images of the proteinosomes with encapsulated FITC-dextran (40, 70, 150 and 2000 kDa) can be seen in **Figure 4.3**. For imaging, the excitation lasers were always set to 15 % and the emission was measured from 566 – 610 nm to ensure a comparable fluorescence was being measured for all experiments. As seen in the images, there is an obvious increase in fluorescence inside the proteinosomes as molecular weight of FITC-dextran increases. This indicates that higher molecular weight dextran is more efficiently encapsulated inside the proteinosome membrane.

The encapsulation efficiency was estimated by measuring the ratio of fluorescence intensity of the inside to the outside of the membrane (**Figure 4.4**). Encapsulation efficiency was calculated to increase from 0 to 62.6 ± 17.4 for 40 to 2000 kDa FITC-dextran respectively. FITC-dextran at 40 kDa molecular weight was unable to be encapsulated as evidenced in the confocal images and corresponding encapsulation efficiency estimation. It can be inferred from these observations that there is a molecular weight cut off associated with the membrane somewhere in the region between 40 and 70 kDa. It was observed that there was a large error associated with the 2000 kDa FITC dextran encapsulation efficiency of ± 17.4. This is likely caused by the same reason as the previous membrane diffusion experiment but is less pronounced at the lower molecular weights.

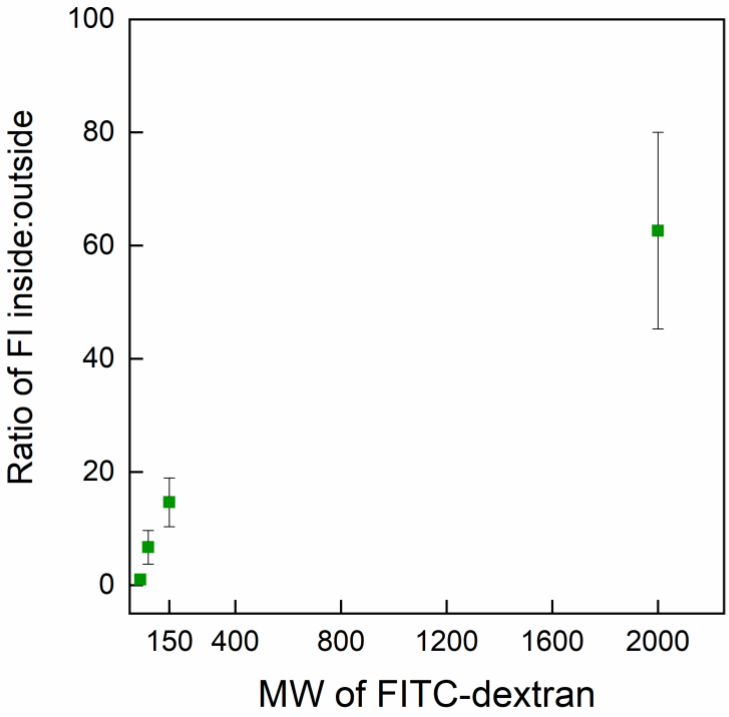

Figure 4.4 A plot of molecular weight (MW) of FITC-dextran versus the ratio of fluorescence intensity (FI) of the inside to the outside of the proteinosome membrane. the ratio of fluorescence intensity (FI) of the inside to the outside of the membrane was named the encapsulation efficiency. As the MW of FITC-dextran increases there is an increase in the ratio of FI indicating more efficient encapsulation of dextran. Encapsulation ratios of 0, 6.7 ± 3.0, 14.6 ± 4.3, and 62.6 ± 17.4 are seen for 40, 70, 150 and 2000 kDa respectively.

4.3.1.2 Theoretical characterisation of the proteinosome membrane MWCO

As described in **section 4.4.1.1** The MWCO of the proteinosome membrane has been examined in previous publications, however, the structure of the membrane is something that has never been explored in detail. If full control of the membrane photolysis is desired, a deeper understanding of the structure of the membrane is required. As a first attempt at modelling the structure of the proteinosome membrane, inspiration was taken from a colloidosome membrane, where the crosslinked nanoconjugates are hexagonally packed on the membrane surface (**Figure 4.5**).

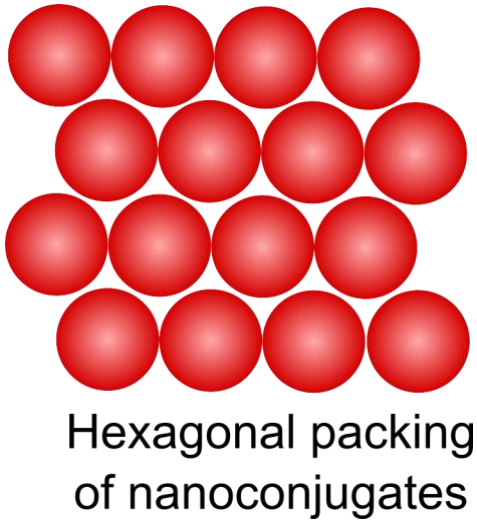

Figure 4.5 Schematic showing RITC-tagged nanoconjugates hexagonally packing to form the proteinosome membrane surface.

In colloidosomes, the self-assembled colloidal particles such as polymers, like polystyrene, are arranged as a perfect hexagonal lattice, where each individual is very close to (or touching) it's neighbours.[33] In this example by Dinsmore *et al*, the assembled particles were sintered to stabilise the membrane, but they can also be crosslinked. The colloidosomes were formed by sintering for varying amounts of time; a long sintering time causing a smaller MWCO. The MWCO is related to the interstitial holes in-between the spheres of diameter, *d*. This gap was roughly estimated to be 0.15*d*, and therefore the pore size in which molecules can pass through can be estimated. Since proteinosomes are a hybrid-material type of colloidosome, it is sensible to consider this option as a way to describe the membrane structure. A schematic of this is shown in **Figure 4.6**, as a magnification of three nanoconjugates with a box highlighting the interstitial gap between them. In order to investigate whether this is the real structure of the membrane, we must first try and estimate the pore size experimentally and then compare this to the theoretical pore size using this equation.

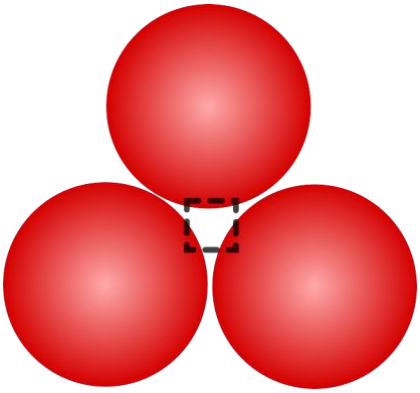

Figure 4.6 Schematic showing three nanoconjugates hexagonally packing and highlighting the interstitial gap (natural membrane pore) between them dictating the size of objects that can diffuse easily through the membrane.

To find the pore size experimentally, the hydrodynamic radii of different molecular weight dextran polymers was measured using DLS and then encapsulated within the membrane. A rough estimate of the pore size was determined by observing which dextran polymers diffuse though the natural proteinosome membrane pores. To perform the DLS experiments, each dextran polymer was dissolved in water at a concentration of 0.1 mg mL^{-1} averaging the size over 3 runs. **Figure 4.7** shows average hydrodynamic radii of the polymers found to be 5.6 ± 1.6 nm, 12.3 ± 0.9 nm, 16.5 ± 1.2 nm and 20.1 ± 1.4 nm for 40, 70, 150 and 2000 kDa FITC-dextran respectively. In comparison to literature[34], 40 kDa dextran agrees with a theoretical value of 4.78 nm (MW 39.1 kDa). Dextran of 70 kDa is measured to be larger than literature calculations (6.49 nm, MW 73.0 kDa). Dextran of 2000 kDa is also measured to be smaller than literature calculations (26.89 nm, 2000 kDa). Since it was demonstrated that 40 kDa dextran was unable to be encapsulated and we see encapsulation of the 70 kDa dextran, this gives an immediate idea about the size of objects that can diffuse through the membrane. This gives an experimental pore size of somewhere between 3.9 and 13.2 nm, the lower and upper experimentally measured hydrodynamic radii of 40 kDa and 70 kDa dextran, respectively.

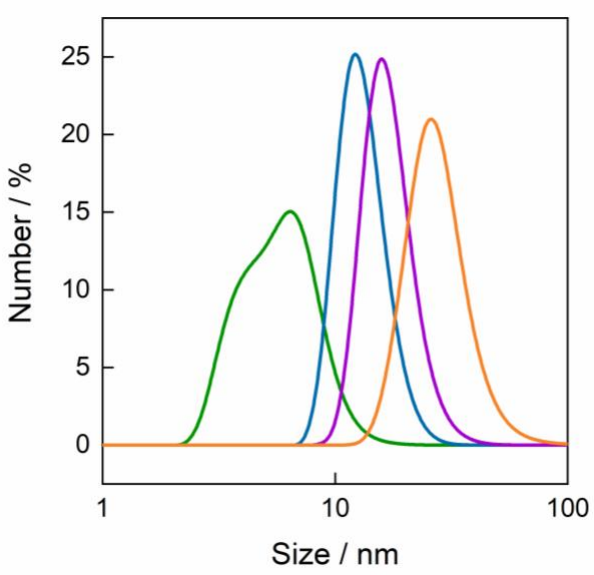

Figure 4.7 Plot of size in nanometres versus number in percentage found using DLS, to determine the hydrodynamic radii of FITC-dextran. Molecular weights of 40 (green), 70 (blue), 150 (purple), and 2000 (orange) kDa were found to be 5.6 ± 1.6 nm, 12.3 ± 0.9 nm, 16.5 ± 1.2 nm and 20.1 ± 1.4 nm

The value *d* was determined by performing the DLS experiment on a solution of nanoconjugates, resulting in a nanoconjugate diameter of 13.6 ± 1.6 nm. Using the equation pore size = 0.15*d*, the membrane pores would be estimated to be 2.04 ± 0.24 nm. This would predict the encapsulation of 40 kDa FITC-dextran as the pores are estimated to be smaller than 5.5 ± 1.6 nm. Since we do not see the encapsulation of 40 kDa FITC-dextran another hypothesis of what the membrane looks like must be considered.

Hexagonal packing does not take into account crosslinking; therefore, it is not a suitable model for the proteinosome membrane. It is well known that during (colloidosome/proteinosome) synthesis, the nanoconjugates will hexagonally pack at the water/oil interface and the crosslinkers will react randomly with primary amine groups on the protein surface.[35] Once the capsules are transferred to water, they expand slightly[36] (due to osmotic effects), and the nanoconjugates spread out with a mesh-like structure of crosslinkers in the space between. Assuming that the polymer crosslinker (PEG-oNB-NHS) concentration in the membrane is in the semi-dilute regime, it will have a characteristic mesh size associated with it which will determine

the size of substrates that can diffuse through the membrane. The volume fraction of the polymer phase of the membrane will be calculated to confirm it sits within the semi dilute regime. With this in mind, polymer physics was used to attempt to estimate this mesh size.

4.3.1.2.1 Estimating the mesh size using polymer physics

As described in the chapter introduction, utilizing pivotal work by de Gennes in 1979[17] and Paul Flory's[19] theories on polymer behaviour in solution, a scaling theory was used to estimate proteinosome mesh size. De Gennes proposed that a polymer network with a concentration in the semi-dilute regime has a characteristic mesh size, ζ (**equation 6**). The mesh size determines the size of objects that can easily diffuse through the polymer solution. Objects smaller than the mesh size will diffuse easily through the pores, and objects larger than the mesh size will find it more difficult or will not diffuse at all. The membrane of a proteinosome can be thought of as a polymer network in the semi-dilute regime; this can be seen more clearly in **Figure 3.5b**. Each nanoconjugate is crosslinked together via the amine groups on the surface of the protein. The polymer crosslinkers will randomly entangle and form a network in the space between the nanoconjugates. There will be a characteristic mesh size associated with this network dictating the permeability of the proteinosome. Assumptions about proteinosomes were made as some parameters and characteristics couldn't be measured, so instead were estimated.

Table 1 in the appendix shows the calculated/measured values for all the parameters needed to estimate the mesh size.

As previously described, the structure of a proteinosome membrane can be thought of as an interconnected network of protein-polymer nanoconjugates joined together with crosslinker molecules, in this case, PEG-*o*NB-NHS. The composition of this network will dictate the size of substrates able to pass through the membrane. We can describe this using polymer physics to attain a physical picture of the membrane and estimate a mesh size. The mesh size of a polymer network in a semi-dilute regime can be described using the following equation[18][17]:

$$\xi = a\phi^{-3/4} \tag{6}$$

where ξ is the mesh size, a is the monomer length and ϕ is the volume fraction of the crosslinker in the membrane. From equation (6) the volume fraction (Φ) and the monomer length (α) are required to calculate the mesh size. The volume fraction describes the amount of space taken up by the crosslinker molecules in the membrane. An analogy can be used to help understand this structure: imagine the proteinosome membrane is like spaghetti (crosslinkers) and tomatoes (nanoconjugates) in a lunchbox (total membrane volume). They will sit inside the lunchbox randomly and therefore there will be space between the spaghetti strands inside the lunchbox; they are only taking up a certain volume fraction of the box.

The volume fraction, ϕ, can be calculated by taking the volume of all spaghetti strands (the molecular volume of the crosslinkers) and dividing it by the total volume available in the lunchbox for spaghetti (total volume pervaded by crosslinkers in the membrane):

$$\phi = \frac{v_L}{V_x} \tag{7}$$

where v_L is the molecular volume of the crosslinkers, and V_x is the total volume pervaded by crosslinkers in the membrane. First an expression for the total volume will be derived, V_x, and then for the molecular volume, v_L.

We can work out V_x simply by taking the total aqueous volume of the membrane, V_s (total volume of the lunchbox), and taking away the volume occupied by nanoconjugates, V_c (the volume taken up by all tomatoes):

$$V_x = V_s - V_c \tag{8}$$

where V_s is the aqueous membrane volume, and V_c is the volume of the membrane occupied by nanoconjugates. Firstly, V_s will be calculated, followed by V_c.

To calculate the total aqueous volume, V_s, we need to make some assumptions. Firstly, we assume that the proteinosome is perfectly spherical, and secondly, that the proteinosome radius is much greater than the thickness of the membrane (**Figure 4.8a**). Using these assumptions, we can estimate, V_s, to be the surface area of a sphere ($4\pi R^2$) multiplied by the thickness of the membrane:

$$V_s \approx 4\pi(R-t)^2 t \approx 4\pi R^2 t \; (for \; t \ll R) \tag{9}$$

where R is the radius of the proteinosome and t is the thickness of the membrane.

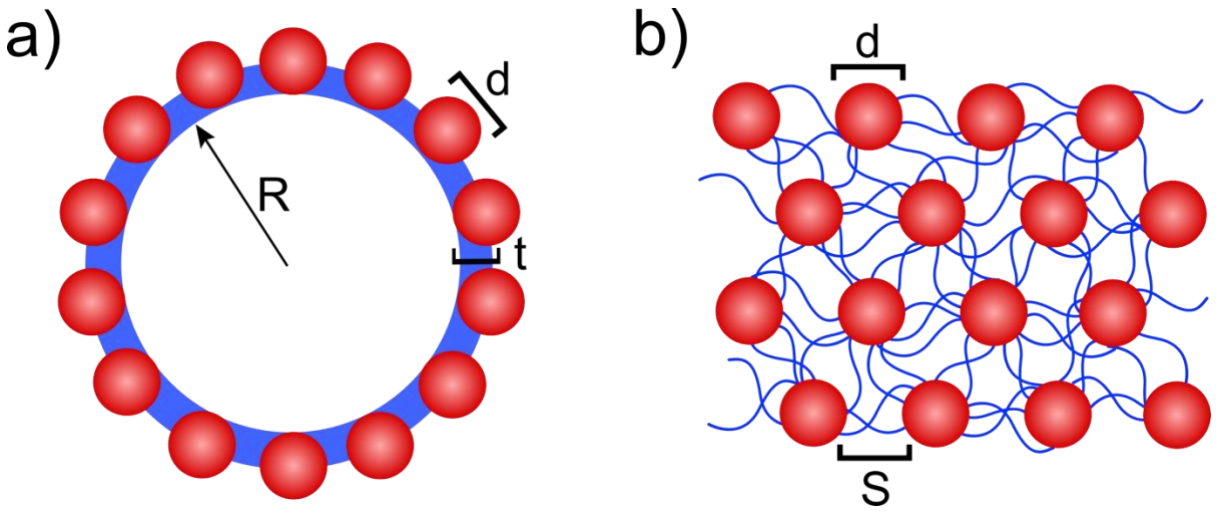

Figure 4.8 a. Schematically drawn proteinosome showing a ring of nanoconjugates (red spheres) on the membrane (blue), where *R* is the average radius per proteinosome, *d* is the average nanoconjugate diameter and *t* is the thickness of the membrane. **b.** Schematic showing the proteinosome membrane where the nanoconjugates are joined together with blue crosslinker molecules. *d* is the average nanoconjugate diameter and *S* is the inter-conjugate distance. These schematics are not to scale.

The next parameter we need to work out in order to get V_x, is the total volume of all nanoconjugates in the membrane, V_c, (volume of all tomatoes, in the analogy). To calculate this, we must assume that nanoconjugates are perfectly round with a certain

diameter, *d*. Subsequently, the membrane volume occupied by the nanoconjugates can be described as:

$$V_c = nv_{nc} = \frac{n\pi t^2}{3}\left(\frac{3}{2}d - t\right) \quad (10)$$

where d is the diameter of a single nanoconjugate, n is the number of nanoconjugates per proteinosome, and v_{nc} is the volume of a single nanoconjugate. Due to the Pickering emulsion technique used to synthesise the proteinosomes, the thickness of the membrane, *t*, depends on the contact angle of the colloidal particles sitting at the oil/water interface. If the assumption is made that the contact angle is 90°, then

$$t = 1/2\, d \quad (11)$$

Using equation (11), we can simplify equation (10):

$$V_c = nv_{nc} = \frac{n}{12}\pi d^3 \quad (12)$$

If we so wish, we can now combine equations (10) and (12) and simplify to:

$$V_x = V_s - V_c = 2\pi R^2 d - \frac{n}{12}\pi d^3 = \frac{\pi d}{12}(24R^2 - nd^2) \quad (13)$$

V_s was calculated using equation (9). The average radius of a proteinosome is 11.25 μm, measured manually via fluorescence microscopy. The value *d* can be measured by DLS as the diameter as 13.6 ± 1.6 nm giving maximum and minimum values of 12.0 and 15.2 nm. Equation (11) can be used to estimate the membrane thickness, then it will have minimum and maximum values of 6 and 7.6 nm, respectively. Using equation (9), the total aqueous volume, V_s is between 9.5x10^9 and 12.1x10^9 nm^3.

We can then use equation (12) to calculate V_c, which takes the volume which one single nanoconjugate is taking up in the membrane multiplied by the total number of nanoconjugates per proteinosome. When proteinosomes are synthesised, only part of

the nanoconjugates will sit submerged within the membrane due to the Pickering emulsion technique. Looking at **Figure 4.9**, the nanoconjugate volume, v_{nc}, is the shaded area of the red nanoconjugate which is submerged within the membrane. The rest of the nanoconjugate volume will not affect the calculations for mesh size. The submerged volume can be estimated using the standard equation determining the volume of part of a sphere which is submerged:

$$\frac{\pi t^2}{3}\left(\frac{3}{2}d - t\right) \quad (14)$$

In this case, the part of the nanoconjugate which is submerged is related to the thickness of the membrane *t*, which calculated earlier gave a value between 6.0 and 7.6 nm. Using this equation, v_{nc} is estimated to be between 452.39 and 919.39 nm^2.

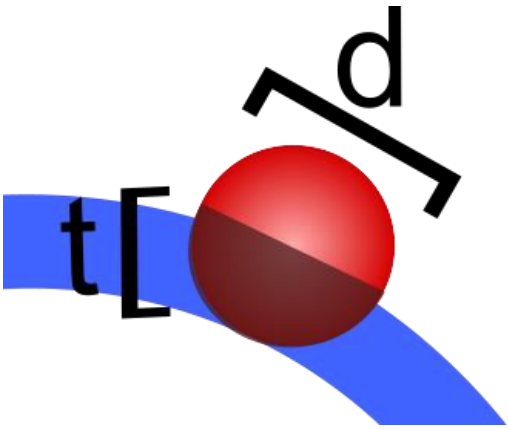

Figure 4.9 Schematic representing a nanoconjugate (red) submerged withing the proteinosome membrane (blue). The amount that the nanoconjugate is submerged is related to the contact angle during the synthesis of the proteinosome, assumed to be 90°. With this assumption, $t = ½\ d$, where *t* is thickness of the membrane in nm, and *d* is the diameter of one nanoconjugate.

The total number of nanoconjugates per proteinosomes, *n*, can be estimated by making some assumptions. Firstly, it is assumed that each nanoconjugate on the membrane takes up a hexagonally shaped area *i.e.* are hexagonally packed in the membrane (**Figure 4.10**).

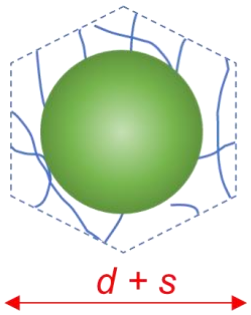

Figure 4.10 Schematic showing the nanoconjugate surrounded by PEG-oNB-NHS crosslinkers forming a hexagonal area, a_{nc}, with a hexagonal diameter, d_h, of d+S.

It can be assumed that there will be space between the crosslinked nanoconjugates (with diameter *d*) of length *S*, and therefore the hexagonal diameter, d_h, is estimated to be *d*+*S* (see **Figure 4.8b** for a schematic showing this). The length S has a minimum and a maximum; the minimum being the hydrodynamic diameter of the smallest FITC-dextran able to diffuse through (5.6 nm), and the maximum being the finite length of a crosslinker molecule (contour length) (15 nm). Therefore, an estimate of *d*+*S* gives a hexagonal diameter, d_h, of between 17.6 and 30.2 nm. The area of one hexagon can be calculated using the following equation:

$$a_{nc} = \frac{\sqrt{3}}{2}(d_h + S)^2 \tag{15}$$

When we use the estimations for d_h and S, we get a hexagonal area a_{nc} of between 218.9 and 912.0 nm^2. Subsequently, to estimate *n*, we can use the following equation:

$$n = \frac{4\pi R^2}{\frac{\sqrt{3}}{2}(d_h+S)^2} \tag{16}$$

The average proteinosome surface area ($4\pi R^2$ = 1.6 x10^9 nm^2) is divided by a_{nc} to get an estimate of between 1.7 x10^6 and 7.3 x10^6 nanoconjugates per proteinosome, *n*. Now we can estimate the total volume of nanoconjugates, V_c, by multiplying v_{nc} by *n* (equation (12)) to get a volume between 2.7 x10^9 and 1.6 x10^9 nm^3.

So far, we have been able to estimate V_s and V_c. Therefore, we can use equation (13) to get an estimate for the total volume pervaded by crosslinkers in the membrane, V_x of between 6.3 x10^9 and 11.0 x10^9 nm^3.

Now that we have V_x, we need to find an estimation of the molecular volume of the crosslinkers (volume of all the spaghetti strands in the lunchbox), v_L, in order to find the volume fraction ϕ (equation (7)). To do this, we need the volume of one crosslinker and multiply that by the total number of crosslinkers in the membrane.

The volume of one crosslinker molecule can be estimated as follows. The molecular mass of one crosslinker molecule, m, divided by the density, ρ, which is equivalent to the molar mass of a crosslinker molecule, M, divided by density and the Avogadro number, N_A:

$$v_L = \frac{m}{\rho} = \frac{M}{\rho N_A} \tag{17}$$

The molar mass of the crosslinker was 2260 g mol^{-1}, which is the final crosslinker without NHS groups. The density is estimated to be equivalent to PEG 2000, which is found to be 121000 gm^{-3} according to Merck Millipore specifications.[37] Using these estimates, v_L can be calculated to be 3.1 nm^3. To give an idea of scale, this means 3.2 x10^{10} crosslinker molecules would fit inside the average human red blood cell.[1]

[1] Average red blood cell volume of 100 μm^3.[39]

Next, the crosslinker molecular density must be multiplied by some fraction to represent the total number of crosslinkers in the membrane. Firstly, its was assumed that 100 % of the available crosslinking sites on the nanoconjugate are used. This is due to the use of ca. 7 times excess of crosslinker to crosslinking site ratio. The available crosslinking sites on each nanoconjugate, *z*, is equivalent to the number of natural nucleophilic amino acid sites (amine containing amino acids, lysine) within BSA protein, plus the number of carboxylic acid moieties that were converted during cationisation, minus the number of grafted PNIPAAm chains. This is calculated to be 60 lysine, 35 converted amino acids, 3 PNIPAAm chains, giving a total of available sites, *z*, of 92.

z must be multiplied by some factor to account for the structure of the crosslinker and the positioning of the nanoconjugates. Each crosslinker has two NHS groups on each end and therefore will react twice so *z* is multiplied by ½ to account for this. Assuming a contact angle of 90° means that $1/2\,d$ of the nanoconjugate submerged in the aqueous membrane, so *z* is multiplied by ½ again. Finally, *z* is multiplied by the total number of nanoconjugates in the proteinosome membrane, *n* (equation (16)) to get a scaling factor:

$$\frac{nz}{4} \tag{18}$$

where n is the total number of nanoconjugates per proteinosome, and *z* is the number of crosslinking sites per nanoconjugate. This scaling factor is estimated to be between 4.0 x10^7 and 1.7 x10^8. Subsequently, this is used to calculate the molecular volume of the crosslinkers using the following equation:

$$v_L = \frac{nz}{4}\frac{m}{\rho} = \frac{nz}{4}\frac{M}{\rho N_A} \tag{19}$$

where m is the molecular mass of the crosslinker, ρ is the density, M is the molar mass, N_A is the Avogadro number, and *n* is the number of nanoconjugates per proteinosome, and z is the number of crosslinking sites per nanoconjugate. The fraction $\frac{nz}{4}$ is an estimation of the number of crosslinkers in the membrane. Using the

estimations for the scaling factor and the molecular volume of a single crosslinker molecule, the calculation for the molecular volume of all crosslinker molecules is found to be between 1.2 x10^8 and 5.2 x10^8 nm^3.

Now that V_x and V_L have been calculated, equation (7) can be used to calculate the volume fraction of the crosslinker, ϕ, to be between 0.012 and 0.062. This is equivalent to between 1.2 and 6.2 % of the membrane volume is taken up by the crosslinker. The semi-dilute regime volume fraction range for polymer solutions is reported to be between 0.05 and 0.2[22], and has been reported to be wider at between 0.0001 and 0.1.[18] The volume fraction of the crosslinker lies within this range suggesting the crosslinker is in a semi-dilute regime concentration.

Using the estimation of ϕ, it is now possible to calculate the mesh size, ξ, of the proteinosome membrane using equation (6). That is what determines the size of objects able to diffuse freely through. According to the equation we need an estimate of the monomer length a. From experiments by Cruje *et al,* the monomer length of an ethylene glycol unit is found to be approximately 0.35 nm.[38] Using this, and the estimates for the volume fraction, we get an estimation of the mesh size to be between 2.8 and 9.7 nm. This result aligns remarkably well with the experimental results from **section 3.4.1**, finding that 40 kDa dextran (5.6 nm) diffused freely through the membrane, and 70 kDa dextran (12.3 nm) was able to be encapsulated.

This type of mathematical modelling has never been done for proteinosome membranes before, to the best of the author's knowledge. The modelling could be used to predict and design the properties of proteinosome membranes to encapsulate a range of desired components. For example, if the molecular weight of the crosslinker was increased from 2000 kDa to 6000 kDa, this model would predict that the volume fraction would increase to between 0.017 and 0.165 and the corresponding mesh size would decrease to be between 1.4 and 7.5 nm. Simply by increasing the molecular weight of the crosslinker, there is could be a significant change in what could be encapsulated within the membrane. This is impactful to the field because researchers can use this model to understand the system is more detail and can more accurately synthesise proteinosome membranes of specific mesh sizes.

4.3.2 Light-induced release of FITC-tagged dextran determined by molecular weight

Proteinosomes synthesised using the PEG-oNB-NHS crosslinker have been shown to have properties allowing them to be fully disassembled using UV-light in **chapter 3**. In the discussion in **section 3.4.2**, a mathematical model was produced to facilitate the understanding of what the proteinosome membrane structure is and how it behaves. This understanding of the specific mesh size, which acts like a pore in the membrane allowing for diffusion of substrates, it is facile to make use of the PEG-oNB-NHS crosslinker to create higher/other functionality in the membrane. It was hypothesised that a system could be created where instead of full disassembly of the membrane, the pores of the polymer mesh could be increased in size using UV light, in order to control selective substrate release in response to an external stimulus. Significantly, it was predicted that the release could be selective dependent on the molecular weight of the substrate, allowing for further control and design of proteinosomes. Previous studies have been able to control the release of substrates using external stimuli[12,13], but the technique proposed in this section is much simpler and exposure to UV can be easily quantified and thus controlled.

Scheme 4.2 explains the concept behind the experiments. A single proteinosome can be seen with red spheres representing the BSA nanoconjugate membrane and they have space between them representing the characterised mesh size, or pores. By using small amounts of light, we can make the pores in the membrane increase in size by initiating the loss of some of the BSA nanoconjugates which the membrane is formed. The creation of small pores in the membrane will allow smaller molecular weight substrates to be released. Larger molecular weight substrates which are larger in size (nm) will remain encapsulated when the same amount of light is used. The creation of larger pores with a subsequent irradiation of light will allow both larger and smaller molecular weight substrates to be released.

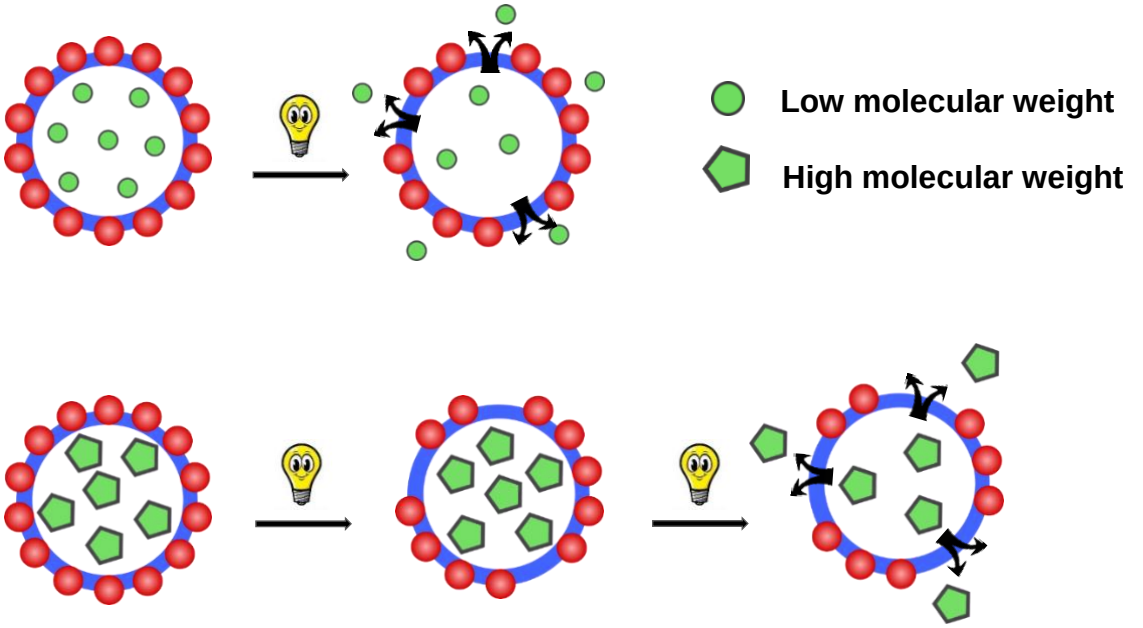

Scheme 4.2. Schematic illustrating the idea of selective release using light. Top - the blue ring with red spheres around the edge represents a proteinosome with red nanoconjugates. The green sphere represents a low molecular weight substrate which is encapsulated inside and is too large to diffuse through the membrane. When the proteinosome is irradiated, pores are created which are large enough to release the substrate into the surrounding environment. **Bottom** - The green pentagons represent a larger substrate encapsulated inside a proteinosome which are also too large to diffuse through the membrane. When the same sized pores are created as before, the large substrate will not be released as it is still too large to diffuse through the pores meaning we can selectively release the smaller substrate. The proteinosomes are irradiated further to create even larger pores which allow the release of the larger substrate.

In the following experiments, FITC-dextran was used as the encapsulated substrate as populations of proteinosomes containing this polymer had been thoroughly characterised, with the fluorescent tags facilitating confocal imaging. Simply by irradiating the proteinosomes for a shorter amount of time, it was predicted that small pores could be created that would allow a lower MW FITC-dextran to be released. Then upon further irradiation, the pores would increase in size allowing a larger molecular weight dextran to be released.

Firstly, proteinosomes containing encapsulated dextran of various molecular weight were synthesised according to the method in **section 4.2.2**. The proteinosomes were washed 3 times to ensure a minimum amount of dextran remained in the surrounding solution. Two populations containing 150 kDa and 2000 kDa were tested, in which the dextran hydrodynamic radius was measured previously by DLS to be 16.5 ± 1.2 and 20.1 ± 1.4 nm, respectively. To form larger pores in the membrane, a 405 nm confocal laser was used at 100 % (2266 mV). The irradiation times were optimised to find an exposure length which enlarged pores sufficiently in the membrane to allow the interior dextran to be released. Any less exposure time did not allow the dextran to diffuse through the membrane.

4.3.2.1 150 kDa FITC-dextran release

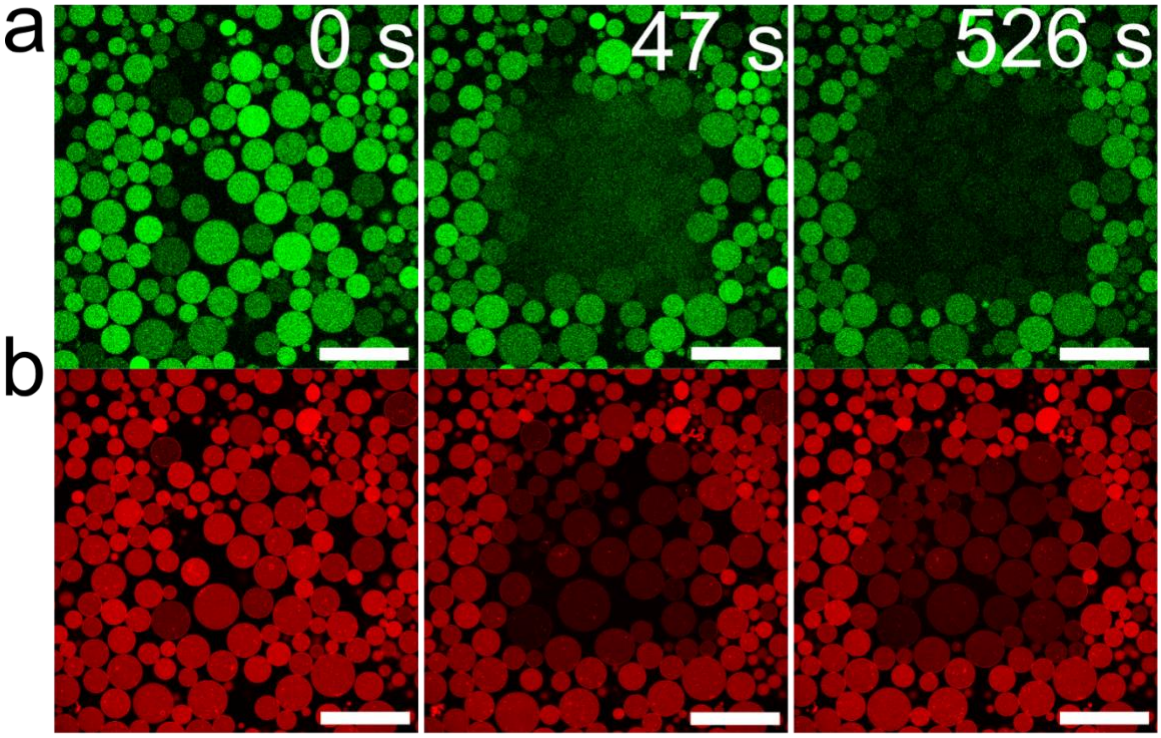

Figure 4.11 A series of confocal images showing the aftermath of 5.5 seconds of 405 nm UV light irradiation on proteinosomes containing 150 kDa FITC-dextran. **Far left green channel** - 150 kDa FITC-tagged dextran encapsulated inside UV light-responsive proteinosomes. **Far left red channel** – RITC-tagged proteinosome population. **Middle green channel** – 47 seconds after the start of the experiment, the dextran can be seen dispersed between the proteinosomes after diffusing through pores in the membrane formed during irradiation. **Middle red channel** - the

proteinosome membranes have become less fluorescent but are still intact. **Far right green channel** – after 526 seconds, most of the dextran has diffused away from the proteinosomes into the solution. **Far right red channel** - the proteinosome membranes are still intact.

Figure 4.11 shows a series of confocal microscopy images of proteinosomes with encapsulated 150 kDa FITC dextran taken at different time points indicated in white on the top right of the image. The first two images on the left at t = 0 seconds show the population of proteinosomes before being exposed to UV light. The images in green are the green channel which shows the FITC-tagged dextran encapsulated within the membrane. The red channel shows the RITC-tagged BSA nanoconjugates making up the membrane. Proteinosomes containing 150 kDa FITC-dextran inside a 200x200 um^2 region of interest in the middle of the image were irradiated with 405 nm UV light for 5.5 seconds. After the irradiation period the green fluorescence was measured for a period of time to investigate the behaviour of the encapsulated dextran. After 47 seconds, the green fluorescence inside the proteinosomes decreases and the fluorescence increases outside the proteinosomes. The red channel shows a visual decrease in fluorescence in the membrane. After 567 seconds, the green fluorescence associated with the dextran around the proteinosomes decreased further, and the red fluorescence associated with the membrane stayed relatively stable.

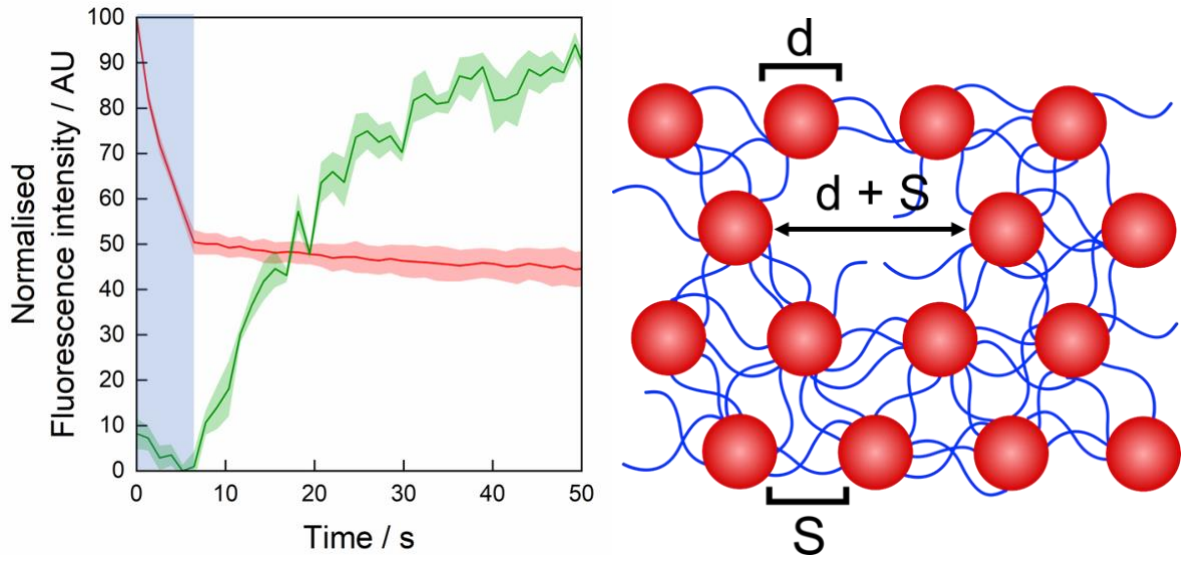

Figure 4.12 Graph showing the behaviour of the normalised fluorescence intensity of the FITC-tagged 150 kDa dextran (green curve) and the RITC-tagged BSA-nanoconjugate proteinosome membrane (red curve) after 5.5 seconds of irradiation using a 405 nm laser at 2266 μW. **Green curve** – during irradiation (initial 5.5 seconds) the green fluorescence outside the membrane increases to a normalised value of 100 AU as the dextran diffuses through the membrane. This value slowly decreases as the dextran diffuses away from the target proteinosomes over the period of the experiment. **Red curve** – During irradiation (initial 5.5 seconds) the membrane fluorescence decreases rapidly before stabilising around 42 ± 7 AU. This decrease indicates the membrane has broken down and pores have been made. The shaded areas above and below the curve are plus and minus the standard deviation of the average normalised fluorescence. Using the membrane model from **section 4.3.1.2.1**, a hole created in the membrane by losing one nanoconjugate would be equal to the size of *d*+*S*, between 17.6 and 30 nm.

The graph in **Figure 4.12** shows the change in normalised fluorescence of both the green and red fluorescence associated with the dextran and proteinosome membrane respectively. This analysis was performed according to method in **section 4.2.5**. During the 5.5 seconds of irradiation, the normalised red fluorescence decreases rapidly from 100 to 50 AU at a rate of -9.1 AU s^{-1}. Once irradiation stops, the fluorescence stabilises at ca. 42 ± 7 AU. Concurrently, the normalised green fluorescence of the solution is very low (just above 0) during irradiation. After

irradiation is stopped 5.5 seconds into the experiment, green fluorescence starts to rise rapidly peaking at 80 to 100 seconds. It then decreases at a slower rate throughout the remaining time of the experiment.

Both **Figures 4.11** and **4.12** are evidence that pores are being formed in the proteinosome membrane due to UV-light breaking the PEG-oNB-NHS crosslinker. The confocal images of the green channel with corresponding graph indicate the dextran diffuses into the surrounding solution shown by the increase in green fluorescence in the solution. Importantly, the increase only begins after the irradiation has stopped, indicating the formation of appropriately sized pores for this MW dextran to fit through. The red fluorescence initial decrease is indicative of the membrane breaking during irradiation. The fluorescence decreases as the BSA make-up of the membrane breaks away and diffuses into solution. The membranes stabilise once irradiation was stopped because the bonds only break upon exposure to UV light. Previous DLS characterisation showed that 150 kDa FITC-dextran was 16.5 ± 1.2 nm in size. Using the model detailed in **section 4.3.1.2.1**, the size of the pores created by losing one nanoconjugate is equal to the size of d+S, between 17.6 and 30 nm. 150 kDa dextran should be able to easily disuse through this sized pore. It is important to note that this size pore was made using these very specific parameters which would have to be accurately mirrored for the experiment to be reproducible.

4.3.2.2 2000 kDa FITC-dextran release

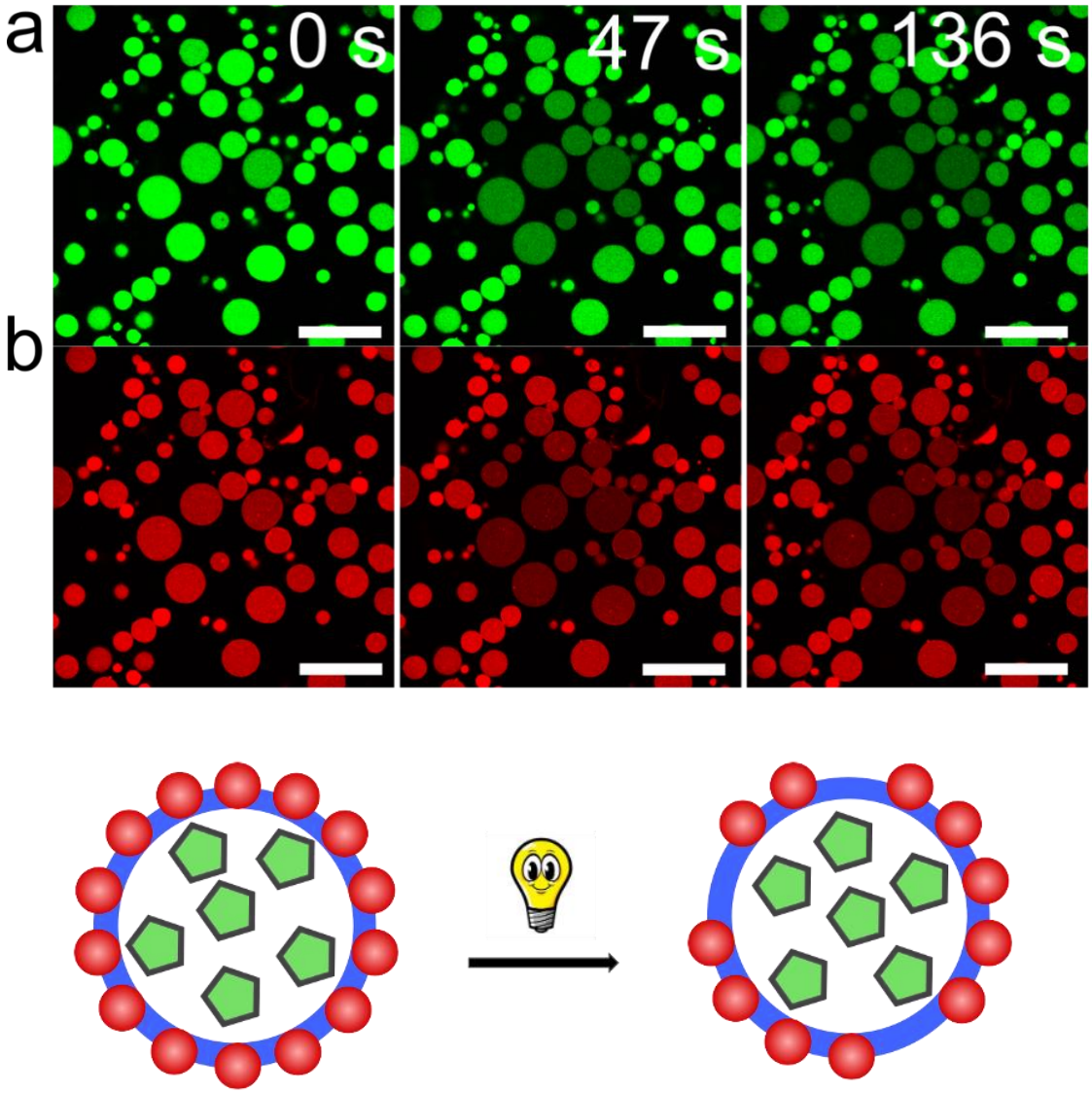

Figure 4.13 A series of confocal images showing the aftermath of 5.5 seconds of 405 nm UV-light irradiation on proteinosomes containing 2000 kDa FITC-dextran. **Far left green channel** - 2000 kDa FITC-tagged dextran encapsulated inside UV light-responsive proteinosomes. **Far left red channel** – RITC-tagged proteinosome population. **Middle green channel** – 47 seconds after the start of the experiment, the dextran fluorescence decreases inside the proteinosome membranes however there is no green fluorescence seen in the surrounding solution. **Middle red channel** - the proteinosome membranes have become less fluorescent but remain intact. **Far right green channel** – after 136 seconds, the dextran fluorescence remains stable. **Far right red channel** - the proteinosome membranes are still intact. The schematic below the microscopy images shows the concept that pores have been created in the

proteinosome membrane however they are not large enough for the large molecular weight substrate to be released.

In order to verify that the pores formed were around the size for only 150 kDa dextran to diffuse through, the same experiment was performed using proteinosomes with encapsulated 2000 kDa dextran. **Figure 4.13** shows a series of confocal microscopy images of proteinosomes with encapsulated 2000 kDa FITC dextran taken at different time points indicated in white on the top right of the image. The experiment was performed under the same conditions as the previous experiment using 5.5 seconds of irradiation. After the irradiation period the green fluorescence was measured for a further period of time to investigate what happens to the encapsulated dextran. After 47 seconds, the green fluorescence inside the proteinosomes decreases but there is no obvious increased fluorescence on the outside of the proteinosomes. Similarly, after 47 seconds, the red channel shows a decrease in fluorescence in the membrane. After 136 seconds, there is no increase in green fluorescence outside the proteinosomes, and the red fluorescence associated with the membrane appears stable.

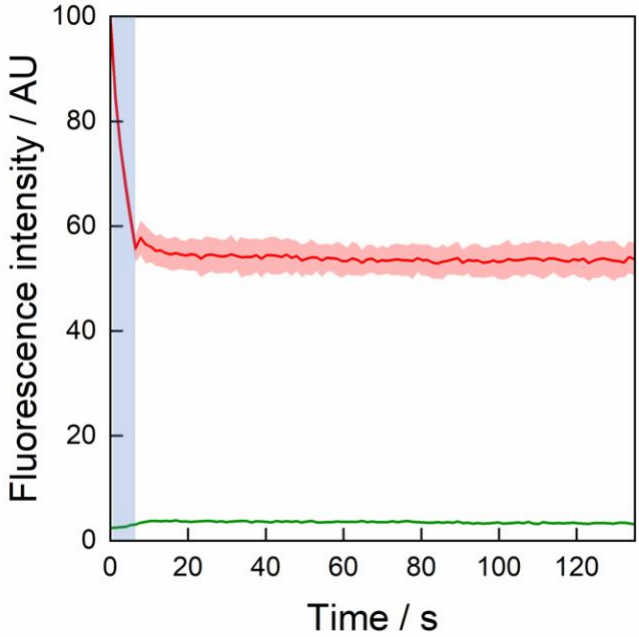

Figure 4.14 Graph showing the behaviour of the fluorescence intensity of the FITC-tagged 2000 k dextran (green curve) and the normalised fluorescence intensity of RITC-tagged BSA-nanoconjugate proteinosome membrane (red curve) after

5.5 seconds of irradiation using a 405 nm laser. **Green curve** – during irradiation (initial 5.5 seconds) the green fluorescence outside the membrane does not increase. After irradiation is terminated, the green fluorescence increases very minimally, indicating a small amount of dextran may have diffused through the membrane. **Red curve** – During irradiation (initial 5.5 seconds) the membrane fluorescence decreases rapidly before stabilising around 57 ± 4 AU. This decrease indicates the membrane has broken down and pores have been made. The red shaded area above and below the curve are the standard deviation of the average normalised fluorescence.

The graph in **Figure 4.14** shows the change in fluorescence of the green fluorescence and normalised red fluorescence associated with the 2000 kDa dextran and proteinosome membrane respectively. During the 5.5 seconds of irradiation, the normalised red fluorescence decreases rapidly from 100 to ca. 57 AU at a rate of 7.8 AU s^{-1}. Once irradiation stops, the fluorescence stabilises at ca. 57 ± 4 AU. Concurrently, the normalised green fluorescence of the solution is very low (just above 0) during irradiation. After irradiation is stopped 5.5 seconds into the experiment, green fluorescence rises very slightly indicating some fluorescent dextran may have diffused through the membrane.

Figures 4.13 and **4.14** show that after 5.5 seconds of irradiation, 2000 kDa dextran is not released through the pores synthesised in the membrane. The confocal images in figure 12 (green channel) show a visual decrease in the fluorescence of the encapsulated dextran which can be attributed to bleaching of the fluorophore. Importantly, there is no visual increase in fluorescence on the outside of the proteinosomes throughout the experiment meaning no dextran is released. Both these observations are reflected in the graph depicting the fluorescence intensity of FITC-tagged 2000 kDa dextran (green curve) outside the proteinosomes, and the RITC-tagged BSA nanoconjugates (red curve). The green curve does not increase significantly, as it did in the previous experiment, staying near to zero throughout further indicating no release of the dextran. The decrease in fluorescence of the RITC-tagged nanoconjugate membrane, both visually and graphically, shows that the membrane is breaking down and pores are being created. According to the model

detailed in **section 4.3.1.2.1**, the size of the pore created with the loss of one nanoconjugate is equal to the size of *d*+S, between 17.6 and 30 nm. The hydrodynamic radius of FITC-dextran at 2000 kDa was determined by DLS to be 20.1 ± 1.4 nm. This agrees with the membrane model, at the lower end of the pore size estimate of *d*+S.

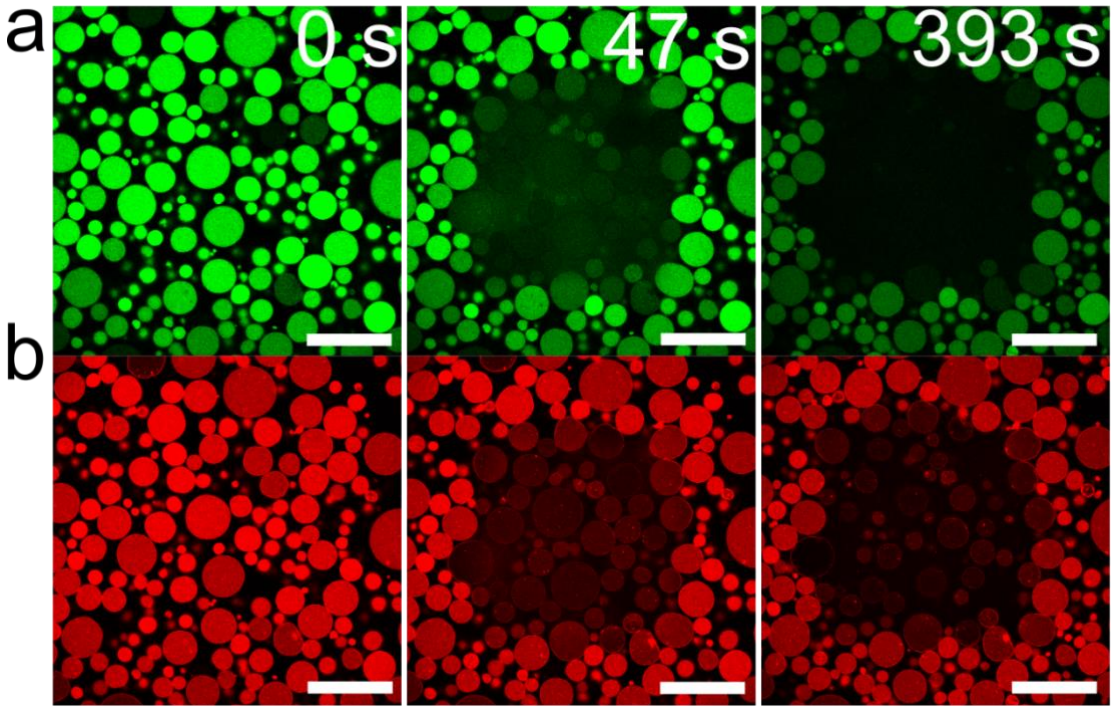

Figure 4.15 A series of confocal images showing the aftermath of 15.5 seconds of 405 nm UV light irradiation on proteinosomes containing 2000 kDa FITC-dextran. **Far left green channel** - 2000 kDa FITC-tagged dextran encapsulated inside UV light-responsive proteinosomes. **Far left red channel** – RITC-tagged proteinosome population. **Middle green channel** – 47 seconds after the start of the experiment, the dextran can be seen dispersed between the proteinosomes after diffusing through pores in the membrane formed during irradiation. **Middle red channel** - the proteinosome membranes have become much less fluorescent but are still intact. **Far right green channel** – after 393 seconds, most of the dextran has diffused away from the proteinosomes into the solution. **Far right red channel** - the proteinosome membranes are significantly smaller but have a very similar level of average fluorescence. The reduction in size is hypothesised to be due to the pores causing the membrane to lose structural integrity and beginning to collapse.

The next experiment used a longer irradiation time which was predicted to create larger pores to facilitate the diffusion of the larger 2000 kDa dextran. **Figure 4.15** shows a series of confocal microscopy images of proteinosomes with encapsulated 2000 kDa FITC dextran taken at different time points indicated in white on the top right of the image. This experiment was performed using the same method as the previous two, except the irradiation time was 10 seconds longer, for 15.5 seconds. After the irradiation period the green fluorescence was measured to investigate the location of the encapsulated dextran. After 47 seconds, the green fluorescence inside the proteinosomes appeared to decrease and the fluorescence on the outside of the proteinosomes increased compared to t=0. The red channel showed a decrease in fluorescence in the membrane in this same period of time. After 393 seconds, the green fluorescence that had accumulated outside the proteinosomes has dissipated, and the red membrane fluorescence has visually stayed about the same.

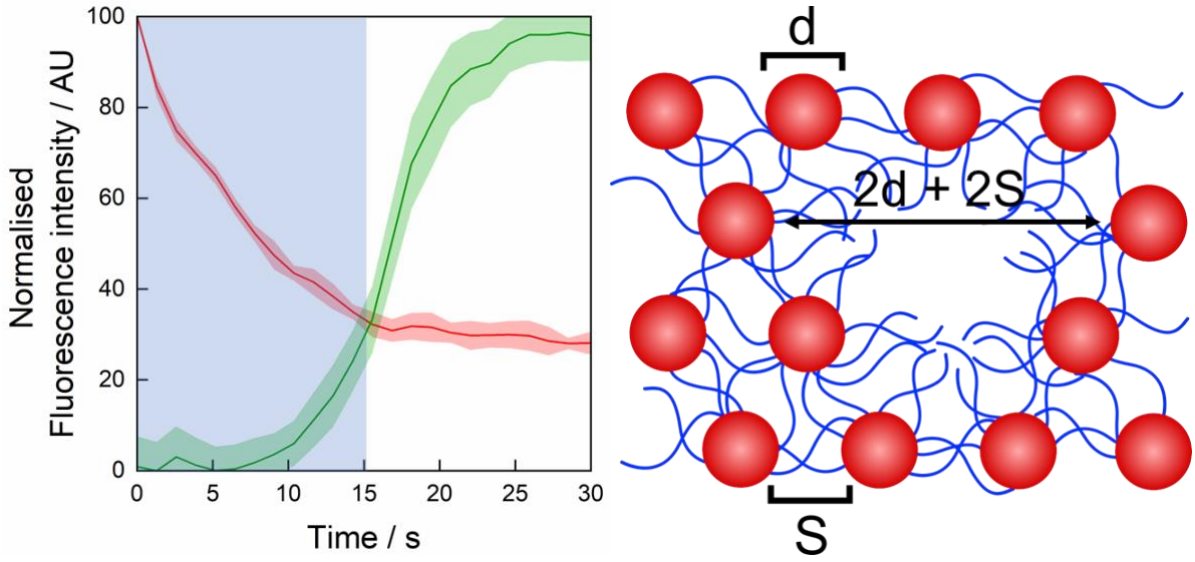

Figure 4.16 Graph showing the behaviour of the normalised fluorescence intensity of FITC-tagged 2000 k dextran (green curve) and the RITC-tagged BSA-nanoconjugate proteinosome membrane (red curve) after 15.5 seconds of irradiation using a 405 nm laser. **Green curve** – during irradiation (initial 15.5 seconds) the green fluorescence outside the membrane begins to increase at ca. 12 s, before increasing rapidly up to a normalised value of 100. This indicates a dextran release beginning during the

irradiation which continues after irradiation is terminated. **Red curve** – During irradiation (initial 15.5 seconds) the membrane fluorescence decreases rapidly before stabilising around 20 ± 1 AU. This decrease indicates the membrane has broken down and as the decrease is much more pronounced, the pores created are much bigger. The red shaded area above and below the curve are plus and minus the standard deviation of the average normalised fluorescence. Using the membrane model from **section 4.3.1.2.1**, a hole created in the membrane by losing two nanoconjugates would be equal to the size of 2(*d*+*S)*, which equates to > 35 nm.

The graph in **Figure 4.16** shows the change in normalised fluorescence of both the green and red fluorescence associated with the 2000 kDa dextran and proteinosome membrane respectively. During the 15.5 seconds of irradiation, the normalised red fluorescence decreases rapidly from 100 to ca. 31 AU at a rate of -5.1 AU s^{-1}. Once irradiation stops, the fluorescence stabilises at ca. 20 ± 1 AU. Concurrently, the normalised green fluorescence of the solution begins to rise rapidly during irradiation. After irradiation is stopped 15.5 seconds into the experiment, green fluorescence outside the proteinosomes rises to a peak at 47 seconds before slowly decreasing towards 0.

Figures 4.15 and **4.16** show that after an extended irradiation time of 15.5 seconds, the larger 2000 kDa FITC-tagged dextran is released from the proteinosome population through the membrane. Both the confocal images and the graph depicting the behaviour of the FITC-dextran and the membrane support this. The confocal images visually show the increased green fluorescence on the outside of the proteinosomes indicating the dextran had diffused through the membrane pores. This is supported by the graph showing the rise in normalised fluorescence intensity to peak at ca. 47 seconds. The red fluorescence associated with the membrane decreased rapidly during the irradiation period and plateaued at a lower normalised average fluorescence than experiments with a lower irradiation time of 5.5 seconds. This indicates that the membrane has broken down further and it is inferred that there are larger pores formed, allowing the larger dextran polymer to diffuse out of the proteinosomes. According to the model detailed in **section 4.3.1.2.1**, the size of the pores created by the loss of 2 nanoconjugates is equal to the size of 2(d+S), < 35 nm.

The hydrodynamic radius of FITC-dextran at 2000 kDa was determined by DLS to be 20.1 ± 1.4 nm which agree with the mathematical description. An interesting additional observation of this experiment is the reduced size of the proteinosomes seen in the far-right red channel in **Figure 4.15**. This is hypothesised to be because of a loss of structural integrity and along with the loss of the internal dextran, this caused the proteinosome membranes to begin to collapse after a long period of time.

4.3.2.3 Evaluation of selective release experiments

The above experiments demonstrate the ability to create pores in the proteinosome membrane using smaller amounts of UV-light irradiation. The size of these pores was shown to be controlled by the length of irradiation, demonstrated with the release of either 150 kDa or 2000 kDa FITC-dextran after 5.5 or 15.5 seconds irradiation, respectively. The experiments agreed with the mathematical description of the pore size in **section 4.3.1.2.1**. If one nanoconjugate, of size *d*+S, is cleaved from the membrane, this would leave a pore between 17.6 and 30 nm. If two nanoconjugates, of size 2(*d*+S), are cleaved, the pore would be larger at > 35 nm. The dextran hydrodynamic radius of 150 kDa FITC dextran at 16.5 ± 1.2 nm would easily diffuse through both pores, however 2000 kDa dextran at 20.1 ± 1.4 nm would not be able to diffuse through the pore from single nanoconjugate loss, at the lower end of the estimate.

Permeability constants were estimated based on work by Joesaar *et al*[28], described in detail in the chapter 4 **appendix**. These constants, in μm min^{-1}, are a description of how the dextran polymer is interacting with the membrane as it diffuses through the pores. It must be noted that bleaching was not accounted for in the estimate for 150 kDa dextran meaning the constant is overestimated. Using **equation 16**, permeability constants of 3.23 and ca. 0.9 μm min^{-1} were found for 2000 and 150 kDa dextran diffusion, respectively. These integers cannot be directly compared to each other as both the pores and the dextran polymers are different sizes, however some insight can be gained by thinking about them individually. A higher permeability constant indicates a higher rate of movement through the pores suggesting the dextran is more easily diffusing through the membrane. Since the constant is larger for 2000 kDa dextran

diffusion, this suggests the pores are much larger than the size of the dextran meaning it diffuses through easily. The 150 kDa dextran has a smaller permeability constant, which suggests the pores are more relative to the size of the dextran hydrodynamic radius meaning diffusion is more hindered. This also agrees with the mathematical description described earlier in the chapter, with pore sizes of between 17.6 and 30 nm for 5.5 seconds irradiation and at > 35 nm for 15.5 seconds.

These experiments could lead to a system in which substrates could be selectively released based on molecular weight using light. A good next step would be an experiment where two populations of proteinosomes (150 kDa dextran encapsulated and 2000 kDa dextran encapsulated) are combined. First, irradiating both populations for 5.5 seconds with UV light will selectively cause the release of the smaller molecular weight dextran (150 kDa) followed by a further 10 seconds of irradiation which will cause the release of the larger 2000 kDa dextran.

4.4 Conclusion

In this chapter, the proteinosome membrane has been analysed experimentally and theoretically to gain a deeper understanding of how the component parts come together and subsequently behave, with special focus on porosity. The membrane MWCO was determined experimentally by encapsulating different MW FITC-dextran polymers inside proteinosomes during synthesis and observing whether remained inside. Encapsulation ratios of 0, 6.7 ± 3.0, 14.6 ± 4.3, and 62.6 ± 17.4 were found for 40, 70, 150 and 2000 kDa respectively. It was inferred from these experiments that the MWCO is somewhere between 40 and 70 kDa, which measured by DLS is between 5.6 ± 1.6 nm and 12.3 ± 0.9 nm. The membrane was subsequently analysed theoretically using De Gennes scaling theory. A polymer network with a concentration in the semi-dilute regime has a characteristic mesh size, ζ (**equation 6**). The PEG-oNB-NHS network in the membrane was assumed to be in the semi-dilute regime, and later confirmed by calculating the volume fraction, ϕ, to be between 0.012 and 0.062. Using the monomer length of 0.35 nm and the estimates for the volume fraction, we get an estimation of the mesh size to be between 2.8 and 9.7 nm. This result aligns remarkably well with the experimental results from **section 4.3.1.1**, finding that 40 kDa dextran (ca. 5.6 nm) diffused freely through the membrane, and 70 kDa dextran (ca. 12.3 nm) was able to be encapsulated. The modelling could be used to predict and design the properties of proteinosome membranes to encapsulate a range of desired components. For example, if the molecular weight of the crosslinker was increased from 2000 kDa to 6000 kDa, this model would predict that the volume fraction would increase to between 0.017 and 0.165 and the corresponding mesh size would decrease to be between 1.4 and 7.5 nm. Simply by increasing the molecular weight of the crosslinker, there is could be a change in the size of the substrates able to be encapsulated. This is impactful to the field because researchers can use this model to understand the system is more detail and can more accurately synthesise proteinosome membranes of more specific mesh sizes.

After previously demonstrating the complete disassembly of the membrane, partial disassembly of the membrane was investigated using smaller bursts of irradiation which caused pores to form. Varying the length of the shorter bursts allowed control over the size of the pores, subsequently allowing selectively of substrate release

based on MW. Two different MW FITC-dextran polymers, 150 and 2000 kDa, were used to demonstrate this behaviour, with the larger polymer unable to diffuse through pores created with smaller irradiation times. The experiments agreed with the mathematical description of the pore size in **section 4.3.1.2.1**. If one nanoconjugate, of size *d*+S, is cleaved from the membrane, this would leave a pore between 17.6 and 30 nm. If two nanoconjugates, of size 2(*d*+S), are cleaved, the pore would be larger at > 35 nm. Using **equation 26**, permeability constants of 3.23 and ca. 0.9 $\mu m\ min^{-1}$ were found for 2000 and 150 kDa dextran diffusion, respectively. These integers cannot be directly compared to each other as both the pores and the dextran polymers are different sizes, however the higher permeability constant for 2000 kDa dextran indicates a higher rate of movement through the pores suggesting the dextran is more easily diffusing through the membrane than the 150 kDa dextran.

This type of in-depth mathematical analysis of the proteinosome membrane has never been performed before, to the best of the authors knowledge, and opens up a new route to the design and synthesis of membranes with specific properties. Of course, there could be improvements to the model to make it more accurate, such as calculating the real contact angle of the nanoconjugates, calculating the real polymer density of PEG-oNB-NHS, and the accounting for the fact that the proteinosomes are not perfectly spherical.

4.5 Appendix

	Units	Mean	Error	Minimum	Maximum
Nanoconjugate diameter / d	nm	13.6	1.6	12	15.2
Inter-conjugate distance / S	nm			5.6	15
Size per nanoconjugate / d + S	nm			17.6	30.2
Hexagon area pervaded per nanoconjugate / a_{nc}	nm^2			268.26	912.04
Proteinosome radius / R	um	11.25			
Proteinosome surface area / $4\pi R^2$	nm^2	1.59E+09			
Number of nanoconjugates per proteinosome / n				5.93E+06	1.74E+06
Number of crosslinking points per nanoconjugate / z		92			
Total number of the crosslinkers in the membrane / $nz/4$				1.36E+08	4.01E+07
molecular mass of PEG-oNB-NHS / m	Da	2260			
Mass of one crosslinker	g	3.75E-21			
Mass density of 2000 PEG / ρ / g	m^{-3}	1.21E+06			
Molecular volume of 2000 Da PEG / v_L	m^3	3.10E-27			
Molecular volume of 2000 Da PEG / v_L	nm^3	3.10			
Fraction of submerged nanoconjugates / δ		0.5			
Shell thickness / $t = \delta d$	nm			6	7.6
Shell volume / V_s	m^3			9.543E-18	1.209E-17
Shell volume / V_s	nm^3			9.543E+09	1.209E+10
Nanoconjugate volume submerged / v_{nc}	nm^3			452.39	919.39
Total volume of nanoconjugates in membrane / V_c	nm^3			2.68E+09	1.60E+09
solution volume pervaded by the crosslinkers / V_x	nm^3			6.86E+09	1.05E+10
solution volume pervaded by the crosslinkers / V_x	m^3			6.86E-18	1.05E-17
Volume fraction of crosslinker / ϕ				0.062	0.012
Monomer size / a	nm				0.35
Mesh size / ξ	nm			**2.8**	**9.7**

Table 1 A table of all the integers used to estimate the volume fraction and therefore the mesh size of the proteinosome membrane crosslinked with PEG-oNB-NHS.

4.5.1 Estimating the permeability constant of the membrane

Assuming a perfectly spherical proteinosome, the flux of a caged chemical species J_i (mol m^{-2} s^{-1}) that diffuses out through the membrane can be described using Fick's first diffusion law in one-dimension:

$$J_i = -D_i \frac{\partial C_i}{\partial x} \tag{20}$$

where D_i is the diffusion coefficient of species *i* (m^2 s^{-1}), C_i is the concentration of species *i* (mol m^{-3}), and x is its position (m). The negative sign takes into account the exit of the caged chemical species from the proteinosome.

For the movement of caged chemical species *i* through the membrane, and assuming the system is well mixed, equation (10) can be written as:

$$J_i = -D_i \frac{\left(C_{,i} - C_{out,i}\right)}{\Delta x} \tag{21}$$

where Δx is the proteinosome membrane's thickness. Assuming that the thickness is uniform, equation (11) can be rearranged in the following way:

$$J_i = \frac{-D_i}{\Delta x}\left(C_{,i} - C_{out,i}\right) = P\left(C_{out,i} - C_{,i}\right) \tag{22}$$

where $P = \frac{-D_i}{\Delta x}$ is the proteinosome permeability constant (m s^{-1}).

To describe the change in moles of caged species *i* over time $\left(\frac{dn_{,i}}{dt}\right)$(mol s^{-1}), multiply J_i (mol m^{-2} s^{-1}) by the surface area of the proteinosome, A (m^2) to produce:

$$\frac{dn_{,i}}{dt} = J_i \cdot A = AP\left(C_{out,i} - C_{,i}\right) \tag{23}$$

To describe the change in concentration of caged species *i* over time $\left(\frac{dC_{,i}}{dt}\right)$(mol m^{-3} s^{-1}), equation (13) is divided by the proteinosome volume, V (m^3):

$$\frac{dC_{,i}}{dt} = \frac{A \cdot J_i}{V} = \frac{3P}{r}\left(C_{out,i} - C_{,i}\right) \tag{24}$$

where *r* is the radius of the proteinosome (m).

Equation (14) can now be rearranged to describe the proteinosome permeability constant (*P*):

$$P = \frac{r}{3\left(C_{out,i} - C_{,i}\right)}\frac{dC_{,i}}{dt} \tag{25}$$

Because at time zero, $C_{out,i} = 0$, consequently:

$$P = -\left(\frac{r}{3C_{,0}}\right)\left(\frac{dC_{,i}}{dt}\right) \tag{26}$$

where $\frac{dC_{,i}}{dt}$ is the initial slope of the graph of variation of concentration over time of the chemical species *i* (*e.g.*, caged fluorescent tagged dextran) caged inside the proteinosome, which is negative (as a result of outward flux), and $C_{,0}$ is the initial concentration of substrate, in M. The proteinosome permeability constant (*P*) is therefore a positive number.

Using the above derivative, the permeability constants for 150 and 2000 kDa FITC-dextran can be estimated. The parameters needed would be the initial concentration ($C_{,0}$), the average proteinosome radius (r), and the change in concentration over time ($\frac{dC_{,i}}{dt}$).

2000 kDa FITC-dextran: The average radius of the proteinosomes can be measured at the beginning of the experiment, when time = 0, to be 17.3 μm (17.3 x10^{-6} m). The initial concentration of the dextran is 1 mg mL^{-1}, which is equal to 0.5 x10^{-6} M. The change in concentration can be determined by plotting the change in concentration against time and finding the gradient of a linear fitting for 16-30 seconds, which is just after irradiation is terminated. The plot was adjusted to take into account bleaching of the FITC-dextran. The gradient was estimated to be -0.28 mM min^{-1}. Using **equation 26** The permeability constant was determined to be 3.23 μm min^{-1}.

150 kDa FITC-dextran: The average radius of the proteinosomes can be measured at the beginning of the experiment, when time = 0, to be 14.2 μm (14.2 x10^{-6} m). The initial concentration of the dextran is 1 mg mL^{-1}, which is equal to 6.67 x10^{-6} M. The

change in concentration can be determined by plotting the change in concentration against time and finding the gradient of a linear fitting for 16-30 seconds, which is just after irradiation is terminated. This plot was not adjusted to take into account bleaching and so the gradient of the linear fit is overestimated. The gradient was estimated to be -1.28 mM min^{-1}. Using **equation 26** The permeability constant was determined to be ca.0.9 $\mu m\ min^{-1}$. In reality, the magnitude of the gradient will be lower (closer to zero) once bleaching has been accounted for, leading to a smaller permeability constant.

References

[1] C. R. Woese, O. Kandlert, M. L. Wheelis, *Proc. Nati. Acad. Sci.* **1990**, *87*, 4576–4579.

[2] M. Bretscher, *Sci. Am.* **1985**, *253*, 100–109.

[3] S. T. Rutherford, B. L. Bassler, *Cold Spring Harb. Perspect. Med.* **2012**, *2*.

[4] D. Sadava, *LIFE: The Science of Biology*, Sinauer Associates, **2014**.

[5] R. Lentini, S. P. Santero, F. Chizzolini, D. Cecchi, J. Fontana, M. Marchioretto, C. Del Bianco, J. L. Terrell, A. C. Spencer, L. Martini, M. Forlin, M. Assfalg, M. D. Serra, W. E. Bentley, S. S. Mansy, *Nat. Commun.* **2014**, *5*.

[6] R. Lentini, N. Y. Martín, M. Forlin, L. Belmonte, J. Fontana, M. Cornella, L. Martini, S. Tamburini, W. E. Bentley, O. Jousson, S. S. Mansy, *ACS Cent. Sci.* **2017**, *3*.

[7] T. Y. D. Tang, D. Cecchi, G. Fracasso, D. Accardi, A. Coutable-Pennarun, S. S. Mansy, A. W. Perriman, J. L. R. Anderson, S. Mann, *ACS Synth. Biol.* **2018**, *7*, 339–346.

[8] S. Sun, M. Li, F. Dong, S. Wang, L. Tian, S. Mann, *Small* **2016**, *12*, 1920–1927.

[9] L. Rodríguez-Arco, M. Li, S. Mann, *Nat. Mater.* **2017**, *16*, 857–863.

[10] Y. Zhou, J. Song, L. Wang, X. Xue, X. Liu, H. Xie, X. Huang, *Biomacromolecules* **2017**, *18*, 2446–2453.

[11] X. Huang, M. Li, D. C. Green, D. S. Williams, A. J. Patil, S. Mann, *Nat. Commun.* **2013**, *4*, 1–9.

[12] P. Zhou, X. Liu, G. Wu, P. Wen, L. Wang, Y. Huang, X. Huang, *ACS Macro Lett.* **2016**, *5*, 961–966.

[13] P. Zhou, S. Wu, X. Liu, M. Hegazy, G. Wu, X. Huang, *ACS Applied Materials and Interfaces* **2018**, 10, 38565-38573.

[14] S. W. Hell, M. Dyba, S. Jakobs, *Curr. Opin. Neurobiol.* **2004**, *14*, 599–609.

[15] M. Ul-Islam, M. W. Ullah, T. Khan, J. K. Park, *Handb. Hydrocoll.* **2021**, 923–974.

[16] N. Vogt, *Nat. Methods 2021 188* **2021**, *18*, 859–859.

[17] P. G. de Gennes, *Scaling Concepts in Polymer Physics*, Cornell University Press, **1979**.

[18] W. H. Briscoe, *Polymers and Nanoscience*, Elsevier B.V., **2014**.

[19] P. J. Flory, *Stat. Mech. Cross-Linked Polym. Networks II. Swelling J. Chem. Phys.* **1941**, *9*, 279.

[20] P. J. Flory, *Principles of Polymer Chemistry*, New York, **1953**.

[21] V. Sorichetti, V. Hugouvieux, W. Kob, *Macromolecules* **2020**, *53*, 2568–2581.

[22] W. W. Graessley, *Polymer (Guildf).* **1980**, *21*, 258–262.

[23] V. Sorichetti, V. Hugouvieux, W. Kob, *Macromolecules* **2020**, *53*, 2568–2581.

[24] A. Y. Grosberg, J. F. Joanny, W. Srinin, Y. Rabin, *J. Phys. Chem. B* **2016**, *120*, 6383–6390.

[25] Y. Rabin, A. Y. Grosberg, **2021**, *14*, 3.

[26] B. Brodin, B. Steffansen, C. Uhd Nielsen, *Mol. Biopharm.* **2010**, *18*, 9–10.

[27] L. Zhou, K. Nyberg, A. C. Rowat, *Adv. Physiol. Educ.* **2015**, *39*, 192–197.

[28] A. Joesaar, S. Yang, B. Bögels, A. van der Linden, P. Pieters, B. V. V. S. P. Kumar, N. Dalchau, A. Phillips, S. Mann, T. F. A. de Greef, *Nat. Nanotechnol. 2019 144* **2019**, *14*, 369–378.

[29] J. Stetefeld, S. A. McKenna, T. R. Patel, *Biophys. Rev.* **2016**, *8*, 409–427.

[30] X. Huang, M. Li, D. C. Green, D. S. Williams, A. J. Patil, S. Mann, *Nat. Commun.* **2013**, *4*, 1-9.

[31] P. Gobbo, A. J. Patil, M. Li, R. Harniman, W. H. Briscoe, S. Mann, *Nat. Mater.* **2018**, *17*, 1145–1153.

[32] Merck, “Fluorescein isothiocyanate–dextran,” can be found under https://www.sigmaaldrich.com/GB/en/product/sigma/fd2000s, **2022**.

[33] A. D. Dinsmore, M. F. Hsu, M. G. Nikolaides, M. Marquez, A. R. Bausch, D. A. Weitz, *Science* **2002**, *298*, 1006–9.

[34] J. K. Armstrong, R. B. Wenby, H. J. Meiselman, T. C. Fisher, *Biophys. J.* **2004**, *87*, 4259–4270.

[35] A. D. Dinsmore, M. F. Hsu, M. G. Nikolaides, M. Marquez, A. R. Bausch, D. A. Weitz, *Science* **2002**, *298*, 1006–9.

[36] I. Myrgorodska, M. Jenkinson-Finch, R. O. Moreno-Tortolero, S. Mann, P. Gobbo, *Macromol. Rapid Commun.* **2021**, *42*.

[37] “Polyethylene glycol 2000 CAS 25322-68-3 | 821037,” can be found under https://www.merckmillipore.com/GB/en/product/Polyethylene-glycol-2000,MDA_CHEM-821037, **2022.**

[38] D. B. Chithrani, *J. Nanomedicine Res. Polyethyl. Glycol Density Length Affect. Nanoparticle Uptake by Cancer Cells Res. Artic.* **2014**, *1*.

[39] “How big is a human cell?,” can be found under http://book.bionumbers.org/how-big-is-a-human-cell/, **n.d.**

Chapter 5: Conclusions and future work

Chapter outline

This chapter concludes the results chapters briefly, and describes future experiments that can be performed to build upon the work.

5.1 The synthesis and characterisation of PEG-based NHS-functionalised and stimuli-responsive crosslinkers

The synthesis and characterisation of two novel stimuli-responsive polymers was described. The first contained a core ketal moiety which was shown to be relatively stable at pH 6.5 and above and was hydrolysed rapidly at pH 6 and below (PEG-ketal-NHS). The second was terminated in *o*-nitrobenzyl derivatives which was shown to have a large molar attenuation coefficient at 347 nm, and photolysed upon irradiation with UV-light of 350 and 365 nm (PEG-oNB-NHS). Both polymers were terminated with NHS-activation allowing facile crosslinking of nucleophilic substrates, such as proteins and CM-chitosan.

With the $t_{1/2}$ of PEG-ketal-NHS of 9 hours at pH 7.5 (physiological pH = ca. 7.4), this indicates it could easily be used in nucleophilic soft-material drug delivery systems targeting tissues such as cancer, small intestines, and the stomach, all of which function at lower pH values. Further, the $t_{1/2}$ could be tuned by modifying the crosslinker to have cyclic ketone moieties for example.

PEG-oNB-NHS was found to photolyse well with UV-light of 350 and 365 nm. A further experiment would be to explore the photolysis at 405 nm where the crosslinker is absorbing much less light, as wavelengths above 400 nm are more suitable to applications in the biomedical industry to avoid cellular damage and increase tissue penetration depth.[1] Further investigations into the calculation of the rate constant for

degradation of PEG-oNB-NHS would complete the characterisation of photolysis behaviour.

Another route for the construction of crosslinkers suited to biomedical applications would be to synthesise a crosslinker which absorbs in the NIR light range, which has been shown to effectively penetrate biological tissue.[1] Moieties such as 4,4-difluoro-4-bora-3a,4a-diaza-s-indacene (BODIPY) have absorption bands in the range of γ_{max} = 490-540 nm in their simple form, but can be modified to absorb up to 650-700 nm with the addition of π-extending and meso-methyl groups (**Figure 5.1**).[2,3] BODIPY has been demonstrated as a photo-caging group with photoactive delivery of histamine in living cells.[4] Considering this, if BOPIDY was used as the photosensitive moiety in an NHS activated PEG crosslinker, the construction of synthetic cells and soft-materials that are able to deliver biologically active molecules and drugs in tissues could be investigated. Alternatively, upconverting nanoparticles which both absorb light in the NIR range, and emit UV-light that would cleave PEG-oNB-NHS, could be incorporated into the system.[5]

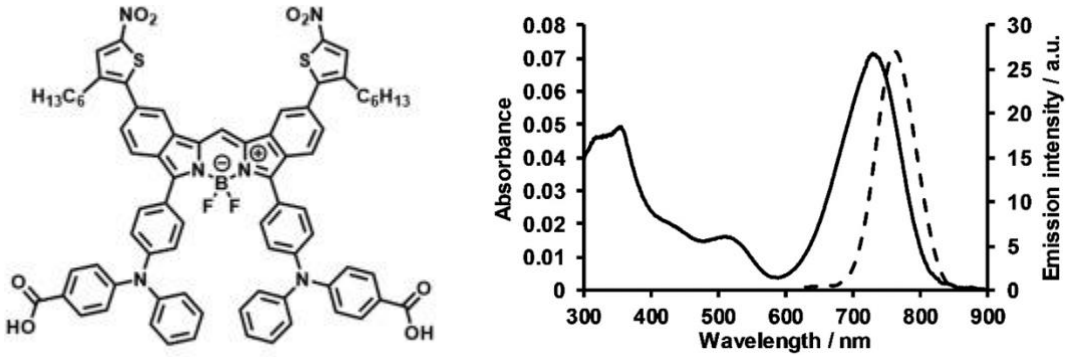

Figure 5.1 An example of a π-extended BODIPY molecule with absorbance in the NIR region, ca. 700 nm. Images reproduced from Kubo *et al*, 2019.

The beauty of light-responsive smart materials is the ability to take advantage of the high specificity of the functional groups. Two functional groups can be used in conjunction that have different properties, such as absorption maxima (λ_{max}).[6] Orthogonal cleavage of the leaving groups with high specificity can subsequently be achieved. This approach could be adopted in this work, by synthesising crosslinkers

with different λ_{max} which could be used to construct different populations of synthetic cells. Light-triggered chemical reactions could subsequently be performed in any order and in the presence of the other population of light-responsive cells.

5.2 The construction of stimuli-responsive proteinosomes

The construction of proteinosomes with light-responsive proteinosome membranes was described, utilising the PEG-oNB-NHS crosslinker synthesised in chapter 2. Disassembly of the membrane was demonstrated and quantified by plotting the fluorescence loss from the membrane. The relationship between the disassembly time and laser power was found to be inversely proportional, whilst there was a positive correlation between disassembly time and laser scan speed. These relationships could be used in future experiments to predict the disassembly time of proteinosome populations when using specific laser powers and scan speeds. A software-controlled positioning system was used to demonstrate photo-patterning of proteinosome populations with positive, negative, and more complex designs. The software also allowed very precise targeting demonstrated through the selective disassembly of an individual capsule out of a large mixed population of responsive and non-responsive proteinosomes. The laser can be used sufficiently precisely that even parts of the membrane can be targeted and disassembled, demonstrated by the selective disassembly of the top half of a proteinosome.

Using this targeting method, investigations into the light-activated communication between protocell populations could be explored to create smart and functional protocell communities. A proof-of-concept experiment is shown in **Figure 5.2**. Light could be used to activate the membrane of proteinosomes causing an encapsulated substrate to be released. As that substrate is detected by the other protocell population, a signal is emitted in response.

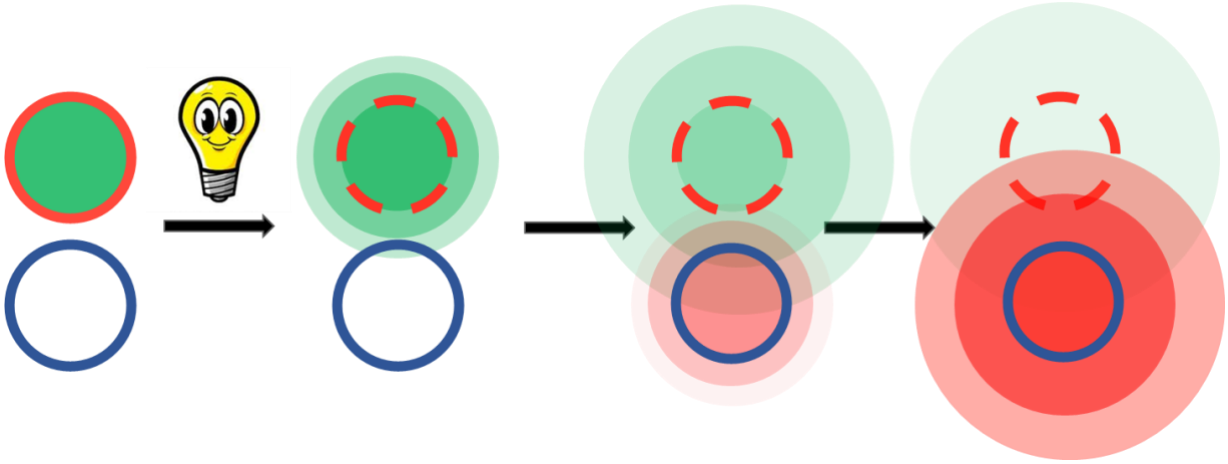

Figure 5.2 From left to right: Two populations of proteinosomes are synthesised, with one constructed using PEG-oNB-NHS (red), endowing it with light-activated disassembly, and containing a substrate which will produce a response in the second population. Light initiates the release of the substrate. As the substrate is sensed by the second population (blue), a signal is emitted.

Enzyme cascade reactions are commonly used to demonstrate primitive forms of communication between proteinosome populations.[7–10] An enzymatic system that would work for proteinosome based systems, in term of design constraints (*i.e.* permeable proteinosome membrane to small molecules), would be the use of amyloglucosidase (AGx), glucose oxidase (GOx), and horseradish peroxidase (HRP) cascade, a commonly used catalytic cascade (**Figure 5.3**).[11] Starch would be a good candidate for encapsulation within the PEG-oNB-NHS proteinosomes with its high molecular mass, which can be treated with sodium hydroxide for more effective enzyme hydrolysis.[12] Starch will be released through the pores upon irradiation and can be broken down into glucose by AGx, which can be present in the solution. GOx, encapsulated within the second population, will convert the glucose to gluconic acid and H_2O_2. HRP will subsequently use H_2O_2 to convert the substrate Amplex Red to resorufin. Importantly, resorufin has a λ_{max} at ca. 580 nm, which is well above the λ_{max} of PEG-oNB-NHS.

Communication between communities of protocells, as described above, could certainly find applications in sensing and biotechnology. However, the communication of protocells with living cells, and the triggering of communications in a controlled

manner, would have a profound impact in the field of biointerfacing. For example, it would facilitate non-invasive drug delivery, and light-triggered, targeted, controlled stem cell differentiation.[13] In terms of communication between networks of protocells, work by Booth et al[14] showed light could be used to precisely control communication pathways through a synthetic tissue comprising hundreds of individual cells. The biocompatibility of proteinosomes invites the possibility of constructing prototissues that can be interfaced with living tissue. Further, the photopatterning technique could be used as a method to create bespoke shaped 3D prototissues or prototissue patterning.[15] There has been recent research developing prototissues using proteinosomes as the building blocks.[16,17] By crosslinking the proteinosomes with PEG-oNB-NHS, the confocal based software-controlled positioning system could be used to carve the prototissues into virtually any desired 3D shape or pattern, providing the opportunity to use the prototissues as smart biocompatible scaffolds in biological tissue engineering.[18,19]

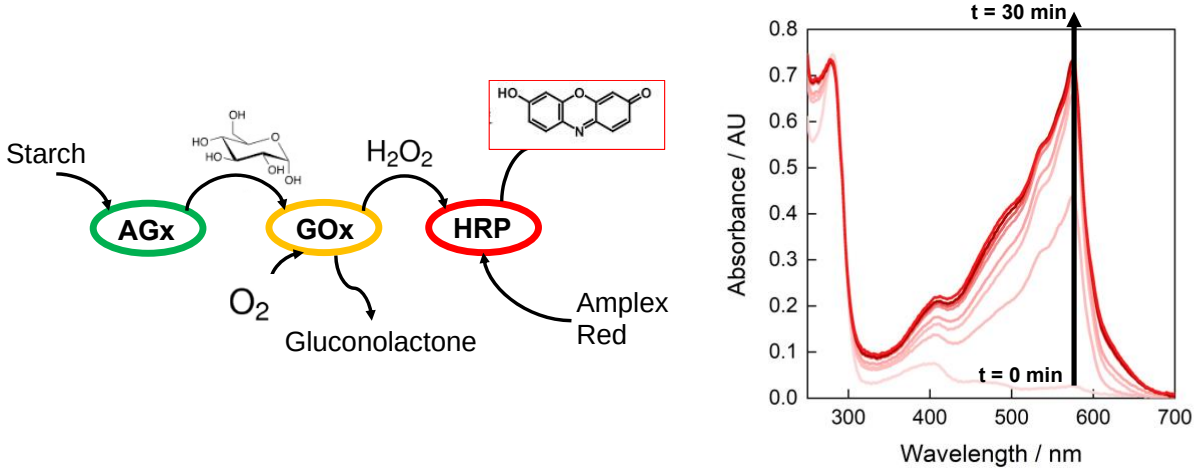

Figure 5.3 Starch is broken down into glucose by AGx into glucose molecules. GOx converts glucose to gluconic acid and H_2O_2 which is utilised by HRP to convert the substrate Amplex Red to resorufin, a molecule with inherent fluorescent properties having a λ_{max} at ca. 580 nm.

When the light-responsive proteinosomes are synthesised, the starting materials are mixed homogeneously, yet the resulting capsules have varying characteristics. Some are more fluorescent than others, some are larger, and some are deformed (less

circular). One big question arising from the analysis of PEG-oNB-NHS crosslinked proteinosome photolysis was the variation in disassembly times within the population. As seen in **Figure 5.4** (repeated for ease), there is a large standard deviation within the fluorescence intensity just after the disassembly time, which decreases as the irradiation continues. This corresponds to the proteinosomes disassembling at varying rates, with some disassembling before others. The question was asked whether the varying characteristics observed bared any influence over the disassembly times of the proteinosomes, much like natural selection processes seen in nature.

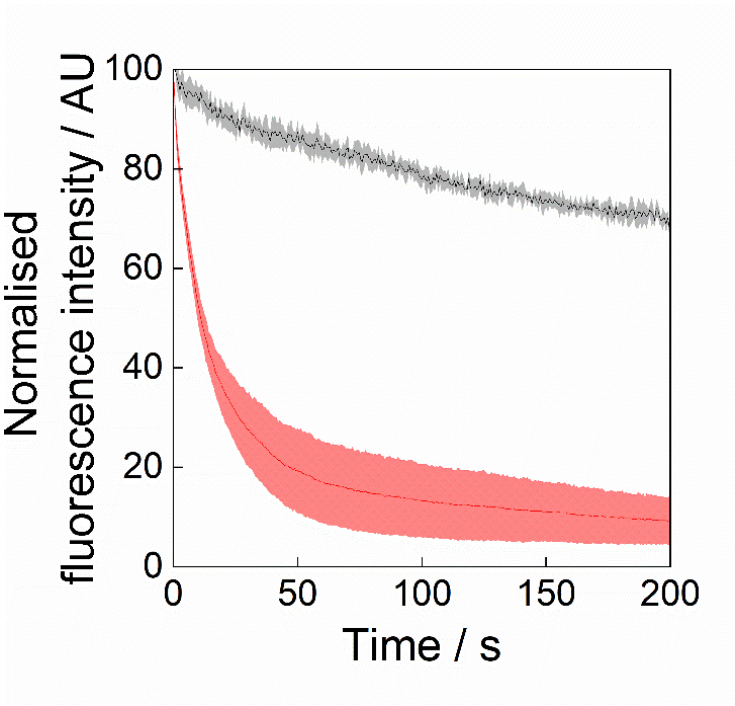

Figure 5.4 A plot of fluorescence intensity versus time during the irradiation of PEG-oNB-NHS crosslinked proteinosomes (from **section 3.3.2.3**). There is a large standard deviation seen in the red curve indicating a large discrepancy in disassembly times.

A preliminary investigation was conducted into elucidating whether proteinosome characteristics influence the disassembly time, whether that be diameter, circularity (how much they conform to a perfect circle), initial brightness, distance to neighbour proteinosome, and porosity. Proteinosomes with a high permeability, for example, might have less membrane crosslinking which allows larger molecules to enter. Firstly, disassembly times were calculated for a large number of proteinosomes using a

programme made for image J software. This work was done in conjunction with colleagues in the Wolfson bioimaging facility. These proteinosomes were irradiated with 70 μW laser (rather than 2266 μW in **Figure 5.4**) to attempt to spread out the disassembly times and more easily see a pattern. A histogram of these results is shown in **Figure 5.5**.

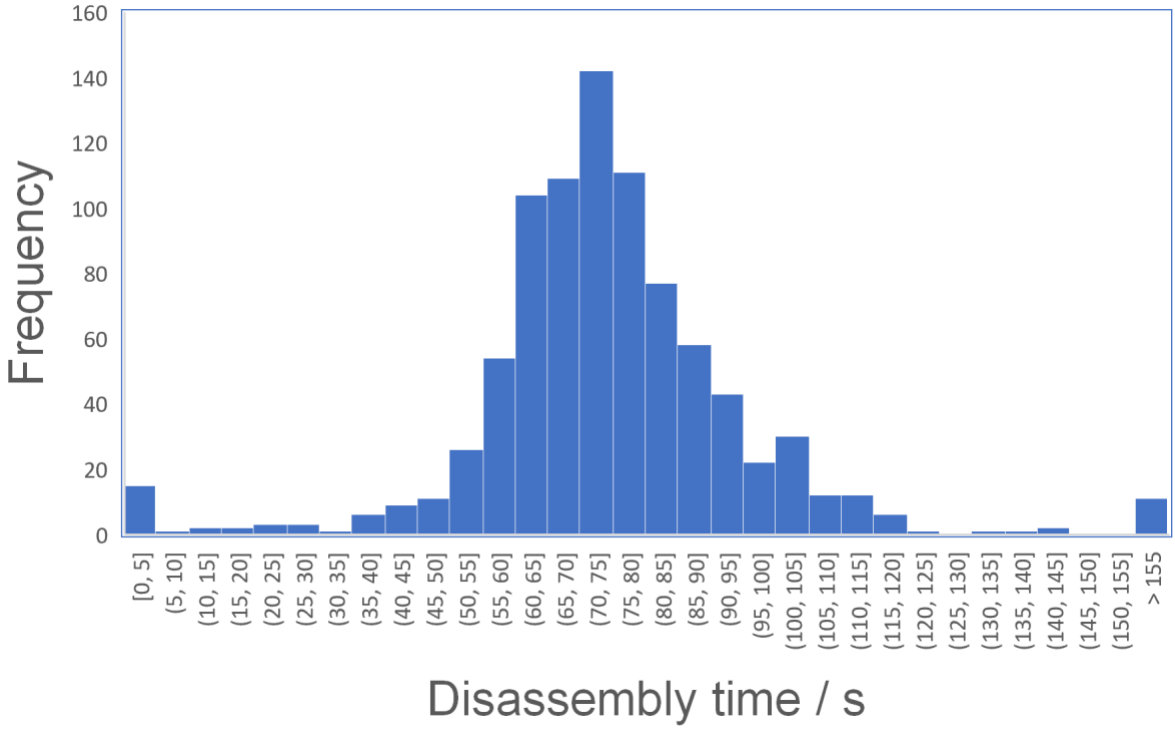

Figure 5.5 A histogram showing the disassembly times of over 800 different proteinosomes.

The characteristics of the proteinosomes were matched to their corresponding disassembly time and then plotted against each other to see if there were any emerging patterns. **Figure 5.6** shows two example plots created from the data. The first set of data showed proteinosomes 20 μm and above all had very similar disassembly times, but smaller proteinosomes (under 20 μm) tended to have a wide range of disassembly times. The second set of data showed no correlation between permeability and disassembly time. To answer the question whether the smaller proteinosomes could be grouped together showing similar disassembly behaviours, machine learning techniques could be implemented to analyse and identify patterns

in the data. The learnings from a detailed investigation like this could be used as a method to create protocells with precise disassembly properties, and therefore would be useful in biointerfacing and controlled delivery of drugs.

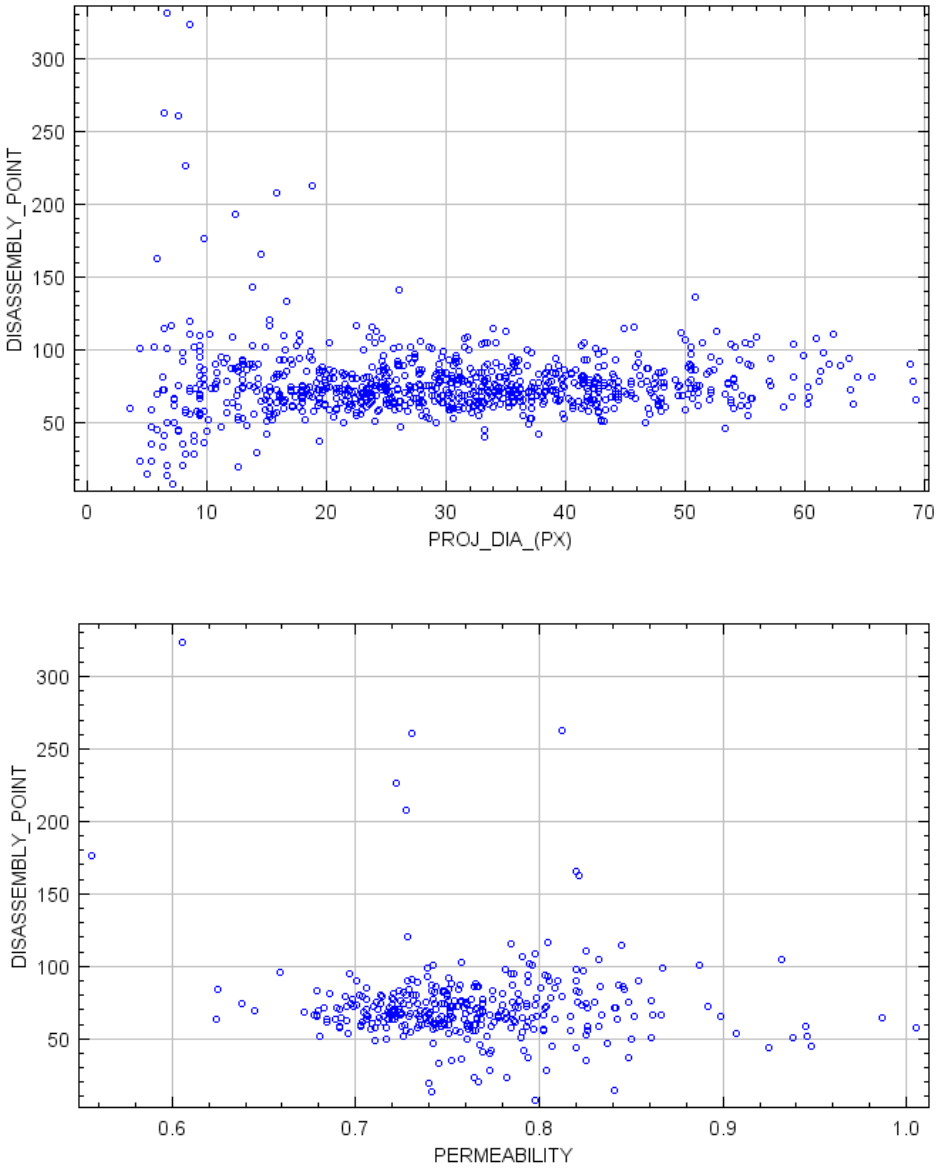

Figure 5.6 Plots of diameter and permeability versus disassembly time (top and bottom plots, respectively). Each point is an individual proteinosome with the corresponding diameter or permeability, and disassembly time. Proteinosome diameter was measured using customised imaging software that fitted a circle on top of the proteinosomes. To calculate permeability, the proteinosomes were incubated

with 70 kDa FITC-dextran for 30 minutes. The ratio of the inside fluorescence to the outside fluorescence was calculated as the permeability for each proteinosome.

5.3 A deeper analysis of proteinosome membrane structure

In this chapter, the proteinosome membrane was analysed experimentally and theoretically to gain a deeper understanding of how the component parts come together and subsequently behave, with special focus on porosity. The membrane MWCO was determined experimentally, and it was inferred from these experiments that the MWCO is somewhere between 40 and 70 kDa, which measured by DLS is between 5.6 ± 1.6 nm and 12.3 ± 0.9 nm. The membrane was subsequently analysed theoretically using De Gennes scaling theory. The proteinosome membrane was calculated to have a volume fraction, ϕ, to be between 0.012 and 0.062, which is the semi dilute regime. Using the monomer length of 0.35 nm an estimation of the mesh size was calculated to be between 2.8 and 9.7 nm. This result aligns remarkably well with the experimental results from **section 4.3.1.1**, finding that 40 kDa dextran (ca. 5.6 nm) diffused freely through the membrane, and 70 kDa dextran (ca. 12.3 nm) was able to be encapsulated. This mathematical description of the membrane is impactful to the field because researchers can use this model to understand the system is more detail and can more accurately synthesise proteinosome membranes of more specific mesh sizes.

Partial disassembly of the membrane was investigated using smaller bursts of irradiation which caused pores to form. Varying the length of the shorter bursts allowed control over the size of the pores, subsequently allowing selectively of substrate release based on MW. Two different MW FITC-dextran polymers, 150 and 2000 kDa, were used to demonstrate this behaviour, with the larger polymer unable to diffuse through pores created with smaller irradiation times. The theoretical pore sizes of d+S and 2(d+S) agreed with the experimental results. Permeability constants of 3.23 and ca. 0.9 μm min^{-1} were found for 2000 and 150 kDa dextran diffusion, respectively with the higher permeability constant for 2000 kDa dextran indicating a higher rate of movement through the pores, suggesting the dextran is more easily diffusing through the membrane than the 150 kDa dextran. This type of membrane specificity is similar

to that of active transport seen in biological cell membranes, and this system could be developed further to demonstrate light-triggered selective uptake of substrates.

This type of in-depth mathematical analysis of the proteinosome membrane has never been performed before, to the best of the authors knowledge, and opens a new route to the design and synthesis of membranes with specific properties. Of course, there could be improvements to the model to make it more accurate, such as: calculating an accurate contact angle of the nanoconjugates; calculating an accurate polymer density of PEG-oNB-NHS; accounting for the fact that the proteinosomes are not perfectly spherical; and accounting for the PNIPAAm on the nanoconjugates. However, this work is an excellent start towards making an accurate model that explains the structure of the proteinosome membrane.

References

[1] M. C. Sharp, *Biophotonics Med. Appl.* **2015**, 79–98.

[2] R. Weinstain, T. T. Slanina, D. Kand, P. K. Klán, *Chem. Rev.* **2020**, 120, 13135-13272.

[3] Y. Higashino, S. Erten-Ela, Y. Kubo, *Dye. Pigment.* **2019**, *170*, 107613.

[4] N. Rubinstein, P. Liu, E. W. Miller, R. Weinstain, *Chem. Commun.* **2015**, *51*, 6369–6372.

[5] Y. Yang, B. Velmurugan, X. Liu, B. Xing, *Small* **2013**, *9*, 2937–2944.

[6] M. J. Hansen, W. A. Velema, M. M. Lerch, W. Szymanski, B. L. Feringa, *Chem. Soc. Rev.* **2015**, *44*, 3358–3377.

[7] X. Huang, M. Li, S. Mann, *Chem. Commun.* **2014**, *50*, 6278–6280.

[8] R. Booth, Y. Qiao, M. Li, S. Mann, *Angew. Chemie Int. Ed.* **2019**, *58*, 9120–9124.

[9] S. Sun, M. Li, F. Dong, S. Wang, L. Tian, S. Mann, *Small* **2016**, *12*, 1920–1927.

[10] T. Y. D. Tang, D. Cecchi, G. Fracasso, D. Accardi, A. Coutable-Pennarun, S. S. Mansy, A. W. Perriman, J. L. R. Anderson, S. Mann, *ACS Synth. Biol.* **2018**, *7*, 339–346.

[11] V. K. Kadambar, M. Bellare, P. Bollella, E. Katz, A. Melman, *Chem. Commun.* **2020**, *56*, 13800–13803.

[12] U. Uthumporn, Y. N. Shariffa, A. Fazilah, A. A. Karim, *Colloid Polym. Sci. 2012 29015* **2012**, *290*, 1481–1491.

[13] P. J. Grimes, A. Galanti, P. Gobbo, *Front. Mol. Biosci.* **2021**, *8*, 1275.

[14] M. J. Booth, V. R. Schild, A. D. Graham, S. N. Olof, H. Bayley, *Sci. Adv.* **2016**, *2*.

[15] K. A. Mosiewicz, L. Kolb, A. J. Van Der Vlies, M. M. Martino, P. S. Lienemann, J. A. Hubbell, M. Ehrbar, M. P. Lutolf, *Nat. Mater.* **2013**, *12*, 1072–1078.

[16] P. Gobbo, A. J. Patil, M. Li, R. Harniman, W. H. Briscoe, S. Mann, *Nat. Mater.* **2018**, *17*, 1145–1153.

[17] A. Galanti, R. O. Moreno-Tortolero, R. Azad, S. Cross, S. Davis, P. Gobbo, *Adv. Mater.* **2021**, *33*, 2100340.

[18] F. Rosso, G. Marino, A. Giordano, M. Barbarisi, D. Parmeggiani, A. Barbarisi, *J. Cell. Physiol.* **2005**, *203*, 465–470.

[19] S. Correia Carreira, R. Begum, A. W. Perriman, *Adv. Healthc. Mater.* **2020**, *9*.